UNIVERSITÀ DEGLI STUDI DI UDINE

DIPARTIMENTO POLITECNICO DI INGEGNERIA E ARCHITETTURA

PHD IN INDUSTRIAL AND INFORMATION ENGINEERING

FLYWHEEL PROOF MASS ACTUATOR FOR VELOCITY FEEDBACK AND VIBRATION CONTROL

AUTHOR:
Aleksander Kras

SUPERVISOR:
Prof. Paolo Gardonio

UDINE 2018

"If you want to find the secrets of the universe,
think in terms of energy, frequency and vibration."

Nikola Tesla

ABSTRACT

This thesis presents a comprehensive study on the design and development of a new inertial actuator for the active vibration control. This linear inertial transducer can be used to implement decentralised velocity feedback control loops to reduce flexural vibration of thin structures.

Such active vibration control system is typically formed by an inertial actuator attached on one side of the structure and a collocated velocity sensor attached on the other side with a constant gain controller. This arrangement creates skyhook damping effect that can be effectively used to reduce the out-of-plane vibrations of the structure. To guarantee the stability and thus good control performance, the fundamental resonance frequency of the actuator must be as low as possible and lower than the fundamental resonance frequency of the hosting structure. This requirement imposes that the inertial actuator is composed by a heavy inertial mass and soft suspension. However, when the hosting structure is exposed to shocks, an actuator with heavy mass will suffer undesired stroke saturation effects, which may also lead to instability of the feedback loop.

The new inertial actuator, presented in this study, is equipped with additional flywheel element, which is used to augment the inertia effect of the inertial mass without increasing the suspended weight. This additional inertia effect produced by the flywheel element improves the actuator robustness to shocks and simultaneously improves the stability of the velocity feedback loop.

The first part of the thesis is focused on the theoretical analysis of vibration control using classical and four new configurations of the proposed flywheel electromagnetic actuator. The kinematic properties of the actuators and effectiveness of point velocity feedback loops are assessed based on mathematical simulations obtained from a lumped parameter model. Finally a parametric and scaling study presents main guidelines for designing flywheel prototypes.

The second part of the thesis presents the design process and experimental tests of two flywheel prototypes. These two prototypes were designed based on a commercially available linear electromagnetic actuator. The electro-mechanical properties of the classical and flywheel configurations were compared with the mathematical simulation obtained from the simplified lumped parameter model.

The third part of the thesis presents the design and experimental results of a flywheel inertial prototype using a piezoelectric transducer. Compared to the electromagnetic flywheel actuator the piezoelectric flywheel actuator presents some interesting properties. This part of the thesis describes the advantages that would arise when implementing a velocity feedback loop with this type of transducer.

The forth part of the thesis presents the experimental implementation of a point velocity feedback control unit with the electromagnetic flywheel actuator to reduce the flexural vibrations of a rectangular thin plate. The stability of the system is assessed based on the sensor-actuator open loop frequency response function, while the performance of the feedback loops is assessed based on the reduction of the total flexural kinetic energy of the plate.

The last part of the thesis briefly presents the potential use of the flywheel prototype as a seismic transducer to harvest energy from the vibrating structure.

ACKNOWLEDGMENTS

Firstly, I would like to express my special thanks of gratitude to my supervisor Professor Paolo Gardonio for his guidance, support and stimulating feedbacks throughout my PhD period at the University of Udine. I would like to sincerely thank him for the assistance and for the excellent opportunity to conduct this PhD thesis within a wonderful project. I gratefully acknowledge the European Commission for its support of the Marie Skłodowska-Curie program through the ITN ANTARES project (GA 606817).

I would like to acknowledge with much appreciation the crucial role of Elvio Castellarin and the staff from the DPIA for their help in ordering the components of the designed prototypes.

I would also like to express my deepest appreciation to my team colleagues, especially to Emanuele Turco, Daniel Casagrande, Michał Zientek and Loris Dal Bo for their suggestions and practical help.

Particular thanks goes to my friends with whom I shared the best moments during my stay in Udine. A special gratitude I give to Catalina, Federica, Nadia, Serena, Kam, Hebert, Sandro and Francesco for all good memories.

I wish to express my sincere thanks to my family for their support. Especially I thanks my parents for their help and endless love. I am thankful to my brother for his encouragement.

CONTENTS

LIST OF FIGURES

LIST OF TABLES

NOMENCLATURE

LIST OF ACRONYMS

BMF	Back Electromotive Force
CAD	Computer Aided Design
EADC	Energy Accumulation and Diffusion Converter
EDM	Electrical Discharge Machining
EM	Electro-Magnet
FEM	Finite Element Method
FRF	Frequency Response Function
MIMO	Multiple-Input Multiple-Output
PZT	Lead Zirconate Titanate
SISO	Single-Input Single-Output

LIST OF SYMBOLS

Latin letters

Parameter	Description	Unit
B	Magnetic field	[T]
c	Damping	[N/m/s]
C	Capacitance	[F]
D	Plate bending stiffness	[Nm]
E	Plate elastic modulus	[N/m^2]
g	Control gain	[-]
h	Plate thickness	[m]
i	Current	[A]
I	Inertia	[kgm^2]
j	Imaginary number defined $j^2 = -1$	[-]
k	Stiffness	[N/m]
KE	Plate kinetic energy	[J/Pa] or [J/N]
l	Plate linear dimension	[m]
L	Scaling law notation	[-]
L	Coil inductance	[H]

m	Mass	[kg]
M	Inertial mass	[kg]
n	Modal indices for the nth mode	[-]
p	Pressure or force plate excitation	[Pa] / [N]
r	Flywheel offset value	[m]
R	Resistance	[Ω]
t	Time	[s]
u	Voltage	[V]
w	Displacement	[m]
$\dot{w}$	Velocity	[m/s]
x	Position in x coordinate (plate axis)	[m]
y	Position in y coordinate (plate axis)	[m]

Greek letters

Parameter	Description	Unit
δ	Actuator static displacement	[m]
Δ	Difference	[-]
ζ	Damping ratio	[-]
ν	Plate Poisson ratio	[-]
π	Mathematical constant	[-]
ρ	Plate density	[kg/m^3]
σ	Gravitational acceleration	[m/s^2]
ϕ	Modal amplitudes	[-]
ψ	Actuator transduction coefficient	[N/A]
ω	Natural frequency	[Hz]
Ω	Plate mass normalised resonant term	[-]

Mobility and Impedances

Parameter	Description	Unit
Y_{bb}	b point plate mobility	[m/s/N]
Y_{bc}	b to c transfer plate mobility	[m/s/N]
Y_{cb}	c to b transfer mobility	[m/s/N]
Y_{cc}	c point plate mobility	[m/s/N]
Y_m	Inertial mass mobility	[m/s/N]
Z_a	Actuator suspension impedance	[N/m/s]

Z_b	Actuator base impedance	[N/m/s]
Z_e	Actuator electrical impedance	[Ω]

Frequency response functions

Parameter	Description	Unit
T_{fi}	Blocked force per unit current	[N/A]
T_{fu}	Blocked force per unit voltage	[N/V]
$T_{u\dot{w}}$	Transduction coefficient FRF	[V/m/s]
$Z_{f\dot{w}}$	Mechanical base impedance	[N/m/s]
Y_{iu}	Electrical admittance	[A/V]
Z_{ui}	Electrical impedance	[V/A]

Subscripts

Parameter	Description
a	Actuator
b	Base / case of the actuator
c	Control position
cl	Velocity feedback control
e	Electrical element
f	Force
h	Hinged configuration
H	Harvested
i	Current
m	Inertial element
n	Natural frequency
p	Pinned configuration
pzt	Piezoelectric
s	Plate structure
u	Voltage
w	Flywheel element
Δw	Stroke
$\dot{w}$	Velocity
x	x – coordinate (plate axis)
y	y – coordinate (plate axis)

1

INTRODUCTION

As it is well known, every mechanical element that has a specific mass and stiffness shows unique vibrational response when being exposes to time varying disturbance [1], [2]. Many mechanical structures with higher performance criteria and refined design specifications require a control of these disturbances [3]. In many cases, the traditional approach to reduce these vibrations by changing the mechanical properties of the structure is insufficient. At the same time, the constant technological growth of smart materials and power electronics give an opportunity to combine them in mechatronic systems for active vibration control. Hence, the combination of smart transducers and control electronics embedded in the hosting structure present many appealing advantages. Although in some cases, vibrational oscillations can be used for a specific purpose, like improvement of the technological processes (smart machine tools [4]), cavitation generation (ultrasonic transducers [5]), defect detection [6], [7], etc., in most cases they are undesired. The excessive vibrations in the mechanical systems are undesired mainly for three reasons:

Fatigue effect on the structure – excessive vibrations may lead to wearing and accelerated failure of the components or the entire structure [8]–[10]. The excessive vibrations may cause delamination of the composite structures [11], [12].

Comfort & health – the comfort improvement in the transportation vehicles. Reduction of noise and vibration in the interior cabin of the airplanes [13], [14], vibration reduction in the helicopters [15]–[17], reduction of noise and vibration generated by the ventilation and air supply systems [18], [19]. Also the improvement of personal protection for the humans exposed to vibration and noise generated by machines [20], [21].

Operational conditions – everywhere where the high precision and small tolerances are required. Most common examples are the measuring equipment, surgical robots [22], large flexible structures [23], [24], machining process, etc. [25], [26].

1.1 ACTIVE CONTROL

Active control of noise and vibration can be achieved with many different methods. This part of the thesis describes the techniques that are used for designing smart structure for active control of noise and vibration. In principle, every mechatronic system for the noise and vibration control is built out of three fundamental components [27], [28]:

- sensor (accelerometer, force cell, strain gauge, etc.),
- actuator (linear actuator, torque motor, hydraulic cylinder, etc.),
- control system and algorithm (feedforward, feedback, etc.).

The final design of a specific active control system depends on several aspects that determine the different type of each component.

1.1.1 Feedforward control

Feedforward control is the primary algorithm of active noise and vibration control of tonal disturbances or stationary stochastic disturbances. This method strongly depends on the availability of the reference signal correlated to the primary disturbance source [29], [30]. In practice, the reference signal is sent and processed in an adaptive filter, where the filter coefficients are tuned to minimise the output error signal of the system. Finally, the output signal from the adaptive filter is applied back to the system via secondary sources. The principle of feedforward control operation is that the secondary source is driven by the adaptive filters to produce a signal that interferes with the primary disturbance source and cancels it out. Essentially, the control algorithm produces a signal equal magnitude and opposite phase to the disturbance source.

As the coefficients of the adaptive filters are tuned to minimise the signal at the location of the error sensor the feedforward algorithm is considered as a local system. Thus, the algorithm does not guarantee that the global response is minimised or that in some areas the response is not amplified. Furthermore, the feedforward control provides good control performance for tonal or stationary stochastic disturbances that can be measured in advance. Beside of these drawbacks, the feedforward control strategy presents several advantages over the feedback systems. Unlike the feedback systems, the feedforward systems are more robust to phase lag effects in the control

system. Additionally, the use of the reference signal does not require the model of the system but only the adaptation process [23].

Feedforward controllers are widely used in applications for which the reference signal can be obtained in advance to overcome any delays caused by the signal processing in the adaptive filter. Practically, the sensor must be placed far enough to provide enough early in time the reference signal, to guarantee the necessary processing delay of the controller.

Often in case of periodic disturbance signals, instead of using the reference sensor the signal can be obtained directly from the machine that produces the disturbance, for example with a tachometer mounted on a rotating machine [29].

1.1.2 Feedback control

A feedback control system relies on an error signal and control actuator such that the error signal is fed back to the actuator via a controller. In theory to implement an active control system, it is necessary to model exact inverse of the plant with the condition that both, the plant and the controller are unconditionally stable. Unfortunately, the properties of the plant change due to the external disturbances that are never known. Thus, the main four reasons for using the feedback control are:

- unknown disturbances,
- plant model uncertainties,
- little knowledge of the system,
- instability of the plant.

The main difference that distinguish a feedback control architecture from a feedforward control architecture is that there is no need for a reference sensor to give enough in advance information about the primary disturbance. The feedback control is mainly used in systems where there are several disturbances or when the primary disturbance cannot be directly observed [29]. In order to benefit from feedback control, high feedback gains are normally required to obtain the inverse of the plant without the need of the exact model. However, the main limitation is the instability, which can be induced by high feedback gains mainly at high frequencies. For this reason, the feedback systems are principally suited for control in limited range of frequencies [31].

One of the most commonly used technique for the active vibration control is the direct velocity feedback system [32]. This technique incorporates a collocated sensor-

actuator pair to increase the effective damping in the system, while keeping the natural frequencies, of the controlled structure, substantially unchanged. The sensor-actuator pair collocation arrangement guaranties observability and controllability of the system. Ideally the system is equipped with a velocity sensor collocated with a point force actuator or equivalently with an angular velocity sensor collocated with a torque motor. Several studies on the velocity feedback control applications can be found in following references [33], [34].

Recent studies has shown that when the control gains of velocity feedback loops are adjusted to minimise the kinetic energy of the controlled structure the power absorbed by feedback loops is then maximised [34]–[38]. Thus, the electromechanical transducers can be used to absorb power from the structure. The collocation and duality of the sensor and transducer facilitates the vibration energy harvesting, which instead of being wasted could be used to operate the control unit itself. In particular, it could be used to operate a local tuning device that sets the feedback control gain to reduce the overall vibration of the structure where it is mounted [39].

Several studies were performed on the active vibration control of lightly damped thin two-dimensional structures, where the inertial actuators were used to reduce the flexural deflections of the structure [33], [40]–[42]. Direct velocity feedback control is widely used to increase the damping effect in the system and to reduce the amplitude of the resonance peaks of the structure. However more complex, techniques can be used depending on the required control purpose, as for example reduction of sound radiation through the structure [27], [43].

1.1.3 Noise and vibration active control applications

Noise and vibration control is a challenging problem in many sectors of industry. Especially vehicles production sector focuses on the noise and vibration control. The studies on the noise and vibration control in the aircrafts started in the mid 40s however, the active control was not exploited until beginning of 80s both in propeller and in turbofan aircrafts [14]. Several studies were done on the active control starting from the ground tests to flight tests and finally to implementation on a commercial aircraft [13]. In the similarly period, the car industry started to take a particular look on an active suspension system. Several solutions were incorporated for the active suspension control using hydraulic systems and electromagnetic actuators [44].

The wide area of interest in active control is presented in noise and vibration cancelation in the ventilation ducts. The decentralised feedback is used to reduce structure-borne noise radiated by the duct wall [18].

1.2 TRANSDUCERS FOR VIBRATION CONTROL

This section presents a review of recent work on various transducers for active vibration control of thin flexural structures. Typically, in smart structures the electromechanical transducers are used, which work as electromechanical energy converters. Indeed transducers can transform vibration energy into electrical energy that is stored (energy harvesting) or dissipated via an electrical shunt [45]–[47]. Alternatively, the electrical energy can be transformed by transducers to produce motion or control forces (actuators) [28]. Electromechanical actuators present several advantages over other types of actuators, for example:

- they are more ecological friendly than the hydraulic pistons that typically suffer from a leakage of the hydraulic fluids,
- they are compact and easy to adapt in the smart structures,
- they can be easily scalable to improve the performance of the vibration control system,
- they require low maintenance,
- they can be simultaneously used for energy harvesting applications,
- they can be adopted in the harsh environments (do not freeze in low temperatures),
- they are easy to control as the electrical signal can be simply modified and processed with dedicated electronics.

There are two mayor types of electromechanical transducers commonly used in active vibration and noise control systems. First, the electromagnetic actuators that are based on the Lorenz force principle. Typically, they are used as proof mass actuators, where the inertial mass produces the so called sky hook force effect above the fundamental resonance frequency of the system. Second, the piezoelectric patches and stacks, which, thanks to the inverse piezoelectric effect produce relative displacement when the electrical field is applied to the electrodes. Typically, these type of transducers are used as reactive actuators in the form of patches attached to the thin flexural plates. Alternatively, they can also be used as stacks reacting between two mechanical components.

This section describes both types of transducers used in the active vibration and noise control systems.

1.2.1 Electromagnetic transducers

Electromagnetic (EM) inertial actuators also known as proof mass actuators or reaction mass actuators have been widely used to implement feedback control loops for the control of flexural vibrations of distributed structures [33], [48]–[65]. The classical proof mass actuators for feedback control systems [28], [66], [67] incorporate a voice coil actuator, which is composed by a cylindrical magnetic element, suspension system and a coil armature [68]. Typically, the magnetic element is mounted via soft springs in an inner cylindrical cut that hosts the coil. Figure 1.1 shows two types of inertial actuator assembly commonly implemented in practical applications. In the first, the coil armature is rigidly fixed to the actuator base and the moving magnet is suspended to the actuator base via soft springs (Figure 1.1a). Instead, in the second, the magnet is joined to the actuator base while the coil armature is suspended to the base by soft springs (Figure 1.1b).

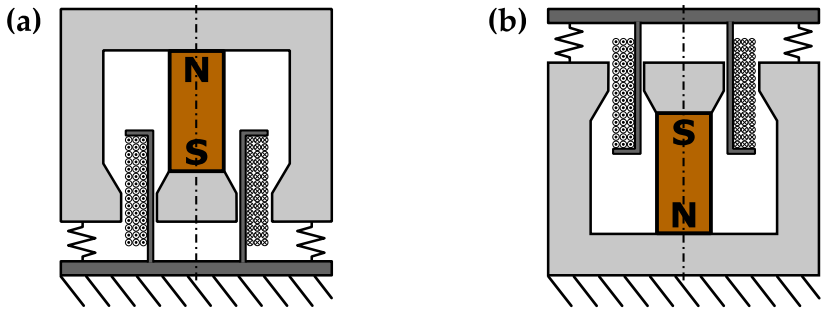

Figure 1.1. Two types of inertial actuator assembly implemented in practical applications, with the coil armature rigidly fixed to the base (a), or with the magnet fixed to the base (b).

In both configurations, when current is applied to the coil placed in the magnetic field generated by the permanent magnet both components experience the Lorentz force. The force effect produced between the coil and the magnet is proportional to the applied current, the magnetic flux and the wire length of the coil [69]. Thus, when current flows through the coil, a reactive force is produced between the coil and the magnet, which sets into relative motion both components. The force applied either to

the moving magnet or to the armature-coil is thus balanced by the inertia effect due to the acceleration experienced by the inertial mass elements. As a result, a net force is generated on the actuator base, which, at frequencies below the fundamental resonance frequency of the springs–inertial mass assembly, grows proportionally with frequency and is out of phase with the driving current, while at higher frequencies, is constant and in phase with the driving current [70]. Thus, when this actuator is used to implement a negative velocity feedback to mimic a sky-hook damper, at frequencies below the fundamental resonance frequency, the feedback loop essentially produces a positive velocity feedback effect that is a negative damping effect, which leads to instability. It is therefore vitally important the fundamental resonance frequency of the actuator is kept as low as possible and the amplitude of the resonance peak is also the minimum possible. However, this solution tends to increase the static displacement of the inertial mass, which, in presence of shocks, may hit the actuator end stops and trigger instability effects. This study is focused on a design of a new EM proof mass actuator with both low fundamental resonance frequency and low static deflection of the inertial mass.

The proposed actuators are foreseen for several control applications. For example, vibro-acoustic control of thin lightweight panels of transportation vehicles (cars, trains, aircraft, etc.) and vibration control of relatively small scale machines (domestic appliances, car engines, manufacturing equipment and machines). Also, vibration control of heavy plate and beam framework structures of industrial plants and buildings, and seismic vibration of relatively large machineries (marine engines, agricultural machinery, industrial plants, etc.) [71], [72].

The designed actuators could be used in the active vibration control systems, which are typically composed by a proof mass actuator and inertial accelerometer placed at the base footprint of the actuator. The integrated accelerometer signal is amplified with the operational amplifier and send to the proof mass actuator. Although the active control system works locally by reducing the vibrations of the structure, the global effects have influence on the feedback loop. Beside of measuring vibrations of the structure at the control position, the inertial sensor also detects accelerations of the entire structure. As discussed in the previous paragraph, to obtain the best control performance of the feedback loop at the control position, the error signals must be send to the proof mass actuator with highest stable gain. Thus, in case of any unexpected shocks or sudden fast movements of the hosting structure, the amplified error signal that is send to the proof mass actuator can exceed the working

limit conditions and thus destroy the vibration control system. Some of the examples of such situations are:

- Turbulences and shocks during landing of the aircraft.
- High tides of the rough sea hitting the ship hull.
- Shocks during the spacecraft or satellite take off.
- Bumpy road during driving a car.

Thus, in practical applications the error signals should not be send to the proof mass actuator with the highest stable gain.

Finally, despite the thesis considers a voice coil transducer, several other transduction technologies and materials could be employed. For instance, electrostatic transducers could be used, which however are more suited for microscopic systems due to very high operating voltages. Alternatively magnetostrictive or moving iron transducers could be directly employed [73]. However, the force reversibility in the voice coil actuators, considered in this study, is an advantage over the other transducer configurations and highly required in the feedback control systems.

1.2.2 Piezoelectric transducers

As mentioned in the previous paragraph, for feedback control systems the electromagnetic inertial actuator provides point force by means of inertial mass suspended on soft springs [56], [57]. However, this type of actuator presents several disadvantages. Firstly, the produced force strongly depends on the size and the weight of the inertial mass causing the actuator to be heavy and bulky. Several scaling studies show that the downsizing of the electromagnetic actuator reduces its ability to produce significant amount of control forces [54], [74]. Thus, this type of inertial actuator is not ideal for working in small and confined spaces. Secondly, the low fundamental resonance frequency and high static displacement of the suspended inertial mass causes velocity feedback loops with high control gains to go unstable in case of shocks and high movements of the hosting structure [75]. Finally, the magnetic flux generated by the electromagnetic transducer can propagate in ferrite materials of the hosting structure, like steel plates or bars and can interfere with the working conditions of the control electronics.

An alternative group of transducers widely used for vibration control systems are piezoelectric transducers. Piezoelectric materials present several advantages over

electromagnetic transducers. The compact dimensions and high force density makes them perfect for use in the smart structures. Additionally, due to the capacitive electrical effect, they use much less power compared to the EM actuators, especially when they are driven with switching amplifiers. Several studies have been conducted on the switching amplifiers with power recovery system dedicated for the piezoelectric actuators. Vibration control system equipped with piezoelectric actuators driven by switching amplifiers could present very high efficiency [76], [77].

Several studies were done on thin piezoelectric patch transducers that are bonded directly onto the surface of the controlled structure [78]–[81]. However compared to inertial actuators, piezoelectric patches require large surfaces to provide sufficient amount of control forces. Thus, these actuators are mainly dedicated to thin structures [79] rather than to large flexible systems as for example the truss structures.

Alternatively, piezoelectric stack transducers connected to a proof mass can be used to form a point force inertial actuator. The main limitation of using these types of actuators to implement feedback control loops is their high fundamental resonance frequency, typically above several kHz [82]. As discussed before, it is crucial for the velocity feedback system that the fundamental resonance frequency of the inertial actuator is below the first resonance frequency of the hosting structure so that the inertial actuator could produce a constant forces effect, which is in phase with the driving signal.

Another main disadvantage of piezoelectric stack actuators is their small stroke [83]. Hence, to use the piezoelectric materials for the inertial actuators they would require an amplification mechanism to generate the strokes necessary to produce significant force level. Several commercially available solutions were proposed to overcome this limitation.

Amplified piezoelectric actuator present several appealing properties for the realisation of inertial actuators [25], [84]. This transducer can provide large displacements, and thus accelerations, of the proof mass, which are required to generate sufficient amount of base forces necessary for the implementation of velocity feedback control loops [77]. To meet the requirement of low resonance frequency, the actuator needs to be equipped with a heavy proof mass. However, this solution tends to increase the static displacement of the inertial mass. Hence, in case the actuator is exposed to shocks, the piezoelectric stack transducer would undergo large deformations, which may lead to cracks of the ceramics and eventually to instability of the control system.

This study is also focused on a design of a new piezoelectric proof mass actuator with both low fundamental resonance frequency and low static deflection of the inertial mass.

1.2.3 Scaling of the transducers

Small electromechanical transducers for smart structures present several advantages over the macroscale mechanisms. By integrating control circuits with sensors they can be used to form compact control system [85]. Additionally, different transduction technologies and materials can be employed for the implementation of feedback control system to reduce flexural vibrations in distributed structures. However, physical and mechanical properties of the materials determine which solution is more suited for a specific type of application. A proper scaling study of the transducer properties can improve the performance of the feedback control loops [54], [55].

The main aim of this study is to increase the control force and minimise the total weight of the transducers. Different studies showed that decentralised multiple-input multiple-output (MIMO) control systems produce higher vibration reductions compared to single-input single-output (SISO) systems [33], [86]. Thus, the scaling study is crucial when multiple actuators are used on lightweight structures. Actuator scaling may improve the stability of the feedback loop by reducing the actuator static deflection and thus reducing stroke saturation effects, which may lead to instability when the system is affected by shocks or fast movements of the hosting structure. Thus, it is very important to take into consideration the scaling laws during the design process of the actuator [87], [88].

The biggest advantage of the velocity feedback control is that it requires little knowledge about the system. However, to improve its performance it is important to take a particular care about the scaling of the crucial mechanical and physical parameters. As for example transducer type, size, sensor-actuator pair sensitivity, maximum feedback gain signals, etc. The scale of the actuator also plays a key role on the selection of the transduction technology. For example, electrostatic transducers are better suited for small scale applications, while electro-magnetic transducers works better on large scale devices. An exhaustive overview of the principal scaling laws of electro-mechanical systems and of the principal transduction materials and technologies can be found in following references [74], [87]–[89].

1.2.4 Vibration energy harvesting

The inertial transducers besides of being used as actuators for the active vibration control applications can be also used as energy harvesters [39]. The two most popular transducers for the energy harvesting applications are the piezoelectric [47], [90] and electromagnetic transducers [46], [91]. The main purpose of vibration energy harvesting is to develop self-powered devices, which are capable of transforming mechanical energy into electrical energy using transducers, store the electrical energy in batteries and finally, to use the stored energy to power small electrical circuits.

The vibration control systems can be easily adopted to harvest energy from ambient vibrations. The stored power can used to power the sensors or control circuits, which can be used for condition monitoring of the machine components, data transmission or secondary control operations. Moreover, besides of the harvested power used for the condition monitoring sensors, the vibration amplitude and thus generated by the transducer electrical power can be a good estimator of the machine components damage or wear. The sensor-transducer pair typically used for the active vibration control applications can be easily adopted for vibration energy harvesting. The sensor is used to detect tonal disturbances at the fundamental resonance frequency of the transducer where the vibration energy absorption can be maximised. Moreover, the ambient vibration energy is typically higher at lower frequencies. Thus, low fundamental resonance of the inertial transducer can improve the effectiveness of both, the vibration control loop by reducing the spillover effect and the vibration energy harvesting by operating at lower frequencies and maximising harvested power.

The inertial transducers present several advantages for the vibration energy harvesting applications. The inertial transducers do not require additional structure react off. Can be compact and installed in the confined spaces where there is little access from outside. Finally, can operate in harsh environments [77].

Although this thesis concentrates on the active vibration control applications, the final chapter shortly discusses the possible use of the designed flywheel inertial transducer for the vibration energy harvesting applications.

1.3 STABILITY

To guarantee good performance of a control system requires knowledge, both about the plant response and about the disturbance. In particular one of the main aspects for the design and implementation velocity feedback control is the stability of the control loop [32], [92]. Open loop frequency response function (FRF) of the sensor-actuator pair can be plotted in the complex plane to assess the system stability via the Nyquist criterion [40], [53], [68], [93], [94]. In general, a system is considered unconditionally stable if and only if all poles of the open loop transfer function is in the right half of the plane. The Nyquist stability criterion gives an information about the conditional stability and thus the maximum feedback control [23], [29], [95].

When the inertial actuator is used to implement a negative velocity feedback, to reduce the flexural deflection of a thin plate structure the dynamic response and the static deflection of the proof mass transducer cause stability and control performance limitations. At frequencies below the fundamental resonance frequency of the transducer, the produced net force at the actuator base, grows proportionally with frequency and has opposite phase with the driving signal. Thus, the feedback loop essentially produces a positive velocity feedback effect that is a negative damping effect, which leads to instability. Only above the fundamental resonance frequency of the transducer, the produced net force at the actuator base is constant and in phase with the driving current. Therefore, when the inertial transducer is used to implement a direct velocity feedback, it is important that its fundamental resonance frequency is as low as possible. By reducing amplitude of the resonant response of the actuator and lowering its fundamental resonance frequency the poles in the left half of the complex plane of the sensor-actuator pair open loop FRF tend to be farther from the imaginary axis that defines the instability limit. Therefore higher stable control gains can be applied to the feedback system such that its performance is increased. Increasing inertial mass and lowering fundamental resonance tends to increase the static displacement of the inertial mass, which, in presence of shock, may hit the actuator end stops and trigger instability effects [75], [96]–[100]. Thus, one of the key parameters that characterises the inertial actuators for vibration control with negative velocity feedback control is the static deflection that defines the robustness and ability to withstand shocks.

Several solutions have been proposed to improve the robustness of the inertial actuators for the negative velocity feedback control. A series of studies has been

performed to implement within the actuator either a relative displacement, or a relative velocity or a force feedback loop [101]–[104].

Alternatively, it was proposed to implement in the velocity feedback loop an active controller that would compensates the dynamics of the springs-inertial mass assembly [105], [106].

Another group of techniques for active vibration control are based on the positive position feedback [107], [108] as for example the modal positive position feedback [109], [110] that uses the positive feedback of the position signals with the first – order filters to reduce the vibrations of the undamped structures. Moreover, the combination the position and velocity feedback control was investigated [111]. The use blended velocity feedback performance and stability was investigation of the vibration attenuation in two degree of freedom system [112].

An ideal solution would be to design of a new proof mass actuator with both low fundamental resonance frequency and low static deflection to improve stability of the feedback loops and robustness to shocks of the hosting structure.

1.4 INERTER AND THE FLYWHEEL ELEMENT

The first use of the flywheel element in the shock and impact reduction mechanism was presented in late 90s in a road barrier prototype called as energy accumulation and diffusion converter (EADC) [113]. The main feature of this barrier was the ability to absorb the impact of the approaching vehicle and convert it into rotational motion of the flywheels. The energy of the impact was converted, stored and slowly dissipated inside the spinning flywheels. The experimental tests showed the impact of the vehicle can be easily absorbed by the EADC mechanism without damaging car exterior bodywork.

Another use of the flywheel element for the vibration control was presented with a new mechanical element called “inerter”, which derived directly from the electro-mechanical analogy [114], [115]. The inerter was defined as a two terminal mechanical device with the property that the opposite and equal force applied to terminals is proportional to the relative acceleration between the terminals. The constant of proportionality that defined the inerter was called the inertance and it was characterised in mass units [kg]. The operation of the inerter was based on the mechanism that could transform the relative linear motion at the terminals into rotational motion of the flywheel element mounted inside the device. Therefore, the

inertance produced at the terminals of the device does not directly depends on the weight but on the flywheel moment of inertia.

Two full size prototypes were build, where one of them was using the pinion-rack mechanism while the other the ballscrew mechanism to transform the linear motion into rotation of the flywheel [116], [117]. A practical solution for the formula one cars was built based on the inerter mechanism and it was named as J-damper [118]. The experimental tests of the prototypes showed several advantages of the inerter that are appealing for the vibration control applications. However, the fabricated prototypes typically are heavy, bulky and designed for large relative displacements, which exclude them for vibration control of large flexible structures [119].

In recent year several studies have shown that inerter devices can improve the stability and the performance of the velocity feedback control loops [120], [121]. Extensive theoretical studies have been carried out on the implementation of the inerter in the tuned vibration absorbers [122]–[124], covering wide variety of applications. From the vibration control of several stories building [125], [126], bridge cables [127], beam structures [128], sculptures [129] to vehicle suspension systems [130]–[133]. Also some studies were dedicated to the energy harvesting using tuned mass-damper [134].

However, these studies considered only an idealised inerter element, which neglects the weight of the components. Additionally, the stiffness and damping effects of the gearing mechanisms that convert axial relative motion at the terminals of the inerter into angular motion of the flywheels are also neglected.

The inerter element present appealing properties for practical implementation in inertial actuators for the active vibration control application. The inerter can be used to increase the inertia of the proof mass and thus to lower fundamental resonance frequency of the actuator, while keeping low static deflection small, which is crucial in case of shocks of the hosting structure.

1.5 SCOPE AND OBJECTIVE OF THE THESIS

The objective of this thesis is to investigate the use of rotational inertial electromechanical actuators for the implementation of velocity feedback loops that control broadband vibration of thin plate and shell structures. In the proposed research, the actuator is used to produce constant force effect proportional to the local velocity at the control position. The control unit is equipped with a rotational element

that can be used to augment the inertia effect of the suspended mass element. This could improve the stability of velocity feedback loops by reducing the static deflection of the proof mass actuator and thus reducing stroke saturation effects in case of shocks or fast movements of the hosting structure. Additionally, by increasing the inertia effect, and thus lowering the fundamental resonance frequency of the control unit, the extent of the out-of-phase force excitation effect, which tends to destabilise the velocity feedback loops is reduced. This control unit should also be much more compact and lightweight than ordinary units with axial inertial actuators.

Another advantage of using rotational element could be cost reduction of the typical linear actuator. In the classical configuration, the flexures or linear flexural bearings are relatively expensive to fabricate. Thus, the proposed solution could lower the costs of the control unit.

Furthermore, the collocation and duality of the sensor and actuator transducers facilitates the harvesting of vibration energy, which instead of being wasted can be used to operate the control unit itself. In particular, it can be used to operate a local tuning device that sets the feedback control gain to reduce the overall vibration of the structure where it is mounted.

1.6 CONTRIBUTIONS OF THE THESIS

The novel contributions of this thesis are:

- A lumped parameter model of an inertial electromagnetic actuator equipped with a flywheel and gearing mechanism to transform axial to rotational motion.
- Detailed guidelines for designing new inertial actuator that incorporates “inerter” element for the decentralised velocity feedback control on a thin structures.
- A practical solution for transforming the oscillatory linear motion of classical inertial actuator into rotational motion of the flywheel element without play and backlash between the components.
- A practical solution for suspending the flywheel element in an inertial actuator that could provide soft torsional motion while keeping the element rigidly in the axial directions.

- A summary on the practical possibility of using other actuation method in the inertial actuators rather than the commonly used electromagnetic effect for the decentralised velocity feedback applications.
- Experimental validation of the stability and control performance of decentralised velocity feedback control on a thin rectangular panel with the inertial actuator, which incorporates the proposed flywheel element.
- Theoretical and experimental investigation of using the inertial transducer with flywheel element for vibration energy harvesting.

1.7 STRUCTURE OF THE THESIS

The thesis is organised in seven chapters.

Chapter two presents the theoretical analysis based on simulations results of active vibration control using classical and four configurations of the proposed flywheel electromagnetic actuator. Firstly, the electro-mechanical properties of the actuators are introduced. Secondly, the performance of the point velocity feedback loops using classical and four new flywheel actuators is assessed. A parametric and scaling study that gives basic guidelines for designing flywheel prototypes is presented in the final section of this chapter.

Chapter three of the thesis presents the design process and experimental results of testing two flywheel prototypes. In this chapter, two mayor problems of flywheel integration in the compact linear actuators are investigated. Firstly, the design of a frictionless mechanism without backlash and wear that can be used to support the flywheel element is investigated. Secondly, the design of a mechanism that can transform the linear motion of the actuator into rotational motion of a flywheel element is presented. The two prototypes are designed based on a commercially available linear electromagnetic actuator. The electromechanical properties of the classical and flywheel configurations are compared based on measurements of the frequency response functions that characterise the inertial actuators. Then, the experimental results are contrasted with the numerical simulation obtained from a simplified lumped parameter model of the inertial actuators.

Chapter four presents the design and experimental results performed on a flywheel inertial prototype using a piezoelectric stack actuator. The piezoelectric stack actuators present several advantages over the electromagnetic actuators that are briefly sumarised in this chapter. The electro-mechanical properties of the

fabricated prototype are measured and compared with numerical results obtained from a simplified lumped parameter model of the actuator.

Chapter five of the thesis presents the experimental implementation of the velocity feedback control using a classical and the proposed flywheel actuator to reduce the flexural vibrations of the thin rectangular plate. The stability of the velocity feedback loops is assessed based on the actuator-sensor open loop frequency response function. Finally, the performance of the feedback loops is assessed based on the total flexural kinetic energy of the plate.

Chapter six of the thesis presents a study on the effectiveness of the flywheel prototype for a vibration energy harvesting. The experimental results are contrasted with the numerical simulations for the inertial transducer connected to a purely resistive load.

Chapter seven presents general conclusions of this thesis and presents new ideas for future work.

2

VELOCITY FEEDBACK WITH FLYWHEEL ACTUATOR

This chapter presents the theoretical study on the use of electromagnetic actuators for the implementation of velocity feedback loops used to control the vibration of distributed flexural structures. The investigated actuators are based on a classical proof mass actuator designs with an additional inerter [114] element that increases the inertia effect of the proof mass. This chapter considers the effective weight and dynamics effects of an inerter element composed by a single flywheel, which is either pinned or hinged to the base mass or to the proof mass of the actuator. Four new flywheel proof mass actuators are presented and evaluated in his study. The aim of these new designs is twofold. Firstly, to lower the fundamental resonance frequency of the springs-proof mass system in such a way as to minimise the out-of-phase force excitation effect, which tends to destabilise the velocity feedback loop. Secondly, to reduce the static deflection of the proof mass actuator and thus reducing stroke saturation effects, which also lead to instability when the system is affected by shocks or fast movements of the hosting machine or flexible structure. This chapter also presents a simulation study on the stability and control performance properties when velocity feedback loops using the four proof mass actuators with flywheel element are implemented on a thin plate structure to reduce the flexural vibration at low frequencies. Finally, a parametric study is introduced to provide basic guidelines for the design and practical realisation of the proposed flywheel proof mass actuators and on the effective implementation of velocity feedback loop with these actuators. The aim of the scaling study is to improve the performance of the velocity feedback control loops, both by increasing the control force and by minimizing the total weight, which is crucial when multiple actuators are used on lightweight structures. Actuator scaling may improve the stability of the feedback loop by reducing the actuator static deflection and thus reducing stroke saturation effects, which may lead to instability when the system is affected by shocks or fast movements of the hosting structure. Thus, it is very important to take into consideration the scaling laws during the design process of the actuator

This chapter is structured in five sections. First section introduces the four proposed flywheel proof mass actuators and the lumped parameter models of the classical and proposed flywheel proof mass actuators. Section two introduces the lumped parameter model used to study the flexural response of a simply supported thin rectangular plate hosting structure, which is excited by an acoustic plane wave and is equipped with a velocity feedback loop using the classical and proposed flywheel inertial actuators. Section three introduces the mobility-impedance formulation used to study the response of the actuators and of the velocity feedback loops. Section four investigates the dynamic and kinematic properties of the classical and proposed flywheel proof mass actuators; i.e. the actuators base impedance, blocked force, proof mass stroke, electrical impedance. Section five contrasts the stability analyses of point velocity feedback loops using four new flywheel proof mass actuators. Section six presents the control performance of the implemented velocity feedback loops using either the classical or the proposed flywheel proof mass actuators. Finally, section seven presents a parametric study on the performance, static deflection and scaling of the inertial actuators.

2.1 FLYWHEEL INERTIAL TRANSDUCERS

The classical proof mass actuator considered in this study is formed by a cylindrical magnetic element with an inner cylindrical gap where a coil is housed [28], [31], [56], [67], [68]. The coil armature is firmly fixed to the base of the actuator. Instead, the magnet element is connected to the base via soft elastic springs. The new actuators, shown in Figure 2.1, are characterised by an additional flywheel element, which is either hinged or pinned by a soft torsional spring to the actuator base or to the proof mass of the actuator. The flywheel is also connected respectively to either the proof mass or the base of the actuator via a pinion-rack gear mechanism such that the small axial relative oscillation between the base and the moving proof mass of the actuator is converted into an angular oscillation of the flywheel.

Although two configurations are presented in this study, several other configurations can be foreseen to hold the flywheel and to convert the axial oscillations between the base and proof mass into angular oscillations of the flywheel. For instance, if the flywheel element is hinged, a simple bushing-shaft or a ball bearing-shaft could be used. Instead, in the pinned case a flexible torsional shaft or flexural bearings could be used. The axial oscillations between the actuator base and

proof mass can be converted into angular oscillation of the flywheel with a pinion-rack or a ball-screw gear system or, alternatively, with metal or plastic flexural hinges. The flywheel axis of rotation can be oriented in axial direction or transverse depending on the mechanism chosen to convert relative axial oscillations into rotational motion and the mounting solution chosen to hold the flywheel element.

When dealing with the practical design and fabrication of the proposed flywheel actuators, the choice amongst the constructive solutions described above strongly depends on the scale of the actuator. For instance, with small scale actuators, which are therefore characterised by small strokes and small forces, it may be favourable to pin the flywheel to the base with flexible shafts or flexural bearings and to use flexural hinges with flexible linkages to convert the axial oscillations to angular oscillations of the flywheel element. Beside practical limitations due to the fabrication of miniaturised components, bushing-shaft and ball bearing-shaft assemblies are very sensitive to stick-slip non-linear phenomena while pinion-rack and ball-screw gearing systems are prone to non-linear gear-meshing effects, all of which may disrupt the correct functioning of the actuator. The non-linear effect can appear especially in the gearing mechanism when the backlash between the pinion element and the rack would be larger than the small relative oscillations between the actuator base and the proof mass. However, with large-scale actuators, which are characterised by large strokes such that stick-slip and gear-meshing effects are less important, a setup with bushing-shaft or a ball bearing assembly to hold the flywheel and pinion-rack or a ball-screw gearing systems to convert the axial to angular motion may be preferable, as presented in [116], [117], since flexible joints and linkages may give rise to undesirable non-linear elastic effects. In fact, the combination of large strokes and large forces could lead to fatigue damage of the flexural hinges.

Figure 2.1 shows the lumped parameter models that have been used to describe the electro-mechanical response of the classical proof mass actuator (Figure 2.1a), which has been taken as a reference system, and the proposed four proof mass actuators, which are equipped with a flywheel hinged to the base (Figure 2.1b), pinned to the base (Figure 2.1c), hinged to the proof mass (Figure 2.1d) and pinned to the proof mass (Figure 2.1e). As shown in Figure 2.1a, the classical actuator is described with a proof mass M_a, which is connected to the base mass m_b via a flexible mount modelled by a spring and a damper in parallel having stiffness k and damping factor c respectively. The coil – magnet transduction effect is modelled in terms of a reactive actuator, with transduction coefficient ψ_a that produces a force F_a proportional to the current flowing in the coil i_a, and a voltage source u_a, with the

same transduction coefficient ψ_a, which produces the so called back electromotive force (BMF), u_{bmf}, proportional to the relative velocity between the proof mass and base mass elements $\dot{w}_m - \dot{w}_b$. The proposed actuators shown in Figure 2.1b-e are based on the same model of the classical proof mass actuator. Where, the flywheel element mass m_w is attached either to the base mass m_b or to the proof mass M_w such that $M_w + m_w = M_a$. The torsional spring (only for the pinned flywheel cases shown in Figure 2.1c and Figure 2.1e) is characterised with angular stiffness coefficient k_w and torsional damper (only for the hinged flywheel cases shown in Figure 2.1b and Figure 2.1d) is characterised with angular damping coefficient c_w. Finally, the flywheel element is characterised by polar moment of inertia I_w with the external radius R_w of the flywheel and the radius r_w of the pinion rack gear mechanism that converts the axial relative motion between the proof mass and base mass into angular motion of the flywheel.

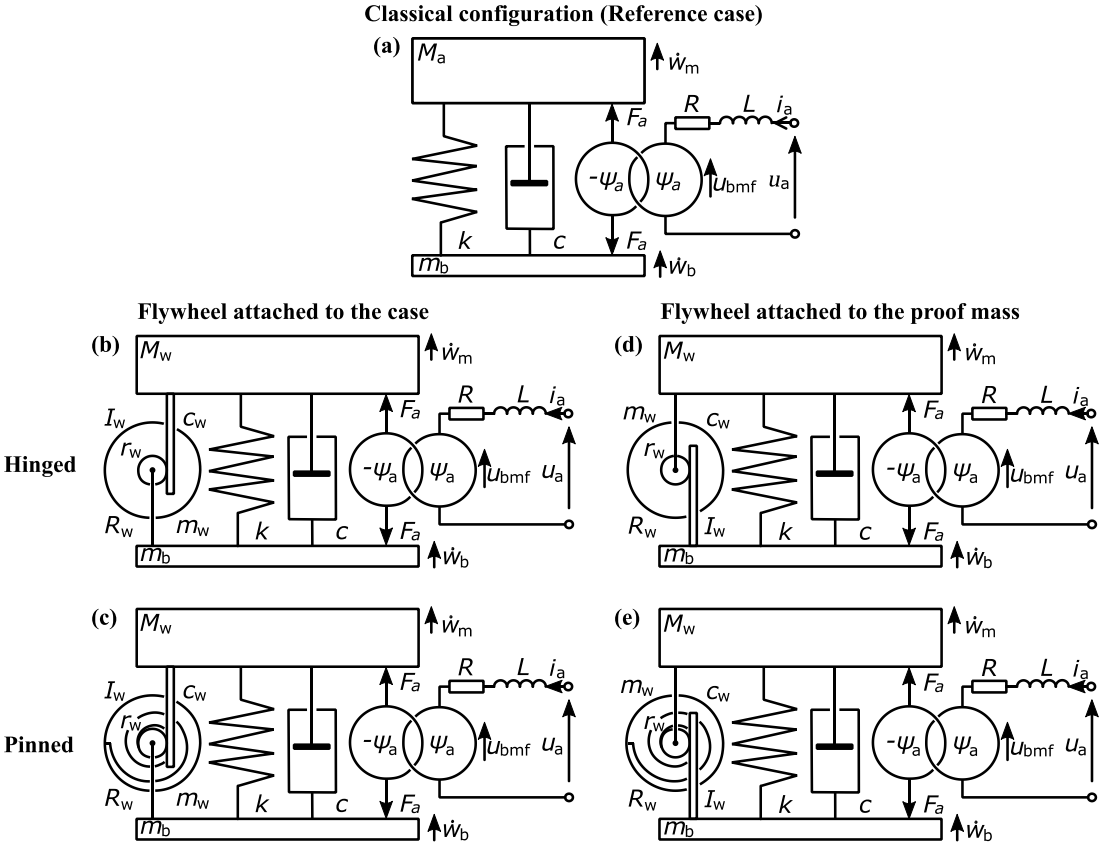

Figure 2.1. Schemes of the proof mass actuators (a) without flywheel (classical configuration), (b) with hinged flywheel attached to the case, (c) with pinned flywheel attached to the case, (d) with hinged flywheel attached to the proof mass, (e) with pinned flywheel attached to the proof mass ($M_a = M_w + m_w$).

The parameters of the actuators, which are summarised in Table 2.1, were set with reference to the geometry and physical properties of the thin rectangular plate hosting structure considered in this study, which are summarised in Table 2.2. It was decided that the total mass of actuator has to be below 10% of the mass of the plate and, at the same time, the mass of the actuator case has to be less than 10% of the total actuator mass. Also it was decided that the combined proof mass M_w and flywheel mass m_w of the proposed actuators should correspond to the proof mass of the classical actuator, i.e. $M_w + m_w = M_a$. The stiffness of the proof mass axial suspension system was adjusted in such a way as to set the fundamental resonance frequency for the axial oscillations of the elastically suspended proof mass without flywheel element at about 20 Hz. The flywheel element is considered as a solid thin cylinder with outer radius R_w. The flywheel is either pinned or hinged to the actuator case or to the proof mass via a tiny shaft. Also, the flywheel is connected via an idealised gear mechanism characterised by a pinion gear of particularly small radius r_w, which magnifies the amplitude of the angular oscillation of the flywheel and thus its inertia effect. The electro–mechanical transduction coefficient has been chosen considering typical values of small scale coil–magnet transducers that can be found in practical applications [53], [54], [56], [57].

Table 2.1. Mechanical parameters of the proof mass actuators ($M_a = M_w + m_w$).

Parameter	Value
Case mass	$m_b = 0.002$ kg
Proof mass classical actuator	$M_a = 0.03$ kg
Proof mass proposed actuators	$M_w = 0.02$ kg
Flywheel mass	$m_w = 0.01$ kg
Axial stiffness	$k = 470$ Nm^{-1}
Axial damping ratio	$\zeta = 0.04$
Flywheel polar moment of inertia	$I_w = 1.125 \times 10^{-6}$ kgm^2
Flywheel radius	$R_w = 0.015$ m
Flywheel pinion radius	$r_w = 0.0015$ m
Torsional stiffness	$k_w = 0.001$ Nmrad^{-1}
Torsional damping ratio	$\zeta_w = 0.01$
Transduction coefficient	$\psi_a = 2.6$ NA^{-1}
Coil resistance	$R = 2\ \Omega$
Coil inductance	$L = 5 \cdot 10^{-4}$ H

Table 2.2. Mechanical parameters of the thin simply supported rectangular plate.

Parameter	Value
Length	$l_x = 0.414$ m
Width	$l_y = 0.314$ m
Thickness	$h = 0.001$ m
Density	$\rho = 2720\ \mathrm{kgm^{-3}}$
Elastic modulus	$E = 71 \times 10^9\ \mathrm{Nm^{-2}}$
Poisson ratio	$\nu = 0.33$
Damping ratio	$\zeta_s = 0.01$
Position of the actuator	$(x_c, y_c) = (0.166\ \mathrm{m}, 0.126\ \mathrm{m})$

2.2 PLATE WITH THE VELOCITY FEEDBACK LOOP USING FLYWHEEL ACTUATOR

In this study, the control performance of the velocity feedback loops using the classical and the proposed flywheel proof mass actuators are investigated considering the flexural response of a simply supported thin rectangular plate hosting structure, which, as shown in Figure 2.2a, is excited by an acoustic plane wave incident at 45° elevation and 45° azimuthal angles. A mobility–impedance [43], [68], [135]–[137] electro–mechanical model [33], [53], [57] has been assembled to derive the response of the plate with the feedback loop using the proof mass actuators. As shown in Figure 2.2b, the system has been divided in four parts: the flexible plate, the base mass, the flexible mounting system with in parallel the coil–magnet transducer, the flywheel element, and the proof mass. Here F_c and F_b represent the forces exerted on the plate respectively by the bottom end of the flexible mounting system with in parallel the flywheel and coil–magnet transducer and by the base mass of the actuator whereas F_m represents the force produced on the proof mass by the top end of the flexible mounting system with in parallel the flywheel and coil–magnet transducer. Also, $\dot{w}_c$ is the velocity of the plate at the control position and the velocity at the base end of the flexible mounting system with in parallel the coil–magnet transducer and it is equal to the velocity of the base mass of the actuator, i.e. $\dot{w}_c = \dot{w}_b$. Finally $\dot{w}_m$ is the velocity of the actuator proof mass and the velocity at the top end of the flexible mounting system with in parallel the flywheel and coil–magnet transducer. A detailed view of the flywheel element is given in Figure 2.2c in which the outer radius

of the flywheel element is defined as R_w and the pinion rack gear mechanism is characterised by inner radius r_w.

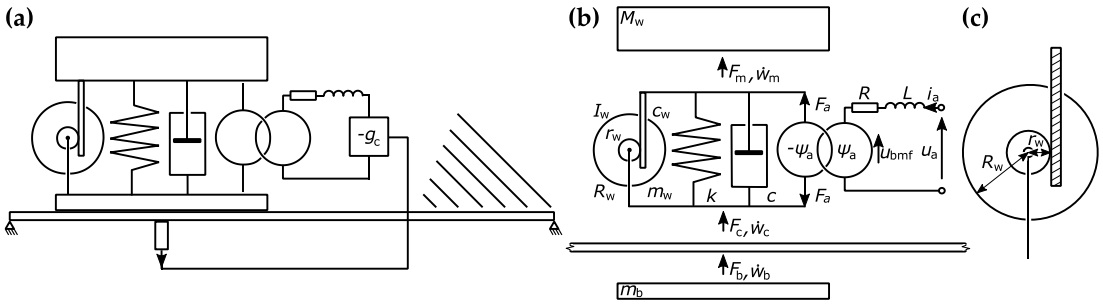

Figure 2.2. Simply supported rectangular plate with a velocity feedback loop using the proposed flywheel proof mass actuator (a). Mobility model (b) and detailed view of the flywheel element (c).

2.3 MATHEMATICAL MODEL

This section presents a frequency domain analysis based on the complex amplitudes $g(\omega)$ of time–harmonic functions given in the form $g(t) = Re\{g(\omega)\exp(j\omega t)\}$, where ω is the circular frequency and $j^2 = (-1)$.

Considering the lumped parameter model shown in Figure 2.2b, the complex velocities at the connecting points between these elements have been expressed with the following mobility relations:

$$\dot{w}_c = Y_{cc}F_c + Y_{cb}F_b + Y_{cp}p\,, \tag{2.1}$$

where $\dot{w}_c$ is the complex velocity at the control position,

$$\dot{w}_m = Y_m F_m\,, \tag{2.2}$$

where $\dot{w}_m$ is the complex velocity of the proof mass,

$$\dot{w}_b = Y_{bc}F_c + Y_{bb}F_b + Y_{bp}p\,, \tag{2.3}$$

where $\dot{w}_b$ is the complex velocity at the base position. The complex velocities at the connecting points can be rewritten and expressed with the following mobility matrix relation:

$$\begin{bmatrix}\dot{w}_c\\ \dot{w}_m\\ \dot{w}_b\end{bmatrix} = \begin{bmatrix}Y_{cc} & 0 & Y_{cb}\\ 0 & Y_m & 0\\ Y_{bc} & 0 & Y_{bb}\end{bmatrix}\begin{bmatrix}F_c\\ F_m\\ F_b\end{bmatrix} + \begin{bmatrix}Y_{cp}\\ 0\\ Y_{bp}\end{bmatrix}p\,, \tag{2.4}$$

where:

$$Y_m = \frac{1}{\mathrm{j}\omega M_a} \quad , \quad Y_m = \frac{1}{\mathrm{j}\omega M_w} \quad , \quad Y_m = \frac{1}{\mathrm{j}\omega (M_w + m_w)} \tag{2.5}$$

are the mobilities respectively for the classical actuator (Figure 2.1a), for the actuators with the flywheel connected to the case (Figure 2.1b,c) and for the actuators with the flywheel connected to the proof mass (Figure 2.1d,e). Also, Y_{cc}, Y_{cb}, Y_{bc}, Y_{bb} are point and transfer plate mobilities, which, considering two generic points r and s of the plate, can be calculated with following matrix expression [68], [136], [137]:

$$Y_{rs}(\omega) = \frac{\dot{w}_r(\omega)}{f_v(\omega)} = \boldsymbol{\phi}^{\mathrm{T}}(x_r, y_r)\boldsymbol{\Omega}(\omega)\boldsymbol{\phi}(x_s, y_s) \,, \tag{2.6}$$

where $\dot{w}_r(\omega)$ and $f_v(\omega)$ are the complex amplitudes of the time – harmonic transverse velocity and transverse force acting at positions (x_r, y_r) and (x_v, y_v) respectively. Also $\boldsymbol{\Omega}(\omega)$ is a diagonal matrix of elements given by [68]:

$$\Omega_n(\omega) = \frac{\mathrm{j}\omega}{[m_s(\omega_{\mathrm{n}}^2 + 2\mathrm{j}\zeta_s\omega_{\mathrm{n}}\omega - \omega^2)]}, \tag{2.7}$$

where ζ_s is the damping ratio, $m_s = l_y l_x h\rho$ is the mass of the plate structure and ω_{n} is the n-th flexural natural frequency. For simply supported plates [15]:

$$\omega_{\mathrm{n}} = \left(\frac{D}{\rho h}\right)^{\frac{1}{2}} \left[\left(\frac{n_1\pi}{l_x}\right)^2 + \left(\frac{n_2\pi}{l_y}\right)^2\right], \tag{2.8}$$

where $D = Eh^3/[12(1-\nu^2)]$, ρ, E and ν are respectively the bending stiffness per unit length, density, Young's modulus of elasticity and Poisson ratio of the plate material, l_x, l_y, h, are the dimensions and thickness of the plate and n_1, n_2 are the two modal indices for the n-th mode. Instead, for clamped plates [136]:

$$\omega_{\mathrm{n}} = \left(\frac{D}{\rho h}\right)^{\frac{1}{2}} \left(\frac{\pi}{l_x}\right)^2 \sqrt{G_{xn}^4 + G_{yn}^4 \left(\frac{l_x}{l_y}\right)^4 + 2\left(\frac{l_x}{l_y}\right)^2 \left[\nu H_{xn} H_{yn} + (1-\nu) J_{xn} J_{yn}\right]}, \tag{2.9}$$

where for first flexural natural frequency $G_1 = 1.506$, $H_1 = 1.248$ and $J_1 = 1.248$. For the n-th mode the constants were obtained with the following expressions $G_n = n + 1/2$, $H_n = (n+1/2)^2(1 - 4/(2n+1)\pi)$ and $J_n = (n+1/2)^2(1 - 4/(2n+1)\pi)$.
Finally $\boldsymbol{\phi}(x, y)$ is a column vector with the flexural modal amplitudes at a given point, which, for the simply supported plate have been taken equal to [68]:

$$\phi_{\mathrm{n}}(x, y) = 2\sin\left(\frac{n_1\pi x}{l_x}\right)\sin\left(\frac{n_2\pi y}{l_y}\right). \tag{2.10}$$

In this study all natural frequencies up to 1.3 kHz and the respective natural modes have been used in the plate mobility expressions. The elements Y_{cp}, Y_{bp} are transfer mobilities between the point c or b and the distributed pressure excitation produced by the acoustic plane wave impinging into the panel at elevation and azimuthal angles α=45° and β=45°, which, as discussed in reference [136] are given by:

$$Y_{rp}(\omega) = \frac{\dot{w}_r(\omega)}{p(\omega)} = \boldsymbol{\phi}^{\mathrm{T}}(x_r, y_r)\boldsymbol{\Omega}(\omega)\boldsymbol{\Phi}(\omega)\,, \tag{2.11}$$

where $\dot{w}_r(\omega)$ and $p(\omega)$ are the complex amplitudes of the time – harmonic transverse velocity and acoustic sound pressure. Also, $\boldsymbol{\Phi}(\omega)$ is the complex vector with the modal excitation terms due to the incident plane wave, which are given by [15], [138]:

$$\Phi_n(\omega) = \int_0^{l_x}\int_0^{l_y} \phi_{\mathrm{n}}(x,y)p_a(x,y,\omega)dxdy\,, \tag{2.12}$$

where, $p_a(x,y,\omega) = \exp\left[-\mathrm{j}(k_x x + k_y y)\right]$, is the complex pressure exerted on the plate surface by a unit amplitude incident acoustic plane wave with complex amplitude $p(\omega)$. Here $k_x = k_0\sin(\alpha)\cos(\beta)$ and $k_y = k_0\sin(\alpha)\sin(\beta)$ are the flexural wavenumbers in x and y directions, where $k_0 = \omega/c_0$ is the acoustic wave number and where c_0 is the speed of sound propagation in air. The integral in Equation (2.12) leads to the expression given by [15], [139]:

$$\Phi_n(\omega) = 4I_{n1}I_{n2}l_x l_y\,, \tag{2.13}$$

where, if $n_1\pi \neq \pm(\omega l_x/c_0)\,\sin\alpha\,\cos\beta$ and $n_2\pi \neq \pm\left(\omega l_y/c_0\right)\sin\alpha\,\sin\beta$ the I_{n1} and I_{n2} vales are given by:

$$I_{n1} = \frac{n_1\pi\left[1-(-1)^{n_1}\mathrm{e}^{-\mathrm{j}(\omega l_x/c_0)\sin(\alpha)\cos(\beta)}\right]}{(n_1\pi)^2 - \left[(\omega l_x/c_0)\,\sin(\alpha)\,\cos(\beta)\right]^2}\,,$$
$$I_{n2} = \frac{n_2\pi\left[1-(-1)^{n_1}\mathrm{e}^{-\mathrm{j}(\omega l_y/c_0)\sin(\alpha)\sin(\beta)}\right]}{(n_2\pi)^2 - \left[\left(\omega l_y/c_0\right)\sin(\alpha)\sin(\beta)\right]^2} \tag{2.14}$$

and, if $n_1\pi = \pm(\omega l_x/c_0)\,\sin\alpha\,\cos\beta$ and $n_2\pi = \pm\left(\omega l_y/c_0\right)\sin\alpha\,\sin\beta$ the I_{n1} and I_{n2} vales are given by:

$$I_{n1} = (\mathrm{j}/2)\,sgn(\sin\alpha\,\cos\beta) \quad \text{and} \quad I_{n2} = (\mathrm{j}/2)\,sgn(\sin\alpha\,\sin\beta)\,. \tag{2.15}$$

To simplify the formulation, Equation (2.4) is rewritten in the following compact form:

$$\dot{\mathbf{w}} = \mathbf{Y}\mathbf{f} + \mathbf{Y}_p p\,. \tag{2.16}$$

Considering the lumped parameter model shown in Figure 2.2b, the complex forces at the connecting points between the elements forming the system have been expressed with the following mobility relations:

$$F_c = -Z_a \dot{w}_c + Z_a \dot{w}_m + \psi_a i_a \,, \tag{2.17}$$

where F_c is the complex force acting at the control position,

$$F_m = Z_a \dot{w}_c - Z_a \dot{w}_m - \psi_a i_a \,, \tag{2.18}$$

where F_m is the complex force acting on the proof mass,

$$F_b = -Z_b \dot{w}_b \,, \tag{2.19}$$

where F_b is the complex force acting at the base position. The complex forces at the connecting points between the elements forming the system at hand shown in Figure 2.2b, have been expressed with the following impedance matrix relation:

$$\begin{bmatrix} F_c \\ F_m \\ F_b \end{bmatrix} = -\begin{bmatrix} Z_a & -Z_a & 0 \\ -Z_a & Z_a & 0 \\ 0 & 0 & Z_b \end{bmatrix} \begin{bmatrix} \dot{w}_c \\ \dot{w}_m \\ \dot{w}_b \end{bmatrix} + \begin{bmatrix} \psi_a \\ -\psi_a \\ 0 \end{bmatrix} i_a \,, \tag{2.20}$$

where:

$$Z_b = \mathrm{j}\omega m_b \quad , \quad Z_b = \mathrm{j}\omega(m_b + m_w) \quad , \quad Z_b = \mathrm{j}\omega m_b \tag{2.21}$$

are the impedances respectively for the classical actuator (Figure 2.1a), for the actuators with the flywheel connected to the case (Figure 2.1b,c) and for the actuators with the flywheel connected to the proof mass (Figure 2.1d,e). Also the actuator impedance Z_a depends on the type of the actuator and can be defined as follows:

$$Z_a = c + \frac{k}{\mathrm{j}\omega} \quad , \quad Z_a = c + \frac{k}{\mathrm{j}\omega} + \mathrm{j}\omega \frac{I_w}{r_w^2} + \frac{c_w}{r_w^2} \quad , \quad Z_a = c + \frac{k}{\mathrm{j}\omega} + \mathrm{j}\omega \frac{I_w}{r_w^2} + \frac{k_w}{\mathrm{j}\omega r_w^2} \tag{2.22}$$

respectively for the classical actuator (Figure 2.1a), for the hinged flywheel actuator (Figure 2.1b,d) and for the pinned flywheel actuator (Figure 2.1c,e). In these expressions k and c are the axial stiffness and damping coefficient of the proof mass suspension. The damping coefficients of the proof mass suspension are calculated with the assumption that the damping ratio is constant for all configurations of the inertial actuators. Thus, for the classical proof mass actuator the damping coefficient is calculated with the following formula $c = 2\zeta\sqrt{kM_a}$. For the hinged configuration with the flywheel connected to the case the damping coefficient is calculated with the following formula $c = 2\zeta\sqrt{k(M_w + I_w/r_w^2)}$, while for the pinned configuration with the following formula $c = 2\zeta\sqrt{(k + k_w/r_w^2)(M_w + I_w/r_w^2)}$. For the hinged configuration with the flywheel connected to the proof mass the damping coefficient

is given with the following formula $c = 2\zeta\sqrt{k(M_w + m_w + I_w/r_w^2)}$, while for the pinned configuration with the flywheel connected to the proof mass is given by $c = 2\zeta\sqrt{(k + k_w/r_w^2)(M_w + m_w + I_w/r_w^2)}$. The k_w and c_w are the torsional stiffness and damping coefficient of the flywheel shaft, where the torsional damping is given by $c_w = 2\zeta_w r_w^2\sqrt{k(M_w + m_w + I_w/r_w^2)}$. The $I_w = \frac{1}{2}m_w R_w^2$ is the polar moment of inertia of the flywheel disk and, as shown in Figure 2.2c, R_w and r_w are respectively the external radius of the flywheel and the radius of the pinion rack gear mechanism. The transduction coefficient of the coil–magnet is given by ψ_a, as specified in Table 2.1. For simplicity, Equation (2.20) has also been rewritten in the following compact form:

$$\mathbf{f} = -\mathbf{Z}\dot{\mathbf{w}} + \boldsymbol{\psi} i_a \,. \tag{2.23}$$

The complex voltage at the terminals of the coil shown in Figure 2.2b, have been expressed with the following impedance relation:

$$u_a = Z_e i_a + \psi_a \dot{w}_c - \psi_a \dot{w}_m \,, \tag{2.24}$$

where Z_e is the coil electrical impedance given by:

$$Z_e = j\omega L + R \tag{2.25}$$

and has also been rewritten in the following compact form:

$$u_a = Z_e i_a + \boldsymbol{\psi}^{\mathrm{T}} \dot{\mathbf{w}} \,. \tag{2.26}$$

After substitution of Equation (2.23) into Equation (2.16), the vector with velocities for the current driven actuator results:

$$\dot{\mathbf{w}} = \mathbf{q}_{ia} i_a + \mathbf{q}_{ip} p \,, \tag{2.27}$$

where:

$$\mathbf{q}_{ia} = (\mathbf{I} + \mathbf{YZ})^{-1}\mathbf{Y}\boldsymbol{\psi} \quad , \quad \mathbf{q}_{ip} = (\mathbf{I} + \mathbf{YZ})^{-1}\mathbf{Y}_p \,, \tag{2.28}$$

and $\mathbf{I}$ is a 3×3 identity matrix. Instead, rewriting Equation (2.26) and substituting it to Equation (2.27) the complex velocity is given:

$$\dot{\mathbf{w}} = \mathbf{q}_{ua} u_a + \mathbf{q}_{up} p \,, \tag{2.29}$$

where:

$$\mathbf{q}_{ua} = \left(\mathbf{I} + \mathbf{q}_{ia}\frac{1}{Ze}\boldsymbol{\psi}^{\mathrm{T}}\right)^{-\mathbf{1}} \mathbf{q}_{ia}\frac{1}{Ze} \quad , \quad \mathbf{q}_{up} = \left(\mathbf{I} + \mathbf{q}_{ia}\frac{1}{Ze}\boldsymbol{\psi}^{\mathrm{T}}\right)^{-\mathbf{1}} \mathbf{q}_{ip} \,. \tag{2.30}$$

The complex velocity at the control position can be expressed in terms of the complex amplitude of the incident wave $p(\omega)$ and the complex amplitude of the current fed to the actuator $i(\omega)$ with the following algebraic expression:

$$\dot{w}_c = G_{ca} i_a + G_{cp} p \,, \tag{2.31}$$

where:

$$G_{ca} = \mathbf{t}_a \mathbf{q}_{ia} \quad , \quad G_{cp} = \mathbf{t}_a \mathbf{q}_{ip} \tag{2.32}$$

and $\mathbf{t}_a = \lfloor 1 \quad 0 \quad 0 \rfloor$. Here the G_{ca} is the open loop sensor – actuator frequency response function (FRF) for the current driven actuator, which is used later on to assess the stability of the feedback loops using the Nyquist criterion.

Simultaneously, the complex velocity at the control position can be also expressed in terms of the complex amplitude of the voltage applied to the actuator $u(\omega)$ with the following algebraic expression:

$$\dot{w}_c = G_{cu} u_a + G_{up} p \,, \tag{2.33}$$

where:

$$G_{cu} = \mathbf{t}_a \mathbf{q}_{ua} \quad , \quad G_{up} = \mathbf{t}_a \mathbf{q}_{up} \,. \tag{2.34}$$

Also in this case the G_{cu} is the open loop sensor – actuator frequency response function (FRF), which is used later on to assess the stability of the feedback loops, however in this case for voltage driven inertial actuator.

When the negative velocity feedback control loop implements a constant gain g_c with a power amplifier, a fixed current signal i_a proportional to the error velocity signal $\dot{w}_c$ is fed to the actuator coil, such that:

$$i_a = -g_c \dot{w}_c \,. \tag{2.35}$$

Instead, when the negative velocity feedback control loop for the voltage driven actuator is implemented the error velocity signal $\dot{w}_c$ is fed to the actuator coil with a constant gain g_c, such that:

$$u_a = -g_c \dot{w}_c \,. \tag{2.36}$$

Therefore, substituting Equation (2.35) into Equation (2.31) the closed loop response at the control position for the current driven actuator is given by the following expression:

$$\dot{w}_c = G_{cli} p \,, \tag{2.37}$$

where:

$$G_{cli} = \frac{G_{cp}}{1 + g_c G_{ca}}. \tag{2.38}$$

However, substituting Equation (2.36) into Equation (2.33), the closed loop response at the control position for the voltage driven actuator is given by the following expression:

$$\dot{w}_c = G_{clu} p\,, \tag{2.39}$$

where:

$$G_{clu} = \frac{G_{up}}{1 + g_c G_{cu}}. \tag{2.40}$$

The time–averaged total flexural kinetic energy, which for brevity will be referred as kinetic energy in the remaining part of the article, is used to evaluate the flexural response of the plate without and with feedback loops. For time–harmonic vibrations, the time–averaged kinetic energy is given by the following formula:

$$KE(t) = \lim_{T\to\infty} \frac{1}{T}\frac{1}{2}\int_T \int_A \rho h \dot{w}^2(x,y,t)\mathrm{dA}\, dt = \frac{1}{4}\int_A \rho h |\dot{w}(x,y,\omega)|^2 \mathrm{dA}\,, \tag{2.41}$$

where A is the area of the plate. Also, the complex velocity of the plate $\dot{w}(x,y,\omega)$ can be derived from the following expression:

$$\dot{w}(x,y,\omega) = \boldsymbol{\phi}^{\mathrm{T}}(x_r,y_r)[\mathbf{a}_c(\omega)\ \mathbf{0}\ \ \mathbf{a}_b(\omega)]\mathbf{f}(\omega) + \boldsymbol{\phi}^{\mathrm{T}}(x_r,y_r)\mathbf{a}_p(\omega)p(\omega)\,. \tag{2.42}$$

Here $\mathbf{0}$ is a n×1 vector of zeros, and

$$\mathbf{a}_c(\omega) = \boldsymbol{\Omega}(\omega)\boldsymbol{\phi}(x_c,y_c)\,,\ \mathbf{a}_b(\omega) = \boldsymbol{\Omega}(\omega)\boldsymbol{\phi}(x_b,y_b)\,,\ \mathbf{a}_{p(\omega)} = \boldsymbol{\Omega}(\omega)\boldsymbol{\Phi}(\omega), \tag{2.43}$$

where the elements in the $\boldsymbol{\Phi}(\omega)$ vector are defined in Equation (2.13) for the plane acoustic wave excitation. Instead for the point force excitation the:

$$\mathbf{a}_{p(\omega)} = \boldsymbol{\Omega}(\omega)\boldsymbol{\phi}(x_p,y_p)\,, \tag{2.44}$$

where the (x_p, y_p) is the position of the primary force that excites the plate.

The complex vector with the junction forces $\mathbf{f}$ in Equation (2.42) for the current driven actuator can be derived with the following steps: first, Equation (2.37) is substituted in Equation (2.35); second, the resulting equation is substituted in Equation (2.27), third the resulting equation is substituted into Equation (2.23), so that:

$$\mathbf{f} = \left(\mathbf{Z}\mathbf{q}_{ia} g_c G_{cli} - \mathbf{Z}\mathbf{q}_{ip} - \boldsymbol{\psi} g_c G_{cli}\right)p\,. \tag{2.45}$$

Instead the complex vector with the junction forces $\mathbf{f}$ in Equation (2.42) for the voltage driven actuator can be derived with the following steps: first, Equation (2.39) is

substituted in Equation (2.36); second, the resulting equation is substituted in Equation (2.29), third the resulting equation and rewritten Equation (2.26) are substituted into Equation (2.23), so that:

$$\mathbf{f} = \left(\left(\mathbf{Z} + \boldsymbol{\psi} \frac{1}{Z_e} \boldsymbol{\psi}^{\mathrm{T}} \right) \left(\mathbf{q}_{ua} g_c G_{clu} - \mathbf{q}_{up} \right) - \boldsymbol{\psi} \frac{1}{Z_e} g_c G_{clu} \right) p \, . \tag{2.46}$$

Substitution of Equation (2.45) into Equation (2.42) gives:

$$\dot{w}(x, y, \omega) = \boldsymbol{\phi}^{\mathrm{T}}(x, y) \mathbf{a}_{cb}(\omega) p(\omega) + \boldsymbol{\phi}^{\mathrm{T}}(x, y) \mathbf{a}_{p}(\omega) p(\omega), \tag{2.47}$$

where for the current driven actuator:

$$\mathbf{a}_{cb} = [\mathbf{a}_c(\omega) \; \mathbf{0} \;\; \mathbf{a}_b(\omega)] \left(\mathbf{Z} \mathbf{q}_a g_c G_{cl} - \mathbf{Z} \mathbf{q}_p - \boldsymbol{\psi} g_c G_{cl} \right) , \tag{2.48}$$

while for the voltage driven actuator:

$$\mathbf{a}_{cb} = [\mathbf{a}_c(\omega) \; \mathbf{0} \;\; \mathbf{a}_b(\omega)] \left(\left(\mathbf{Z} + \boldsymbol{\psi} \tfrac{1}{Z_e} \boldsymbol{\psi}^{\mathrm{T}} \right) \left(\mathbf{q}_{ua} g_c G_{clu} - \mathbf{q}_{up} \right) - \boldsymbol{\psi} \tfrac{1}{Z_e} g_c G_{clu} \right). \tag{2.49}$$

Thus, recalling that for the flexural natural modes given above the following orthogonality properties holds, $\int_A \; \phi_n^2 \, (x, y) dA = A$ and $\int_A \; \phi_n(x, y) \phi_{m \neq n}(x, y) \, dA = 0$ the kinetic energy of the plate with the passive effects of the flywheel proof mass actuator and the active effects of the velocity feedback loop is given by:

$$KE(\omega) = \frac{1}{4} M_p \left[\mathbf{a}_p + \mathbf{a}_{cb} \right]^{\mathrm{H}} \left[\mathbf{a}_p + \mathbf{a}_{cb} \right] |p|^2 \, . \tag{2.50}$$

where p is pressure for the plane acoustic wave excitation or force for point force excitation. The kinetic energy for the plate with the feedback loop open can be derived after setting $g_c = 0$ in the expression for the vector $\mathbf{a}_{cb}$. Also the kinetic energy for the plain plate without proof mass actuator can be derived by setting $\mathbf{a}_{cb} = \mathbf{0}$.

2.4 DYNAMIC CHARACTERISTICS OF THE PROPOSED ACTUATORS

This section investigates the dynamic and kinematic properties of the classical and four proposed flywheel proof mass actuators. The mathematical derivation is given for each principal electromechanical property. The equations are used to obtain the typical properties of the inertial actuators used in active vibration control applications based on the frequency response functions (FRF) of the base impedance, the actuators blocked force per unit driving current, the actuators transduction FRF, the actuators blocked force per unit applied voltage, the electrical impedance and the actuators proof mass stroke per unit driving current. The base impedance FRF is used to

characterise the mechanical components of the inertial actuators. The parameters of the mechanical components can be used to calculate the inertial mass static deflection, which is a principal parameter used to assess the actuator robustness in case of shocks. The blocked force FRFs define the extent of the force generated at the actuator base per unit driving signal (current or voltage). The electrical impedance FRF is used to characterise the electrical components of the inertial actuators. Finally, the actuator stroke defines the maximum displacement of the inertial mass per unit driving signal.

2.4.1 Base impedance

The base impedance of the open loop actuators is given by $Z_{f\dot{w}}(\omega) = F_i/\dot{w}_c|_{i_a=0}$, where $F_i = -(F_b + F_c)$. Assuming $i_a = 0$ and $p = 0$, the following impedance and mobility equations can be extracted from Equation (2.20) and Equation (2.4): $F_c = -Z_a\dot{w}_c + Z_a\dot{w}_m$, $F_m = Z_a\dot{w}_c - Z_a\dot{w}_m$, $F_b = -Z_b\dot{w}_c$ and $\dot{w}_m = Y_m F_m$, which can be combined to give the following expression for the actuator base impedance:

$$Z_{f\dot{w}} = \frac{-F_i}{\dot{w}_c}\bigg|_{i_a=0} = \frac{Z_b + Z_b Y_m Z_a + Z_a}{1 + Y_m Z_a}. \tag{2.51}$$

Table 2.3 gives the natural frequencies and the fundamental resonance frequency and antiresonance frequencies that characterise the dynamic response of the classical and four proposed flywheel proof mass actuators obtained from base impedance simulations.

The Bode plots in Figure 2.3 show the base impedance FRFs of the classical and the four proposed proof mass actuators. The solid blue lines in the two plots are for the classical proof mass actuator. Plot (a) shows the base impedance of the actuators with the flywheel either hinged (dashed black lines) or pinned (dashed-dotted red lines) to the base of the actuator while plot (b) shows the base impedance of the actuators with the flywheel either hinged (dashed black lines) or pinned (dashed-dotted red lines) to the proof mass of the actuator.

The base impedance of the classical proof mass actuator (solid blue lines in Figure 2.3a,b) has low and high frequency asymptotes characterised by a modulus that rises proportionally to frequency with phase equal to +90°, which are spaced out by a resonance peak, at about 19.90 Hz, and an antiresonance low, at about 79.9 Hz. The resonance peak occurs in the vicinity of the fundamental natural frequency of the actuator, i.e. 19.92 Hz as given in Table 2.3. The resonance peak and antiresonance low are connected by a segment that decreases proportionally to frequency and has

phase equal to -90°. These features indicate that the base impedance is characterised by low and high frequency mass-laws, as given in Table 2.4, connected via a stiffness law, given by $Z \cong k/(\mathrm{j}\omega)$. The amplitude of the resonance peak with reference to the low frequency mass asymptote and the stiffness asymptote is controlled by the damping of the mounting system and is given by $1/(2\zeta\sqrt{1-\zeta^2})$, thus about 22 dB. These properties indicate that, at low frequencies, below 19.90 Hz, the case and proof masses oscillate together as a solid body and produce an overall mass–impedance effect. At higher frequencies, the proof mass is characterised by little oscillations and behaves like a seismic reference system such that in the frequency range between 19.90 Hz and 79.9 Hz, the elastic suspension of the proof mass controls the actuator base dynamics and produces a sky-hook stiffness–impedance effect. At frequencies above 79.9 Hz, the case controls the actuator base dynamics and produces a base mass–impedance effect.

Table 2.3. Characteristic natural, resonance and antiresonance frequencies of the actuators (the values are given with two decimal digits merely to highlight the difference between natural and resonance frequency values).

Actuator configuration	**Natural frequency ω_n [Hz]**	**Resonance frequency ω_r [Hz]**	**Antiresonacne frequency ω_a [Hz]**
Classical configuration	$\omega_n = \sqrt{\frac{k}{M_a}} = 19.92$	19.90	79.9
Flywheel hinged to the base	$\omega_n = \sqrt{\frac{k}{(M_w+\frac{I_w}{r_w^2})}} = 4.79$	4.78	5.0
Flywheel pinned to the base	$\omega_n = \sqrt{\frac{k+\frac{k_w}{r_w^2}}{(M_w+\frac{I_w}{r_w^2})}} = 6.67$	6.67	6.9
Flywheel hinged to the proof mass	$\omega_n = \sqrt{\frac{k}{(M_w+m_w+\frac{I_w}{r_w^2})}} = 4.74$	4.73	5.0
Flywheel hinged to the proof mass	$\omega_n = \sqrt{\frac{k+\frac{k_w}{r_w^2}}{(M_w+m_w+\frac{I_w}{r_w^2})}} = 6.61$	6.60	6.9

Table 2.4 provides low-frequency and high-frequency asymptotic expressions of the base impedance for the classical and four proposed flywheel proof mass actuators.

Table 2.4. Low-frequency and high-frequency asymptotic expressions of the base impedance.

Actuator configuration	**Base impedance $Z_{f\dot{w}}$ for $\omega < \omega_r$**	**Base impedance $Z_{f\dot{w}}$ for $\omega > \omega_r$**
Classical configuration	$\sim j\omega(M_a + m_b)$	$\sim j\omega m_b$
Flywheel hinged to the base	$\sim j\omega(M_w + m_w + m_b)$	$\sim j\omega(m_b + m_w + \frac{I_w/r_w^2}{1 + \frac{I_w}{r_w^2}\frac{1}{M_w}})$
Flywheel pinned to the base	$\sim j\omega(M_w + m_w + m_b)$	$\sim j\omega(m_b + m_w + \frac{I_w/r_w^2}{1 + \frac{I_w}{r_w^2}\frac{1}{M_w}})$
Flywheel hinged to the proof mass	$\sim j\omega(M_w + m_w + m_b)$	$\sim j\omega(m_b + \frac{I_w/r_w^2}{1 + \frac{I_w}{r_w^2}\frac{1}{M_w}})$
Flywheel hinged to the proof mass	$\sim j\omega(M_w + m_w + m_b)$	$\sim j\omega(m_b + \frac{I_w/r_w^2}{1 + \frac{I_w}{r_w^2}\frac{1}{M_w}})$

The base impedance of the proposed actuator with the flywheel hinged to the case (dashed black line in Figure 2.3a) shows a similar spectrum as that of the classical proof mass actuator, although it is characterised by significant scaling effects. In fact, although, the low frequencies mass-law is still given by overall mass–impedance effect, the higher frequencies mass law is about 24 dB greater than that of the classical proof mass actuator. At higher frequencies, the mass–impedance effect is controlled by the axial inertia effects produced by the base mass, by the mass of the flywheel and by the polar moment of inertia of the flywheel, as given in Table 2.4. The additional inertia effect produced by the angular oscillation of the flywheel also diminishes the fundamental natural frequency of the actuator to 4.79 Hz, as given in Table 2.3. Thus the resonance peak occurs at about 4.78 Hz while the antiresonance low occurs only at a slightly higher frequency of about 5 Hz. The vicinity between the resonance peak and antiresonance low essentially cancels the sky-hook stiffness effect in between the

resonance and antiresonance frequency and also significantly lowers the amplitudes of the resonance peak and antiresonance low. If rather than being hinged, the flywheel is pinned with a torsional spring to the actuator case (dashed-dotted red line in Figure 2.3a), the spectrum of the base impedance varies by little. The torsional spring slightly increases the fundamental natural frequency of the actuator, which becomes 6.67 Hz, as given in Table 2.3. As a result the resonance peak and antiresonance low occurs at about 6.67 Hz and 6.9 Hz respectively and thus the amplitudes of the resonance peak and antiresonance low are somewhat more marked.

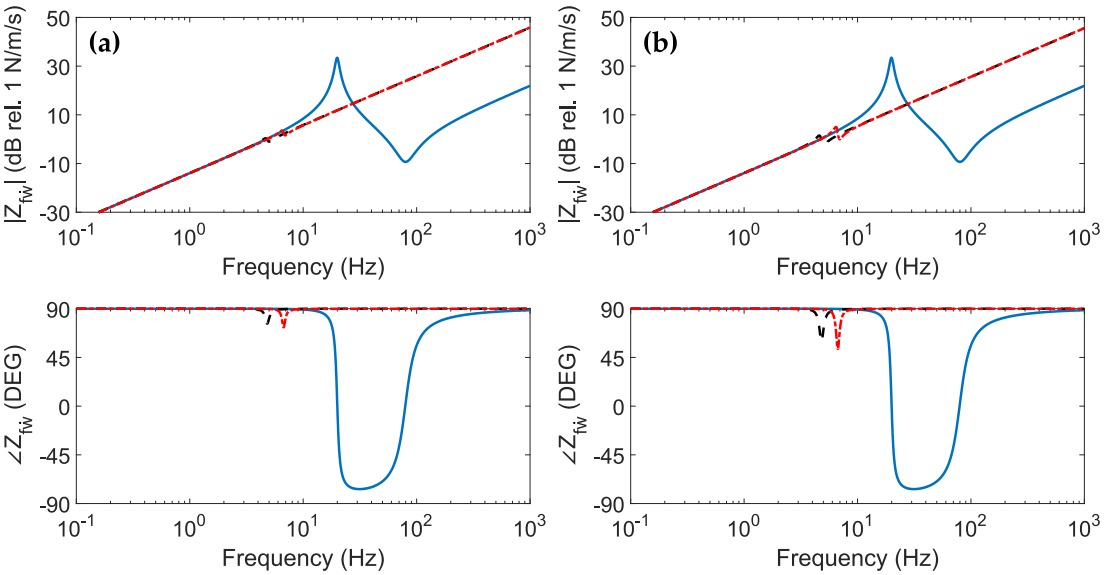

Figure 2.3. Base impedance for the actuator with flywheel attached to base (a) and flywheel attached to proof mass (b). Classical configuration (Solid blue lines). Hinged flywheel actuator (dashed black lines). Pinned flywheel actuator (dashed-dotted red lines).

The base impedance of the proposed actuator with the flywheel hinged to the proof mass (dashed black line in Figure 2.3b) shows similar asymptotic behaviour to those found when the flywheel is hinged to the actuator case. However, in this circumstance, the fundamental natural frequency of the actuator is slightly lowered since it is affected also by the additional inertia effect produced by the axial oscillation of the flywheel and becomes 4.74 Hz, as given in Table 2.3. Thus, the resonance peak and antiresonance low occurs at slightly lower frequencies, i.e. about 4.73 Hz and 5 Hz respectively, as given in Table 2.3. The low frequencies mass-law is given by overall mass-impedance effect, while the higher frequencies mass law is about 23 dB

greater than that of the classical proof mass actuator, since it is controlled by the axial inertia effects produced by the mass of the case and by the polar moment of inertia of the flywheel, as given in Table 2.4. As a result, the resonance peak and antiresonance low are slightly more marked than those of the proposed actuator with the flywheel hinged to the case. Also for this configuration, if rather than being hinged, the flywheel is pinned with a torsional spring to the actuator proof mass (dashed-dotted red line in Figure 2.3b), the spectrum of the base impedance varies by little. Again, the torsional spring slightly increases the fundamental natural frequency of the actuator, to 6.61 Hz, as given in Table 2.3. While the resonance peak and antiresonance low occurs at about 6.60 Hz and 6.9 Hz respectively so that the amplitudes of the resonance peak and antiresonance low are slightly more marked.

2.4.2 Blocked force per unit current fed to the actuator

The blocked force produced by the actuators per unit current fed to the actuators is given by $T_{fi} = F_c/i_a|_{\dot{w}_c=0}$. In this case, assuming $\dot{w}_c = 0$ and $p = 0$, the following impedance and mobility equations can be derived from Equation (2.20) and Equation (2.4): $F_c = Z_a\dot{w}_m + \psi_a i_a$, $F_m = -Z_a\dot{w}_m - \psi_a i_a$ and $\dot{w}_m = Y_m F_m$, which can be combined to give the following expression of the blocked force per unit current fed to the actuator:

$$T_{fi} = \left.\frac{F_c}{i_a}\right|_{\dot{w}_c=0} = \frac{\psi_a}{1 + Y_m Z_a}\,. \tag{2.52}$$

Table 2.5 provide low-frequency and high-frequency asymptotic expressions of the blocked force per unit current fed to the classical and four proposed flywheel proof mass actuators.

The Bode plots in Figure 2.4 show the blocked force per unit current fed to the classical and the four proposed proof mass actuators. The solid blue lines in the two plots are for the classical proof mass actuator. Plot (a) shows the blocked force of the actuators with the flywheel either hinged (dashed black lines) or pinned (dashed-dotted red lines) to the base of the actuator while plot (b) shows the blocked force of the actuators with the flywheel either hinged (dashed black lines) or pinned (dashed-dotted red lines) to the proof mass of the actuator.

The amplitude of the blocked force per unit current fed to the classical proof mass actuator at low frequencies rises proportionally to ω^2, as given by asymptote in Table 2.5 and is characterised by phase equal to +180°. In other words, it has opposite phase

than that of the driving current signal fed to the actuator coil. The amplitude reaches a peak value at the resonance frequency of the actuator at 19.90 Hz, as given in Table 2.3 and then it settle to a constant value. Around the resonance frequency, the phase undergoes a -180° lag such that, at higher frequencies, the blocked force produced by the actuator is in phase with the driving current signal i_a and is equal to actuator transduction coefficient as given in Table 2.5.

Table 2.5. Low-frequency and high-frequency asymptotic expressions of the blocked force per unit current fed to the actuators.

Actuator configuration	**Blocked force T_{fi} for $\omega < \omega_r$**	**Blocked force T_{fi} for $\omega > \omega_r$**
Classical configuration	$\sim(\mathrm{j}\omega)^2 \frac{\psi_a M_a}{k}$	$\sim\psi_a$
Flywheel hinged to the base	$\sim(\mathrm{j}\omega)^2 \frac{\psi_a M_w}{k}$	$\sim \psi_a/(1+\frac{I_w}{M_w r_w^2})$
Flywheel pinned to the base	$\sim(\mathrm{j}\omega)^2 \frac{\psi_a M_w}{k+k_w/r_w^2}$	$\sim \psi_a/(1+\frac{I_w}{M_w r_w^2})$
Flywheel hinged to the proof mass	$\sim(\mathrm{j}\omega)^2 \frac{\psi_a (M_w+m_w)}{k}$	$\sim \psi_a/(1+\frac{I_w}{(M_w+m_w) r_w^2})$
Flywheel hinged to the proof mass	$\sim(\mathrm{j}\omega)^2 \frac{\psi_a (M_w+m_w)}{k+k_w/r_w^2}$	$\sim \psi_a/(1+\frac{I_w}{(M_w+m_w) r_w^2})$

The blocked force produced by the proposed actuator with the flywheel hinged to the case (dashed black line in Figure 2.4a) shows similar asymptotic behaviours as the classical proof mass actuator, although the resonance peak occurs at a much lower resonance frequency of 4.78 Hz as given in Table 2.3. At higher frequencies, the constant force effect per unit driving current signal is about 28.3 dB lower and it settles to a constant value as defined by an asymptote, in Table 2.5. Thus the presence of the flywheel component lowers the cut off resonance frequency above which the actuator produces a constant force in phase with the driving current signal but also reduces the amplitude of the force by a factor $1/(1+I_w/M_w r_w^2)$. If rather than being hinged, the flywheel is pinned with a torsional spring to the actuator case (dashed-dotted red line in Figure 2.4a), the spectrum of the blocked force per unit current fed to the actuator varies by little. The cut off resonance frequency occurs at a slightly

higher frequency of 6.67 Hz, as given in Table 2.3 while the constant force produced at higher frequencies is still defined by the same asymptote, as given in Table 2.5.

The blocked forces produced by the proposed actuators with the flywheel hinged to the proof mass (dashed black line in Figure 2.4b) shows similar asymptotic effects to those found with the flywheel hinged to the actuator case. In this circumstance, the cut off resonance frequency occurs at a slightly lower value of 4.73 Hz, as given in Table 2.3 and the constant force produced at higher frequencies is slightly higher, as given in Table 2.5. If rather than being hinged, the flywheel is pinned with a torsional spring to the actuator proof mass (dashed-dotted red line in Figure 2.4b), the spectrum of the blocked force varies by little since the cut off resonance frequency occurs at slightly higher frequency of 6.60 Hz, as given in Table 2.3. However, the constant force produced at higher frequencies remains defined by the same asymptote, as given in Table 2.5.

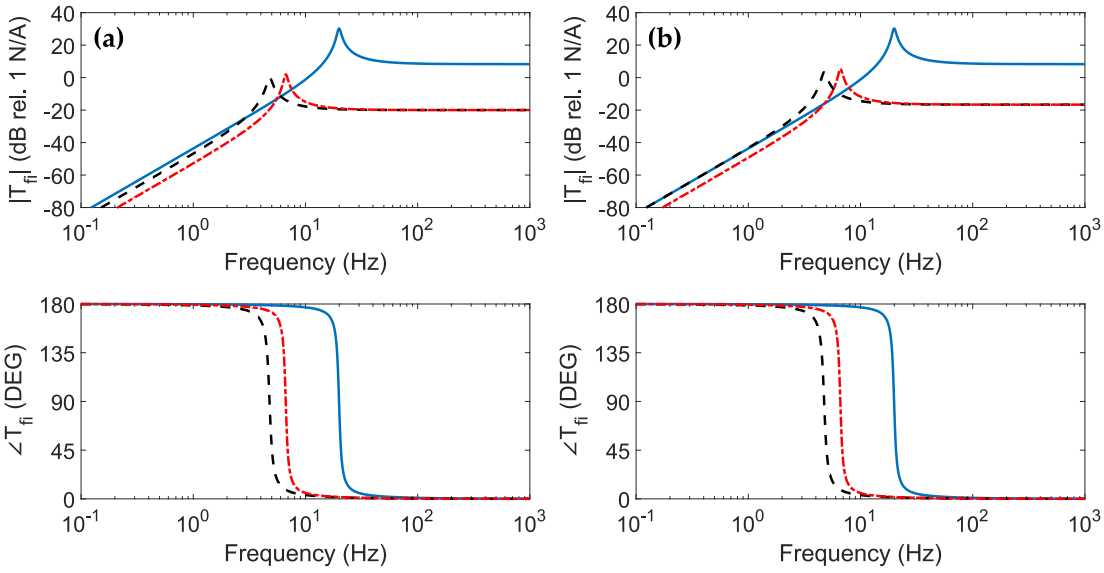

Figure 2.4. Blocked force per unit current fed to the actuator with flywheel attached to base (a) and flywheel attached to proof mass (b). Classical configuration (Solid blue lines). Hinged flywheel actuator (dashed black lines). Pinned flywheel actuator (dashed-dotted red lines).

2.4.3 Transduction FRF

The actuators transduction FRF is given by $T_{u\dot{w}} = u_a/\dot{w}_c|_{i_a=0}$. In this case, assuming $i_a = 0$ and $p = 0$, the following impedance and mobility equations can be

derived from Equation (2.4), Equation (2.20) and Equation (2.24): $\dot{w}_m = Y_m F_m$, $F_c = -Z_a \dot{w}_c + Z_a \dot{w}_m$, $F_m = Z_a \dot{w}_c - Z_a \dot{w}_m$, $F_b = -Z_b \dot{w}_c$ and $u_a = \psi_a \dot{w}_c - \psi_a \dot{w}_m$, which can be combined to give the following expression of the actuator transduction FRF:

$$T_{u\dot{w}} = \frac{-u_a}{\dot{w}_c}\bigg|_{i_a=0} = \frac{-\psi_a}{1 + Y_m Z_a} \tag{2.53}$$

It is important to note that the expression obtained for the actuator transduction FRF $T_{u\dot{w}}$ in Equation (2.53), is bound to be equal to the expression obtained for the blocked force per unit current fed to the coil of the actuator obtained in Equation (2.52). Thus, the low-frequency and high-frequency asymptotic expressions of the blocked force per unit current fed to the classical and four proposed flywheel proof mass actuators given in Table 2.5 can be also used for the actuator transduction FRF. The negative sign in Equation (2.53) indicates that the generated voltage has opposite direction to the direction defined in the Figure 2.2b.

The Bode plots in Figure 2.5 show the actuator transduction FRF of the classical and the four proposed proof mass actuators. The solid blue lines in the two plots are for the classical proof mass actuator. Plot (a) shows the transduction FRF of the actuators with the flywheel either hinged (dashed black lines) or pinned (dashed-dotted red lines) to the base of the actuator while plot (b) shows the transduction FRF of the actuators with the flywheel either hinged (dashed black lines) or pinned (dashed-dotted red lines) to the proof mass of the actuator.

The amplitude of the classical proof mass actuator transduction FRF at low frequencies rises proportionally to ω^2, as given in Table 2.5 and is characterised by phase equal to 0°. The amplitude reaches a peak value at the resonance frequency of the actuator at 19.90 Hz, as given in Table 2.3 and then it settle to a constant value. Around the resonance frequency, the phase undergoes a lag such that, at higher frequencies is equal to -180°, and the amplitude is equal to actuator transduction coefficient as given in Table 2.5.

The transduction FRFs of the proposed actuator with the flywheel hinged to the case (dashed black line in Figure 2.5a) shows similar asymptotic behaviours as the classical proof mass actuator, with the resonance peak that occurs at a much lower resonance frequency of 4.78 Hz as given in Table 2.3. At higher frequencies, the produced voltage per unit velocity of excitation is about 28 dB lower and it settles to a constant value as given in Table 2.5. The presence of the flywheel component reduces the amplitude of the produced voltage above the actuator resonance frequency. If rather than being hinged, the flywheel is pinned with a torsional spring

to the actuator case (dashed-dotted red line in Figure 2.5a), the spectrum of the actuator transduction FRF varies by little. The cut off resonance frequency occurs at a slightly higher frequency of 6.67 Hz, as given in Table 2.3 while the produced constant voltage at higher frequencies is still defined by the same asymptote, as given in Table 2.5.

The transduction FRF of the actuators with the flywheel hinged to the proof mass (dashed black line in Figure 2.5b) shows similar asymptotic effects to those found with the flywheel hinged to the actuator case. The cut off resonance frequency occurs at a slightly lower value of 4.73 Hz, as given in Table 2.3 and the constant force produced at higher frequencies is slightly higher, as given in Table 2.5 but it is still about 25 dB lower compared to the classical proof mass actuator. For the pinned flywheel with a torsional spring attached to the actuator proof mass (dashed-dotted red line in Figure 2.5b), the spectrum of the transduction FRF varies by little since the cut off resonance frequency occurs at slightly higher frequency of 6.60 Hz. The constant voltage effect produced at higher frequencies remains defined by the same asymptote, as given in Table 2.5.

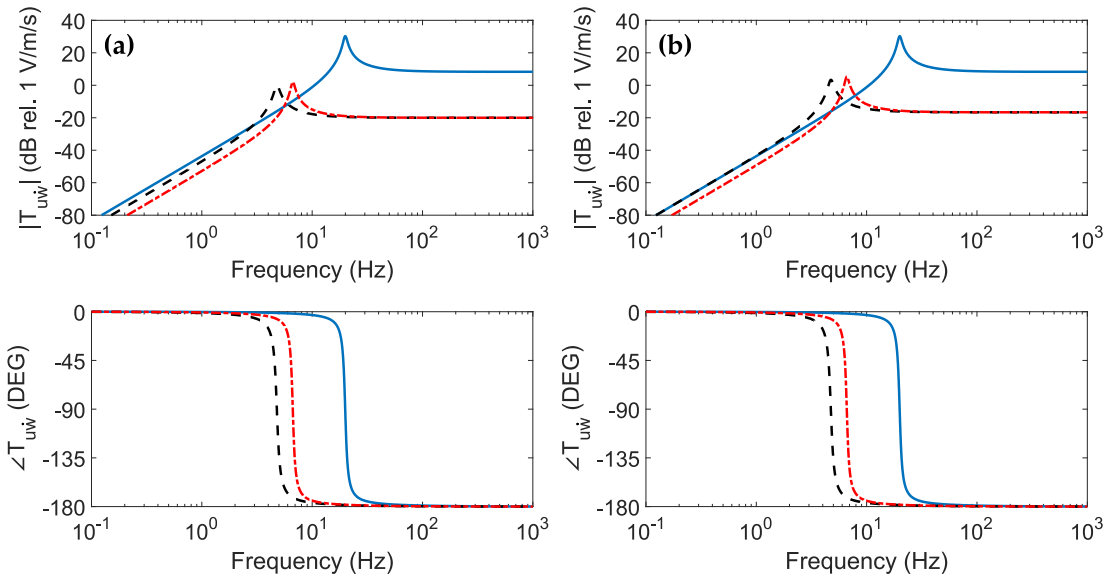

Figure 2.5. Actuator transduction FRF with flywheel attached to case (a) and flywheel attached to proof mass (b). Classical configuration (Solid blue lines). Hinged flywheel actuator (dashed black lines). Pinned flywheel actuator (dashed-dotted red lines).

2.4.4 Blocked force per unit voltage applied to the actuator

The produced blocked force per unit voltage applied to the actuators is given by $T_{fu} = F_c/u_a|_{\dot{w}_c=0}$. In this case, assuming $\dot{w}_c = 0$ and $p = 0$, the following impedance and mobility equations can be derived from Equation (2.4), Equation (2.20) and Equation (2.24): $\dot{w}_m = Y_m F_m$, $F_c = Z_a \dot{w}_m + \psi_a i_a$, $F_m = -Z_a \dot{w}_m - \psi_a i_a$ and $u_a = Z_e i_a - \psi_a \dot{w}_m$, which can be combined to give the following expression for the blocked force per unit voltage applied to the actuator:

$$T_{fu} = \frac{F_c}{u_a}\Big|_{\dot{w}_c=0} = \frac{\psi_a}{Z_e + Z_e Y_m Z_a + Y_m \psi_a^2}. \tag{2.54}$$

Table 2.6 provide low-frequency and high-frequency asymptotic expressions of the blocked force per unit voltage applied to the classical and four proposed flywheel proof mass actuators.

Table 2.6. Low-frequency and high-frequency asymptotic expressions of the blocked force per unit voltage applied to the actuators.

Actuator configuration	**Blocked force T_{fu} for $\omega < \omega_r$**	**Blocked force T_{fu} for $\omega > \omega_r$**
Classical configuration	$\sim(\mathrm{j}\omega)^2 \frac{\psi_a M_a}{kR}$	$\sim \frac{\psi_a}{(R + j\omega L)}$
Flywheel hinged to the base	$\sim(\mathrm{j}\omega)^2 \frac{\psi_a M_w}{kR}$	$\sim \frac{\psi_a}{(1 + \frac{I_w}{M_w r_w^2})(R + j\omega L)}$
Flywheel pinned to the base	$\sim(\mathrm{j}\omega)^2 \frac{\psi_a M_w}{(k + k_w/r_w^2)R}$	$\frac{\psi_a}{(1 + \frac{I_w}{M_w r_w^2})(R + j\omega L)}$
Flywheel hinged to the proof mass	$\sim(\mathrm{j}\omega)^2 \frac{\psi_a (M_w + m_w)}{kR}$	$\sim \frac{\psi_a}{(1 + \frac{I_w}{(M_w + m_w) r_w^2})(R + j\omega L)}$
Flywheel hinged to the proof mass	$\sim(\mathrm{j}\omega)^2 \frac{\psi_a (M_w + m_w)}{(k + k_w/r_w^2)R}$	$\sim \frac{\psi_a}{(1 + \frac{I_w}{(M_w + m_w) r_w^2})(R + j\omega L)}$

The Bode plots in Figure 2.6 show the blocked force per unit voltage applied to the the classical and the four proposed proof mass actuators. The solid blue lines in the

two plots are for the classical proof mass actuator. Plot (a) shows the blocked force of the actuators with the flywheel either hinged (dashed black lines) or pinned (dashed-dotted red lines) to the base of the actuator while plot (b) shows the blocked force of the actuators with the flywheel either hinged (dashed black lines) or pinned (dashed-dotted red lines) to the proof mass of the actuator.

The amplitude of the blocked force produced by the classical proof mass actuator at low frequencies rises proportionally to ω^2 as given by asymptote in Table 2.6 and is characterised by phase equal to +180°. The amplitude reaches a highly damped peak value at the resonance frequency of the actuator at 19.90 Hz and then it settle to a constant value as given in Table 2.6. Compared to the blocked force for the unit current fed to the actuator, the blocked force for the voltage signal presents highly damped resonance peaks. The resistive effect of the coil rounds off the peaks at the resonance frequency of the actuator. Around the resonance frequency, the phase undergoes a smooth -180° lag such that, at higher frequencies, the blocked force produced by the actuator is in phase with the voltage signal. At higher frequencies, the inductive effect of the actuator coil starts to take more important role and thus making the produced blocked force to drop with frequency. At the same time, the phase undergoes additional lag such that, at higher frequencies, the produced by the actuator blocked force starts to be out phase with the voltage signal.

The blocked force produced by the proposed actuator with the flywheel hinged to the case (dashed black line in Figure 2.6a) shows similar asymptotic behaviours as the classical proof mass actuator, although the resonance peak occurs at a much lower resonance frequency of 4.78 Hz, as given in Table 2.3. The constant force effect per unit voltage signal is about 29 dB lower due to the axial inertia effect produced by the flywheel as given in Table 2.6. If rather than being hinged, the flywheel is pinned with a torsional spring to the actuator case (dashed-dotted red line in Figure 2.6a), the spectrum of the blocked force per unit voltage applied to the actuator varies by little. The cut off resonance frequency occurs at a slightly higher frequency of 6.67 Hz, as given in Table 2.3 while the constant force produced at higher frequencies is still given by the same asymptote as given in Table 2.6.

The blocked forces produced by the proposed actuators with the flywheel hinged to the proof mass (dashed black line in Figure 2.6b) shows similar asymptotic effects to those found with the flywheel hinged to the actuator case. In this circumstance, the cut off resonance frequency occurs at a slightly lower value of 4.73 Hz as given in Table 2.3. The constant force produced at higher frequencies is slightly higher as given by an asymptote in Table 2.6 but is still about 25 dB lower compared to the classical

proof mass actuator. If rather than being hinged, the flywheel is pinned with a torsional spring to the actuator proof mass (dashed-dotted red line in Figure 2.6b), the spectrum of the blocked force varies by little since the cut off resonance frequency occurs at slightly higher frequency of 6.60 Hz as given in Table 2.3. The constant force produced at higher frequencies remains equal as given by an asymptote in Table 2.6.

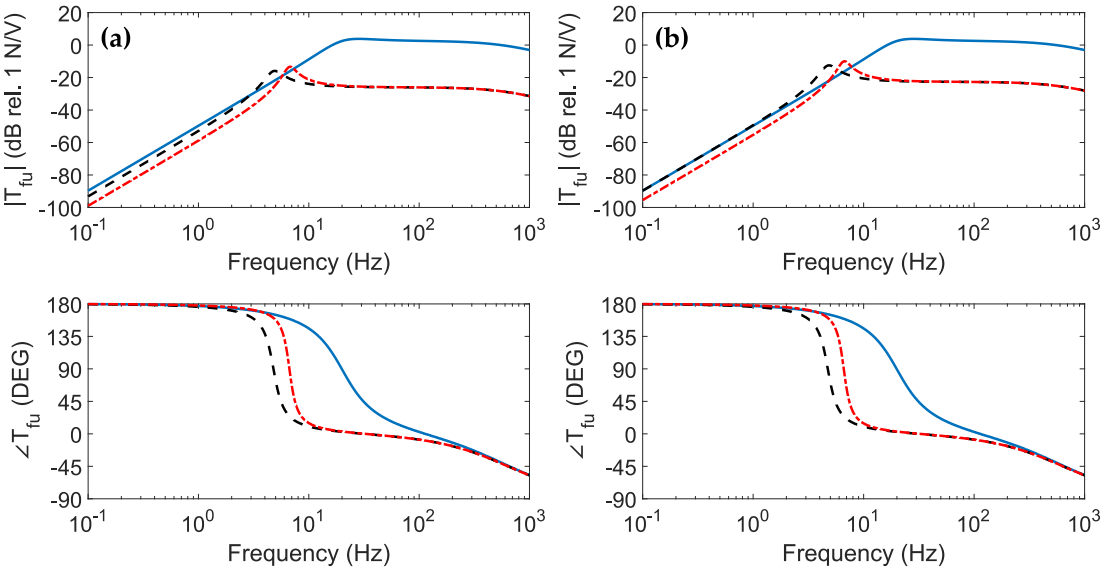

Figure 2.6. Blocked force per unit voltage applied to the actuator with flywheel attached to base (a) and flywheel attached to proof mass (b). Classical configuration (Solid blue lines). Hinged flywheel actuator (dashed black lines). Pinned flywheel actuator (dashed-dotted red lines).

2.4.5 Electrical impedance

The electrical impedance of the actuators is given by $Z_{ui} = u_a/i_a|_{\dot{w}_c=0}$. In this case, assuming $\dot{w}_c = 0$ and $p = 0$, the following impedance and mobility equations can be derived from Equation (2.4), Equation (2.20) and Equation (2.24): $\dot{w}_m = Y_m F_m$, $F_c = Z_a \dot{w}_m + \psi_a i_a$, $F_m = -Z_a \dot{w}_m - \psi_a i_a$ and $u_a = Z_e i_a - \psi_a \dot{w}_m$, which can be combined to give the following expression for the actuator electrical impedance:

$$Z_{ui} = \frac{u_a}{i_a}\bigg|_{\dot{w}_c=0} = \frac{Z_e + Z_e Y_m Z_a + Y_m \psi_a^2}{1 + Y_m Z_a}. \tag{2.55}$$

The Bode plots in Figure 2.7 show electrical impedance FRFs of the classical and the four proposed proof mass actuators. The solid blue lines in the two plots are for

the classical proof mass actuator. Plot (a) shows the electrical impedance of the actuators with the flywheel either hinged (dashed black lines) or pinned (dashed-dotted red lines) to the base of the actuator while Plot (b) shows the electrical impedance of the actuators with the flywheel either hinged (dashed black lines) or pinned (dashed-dotted red lines) to the proof mass of the actuator.

At low frequencies, the amplitude of the electrical impedance for the classical proof mass actuator is characterised by the constant value equal to coil resistance, with the phase equal to 0°. The amplitude reaches a peak value equal to 27.8 dB at the resonance frequency of the actuator at 19.90 Hz, as given in Table 2.3 and it drops to a constant value equal to coil resistance. Below the resonance frequency, the phase slowly increases and then undergoes almost -180° lag at the actuator resonance frequency. Above the resonance frequency, the phase slowly increases to a constant value equal to 0°. At higher frequencies, the inductive effect of the actuator coil starts to take more important role making the electrical impedance amplitude and phase rise with frequency.

The electrical impedance of the proposed actuator with the flywheel hinged to the case (dashed black line in Figure 2.7a) shows similar asymptotic behaviours as the classical proof mass actuator, although the resonance peak occurs at a much lower resonance frequency of 4.78 Hz, as given in Table 2.3 and with much lower amplitude equal to 16 dB. Thus the presence of the flywheel component lowers the resonance frequency and increases the damping effect as given in Equation (2.22). When the flywheel is pinned with a torsional spring to the actuator case (dashed-dotted red line in Figure 2.7a), the spectrum of the electrical impedance varies by little. The resonance frequency occurs at a slightly higher frequency of 6.67 Hz with amplitude equal to 15.4 dB.

The electrical impedance of the flywheel hinged to the proof mass (dashed black line in Figure 2.7b) shows similar asymptotic effects to those found with the flywheel hinged to the actuator case. The resonance frequency occurs at 4.73 Hz with the amplitude equal to 16 dB. If rather than being hinged, the flywheel is pinned with a torsional spring to the actuator proof mass (dashed-dotted red line in Figure 2.7b), the spectrum of the electrical impedance shows that the resonance frequency occurs at 6.60 Hz with the amplitude equal to 15.3 dB.

The classical and the four proposed proof mass actuator configurations are based on the same electrical circuit, thus the low and high frequency asymptotes are equal to the each other.

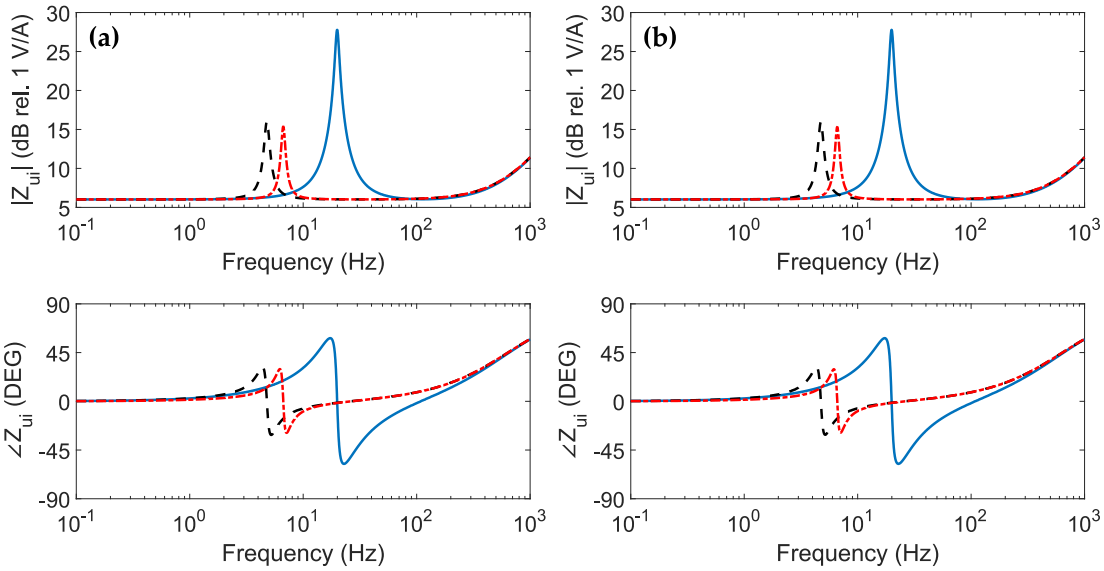

Figure 2.7. Electrical impedance of the actuator with flywheel attached to base (a) and flywheel attached to proof mass (b). Classical configuration (Solid blue lines). Hinged flywheel actuator (dashed black lines). Pinned flywheel actuator (dashed-dotted red lines).

2.4.6 Proof mass stroke

The stroke of the actuators proof mass per unit current fed to the actuators is given by $T_{\Delta wi} = \Delta w/i_a|_{w_c=0}$, where $\Delta w = w_m - w_c$. Assuming $w_c = 0$ and $p = 0$, the following impedance and mobility equations can be derived from Equation (2.4), Equation (2.20): $\dot{w}_m = Y_m F_m$, $F_c = Z_a \dot{w}_m + \psi_a i_a$, $F_m = -Z_a \dot{w}_m - \psi_a i_a$ and $u_a = Z_e i_a - \psi_a \dot{w}_m$, which can be combined to give the following expression of the actuator for the stroke per unit current fed to the actuator:

$$T_{\Delta wi} = \frac{\Delta w}{i_a}\bigg|_{w_c=0} = -\frac{1}{j\omega}\frac{Y_m \psi_a}{1 + Y_m Z_a}. \tag{2.56}$$

Rewriting Equation (2.52) and substituting it to Equation (2.56) the blocked force produced by the actuators is given by:

$$F_c = -\frac{1}{j\omega}\frac{\Delta w}{Y_m}. \tag{2.57}$$

The obtained equation highlights that the produced force is proportional to the stroke of the inertial actuator. Thus, to maximise the control force produced by the proof mass actuator the designed transducer should move with large strokes.

Table 2.7 provide low-frequency and high-frequency asymptotic expressions of the proof mass stroke per unit current fed to the classical and four proposed flywheel proof mass actuators.

Table 2.7. Low-frequency and high-frequency asymptotic expressions of the proof mass stroke per unit current fed to the actuators.

Actuator configuration	**Stroke $T_{\Delta wi}$ for $\omega < \omega_r$**	**Stroke $T_{\Delta wi}$ for $\omega > \omega_r$**
Classical configuration	$\sim \frac{\psi_a}{k}$	$\sim \frac{1}{(j\omega)^2}\frac{\psi_a}{M_a}$
Flywheel hinged to the base	$\sim \frac{\psi_a}{k}$	$\sim \frac{1}{(j\omega)^2}\frac{\psi_a}{M_w + I_w/r_w^2}$
Flywheel pinned to the base	$\sim \frac{\psi_a}{k + \frac{k_w}{r_w^2}}$	$\sim \frac{1}{(j\omega)^2}\frac{\psi_a}{M_w + I_w/r_w^2}$
Flywheel hinged to the proof mass	$\sim \frac{\psi_a}{k}$	$\sim \frac{1}{(j\omega)^2}\frac{\psi_a}{M_w + m_w + I_w/r_w^2}$
Flywheel hinged to the proof mass	$\sim \frac{\psi_a}{k + \frac{k_w}{r_w^2}}$	$\sim \frac{1}{(j\omega)^2}\frac{\psi_a}{M_w + m_w + I_w/r_w^2}$

The Bode plots in Figure 2.8 show the proof mass stroke per unit current fed to the classical and the four proposed proof mass actuators. The solid blue lines in the two plots are for the classical proof mass actuator. Plot (a) shows the stroke of the actuators with the flywheel either hinged (dashed black lines) or pinned (dashed-dotted red lines) to the base of the actuator while Plot (b) shows the stroke of the actuators with the flywheel either hinged (dashed black lines) or pinned (dashed-dotted red lines) to the proof mass of the actuator.

At low frequencies the proof mass stroke of the classical actuator (blue lines in Figure 2.8a,b) is characterised by a constant amplitude, as given in Table 2.7, which grows to a peak value at the fundamental resonance frequency at about 19.90 Hz, and then drops at a rate proportional to $1/\omega^2$, as given in Table 2.7. The actuators with the flywheel hinged to either the case (dashed black line in Figure 2.8a) or to the proof mass (dashed black line in Figure 2.8b) are characterised by the same stroke at low frequencies. The cut off resonance frequencies where the stroke peaks and then drops,

are instead much lower and occur respectively at 4.78 Hz and 4.73 Hz as given in Table 2.3. The actuators with the flywheel pinned to either the case (dash-dotted red line in Figure 2.8a) or to the proof mass (dash-dotted red in Figure 2.8b) are instead characterised by a smaller low frequency stroke, as given in Table 2.7. This is due to the additional stiffness effect produced by the torsional spring used to pin the flywheel. The cut off resonance frequencies where the stroke peaks and then drops occurs in these two cases respectively at 6.67 Hz and 6.60 Hz, as given in Table 2.3. The peak strokes of the proposed actuators are 2 to 6 dB lower than the peak stroke of the classical actuator.

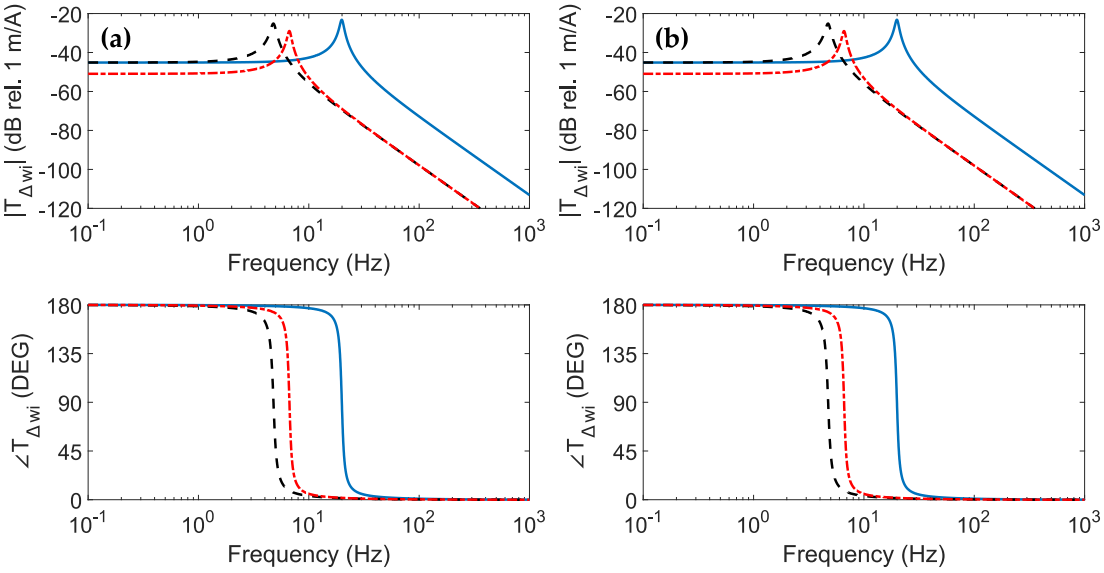

Figure 2.8. Proof mass stroke per unit driving current for the actuator with flywheel attached to base (a) and flywheel attached to proof mass (b). Classical configuration (Solid blue lines). Hinged flywheel actuator (dashed black lines). Pinned flywheel actuator (dashed-dotted red lines).

2.5 OPEN LOOP STABILITY ANALYSIS

The stability of the velocity feedback loops using the classical and the four proposed flywheel proof mass actuators is assessed using the Nyquist criterion [29], [95]. Figure 2.9 shows the Bode plots while Figure 2.10 shows the Nyquist plots of the open loop sensor – actuator FRFs, which are given by G_{ca} as specified in Equation (2.32). The solid blue lines in the two plots of Figure 2.9 are for the feedback loop with the classical proof mass actuator. The plots in Figure 2.9a consider the feedback loop

with the flywheel either hinged (dashed black lines) or pinned (dashed-dotted red lines) to the base of the actuator while the plots in Figure 2.9b consider the feedback loop with the flywheel either hinged (dashed lines) or pinned (dashed-dotted lines) to the proof mass of the actuator.

Considering first the Bode plot for the classical actuator (solid blue lines), it is noted that the amplitude is characterised by a resonance peak at about 19.9 Hz, which is due to the fundamental resonance of the proof mass actuator, and then a sequence of sharp resonance peaks and narrow antiresonance lows pairs. The phase plot is characterised by a -180° phase lag at the fundamental resonance frequency and then a sequence of -180° phase lag and +180° phase lead for each resonance peak and antiresonance low pair.

Thus, except for the first resonance peak and -180° phase lag, the open loop sensor–actuator FRF shows the typical Bode plot for collocated point velocity sensor and point force actuator pairs [86], [138]. The Bode plots of the open loop frequency response function with the flywheel hinged either to the base or proof mass (dashed black lines) present similar features, except three main differences. Firstly, the fundamental resonance peak and -180° phase lag are moved to a much lower resonance frequency of about 4.7 Hz. Secondly, the fundamental resonance peak has now a much lower amplitude than that obtained when the classical proof mass actuator is employed. Finally, above about 200 Hz, the sequence of resonance peaks and antiresonance lows pairs tends to smoothen rapidly as the frequency rises.

These effects are due to the additional inertia offered by the flywheel, which reduces the fundamental natural frequency of the actuator. Also, because of the gearing mechanism, the flywheel produces primarily a relative inertia effect, thus no matter whether it is fixed to the case or to the proof mass of the actuator, the net result is an additional inertia effect on the plate at the control point so that the sensor–actuator open loop FRF presents a smoothened spectrum at frequencies above 200 Hz. The Bode plots of the open loop FRF with the flywheel pinned either to the case or to the proof mass (dash-dotted red lines) present very similar features to those found for the hinged flywheel element, except that the resonance peak for the fundamental resonance frequency of the actuator occurs at about 6.6 Hz. This is due to the fact that the pinned shaft introduces an additional stiffness effect that rises a little the fundamental natural frequency of the proof mass compared to the hinged configuration.

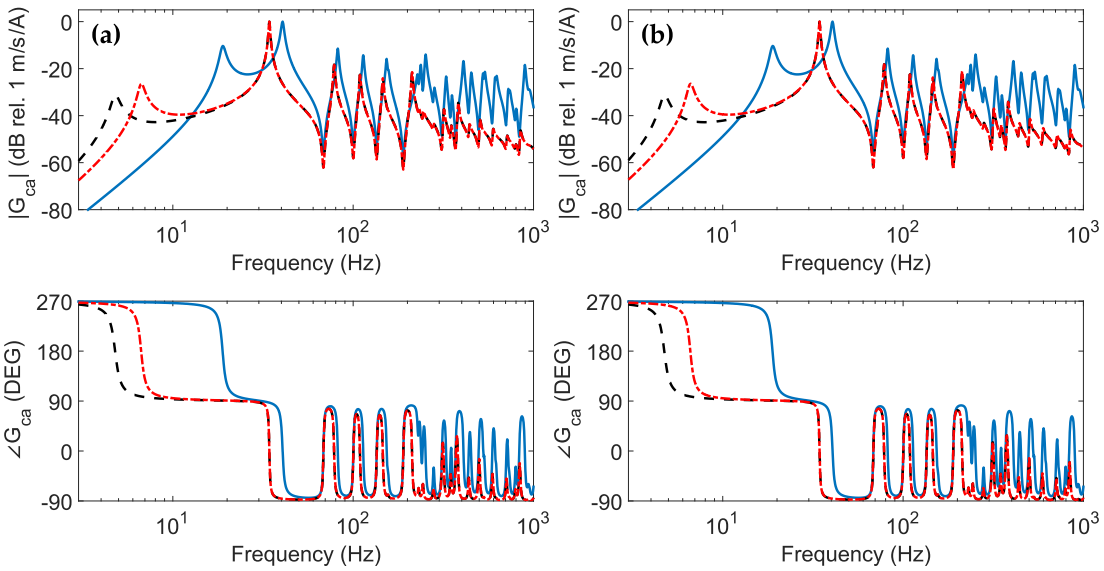

Figure 2.9. Open loop sensor–actuator FRFs for the actuator with flywheel attached to base (a) and flywheel attached to proof mass (b). Classical configuration (Solid blue lines). Hinged flywheel actuator (dashed black lines). Pinned flywheel actuator (dashed-dotted dotted red lines).

The Nyquist plots in Figure 2.10 confirm the analysis presented with the Bode plots. Figure 2.10a highlights that the Nyquist diagram for the feedback loop with the classical proof mass actuator is characterised by a circle in the real negative quadrants centred along the real axis, which is due to the resonance peak of the fundamental natural frequency, and then a series of progressively smaller circles in the real positive quadrants, centred along the real axis. The circle on the left hand quadrants indicates that the feedback loop is only conditionally stable. More precisely the stability gain margin is about 10 dB. The Nyquist plots for the feedback loops with the flywheel either hinged (Figure 2.10b, d) or pinned (Figure 2.10c, e) to either the case (Figure 2.10b, c) or proof mass (Figure 2.10d, e) show similar characteristics than those found for the feedback loop with the classical proof mass actuator apart from a very important detail: in all four cases, the circle in the real negative quadrants is much smaller than that found for the feedback loop with the classical proof mass actuator. Thus, the feedback loops with the proposed actuators are characterised by much higher gain margins, which reach the limit of about 31 dB for the hinged configurations and about 27 dB for the pinned configurations.

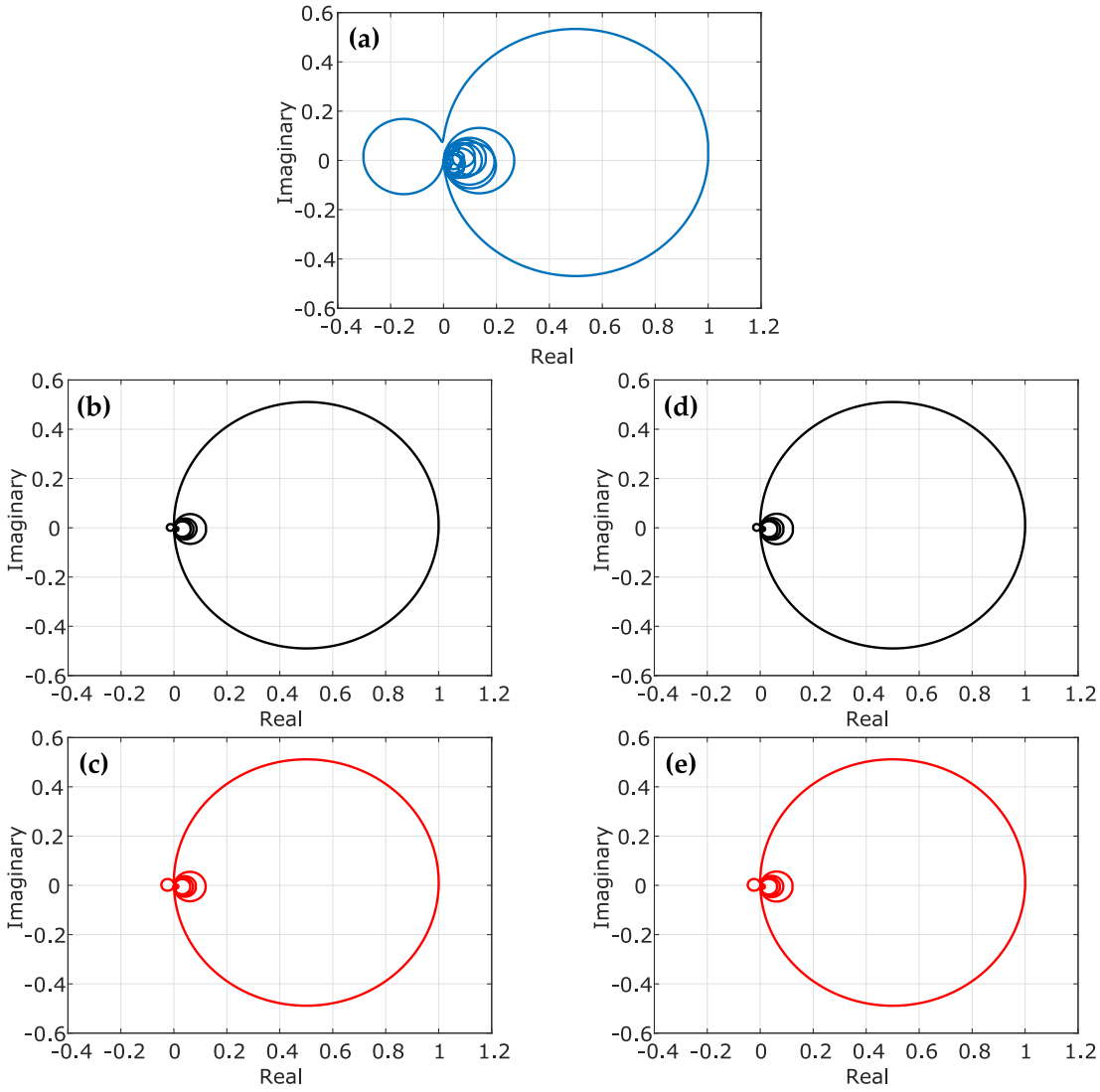

Figure 2.10. Nyquist plots of the open loop sensor – actuator FRFs. (a) Classical configuration, (b) Hinged flywheel attached to case, (c) Pinned flywheel attached to case, (d) Hinged flywheel attached to proof mass, (e) Pinned flywheel attached to proof mass. The plots have been normalised such that the largest circle in the real positive quadrants has unit diameter.

2.6 CONTROL PERFORMANCE

The performance of the feedback loops with the proposed flywheel actuators has been assessed considering the total flexural kinetic energy of the hosting plate as defined in Equation (2.50). The two plots in Figure 2.11 show the 3 Hz – 1 kHz spectra of the kinetic energy per unit acoustic excitation for the plate without proof mass

actuator, for the plate with open loop proof mass actuator and for the plate with the closed loop feedback control systems using the proof mass actuator without flywheel and with the flywheel either hinged or pinned to the case (Figure 2.11a) and to the proof mass (Figure 2.11b) of the actuator. The feedback loops implement stable gains with gain margin of about 2 dB.

The kinetic energy spectrum for the plain plate (dotted green lines), is characterised by a dominant resonance peak at about 40 Hz, which is due to the fundamental flexural natural mode of the plate. Above this resonance frequency, the spectrum rapidly rolls off following a typical mass law for acoustic excitations [68]. The fundamental resonance peak is followed by other sharp peaks due to flexural modes of the plate with one or both indices even, which are effectively excited by acoustic waves [15], [68], [138].

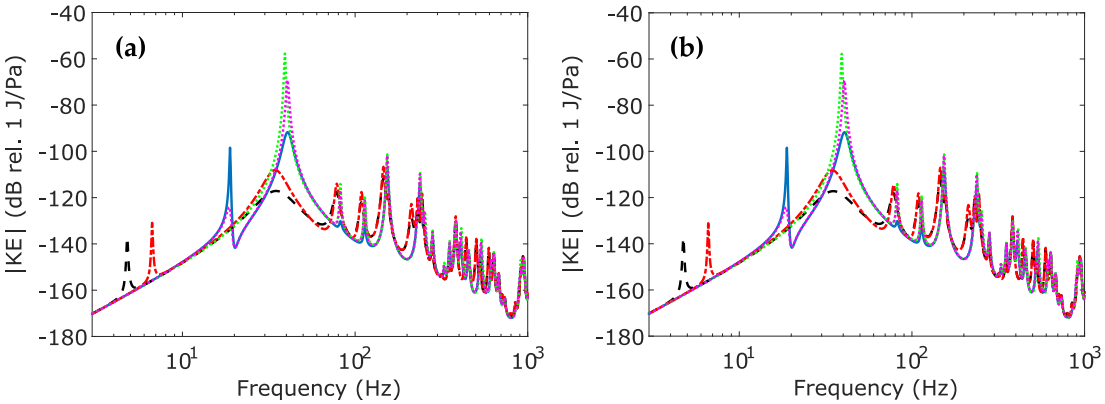

Figure 2.11. Total flexural kinetic energy per unit acoustic excitation of the plate without proof mass actuator (dotted green lines), for the plate with open loop proof mass actuator (thick dotted magenta line) and for the plate with the closed loop feedback control systems using the proof mass actuator without flywheel (solid blue lines) and with the flywheel either hinged (dashed black lines) or pinned (dashed-dotted red lines) to the case (plot a) and to the proof mass (plot b) of the actuator.

When the classical proof mass actuator is mounted to the plate (thick dotted magenta lines), the amplitude of the resonance peak of the fundamental mode is rounded off by about 11 dB. At higher frequencies the actuator produces much smaller effects, which are negligible. When for the same actuator the feedback loop is closed (solid blue line), with a 2 dB signal gain margin, an additional 22 dB vibration reduction is noticed at the fundamental resonance frequency. Instead, when the feedback loops using the proposed proof mass actuator with the flywheel is

implemented an additional 39 dB for pinned (dashed-dotted red lines) and 48 dB for hinged (dashed black lines) either to the case (plot a) or to the proof mass (plot b) vibration reduction is noticed at the fundamental resonance frequency. This is principally due to the improved stability properties of the control loops with these actuators that can implement a much larger feedback control gain. The two plots clearly show that the feedback loop with the classical proof mass actuator also generates a rather high control spillover effect at the fundamental resonance frequency of the actuator at about 19.9 Hz. In contrast, the feedback loops using the proposed actuators, produce much smaller control spillover effect at the fundamental resonances at about 4.7 and 6.6 Hz.

To better asses the effectiveness of the proposed control systems, the 1 Hz to 1 kHz frequency averaged plate kinetic energy reduction is considered. The reductions are normalised with reference to the frequency averaged kinetic energy of the plate with open loop control systems. Figure 2.12 shows the reduction of the frequency average kinetic energy when the feedback loops are closed with increasing feedback control gains. The solid blue lines in the two plots indicate that the feedback loop with the classical proof mass actuator produces up to about 10 dB reduction of the frequency averaged kinetic energy when the maximum stable gain is implemented as marked with blue circles in Figure 2.12. Alternatively, the feedback loops using the proof mass actuator with the flywheel hinged (dashed black lines) either to the base (Figure 2.12a) or to the proof mass (Figure 2.12b) can implement much larger feedback control gains, as shown in Figure 2.10, such that the frequency averaged kinetic energy of the plate is reduced by up to 21 dB, as marked with black circles in Figure 2.12. The feedback loops using the proof mass actuator with the flywheel pinned (dashed-dotted red lines) either to the base (Figure 2.12a) or to the proof mass (Figure 2.12b) can implement slightly lower feedback control gains compared to hinged configuration, such that the frequency averaged kinetic energy of the plate is reduced by 19 dB as marked with red circles in Figure 2.12. It should be emphasised that the improved control performance are obtained thanks to the possibility of implementing about 20 dB higher control gains, that is about one order of magnitude higher control signals. Thus, it is important the scale of the actuator, and in particular the scale of the coil, can withstand the high current signals that would be fed to the coil when the maximum feedback control gains are implemented [54], [55], [87].

Figure 2.12 also shows the predicted frequency average kinetic energy when the feedback loops are closed with increasing feedback control gains above the stability gain margins. The dotted blue lines in the two plots indicate that the feedback loop

with the classical proof mass actuator could produces up to about 20 dB reduction of the frequency kinetic energy when the feedback loops would allow implementing 29 dB signal gain. Instead, the feedback loops using the proof mass actuator with the flywheel either hinged (dotted black lines) or pinned (dotted red lines) to the base (Figure 2.12a) or to the proof mass (Figure 2.12b) could produces up to about 22 dB reduction of the frequency kinetic energy when the feedback loops would allow implementing 37 dB signal gain.

Figure 2.12 shows that implementing high signal gains lead to drop of the feedback loop effectiveness and control performance. High signal gains lead to the pinning effect of the rectangular plate at the control position. Thus, the implemented feedback loops generate additional pinning point, which instead of reducing vibrations of the structure change its dynamics.

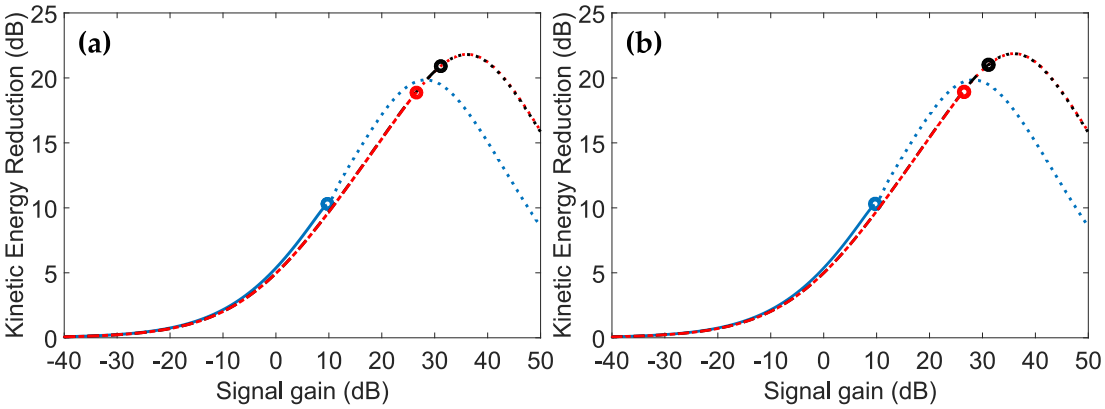

Figure 2.12. Reductions of the 1 Hz – 1 kHz frequency averaged kinetic energy produced by the feedback loops using either the classical inertial actuator (solid blue lines) or the proposed proof mass actuators with the flywheel either hinged (dashed black lines) or pinned (dashed-dotted red lines) to the case (plot a) and to the proof mass (plot b) of the actuator. The doted lines show predicted frequency averaged kinetic energy produced by the feedback loops using the inertial actuators.

2.7 PARAMETRIC STUDY

The parametric study presented in this paragraph investigates several aspects of influence of the flywheel element on the performance and the static deflection of the inertial transducer. In the last part of this paragraph, the scaling study investigates how size influences the design of the proposed flywheel proof mass actuators in order to have feedback loops with high gain margins and thus high vibration control effects.

2.7.1 Performance

The simulation results presented in the previous two sections have shown that adding the flywheel element in the proof mass actuator increases the stability gain margin of the feedback loop and consequently the control effectiveness of the feedback loop. The flywheel introduces an additional inertia effect which is proportional to the relative acceleration of the proof mass with reference to the case of the actuator. As reported in Equation (2.22), this inertia effect is given by I_w/r_w^2, where $I_w = \frac{1}{2}m_w R_w^2$. Thus it depends on the mass of the flywheel, m_w, the external radius of the flywheel R_w and the radius r_w of the pinion rack gear mechanism. A parametric study is therefore introduced to assess how the control effectiveness of the feedback loops using the four proposed actuators vary with the mass and the geometry of the flywheel. The maximum reduction of the frequency averaged kinetic energy considered in previous section is plotted with reference to the radius ratio R_w/r_w and with reference to the mass ratio m_w/M_a. The four plots in Figure 2.13 show that with all flywheel proof mass actuators considered in this study, the control performance of the feedback loops improve as the ratio R_w/r_w and the ratio m_w/M_a increases. In other words, the performance of the feedback loop improves as the inertia of the flywheel is augmented by either increasing the outer radius of the flywheel R_w or by magnifying the conversion of the axial stroke into the angular oscillation of the flywheel, i.e. by reducing the radius r_w of the pinion rack gear mechanism. Also the performance of the feedback loops improves when the balance between the masses M_w and m_w, whose sum is assumed constant, i.e. $M_w + m_w = M_a$, is shifted towards the mass m_w of the flywheel element.

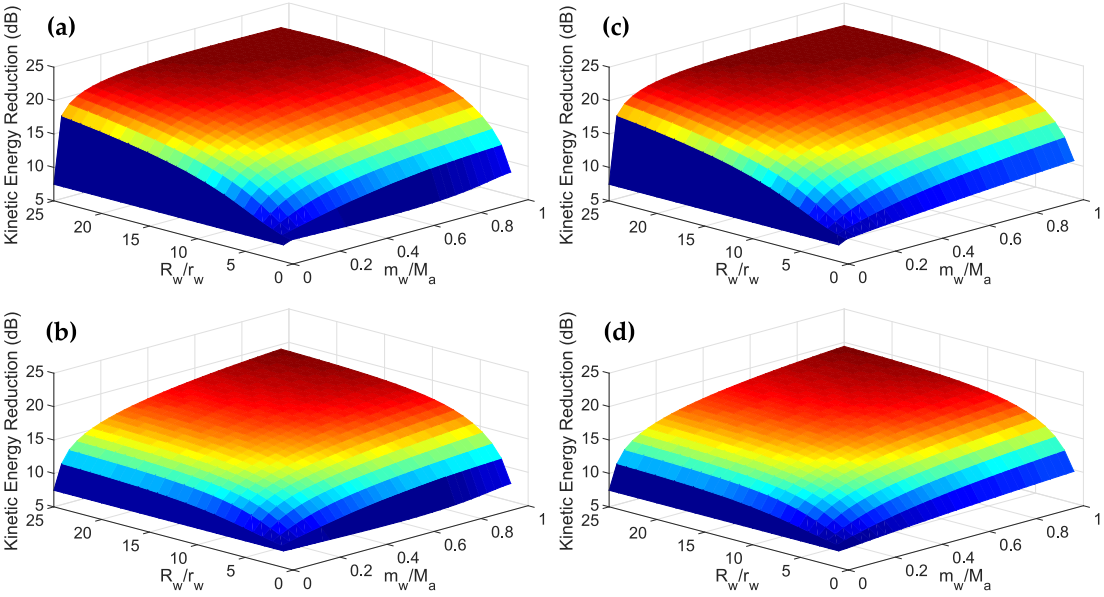

Figure 2.13. Maximum reductions of the 20 Hz – 1 kHz frequency averaged kinetic energy produced by the feedback loops using the proposed actuators with the flywheel either hinged (a) or pinned (b) to the case of the actuator or the flywheel either hinged (c) or pinned (d) to the proof mass of the actuator.

2.7.2 Static deflection

As discussed in the introduction, to improve the stability, and thus control performance of feedback loops with proof mass actuators, the fundamental natural frequency of the actuator has to be kept the lowest possible. However, this condition contrasts with the need of limiting the static displacement of the actuator proof mass to allow for a correct operation of the actuator also in presence of shocks or fast movements of the hosting structure, which could cause undesired stroke saturation effects that would lead to instability of the feedback loops.

Considering the models in Figure 2.1, the static deflection is given by:

$$\delta = \frac{\sigma M_a}{k} \tag{2.58}$$

for the classical configuration (Figure 2.1a), where σ is the nominal gravitational acceleration. Also, the static deflections for the actuator with the flywheel hinged (Figure 2.1b) or pinned (Figure 2.1c) to the case are given respectively by:

$$\delta = \frac{\sigma M_w}{k} \quad , \quad \delta = \frac{\sigma M_w}{k + \frac{k_w}{r_w^2}} \tag{2.59}$$

and the static deflections for the actuator with the flywheel hinged (Figure 2.1d) or pinned (Figure 2.1e) to proof mass are given respectively by:

$$\delta = \frac{\sigma(M_w + m_w)}{k} \quad , \quad \delta = \frac{\sigma(M_w + m_w)}{k + \frac{k_w}{r_w^2}}. \tag{2.60}$$

Figure 2.14 shows how the static deflection varies with reference to the radius ratio R_w/r_w and with reference to the mass ratio m_w/M_a. When the flywheel is hinged to the base, Figure 2.14a shows that the static deflection tends to diminish as the balance of the actuator mass $M_w + m_w = M_a$ is shifted towards the flywheel element m_w. Yet the static deflection does not vary with the radius ratio R_w/r_w that controls the rotational inertia effect of the flywheel. In fact, the rotational inertia of the flywheel does not contribute to the weight of the proof mass and thus does not produce effects on the static deflection. If instead the flywheel is elastically pinned to the base, as shown in Figure 2.14b, the radius ratio R_w/r_w influences the static deflection. This is because the radius r_w of the pinion rack gear mechanism affects the axial stiffness effect produced by the torsional stiffness of the shaft used to pin the flywheel to the actuator base.

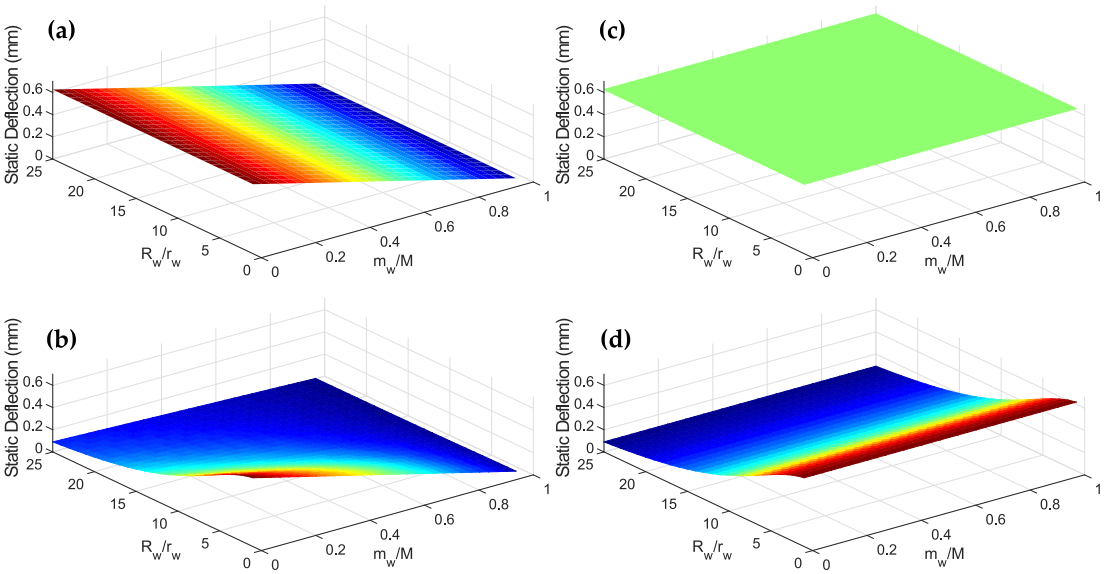

Figure 2.14. Static deflection of the actuator with the flywheel either hinged (a) or pinned (b) to the case of the actuator or the flywheel either hinged (c) or pinned (d) to the proof mass of the actuator.

When the flywheel is hinged to the proof mass, Figure 2.14c shows that the static deflection does not depend on the balance of the actuator inertial mass since, both the proof mass M_w and the flywheel mass m_w contribute to the total weight of the suspended components, which influences the static deflection. As seen for the previous two configurations, also in this case the static deflection does not vary with the radius ratio R_w/r_w, since it controls the rotational inertia effect of the flywheel only. However, if the flywheel is elastically pinned to the case, as shown in Figure 2.14d the radius ratio R_w/r_w influences the static deflection since the radius r_w of the pinion rack gear mechanism affects the axial stiffness effect produced by the torsional stiffness of the shaft used to pin the flywheel to the actuator case.

In summary the plots in Figure 2.14 suggest that, to reduce the static deflection, it is preferable that the flywheel is hinged or pinned to the case of the actuator and the balance of the actuator mass $M_w + m_w = M_a$ is shifted towards the flywheel element, i.e. towards m_w. Also, when the flywheel is pinned, with a shaft of given stiffness, either to the case or proof mass of the actuator, the static deflection tends to decrease as the radius r_w of the pinion rack gear mechanism is lowered, i.e. as the conversion factor between axial and angular motions is increased.

2.7.3 Scaling study

The scaling study presented in this section investigates how size influences the design of the proposed flywheel proof mass actuators in order to have feedback loops with high gain margins and thus high vibration control effects. Following the scaling study presented in references [54], [55], the scaling laws of the proof mass actuators mechanical and electrical properties are first revised. The scaling laws for the mechanical parameters of the actuators are then introduced. As presented in references [74], [140] the scaling laws are defined with the $[L^n]$ notation, where n identifies the power of the linear dimension L. The scaling study presented here considers an isometric (or isomorphic) scaling, which preserves the aspect ratio and geometric integrity of the actuator components [74], [87], [89].

The scaling laws for the inertia, stiffness and damping properties of the principal components of the classical and proposed proof mass actuators are derived in this section in view of the lumped parameter models shown in Figure 2.1. The first parameter analysed, of the actuator physical properties, is the suspended inertial mass. The linear inertia effects depend on the mass of the actuator components, that

is the mass of the elastically suspended magnetic element M_a or M_w, the mass of the case m_b and the mass of the flywheel m_w, which are all proportional to the material density and volume of the components, so that:

$$M_a \propto [L^3] \quad , \quad M_w \propto [L^3] \quad , \quad m_b \propto [L^3] \ , \ m_w \propto [L^3] \, . \tag{2.61}$$

The angular inertial effect produced by the rotation of the flywheel is instead proportional to the polar moment of inertia of the flywheel, which for a disc element is given by $I_w = \frac{1}{2} m_w R_w^2$, where R_w is the external flywheel radius. Thus, the flywheel angular inertia effect scales with:

$$I_w = \frac{1}{2} m_w R_w^2 \propto [L^5] \, . \tag{2.62}$$

Instead, the flywheel axial inertia effect scales with:

$$\frac{I_w}{r_w^2} \propto [L^3] \, , \tag{2.63}$$

where r_w is the radius of the pinion-rack gear mechanism. As can be found in reference [140], the axial and torsional stiffness of the springs holding the proof mass and flywheel elements depends on the length of the elastic element (spiral metal sheet, metal coil, tiny shaft, etc.):

$$k \propto [L^1] \quad , \quad \frac{k_w}{r_w^2} \propto [L^1] \, . \tag{2.64}$$

The principal damping mechanism is given by the viscous damping effect produced by the air flow in the gap between the magnet and the coil. Considering the axial and torsional damping of the suspension system as presented in previous work [74] this parameter scales with the following factor:

$$c \propto [L^1] \quad , \quad \frac{c_w}{r_w^2} \propto [L^1] \, . \tag{2.65}$$

The first parameter analysed, of the actuator mechanical properties, is the static deflection of the proof mass, which for the classical actuator (Figure 2.1a) is given by:

$$\delta = \frac{\sigma M_a}{k} \propto [L^2] \, , \tag{2.66}$$

where σ is the nominal gravitational acceleration. Also, the static deflections for the actuator with the flywheel hinged to either the case (Figure 2.1b) or proof mass (Figure 2.1d) are given respectively by:

$$\delta = \frac{\sigma M_w}{k} \propto [L^2] \quad , \quad \delta = \frac{\sigma (M_w + m_w)}{k} \propto [L^2] \tag{2.67}$$

and the static deflections for the actuator with the flywheel pinned to either the case (Figure 2.1c) or proof mass (Figure 2.1e) are given respectively by:

$$\delta = \frac{\sigma M_w}{k + \frac{k_w}{r_w^2}} \propto [L^2] \quad , \quad \delta = \frac{\sigma (M_w + m_w)}{k + \frac{k_w}{r_w^2}} \propto [L^2] \,. \tag{2.68}$$

Thus, in all cases, the static deflection of the proof mass scales proportionally to L^2. Also, it is noticed that the design with the pinned flywheel could reduce the static displacement, particularly when the flywheel is pinned to the case of the actuator. The damping ratio for the classical actuator (Figure 2.1a) is given by:

$$\zeta = \frac{c}{2\sqrt{kM_a}} \propto [L^{-1}] \,. \tag{2.69}$$

Also, the damping ratio of the actuator with the flywheel hinged to either the case (Figure 2.1b) or proof mass (Figure 2.1d) are given respectively by:

$$\zeta = \frac{c}{2\sqrt{k\left(M_w + \frac{I_w}{r_w^2}\right)}} \propto [L^{-1}] \quad , \quad \zeta = \frac{c}{2\sqrt{k\left(M_w + m_w + \frac{I_w}{r_w^2}\right)}} \propto [L^{-1}] \tag{2.70}$$

and the damping ratio of the actuator with the flywheel pinned to either the case (Figure 2.1c) or proof mass (Figure 2.1e) are given respectively by:

$$\begin{aligned} \zeta &= \frac{c}{2\sqrt{\left(k + \frac{k_w}{r_w^2}\right)\left(M_w + \frac{I_w}{r_w^2}\right)}} \propto [L^{-1}] \quad , \\ \zeta &= \frac{c}{2\sqrt{\left(k + \frac{k_w}{r_w^2}\right)\left(M_w + m_w + \frac{I_w}{r_w^2}\right)}} \propto [L^{-1}] \end{aligned} \tag{2.71}$$

Thus, in all cases, the damping ratio scales proportionally to L^{-1}. The fundamental natural frequency of the classical actuator (Figure 2.1a) is given by:

$$\omega_n = \sqrt{\frac{k}{M_a}} \propto [L^{-1}] \,. \tag{2.72}$$

Also, for the actuator with the flywheel hinged to either the case (Figure 2.1b) or the proof mass (Figure 2.1d) they are given respectively by:

$$\omega_n = \sqrt{\frac{k}{M_w + \frac{I_w}{r_w^2}}} \propto [L^{-1}] \quad , \quad \omega_n = \sqrt{\frac{k}{M_w + m_w + \frac{I_w}{r_w^2}}} \propto [L^{-1}] \tag{2.73}$$

and for the actuator with the flywheel pinned to either the case (Figure 2.1c) or the proof mass (Figure 2.1e) they are given respectively by:

$$\omega_n = \sqrt{\frac{k + \frac{k_w}{r_w^2}}{M_w + \frac{I_w}{r_w^2}}} \propto [L^{-1}] \quad , \quad \omega_n = \sqrt{\frac{k + \frac{k_w}{r_w^2}}{M_w + m_w + \frac{I_w}{r_w^2}}} \propto [L^{-1}] \, . \tag{2.74}$$

These expressions show that the natural frequencies for the five actuator configurations scales proportionally to L^{-1}. Also, it is noticed that the designs with the flywheel pulls down the natural frequency, particularly when the flywheel is hinged to the proof mass. In general it can be concluded that on one hand, to reduce the static displacement, configurations (b) and (c) shown in Figure 2.1 would be preferable, since the flywheel would not increase the amount of suspended mass and actually, for configuration (c), the additional torsional pinning spring would increase the stiffness holding the suspended mass, as shown in Equation (2.68). On the other hand, to reduce the fundamental natural frequency of the actuator, configurations (d) and (e) shown in Figure 2.1 would be preferable, since the inertia of the proof mass would be enhanced by the linear and angular inertia of the flywheel. Possibly the best compromise that would guarantee a reduction of both the static displacement and the fundamental natural frequency of the actuator is given by configuration (c) shown in Figure 2.1, which actually uses the more practical torsional pinning spring to fix the flywheel. The equations derived above and Equations (2.62) and (2.63) also highlight that it is important the ratio between the radius of the flywheel R_w and the radius of the pinion-rack gear mechanism r_w should be as high as possible to guarantee the highest angular inertia effect I_w with the smaller linear inertia m_w penalty.

As discussed in references [54], [55], [87], [88], the scaling laws of the force generated by the moving magnet actuators, can be considered based on three major cases: a) constant current density in the coil, b) constant heat dissipation rate, c) constant temperature rise across the winding. The scaling factors for the three cases are summarised in the Table 2.8.

Table 2.8. Scaling laws for coil-magnet actuator transduction effect.

Transduction hypothesis	**Actuation force F_a scaling law**
Constant current density	$[L^3]$
Constant heat dissipation rate	$[L^{2.5}]$
Constant temperature rise	$[L^2]$

In many practical cases, the constant temperature assumption is employed since the coil winding overheating problem typically limits the actuation force produced by the transducer. In this case, the generated force is given by:

$$F_a = -Bli_a \propto [L^2]\,, \tag{2.75}$$

where B is the magnetic field in the gap where the coil is housed and l is the length of the winding. For a given material of the coil winding, the law of heat conduction is given by:

$$\dot{Q} = t_c A_s \frac{dT}{dz}\,, \tag{2.76}$$

where $\dot{Q}$ is a heat power dissipation, t_c is the thermal conductivity, A_s is the total area of conductor, T is the temperature and z is the normal to the surface A_s of heat flow. Additionally it is known that:

$$\dot{Q} = Ri_a^2\,, \tag{2.77}$$

where R is the conductor resistance and i_a is the actuator driving current. Substituting Equation (2.76) into Equation (2.77) for the assumption that the heat rise ΔT is kept constant, the actuator driving current is given by:

$$i_a = \sqrt{\frac{1}{R} t_c A_s \frac{dT}{dz}} \propto [L^1]\,. \tag{2.78}$$

Thus, assuming constant temperature in the coil, the current flow in the coil scales proportional to L^1. Also according to Equation (2.75) the force generated by the transducer scales proportionally to L^2.

Figure 2.15 shows the graphical representation of the scaling laws for the physical properties (Figure 2.15a) and mechanical parameters (Figure 2.15b) of the flywheel proof mass actuators. In general, it can be concluded that when the actuator is down-scaled the fundamental natural frequency and damping ratio tend to rise, the static displacement and the actuation force tend to decrease. Thus, there is no univocal conclusion on the best scaling law for a coil-magnet proof mass actuator, which ideally should be characterised by low fundamental natural frequency, high damping ratio, low static displacement and high actuation force. Nevertheless, it could be agreed that, since the flywheel element tends to increase the inertia effect, and thus to reduce the fundamental natural frequency, without affecting the static displacement, the proposed flywheel proof mass actuators are better suited than the classical proof mass actuators for the implementation of small scale control units.

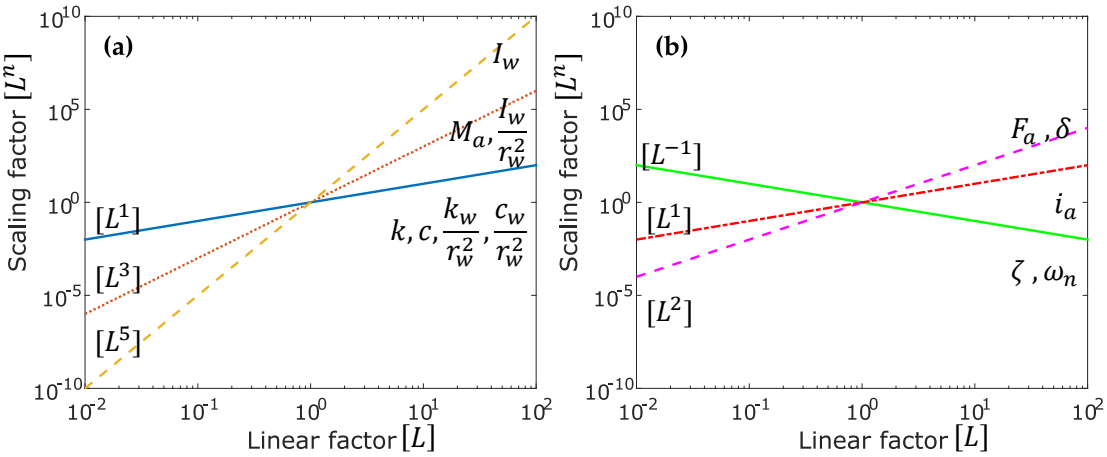

Figure 2.15. Scaling laws for the physical properties (a) and mechanical parameters (b) of a flywheel proof mass actuator. Flywheel angular inertia I_w, Mass of the actuator M_a, Flywheel axial inertia I_w/r_w^2, Stiffness k, Damping coefficient c, Torsional stiffness k_w/r_w^2, Torsional damping c_w/r_w^2, Electromagnetic force F_a, Actuator static displacement δ, Driving current i_a, Damping ratio ζ, Fundamental natural frequency ω_n.

From a practical point of view it is worth to point out that the downscaling of the actuators is not always simple and straightforward task, since external forces that can be neglected at macroscale may become dominant at the microscale level. The frictional loads and stick-slip phenomena mainly determine the type of the flywheel actuator configuration that can be used depending the size of the actuator. As it was shown in previous section, the highest control performance can be obtained for the hinged configuration of the flywheel proof mass actuator. This configuration can be efficiently used when the actuator is exposed to relatively high displacement of the vibrating structure and when the stiction effect between the surfaces can be neglected. The pinned configuration is more appealing for the micro actuators in which the flexural hinges are used for motion conversion and where the dominant frictional loads are no longer a problem.

2.8 CHAPTER SUMMARY

This chapter has presented a new inertial electrodynamic actuator with a flywheel element for velocity feedback control loops on flexible structures. Four different configurations have been considered where the flywheel is either hinged or pinned to either the proof mass or the case of the actuator. The study has introduced a lumped

parameter model and an impedance – mobility electromechanical formulation for the operation of the velocity feedback loop.

The kinetic and kinematic response of the classical and four proposed flywheel proof mass actuators were first investigated considering spectra of six electromechanical properties. The actuators were compared based on FRFs of the base impedance, the actuators blocked force per unit driving current, the actuators transduction FRF, the actuators blocked force per unit applied voltage, the electrical impedance and the actuators proof mass stroke per unit driving current.

The base impedance study has shown that a classical proof mass actuator is characterised by low and high frequencies mass–impedances proportional respectively to the total and the case mass of the actuator, which are connected via a resonance peak and antiresonance low linked by a stiffness–impedance segment. The actuators with the flywheel element present a similar impedance spectrum although the high frequency mass–impedance is in this case nearly equal to the low frequency mass–impedance. In addition, the amplitude of the resonance peak and antiresonance low are much smaller as the resonance and antiresonance frequencies are moved to lower frequencies and are much closer to each other. Thus, the proposed flywheel actuators are characterised by a constant mass–impedance effect in the whole frequency range except a very small band delimited by the fundamental resonance and antiresonance frequencies of the actuator.

The blocked force per unit current fed to the actuator has highlighted that when the actuator with the flywheel element is used, the additional inertia effect produced by the oscillations of the flywheel tends to lower the low frequency range where the produced force is out of phase with the driving current. However, the axial inertia effect produced by the flywheel element also lowers the constant force effect produced above fundamental resonance frequency of the actuator.

The transduction FRF is characterised with the equal expression to the blocked force per unit current fed to the transducers. Thus, the low-frequency and high-frequency asymptotic expressions of the blocked force per unit current fed to the classical and four proposed flywheel proof mass actuators can be also used for the characterisation of the actuator transduction FRF.

The blocked force per unit voltage applied to the actuator has highlighted that the electrical impedance of the coil rounds off the peaks at the fundamental resonance frequencies of the actuators. Additionally, the inductive effect of the actuator coil starts to take important role at higher frequencies making the produced blocked force drop with frequency.

The results of the electrical impedance showed that the fundamental resonance frequency of the transducers could be lowered both in frequency and amplitude with the axial inertia effect produced by the flywheel element.

Finally, the stroke study has shown that, at low frequencies below the fundamental resonance frequency of the actuators, the proof mass stroke of the actuators with the flywheel hinged to either the actuator base or actuator proof mass is the same as that of the classical actuator and it is controlled by the axial stiffness of the suspension system. Alternatively, the proof mass stroke of the actuators with the flywheel pinned to either the actuator case or actuator proof mass is smaller since it is controlled by a higher stiffness effect due to the axial stiffness of the suspension system and the torsional stiffness acting on the flywheel.

The stability and control performance of velocity feedback loops using classical and four proposed flywheel proof mass actuators was considered assuming that the control loops operate on a thin rectangular panel excited by an acoustic plane wave. The stability analysis has shown that for all configurations of the actuator, the addition of the flywheel element increases the gain margin of the feedback loop without any increase of the actuator mass. As a result, the feedback loops using the proposed proof mass actuators with the flywheel element are characterised by improved control performance. More specifically, the maximum vibration reduction produced by a feedback loop with a classical actuator is about 10 dB while the maximum vibration reductions produced by the feedback loops with the proposed flywheel actuators is about 21 dB. Results showed that the actuators equipped with the flywheel element attached either to base or to proof mass present similar control performance. However, slightly higher reductions were obtained when the flywheel was attached to the proof mass. The control performance study has highlighted that when the actuator with the flywheel element is used to implement a velocity feedback, the additional inertia effect produced by the flywheel element tends to lower the low frequency range where the destabilising positive feedback effect occurs. The parametric study has also been introduced to investigate both the vibration control performance of the feedback loops with the proposed actuators and the static deflection of the proposed actuators, which influence the robustness of the control system. The study has shown that both vibration control effectiveness and static deflection are improved when the balance of the actuator mass $M_w + m_w = M_a$ is shifted towards the mass m_w of the flywheel element. Secondly, when the radius of the flywheel R_w and thus polar moment of inertia of the flywheel, is increased. Finally

when the radius r_w of the pinion rack gear mechanism for the conversion of the axial stroke into the angular oscillation of the flywheel is reduced.

The parametric study presented in this chapter suggests a new configuration of the proof mass actuator, where the inertial mass of the actuator $M_a = M_w + m_w$ is primarily allocated to the flywheel mass m_w and the proof mass M_w is reduced to the minimum compatibly with the construction constraints. The improved control performance was obtained thanks to the possibility of implementing higher control gains. Thus, it is important to scale the electromechanical components of the actuator that could withstand the high current signals that would be fed to the coil when the maximum feedback control gains are implemented.

The scaling study has considered a linear model of the actuator, which does not take into account the typical nonlinear effects of friction in the hinge joint and the nonlinear effects that arise for the gear meshing in the pinion rack mechanism used to convert the axial oscillations of the proof mass into angular oscillations of the flywheel. Nevertheless, the study has shown that there is no univocal conclusion on the best scaling law for a coil-magnet proof mass actuator. For instance to obtain low fundamental natural frequency and large control forces the actuator should be up-scaled. Alternatively, to have low static displacement, the actuator should be down-scaled. Nevertheless, the study has shown that the proposed flywheel element could be used to effectively reduce the fundamental natural frequency of the actuator allowing then the use of small-scale devices.

3

FLYWHEEL COIL MAGNET TRANSDUCER

This chapter presents the mechanical design and characterisation of electromagnetic proof mass actuators equipped with two different flywheel elements. Both prototypes are based on a standard and commercially available coil magnet linear transducer. In both configurations, the flywheel element is mounted in parallel with the actuator suspension spring and connects the magnet with coil armature. Thus, the relative axial motion between the inner magnet and exterior armature coil element produces the rotational motion of the flywheel element. Furthermore, the prototypes are designed to have similar physical characteristics to the configurations presented in the analytical study of the previous chapter.

In the first configuration, the classical coil-magnet transducer is equipped with a flywheel element designed in from of a balanced beam (rocker arm) having lumped masses at the ends, which produces the desired rotational inertia effect. The flywheel element is designed in such a way as to allow changes in the position of the lumped masses that control the rotational inertia. The first prototype uses hinges, similarly to the configuration presented in the analytical study of the previous chapter. Thus, in this chapter the first prototype of the flywheel inertial actuator is called "hinged configuration". The linear motion of the actuator is converted into a rotation of the flywheel by hinging one side of the rocker arm to a pin connected to the inner magnet, while the other side to a bracket fixed to the external coil armature. The bracket and the rocker arm was designed with four different hinging points, so that the conversion offset from axial to rotational motion could be changed and thus the rotational inertia effect can be modified.

The second prototype is equipped with a round flywheel element with dimensions optimised in such a way as to minimise weight and to maximise polar moment of inertia. Compared to the first prototype, this configuration adopted the pivot bearings in order to minimise stick-slip effects and reduce the backlash effects between the moving components. The flywheel element is attached via two flexural bearings to the bracket fixed to the external coil armature. The linear motion of the actuator is converted into a rotation of the flywheel by a pushing pin link attached to the inner

magnet and the third pivot bearings that was mounted on one of the flywheel arms. The frictionless flexural bearings used in this prototype can be modelled as a torsional springs, similarly to the second configuration presented in the analytical study of the previous chapter. Thus, in this chapter the second prototype of the flywheel inertial actuator is called “pinned configuration”.

The first part of this chapter presents a detailed design of the flywheel prototypes. Selection of the components and assembly process is described in order to clarify the operation of each prototype. The second part of this chapter presents the characterisation of the electromechanical properties. Also, the experimental tests carried out on a new prototypes are compared with the simulation results based on the lumped parameter models. The mathematical formulations of the electromechanical model presented in the previous chapter are used to obtain the simulation results that are contrasted with experimental results. Additionally, the results for both flywheel prototypes are compared with the results for the classical coil magnet linear actuator having equal mass as two flywheel actuator prototypes.

3.1 ELECTROMAGNETIC TRANSDUCER

The electromagnetic (EM) transducer presented in Figure 3.1, described as reference or classical configuration in the remaining part of this document, was used as a base for designing two flywheel prototypes. The EM transducer produced by H2W Technologies (NCM02-17-035-2F) shown in Figure 3.1a, can be used either as an actuator or as an energy harvester. It was decided to use this actuator for building the prototypes mainly due to the availability, which did not require any additional purchasing and shipment delay. Moreover, the actuator showed favourable properties for the active vibration control applications, which are high damping coefficient and large stroke without hard end-stops. The symmetric arrangement of the transducer is ideal for designing new prototypes. The transducer provides easy access and connections from both sides (top and bottom shown in Figure 3.1) to the magnet element and to the external coil armature, which can be used as an inertial mass. Three symmetrically distributed tapped holes on both sides of the coil armature and one in the centre of the magnet element enable to integrate additional elements in the transducer to build a new prototype. Moreover, the tapped holes on both ends allow to use this actuator either as an inertial or as a reactive transducer.

The transducer is designed with a cylindrical magnetic element placed in the centre of the round coil armature as shown with the schematic section view in Figure 3.1b. The magnet is suspended with two flexural axial springs that are attached to both sides of the coil armature. The two springs are characterised by soft axial stiffness and comparatively much higher transverse stiffness. The springs allow this transducer to work in axial oscillatory motion, so that it can move as a balanced spring mass system. The damping effect in this actuator is created by the eddy currents generated between the magnet and the metal armature around the external coil and by the air damping that develops in the gap between the coil and the magnet. The design allows to us this actuator either as a moving magnet or as a moving coil armature actuator. However, from the practical point of view, the actuator is used as a moving coil actuator due to heavier inertial mass (lower fundamental resonance frequency) and attachment simplicity to a hosting structure as it requires only one screw. Design studies of a similar electromagnetic actuator can be found in references [141]–[143] for example.

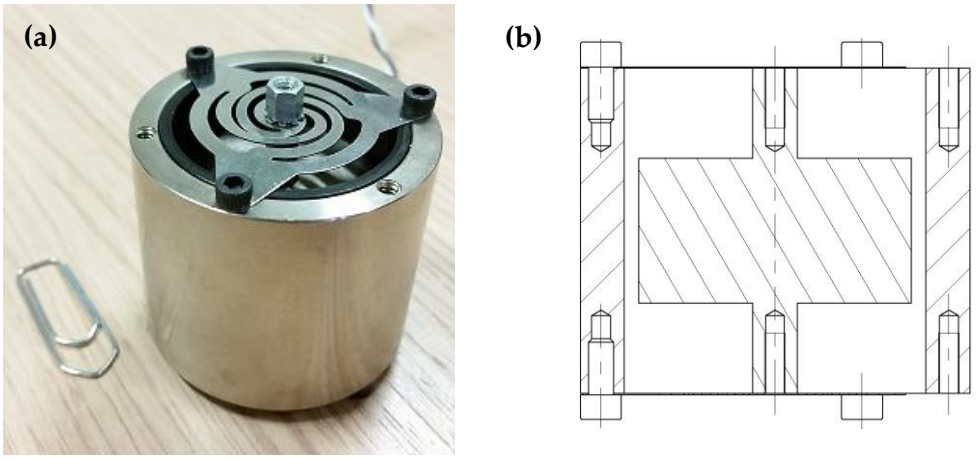

Figure 3.1. Coil magnet transducer. Picture (a) and schematic section view (b).

The actuator presented in Figure 3.1 can be easily adopted for prototypes thanks to three 4-40 threaded holes on each sides of the coil armature that can be used to attach the bracket support for the flywheel prototype. The electromechanical properties of the actuator are summarised in Table 3.1. The electromechanical properties of the EM transducer were obtained from the producer datasheet [144].

Table 3.1. Electromechanical properties of the transducer [144].

Parameter	Value
Stroke	5.6 mm
Magnet Mass	115 g
Total Mass	300 g
Resistance at 20°C	22 Ω
Inductance at 20°C	4.35 mH
Force Constant	22.5 N/A
Back EMF	22.5 V/m/s
Force at 100% Duty	15.6 N
Power at 100% Duty	11.0 W
Current at 100% Duty	0.70 A

3.2 HINGED CONFIGURATION OF THE FLYWHEEL TRANSDUCER

The first prototype considered here is based on the hinged configuration. Figure 3.2 shows the computer added design (CAD) view of the hinged configuration of the flywheel transducer. Rendered view is shown in Figure 3.2a while the schematic view is shown in Figure 3.2b. The analytical study presented in the previous chapter showed that the actuators used in the velocity feedback control system present better performance when the flywheel element is attached to the inertial mass. Thus, the hinged prototype is designed with the flywheel support that is attached to the heavier coil armature of the reference actuator, which is presented in Figure 3.1. The flywheel element was designed with rocker arm having several holes at both ends. The holes are used to attach the lumped masses that increase the inertia of the rocker arm as they are fixed further apart from the centre point of rotation. The position of the masses can be easily shifted to change the polar moment of inertia of the flywheel element. A special bracket was designed to hold the rocker arm element that is connected to a coil armature with three 4-40UNC screws. The linear motion of the actuator is converted into a rotation of the rocker arm by hinging one side of the arm to a bracket and the other side to a yoke that is attached to the inner magnet. For both connections two screws are used that act as pins. The bracket and the rocker arm was designed with four additional holes that are used to change the position of the pin and to change the hinging points. By changing the position of the pin, the relative offset between the axis of the actuator linear motion and axis of the flywheel

rotational motion is shifted. This parameter has influence on the axial inertia effect produced by the rocker arm element and corresponds to the small radius defined with r_w symbol in the theoretical study of the previous chapter. The fabricated components were made of aluminium while the pins and screws for the masses were made of steel. The physical properties of the hinged inertial transducer with the flywheel element are summarised in Table 3.2. The technical drawings of the manufactured components for hinged EM flywheel prototype are presented in appendix A.

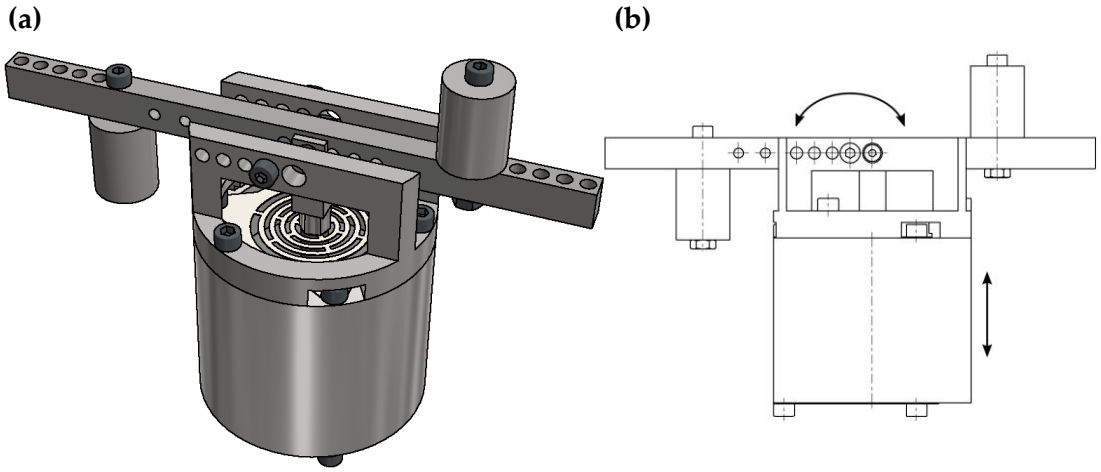

Figure 3.2. Design view of the hinged configuration of the flywheel prototype. Rendered view (a) and schematic view (b).

Table 3.2. Physical properties of the hinged flywheel inertial actuator.

Parameter	Value
Inertial mass	0.205 kg
Case mass	0.117 kg
Flywheel mass with 2 ballasts	0.021 kg
Flywheel mass with 4 ballasts	0.033 kg
Torsional damping ratio	0.005
Hinged flywheel inertia value	Depends on the ballast position
4 Offset values	$17, 13, 9, 5$ mm
Axial flywheel mass effects	Vary

3.2.1 *Hinged configuration: rocker arm design*

The design of the hinged configuration started from the rocker arm element. Figure 3.3 shows the designed rocker arm element for the hinged configuration of the inertial actuator. The flywheel element was designed in a form of a rocker arm out of a long beam. Several connecting holes were designed in the rocker arm. The six holes at both ends are used to attach the lumped masses in a form of ballasts that increase the polar moment of inertia of the rocker arm. Five holes for the pins were designed on the front-left side of the rocker arm. Particular attention was given to the flywheel centre of gravity. Figure 3.3 shows the location of the flywheel centre of gravity when four lumped masses are attached to the rocker arm. In order to obtain the centre of gravity that intersects the axis of the central hole, the two additional holes were designed on the front-right side of the rocker arm.

The offset from the flywheel centre point (defined with the black-white circle) for each axis direction is:

X = 0.000 mm (red arrow in the drawing)

Y = 0.000 mm (green arrow in the drawing)

Z = 0.000 mm (blue arrow in the drawing)

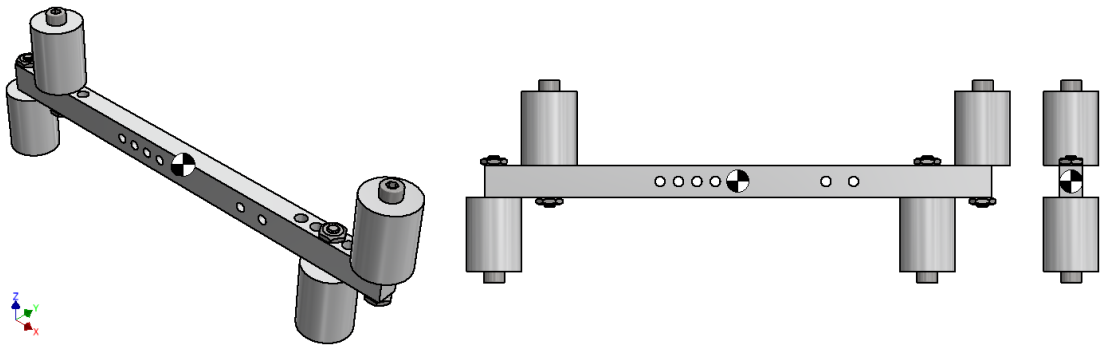

Figure 3.3. Flywheel element of the hinged configuration with marked centre of gravity.

The rocker arm was designed to be equipped either with two or with four ballasts. However, to ensure that the flywheel centre of gravity always intersects the axis of the central hole, the ballasts must be equally distributed along the rocker arm. Additionally, the ballasts must be placed on the opposite sides of the rocker arm. The mass distribution of the ballasts must be mirrored with respect to the XY surfaces shown in Figure 3.3. To prevent mistakes while mounting the flywheel element in the

brackets and yoke the rocker arm was designed with just one ø2.7 mm hole for the M2.5. This ensures that the centre of gravity of the flywheel element is always attached to the inertial mass of the actuator via the bracket.

3.2.2 Assembly process of the hinged prototype

The assembly process of the hinged rocker arm prototype is presented in order to clarify the structure of the prototype. Figure 3.4 shows the exploded view of an actuator with numbered parts. The exploded view is shown to demonstrate the principal concept and the mechanism of transforming linear motion of the actuator into rotational motion of the cker arm element. The assembly process of the hinged configuration of the flywheel prototype is performed in several steps.

Firstly, the bracket (No. 1) needs to be attached to the actuator (No. 2) with three 4-40UNC screws (No. 3). Then the yoke (No. 12) should be attached to the central connector of the actuator (No. 2) with the additional 4-40UNC screw (No. 4). The two holes in the fins of the yoke (No. 12) must be concentric and aligned with the holes of the bracket (No. 1). Then the rocker arm (No. 5) can be placed between the fins of the yoke (No. 12). When the rocker arm are placed in the position the M2x0.4 screw (No. 7) can be pushed through the ø4.2 mm hole of the bracket (No. 1) and should go through the hole of the yoke (No. 12) and one of four ø2.2 mm holes in the rocker arm (No. 5). The M2 screw (No. 7) should be pushed all the way through and slightly tight with the M2 nut (No. 13) on the other side of the yoke (No. 12). After that, the M2.5 screw (No. 11) can be used to attach the rocker arm (No. 5) with the bracket (No. 1). To connect both components one of the four ø2.7mm holes in the bracket (No. 1) and one ø2.7mm hole in rocker arm (No. 5) should be used. Finally, the screw should be blocked (No. 11) with M2.5 nut (No. 8). To create sufficient polar moment of inertia the ballasts (No. 16) that act as a lumped masses should be attached to the rocker arm (No. 5). In total four ballast were fabricated, allowing to attach two of them on each side of the rocker arm. The M2.5 screws (No. 10) and M2.5 nuts (No. 9) are used to attach the ballasts (No. 16) to the rocker arm (No. 5). The lumped masses must be attached on each side of the rocker arm with the same distance to the centre of the rocker arm. This ensures that the flywheel centre of the gravity intersects the axis of rotation defined with the M2.5 screw (No. 11). With the configuration, the mass of the flywheel element is supported by the M2.5 screw (No. 11) that is attached to the bracket (No. 1) and to the inertial mass of the actuator (external coil aramature).

The advantage of the hinged configuration is that the relative distance between the hinges can be easily changed and thus the produced axial inertia effect can be easily modified.

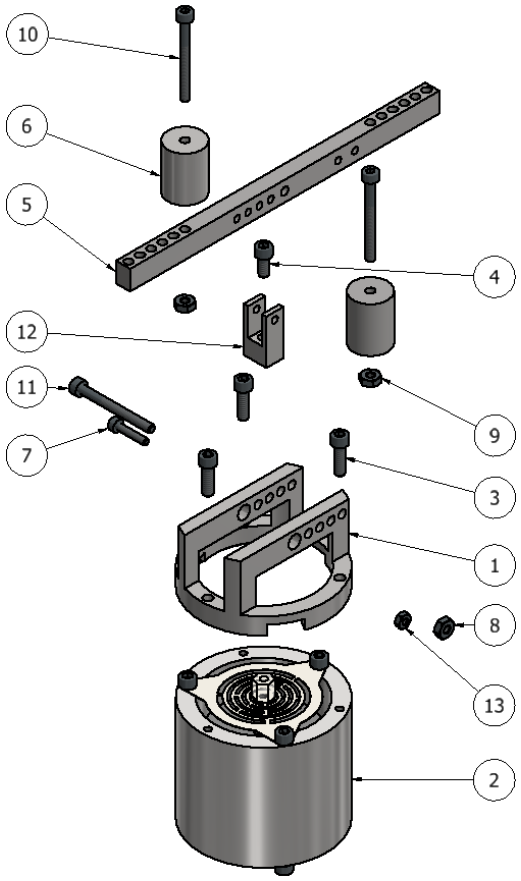

Figure 3.4. Exploded view of the designed hinged configuration of the flywheel prototype.

3.2.3 Backlash and play cancelation

After first assembly of the hinged prototype, it was observed that the screws, which are used as pins, do not ensure proper contact between the elements. The play between the pin and the bushing in the bracket was too big to create rotational motion of the rocker arm element. In order to improve the performance and establish tight connection between the pins and the bushings, the two screws were wrapped with aluminium tape, as shown in the Figure 3.5. This additional aluminium tape reduced nonlinearities and cancelled backlash and play between components. The preliminary tests showed that the pins with aluminium tape present sufficient

performance to transform the linear motion of the actuator into rotational motion of the flywheel element. It was also observed that the flywheel mechanism was working better and smoothly when the pins were dry, rather than when a small amount of lubricant was used.

Figure 3.5. Screws used as a shafts wrapped with the aluminum tape.

3.3 PINNED CONFIGURATION OF THE FLYWHEEL TRANSDUCER

The second prototype of the flywheel inertial actuator presented in Figure 3.6 is based on the pinned configuration. Rendered view is shown in Figure 3.6a while the schematic view is shown in Figure 3.6b. The physical properties of the designed pinned inertial actuator with the flywheel element are summarised in Table 3.3. The analytical study presented in the previous chapter showed that a velocity feedback control loop presents better control performance when the flywheel element of the actuator is attached to the inertial mass. Thus, also the pinned prototype was designed with the flywheel element attached to the heavier coil armature of the reference actuator, which is presented in Figure 3.1. The flywheel element was designed in a form of a round wheel with dimensions optimised in such a way as to minimise weight and to maximise the polar moment of inertia. Compared to the hinged prototype, this configuration adopted the flexural bearings in order to minimise backlash and the play between the components. Additionally, the pivot bearings reduced the stick-slip effects between the pins and bushings when the actuator was performing small amplitude oscillations. The flywheel element is supported by two flexural bearings attached to the bracket mounted on the external coil armature of the inertial actuator. The linear motion of the actuator is converted into a rotation of the flywheel by a pushing pin attached to the inner magnet. In the preliminary design, the pushing pin was designed with the flexural hinge that

transforms the linear motion of the actuator into rotational motion of the flywheel element. However, the first tests showed that the fabricated pushing pin did not present the necessary flexibility. Thus, a different pushing pin was fabricated that was equipped with a flexural bearing. On the one side, the pushing pin was attached to the inner magnet of the actuator while on the other side via frictionless pivot bearing to the one of the flywheel arms. The distance between the horizontal flywheel axis of rotation to the vertical axis of the actuator linear motion was defined as a offset value. This parameter has direct influence on the axial inertia effect produced by the flywheel element and corresponds to a small radius defined with r_w symbol in the theoretical study of the previous chapter. The fabricated components were made of aluminium. The three frictionless flexural bearings used in this prototype can be modelled as a torsional springs, similarly to the second configuration presented in the analytical study of the previous chapter. Thus, in this remaining part of this document the second prototype is called the pinned configuration. The technical drawings of the manufactured components for pinned EM flywheel prototype are presented in appendix A.

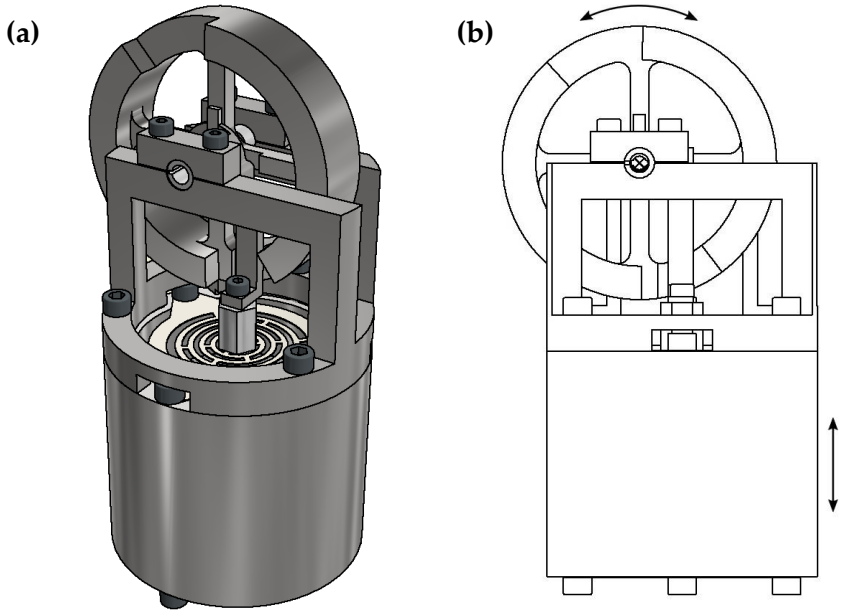

Figure 3.6. Design view of the pinned configuration of the flywheel prototype. Rendered view (a) and schematic view (b).

Table 3.3. Physical properties of the pinned flywheel inertial actuator.

Parameter	Value
Inertial mass	0.227 kg
Case mass	0.117 kg
Flywheel mass	0.019 kg
Torsional stiffness	$0.003\ \mathrm{Nmrad^{-1}}$
Flywheel inertia	$6.8 \cdot 10^{-6}\ \mathrm{kgm^2}$
Pushing pin offset	$r_w = 6.4$ mm
Axial flywheel mass effect	0.166 kg

3.3.1 Pinned configuration: flywheel element design

The designed flywheel element for the pinned prototype is presented in Figure 3.7. The dimensions of the flywheel element were chosen based on results of the scaling study presented in previous chapter. More specifically, the dimensions of the flywheel element were optimised in such a way as to minimise weight and to maximise the polar moment of inertia. A particular emphasis was given to obtain the centre of flywheel gravity exactly in the centre of the flywheel hole where the supporting flexural bearings are mounted. Figure 3.7 shows the centre of gravity offset from the flywheel central point (defined with the black-white circle) for each axis direction:

X = 0.002 mm (red arrow in the drawing)

Y = 0.001 mm (green arrow in the drawing)

Z =-0.003 mm (blue arrow in the drawing)

The flywheel was designed with two groves in the external ring. The bottom grove was designed for the pushing pin that had to be placed as close as possible to the flywheel centre of gravity. Instead, the top grove was designed to counterbalance the bottom grove and to equilibrate the flywheel centre of gravity. The two tenons on the top and left arm of the flywheel element were designed as connectors for the pushing pin. Finally, the small grove on the right arm of the flywheel element was designed to prevent contact between the moving parts of the pushing pin and the flywheel element.

Based on the designed flywheel element, the dimensions of the bracket support for the actuator was also optimised. The flywheel was fabricated out of aluminium with total mass of 19g. The previsioned polar moment of inertia over the Z axis (blue

arrow in the drawing) with CAD software equals $6.8 \cdot 10^{-6}$ kgm^2. The dimensions of the pinned flywheel prototype components are presented in the detailed drawings attached in annex 4.

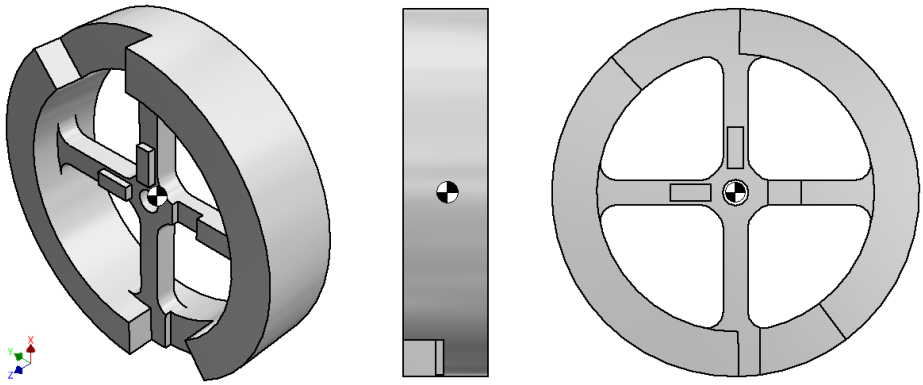

Figure 3.7. Flywheel element of the pinned configuration with marked centre of gravity.

3.3.2 Flexural rotational bearing

One of the key problems in designing small oscillatory mechanisms is backlash and play between the components, especially when the tolerances between the parts are much greater than the oscillation amplitude. In such case, the motion of the actuator is not transmitted to the other component but it is dissipated in the backlash. Additionally, the classical parts typically suffer from the wear effects and introduce additional friction. Due to these constraints, the typical mechanisms as ball bearings or hinges should be avoided in the design of the pinned configuration. Additionally the flywheel is designed to perform rotational oscillations with small angles of rotation. In case of small displacements and harmonic oscillations, the standard mechanisms introduce nonlinear friction effect (stick-slip) that can disrupt proper operation of the system.

One of the solutions to the described problem is to use monolithic structure with compliant joints. The structure could be fabricated as a one single element with local flexural hinges that could provide rotational motion of the flywheel. However, this technique requires high precision machining typically based on Electrical Discharge Machining (EDM). Furthermore, the components need to be fabricated out of special materials that are strong, flexible and typically expensive.

Another solution is to use commercially available components that could provide required rotational motion. It was decided to use flexural bearings presented in Figure 3.8 that are the cylindrical, limited rotational pivots, with a high radial and axial stiffness with relatively low torsional spring rates. Depending on the torsional spring stiffness, the angle of deflection could be reach up 30°. Two companies were found that provide the flexural bearings:

- Riverhawk Company with the product called the pivot bearing [145]
- C-Flex Bearing Co. with the product called the C-Flex bearing [146]

Both companies are specialized in manufacturing flexural bearings.

Figure 3.8. Flexural bearings used in the pinned configuration of the flywheel prototype [145].

The minimum torsional stiffness of the flexural bearings is 0.003 Nm/rad, which is similar to the value of 0.001 Nm/rad used in the analytical study presented in the previous chapter. The bearing itself is build out of two stainless steel sleeves held in position by three leaf springs on two planes. There is no contact between the sleeves eliminating friction and wear effects of the parts. Additionally, the bearings do not require any lubrication making it low maintenance mechanisms. The three leaf springs allow for the pivotal motion, while maintaining the self centring effect. The external diameter of the bearings is 1/8in (3.175mm) with total length of a 0.2in (5.08mm). The miniature size of the bearing allows to used them in the compact mechanisms.

3.3.3 Pushing pin

The second challenge in the development of the pinned prototype is to design a mechanism that could transform linear motion of the actuator into rotation of the flywheel element. The pinion rack mechanism, commonly used in inerters and considered in the theoretical study of the previous chapter, was rejected in the design

of the pinned prototype. The pinion rack mechanism could be implemented in cases characterised by large relative displacement. However, the small oscillations of the inertial actuator in the prototype considered here could be easily dissipated between the connections of the gearing mechanism components.

The first solution of the pushing pin, shown in Figure 3.9, was based on the concept of flexural hinges. Figure 3.9 shows the pushing pin optimisation stages from the conceptual idea to the final solution, while Figure 3.10a shows the pushing pin assembled in the flywheel element of the pinned prototype. The pushing pin optimisation process was done using the FEM software based on several parameters. The key parameters were the actuator maximum static deflection, the flywheel angle of rotation and the component manufacturing. The optimisation process was done in several steps by changing the geometrical properties of the pushing pin and compering the key parameters. The optimisation study showed that with reduction of the flexural hinge thickness the ability of the pushing pin to transform the linear motion into rotation increased. However, the minimum thickness of the flexural hinge was limited by the manufacturing feasibility of the component. In the final solution, it was decided to use aluminium to reduce costs and facilitate the fabrication process. However, to improve the performance of the designed pushing pin it is strongly recommended to fabricate it out of APX4 high strength stainless steel (commonly designated as X4CrNiMo16.5.1).

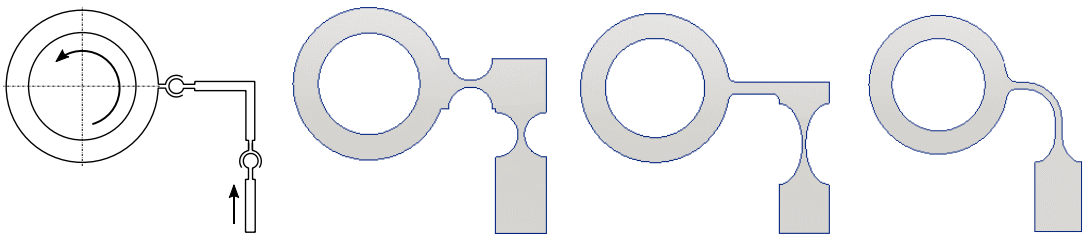

Figure 3.9. Pushing pin optimisation stages from the conceptual idea (left hand side) to the final solution (right hand side).

The preliminary tests of the pinned flywheel prototype showed that the fabricated pushing pin (Figure 3.10a) did not demonstrate the required flexibility. After examination, it was observed that the pushing pin was fabricated with flexural hinge that was much thicker and above tolerances previsioned in the design. Thus, a different pushing pin was fabricated that could be equipped with a flexural bearing as shown in Figure 3.10b. In this design, the pivot bearing is used as a flexural hinge

that can transmit the linear motion of the actuator into rotation of the flywheel. One side of the pushing pin was attached to the inner magnet of the actuator while the other side was attached to the right arm of the flywheel via frictionless pivot bearing.

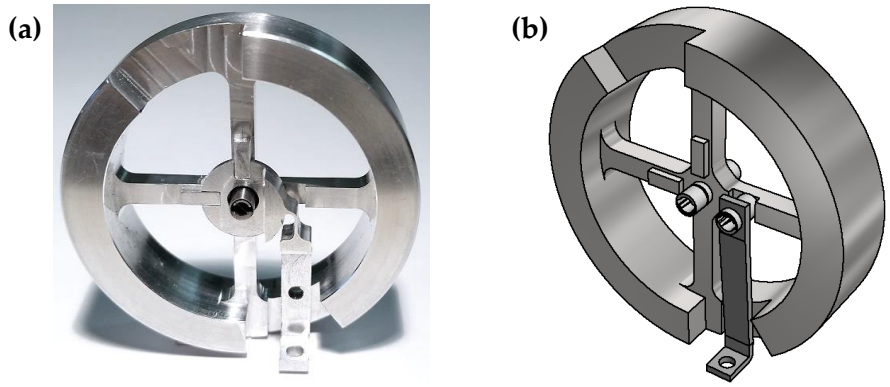

Figure 3.10. Pinned configuration flywheel elements with the two different pushing pins. Pushing pin based on the flexural hinge (a), Pushing pin design with third pivot bearing (b).

The distance between the horizontal flywheel axis of rotation to the vertical axis of the actuator linear motion was defined as a offset value. This parameter has a direct influence on the axial inertia effect produced by the flywheel element and corresponds to a small radius defined with r_w symbol in the theoretical study of the previous chapter.

3.3.4 Assembly process of the pinned prototype

The assembly process of the pinned flywheel prototype is described to clarify the construction of the prototype. Figure 3.12 shows the exploded CAD view of an actuator with numbered parts. The exploded view is shown to demonstrate the principal concept and the mechanism used to transform the linear motion of the actuator into rotation of the flywheel element. The assembly process of the pinned configuration of the flywheel prototype is performed in several steps.

Firstly, the flexural bearings (No. 2) should be glued in the central hole of the flywheel element (No. 1) with a small amount of epoxy glue. It is recommended to take a particular care while gluing the components especially, to prevent the situation when the glue might penetrate between the sleeves and leaf springs of the flexural bearings. After placing the two flexural bearings in the hole, the distances should be

adjusted so that both of them equally stick out of the flywheel element. The flexural bearings must be rotated as shown in the Figure 3.11. Before proceeding to the next phase, it is recommended to wait until the glue dries.

Figure 3.11. Position of the flexural bearings in the flywheel and sleeve.

The third flexural bearing (No. 12) should be also glued to the right, horizontal arm of the flywheel element. The third flexural bearing (No. 12) should be placed in the machined grove of the flywheel arm. The other side of the flexural bearing should be glued to pushing pin (No. 6) as shown in Figure 3.12.

While the glue dries, the fabricated connector (No. 5) can be attached to the central hole in the actuator (No. 8). Then the bracket (No. 7) can be attached to the actuator (No. 8) with three 4-40UNC screws (No. 9). Only after ensuring that the epoxy glue has dried, the sleeves (No. 4) can be mounted on both flexural bearings (No. 2). The sleeves should be pushed not more than a half of the flexural bearing length, to enable the rotational motion of the bearings. Then, the assembled flywheel (No. 1) can be placed in the bracket (No. 7). The sleeves (No. 4), attached to the flexural bearings (No. 2) and flywheel (No. 1), should be placed in the rounded grooves of the bracket (No. 7) as shown in Figure 3.12. The sleeves (No. 4) should be rotated in such a way that the extrusions in the sleeves (No. 4) are aligned with the top surface of the bracket (No. 7). It is recommended to take a particular care while rotating the sleeves (No. 4), in order to not twist or damage the flexural bearings (No. 2). Using measuring gauge the assembled flywheel (No. 1) should be centred in the bracket (No. 7) so that both components are distanced by 1.5mm from each other, from both sides.

Then, the sleeves (No. 4) can be attached to the support (No. 7) with two clamps (No. 3) by using four M2 screws (No. 11). The sleeves (No. 4) with the extrusions were designed to be squeezed and to compressed the flexural bearings (No. 2) providing tight connection.

Finally, the pushing pin (No. 6) can be attached with the actuator (No. 8) via a connector (No. 5) and small M2 screw (No. 10). After mounting all the components it

is recommended to check the position of all the components and tightening of the screws.

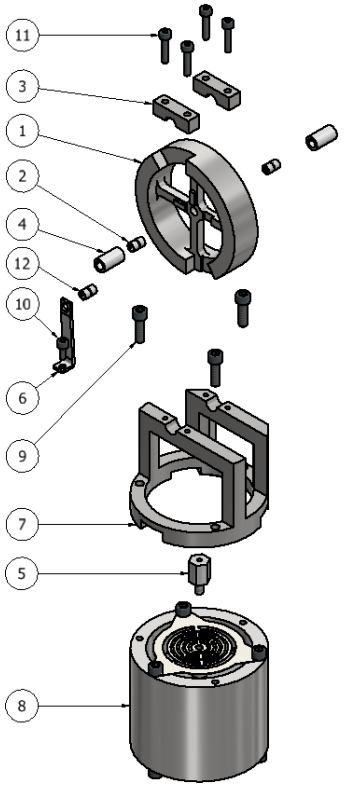

Figure 3.12. Pinned configuration of the flywheel prototype.

3.4 ELECTROMECHANICAL PROPERTIES

This section investigates the electromechanical properties of the classical and two prototypes by analysing the actuators base impedance, the actuators blocked force per unit driving current, the actuators blocked force per unit applied voltage, the transduction coefficient and the actuators electrical impedance. The simulation results based on lumped parameter models of the classical and two prototypes are contrasted with measurement results. The mathematical derivation of each principal electromechanical property is given in the section 2.4 of the previous chapter.

3.4.1 Characterisation of the actuators

This section presents the lumped parameter models, used to derive the electromechanical properties of the classical and two prototypes of the flywheel inertial actuators. The classical inertial actuator considered in this study is made with the coil–magnet linear transducer as shown in Figure 3.13a. The electromechanical response has been studied with the lumped elements model shown in Figure 3.13e. The transducer is based on the classical configuration formed by an inner round magnet and an outer cylindrical coil armature as described in details in section 3.1 of this chapter. The lighter inner magnet is attached to the structure and acts as a base mass m_b. Instead, the external and heavier coil armature acts as a inertial mass M_a, which is suspended to the inner element via two flexural springs of stiffness k and damping c as depicted schematically in Figure 3.13e. The electromagnetic effect that produces a pair of reactive forces F_a between the base mass (magnet) and inertial mass (coil) of the actuator is modelled in terms of transduction coefficient ψ_a and current i_a flowing in the coil. The voltage u_a applied at the electrical terminals of the actuator is proportional to the coil resistance R, inductance L and back electromotive force u_{bmf} that is proportional to the relative velocity $\dot{w}_m - \dot{w}_b$ between the inertial mass and the base mass of the actuator.

Figure 3.13b presents the classical configuration with the same inertial mass as that of the flywheel prototypes. This configuration was used to compare the properties and performance of the classical inertial actuator with the fabricated prototypes. To obtain the best similarity to the fabricated prototypes the classical configuration with the same inertial mass was based on the pinned prototype of the flywheel inertial actuator. The flywheel and the supporting bracket was attached to the inertial mass. The pushing pin was disconnected from the base mass to deactivate the axial inertia effect produced by the flywheel element. Figure 3.13b shows the picture while Figure 3.13f lumped elements model of the classical actuator configuration with the same inertial mass as the flywheel prototypes with disconnected pushing pin. The flywheel element was firmly attached to the supporting bracket to prevent any undesired rotational motion that could induce additional dynamics during measurements. The lumped parameter model for this configuration is characterised with the same elements as for the classical configuration. The total inertial mass is equal to the sum of proof mass M_a and flywheel mass m_w.

The first porotype, which will be referred in the remaining part as the hinged flywheel inertial actuator is shown in Figure 3.13c, with the lumped elements model

shown in Figure 3.13g. The prototype was based on classical actuator and equipped with a rocker arm having lumped masses symmetrically located at the ends ensuring that its mass centre is in line with the axis of rotation and that the rocker arm works as a flywheel element. The produced rotational inertial effect is proportional to the relative axial motion between the base mass (magnet) and inertial mass (coil) of the actuator. The additional relative inertia effect, which, as depicted in Figure 3.13g, is modelled with a flywheel element connected in parallel with the suspension spring and damper elements. This element is characterised by a mass m_w, which adds to the inertial mass M_a, and by a polar moment of inertia I_w. Considering mathematical model given in section 2.3 of the previous chapter the symbols for the inertial masses are equal $M_a = M_w$. The rotational motion of the rocker arm is guaranteed by a pair of hinged joints. The first hinge connects the inner cylindrical magnet with the rocker arm, while the second hinge connects the rocker arm with the external coil armature element. The aluminium bracket attached to the coil armature element was designed with several hinging points, so that the axial inertia effect produced by the flywheel I_w/r_w^2 can be varied by changing the conversion offset r_w from axial to rotational motion. The hinges produce a rotational damping effect c_w, which is also converted into axial damping given by c_w/r_w^2.

The second porotype, which will be referred in the remaining part as the pinned flywheel inertial actuator is shown in Figure 3.13d, with the lumped elements model shown in Figure 3.13h. The additional flywheel element was designed in the form of a round wheel with polar moment of inertia I_w and mass m_w that adds to the inertial mass M_a. Considering mathematical model given in section 2.3 of the previous chapter the symbols for the inertial masses are equal $M_a = M_w$. As can be seen in Figure 3.13d, the shape and the dimensions of the flywheel element were optimised to minimise weight and to maximise the polar moment of inertia. The rotational inertial effect produced by the flywheel element is proportional to the relative axial motion between the base mass and inertial mass of the actuator and is transferred with tree frictionless pivot bearings of torsional stiffness k_w to the flywheel element. The flywheel element is suspended via two flexural bearings to the designed bracket attached to the coil armature. The third frictionless pivot bearing connects the flywheel element with the case of the actuator via designed pushing pin mounted with an offset r_w from the flywheel horizontal axis of rotation, which was set to intersect the vertical axis of the transducer to keep the whole system in balance.

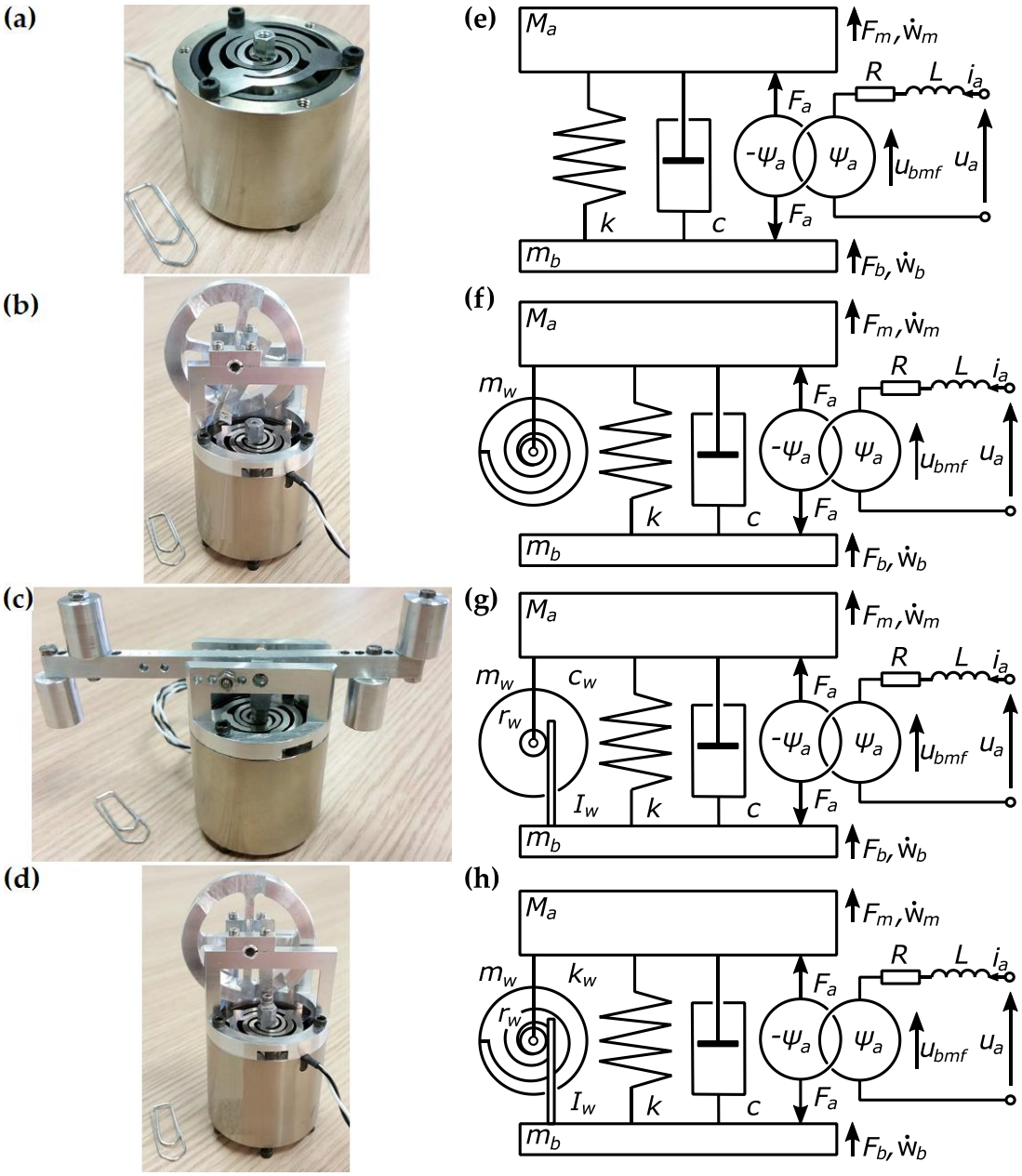

Figure 3.13. Pictures (a,b,c,d) and schemes (e,f,g,h) of the tested classical (a,e), classical with the same inertial mass as that of the flywheel configuration (b,f), the hinged flywheel inertial actuator (c,g) and the pinned flywheel inertial actuator (d,h).

The physical properties of the classical coil-magnet actuator and two flywheel actuator prototypes are summarised in Table 3.4. The table specifies the equivalent axial inertia I_w/r_w^2 effects of the rocker arm and the flywheel element with reference to the tree offsets r_w for the hinged configuration and pushing pin offset r_w for the pinned configuration of the actuator.

Table 3.4. Mechanical parameters of the classical and flywheel inertial actuators.

Parameter	Value
Proof mass / Coil mass	$M_a = 0.185$ kg
Case mass / Magnet mass	$m_b = 0.115$ kg
Hinged flywheel mass system	$m_w = 0.048$ kg
Pinned flywheel mass system	$m_w = 0.045$ kg
Axial stiffness	$k = 2950$ Nm^{-1}
Torsional stiffness	$k_w = 0.003$ Nmrad^{-1}
Damping ratio	$\zeta = 0.2$
Torsional damping ratio	$\zeta_w = 0.005$
Hinged flywheel inertia values	$I_{w1} = 74 \cdot 10^{-6}$ kgm^2 $I_{w2} = 70 \cdot 10^{-6}$ kgm^2 $I_{w3} = 67 \cdot 10^{-6}$ kgm^2 $I_{w4} = 65 \cdot 10^{-6}$ kgm^2
Hinged offset values	$r_{w1} = 17$ mm $r_{w2} = 13$ mm $r_{w3} = 9$ mm $r_{w4} = 5$ mm
Axial hinged flywheel mass effects	$I_{w1}/r_{w1}^2 = 0.256$ kg $I_{w2}/r_{w3}^2 = 0.415$ kg $I_{w3}/r_{w3}^2 = 0.831$ kg $I_{w4}/r_{w4}^2 = 2.618$ kg
Pinned flywheel inertia value	$I_w = 6.8 \cdot 10^{-6}$ kgm^2
Pinned pushing pin offset values	$r_w = 6.4$ mm
Axial pinned flywheel mass effect	$\frac{I_w}{r_w^2} = 0.166$ kg
Coil resistance	$R = 22.5\ \Omega$
Coil inductance	$L = 4.35 \cdot 10^{-3}$ H
Transduction coefficient	$\psi_a = 22.5$ NA^{-1}

3.4.2 Actuator mathematical model

The mathematical derivation of the principal electromechanical property was given in section 2.4 of the previous chapter. However, after preliminary tests the damping coefficients used in the simulations for each EM transducer had to be adjust. Thus, the following section presents the mathematical derivation of the damping values used in the actuator impedance Z_a given in Equation (2.22).

The damping coefficient of the proof mass suspension for the classical configuration was calculated with the following formula:

$$c = 2\zeta\sqrt{kM_a}\,. \tag{3.1}$$

The same formula was used for the classical actuator with the same inertial mass as the flywheel configuration.

$$c = 2\zeta\sqrt{k(M_a + m_w)}\,. \tag{3.2}$$

The damping coefficient of the proof mass suspension for the hinged configuration was calculated with the following formula:

$$c = 2\zeta\sqrt{k\left(M_a + \frac{I_w}{r_w^2} + m_w\right)}\,, \tag{3.3}$$

while for torsional damping with the following:

$$c_w = 2\zeta r_w^2\sqrt{k\left(M_a + \frac{I_w}{r_w^2} + m_w\right)}\,. \tag{3.4}$$

Finally the damping coefficient of the proof mass suspension for the the pinned configuration was calculated with the following formula:

$$c = 2\sqrt{\left(k + \frac{k_w}{r_w^2}\right)(M_a + m_w)}\,. \tag{3.5}$$

This result indicates that, although the axial mass effect produced by the flywheel element reduces the fundamental resonance frequency of the transducer, it does not influence the mechanical damping, which, actually, plays a key role in energy harvesting applications.

3.4.3 Base impedance

Figure 3.14 shows scheme (Figure 3.14a) and picture (Figure 3.14b) of the base impedance test setup. The tested actuators were mounted on a shaker as shown in Figure 3.14b. The shaker was excited with a sine logarithmic sweep signal up to 100Hz. Two parameters were measured simultaneously during tests using signal analyser. Input channel A measured force excreted to the actuator base while input channel B measured the base acceleration. The shaker amplifier was used to drive the shaker with required excitation signal. As shown in Figure 3.14b, the impedance head mounted between shaker and the actuator was used to measure force and acceleration. Appendix D lists all the equipment used in the measurements of the transducer elecromechanical properties.

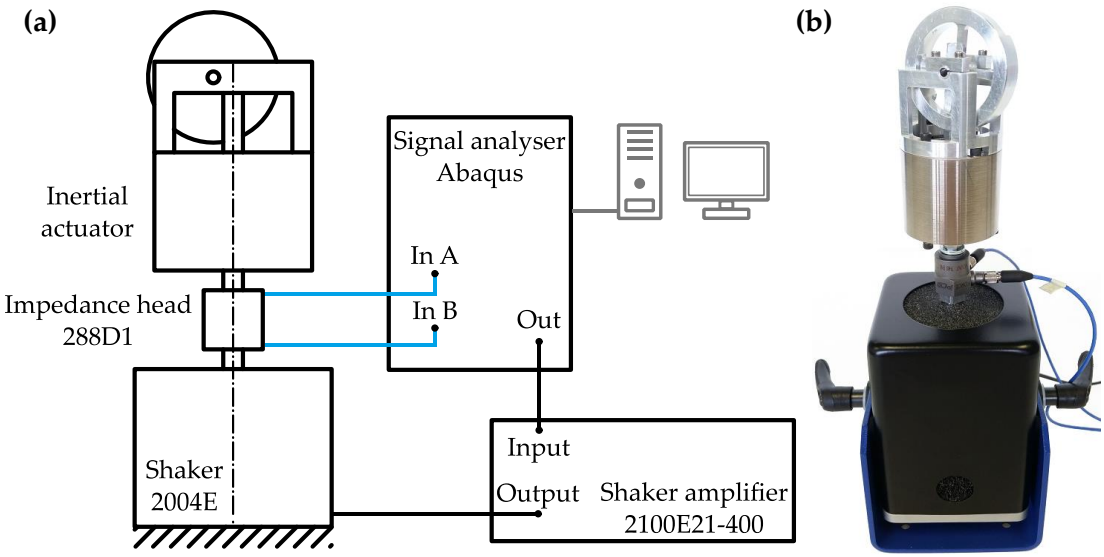

Figure 3.14. Scheme (a) and picture (b) of the base impedance test setup.

The Bode plots in Figure 3.15 show the base impedance FRFs of the classical, classical with the same inertial mass as the flywheel configuration and hinged and pinned configurations of the flywheel inertial actuators as given in Equation (2.51). The figure is organised in two columns where, the left column shows the modulus diagrams while the right column shows the phase diagrams of the mechanical base impedance. The solid blue lines in the diagrams present the measurement results, while the dashed-dotted red lines present the simulation results. Plot (a) shows the base impedance for the classical actuator. Plot (b) shows the base impedance for the

classical actuator with the same inertial mass as the flywheel configuration. Plots (c-f) show the base impedance for the hinged flywheel inertial actuator with increasing value of the equivalent axial inertia I_w/r_w^2 effect of the rocker arm ($I_{w1}/(r_{w1}^2) < I_{w2}/(r_{w2}^2) < I_{w3}/(r_{w3}^2) < I_{w4}/(r_{w4}^2)$). The bottom plot (g) shows the base impedance for the pinned flywheel inertial actuator.

The modulus of the base impedance for the classical configuration shown in left diagram of the Figure 3.15a is characterised by low and high frequencies asymptotic mass behaviours separated by a resonance peak and antiresonance through. The resonance peak appears at about the fundamental resonance frequency of 20 Hz while the antiresonance through at about 35 Hz. Between the resonance peak and antiresonance through the actuator produces a sky-hook stiffness effect. The low frequency asymptote is proportional to the total mass ($M_a + m_b$) while the high frequency asymptote is proportional to base mass (m_b) of the inertial actuator. The phase of the base impedance for the classical configuration showed in the right diagram of the Figure 3.15a is characterised by the two shifts. The damping of the inertial mass suspension system controls the amplitude and the phase shift at the resonance peak. At the resonance peak the base impedance phase shifts from +90° to around 0° while at the antiresonance the phase shifts back from 0° to +90°. The measured base impedance for the classical configuration agree well with the simulated values.

The base impedances for the classical configuration with the same inertial mass as the flywheel configuration is shown in Figure 3.15b. The modulus of the base impedance shown in the left diagram presents almost identical characteristic to the classical configuration. However, there are two major differences that are due to the heavier inertial mass. Firstly, the resonance peak appears at slightly lower frequency of about 18 Hz and has higher amplitude. Secondly, the low frequency asymptote is slightly increased and is proportional to the total mass ($M_a + m_b + m_w$) of the inertial actuator. The high frequency asymptote remained proportional to base mass (m_b). The phase of the base impedance shows the phase shifts from +90° to around -10° at the resonance frequency. This shows that the damping coefficient of the suspension system of the classical configuration with the same inertial mass as the flywheel configuration is the same as for the classical configuration. The measured base impedance agree well with the simulated values.

The base impedance for the first prototype of the flywheel inertial actuator shown in Figure 3.15c-f present similar characteristics to that of the classical configurations, with small differences. Firstly, the axial inertia effect I_w/r_w^2 produced by the hinged

rocker arm shifts the fundamental resonance frequency to a lower value with a progressively smaller offset values r_w. Thus, the fundamental resonance frequency is moved to about 12 Hz (Figure 3.15c) for the first value of the inertia effect I_{w1}/r_{w1}^2, to about 10 Hz (Figure 3.15d) for the second value of the inertia effect I_{w2}/r_{w2}^2, to about 8.5 Hz (Figure 3.15e) for the third value of the inertia effect I_{w3}/r_{w3}^2 and to about 5.5 Hz (Figure 3.15f) for the fourth value of the inertia effect I_{w4}/r_{w4}^2. Consequently, the antiresonance through is also influenced by the axial inertia effect produced by the hinged rocker arm. The antiresonance through is moved to about 16.5 Hz (Figure 3.15c) for the first value of the inertia effect I_{w1}/r_{w1}^2, to about 13.5 Hz (Figure 3.15d) for the second value of the inertia effect I_{w2}/r_{w2}^2, to about 10 Hz (Figure 3.15e) for the third value of the inertia effect I_{w3}/r_{w3}^2 and to about 6.5 Hz (Figure 3.15f) for the fourth value of the inertia effect I_{w4}/r_{w4}^2. The vicinity of the resonance peak and antiresonance through almost completely cancels the sky-hook stiffness effect. Secondly, the amplitude of the higher frequency asymptotic mass behaviour is progressively increased as the equivalent axial inertia I_w/r_w^2 effect of the rocker arm is increased ($\frac{I_{w1}}{r_{w1}^2} < \frac{I_{w2}}{r_{w2}^2} < \frac{I_{w3}}{r_{w3}^2} < \frac{I_{w4}}{r_{w4}^2}$) with the following relation $m_b + I_w/r_w^2$. Compared to the classical configuration also the amplitude of the lower frequency asymptotic mass behaviour is increased. However, in this case, it is not because of the axial inertia effect, but because of the additional mass of the flywheel mechanism that can be defined with the following relation $M_a + m_w + m_b$. Finally, the internal damping effect in the inertial actuator is also increased, such that the resonance peak and antiresonance through are progressively rounded. The increase of the internal damping effect can be also observed in the phase diagrams of the base impedance FRFs. The phase presented in the right diagrams of the Figure 3.15c-f show a shift between +90° to around +44° for the first value of the inertia effect I_{w1}/r_{w1}^2, a shift between +90° to around +55° for the second value of the inertia effect I_{w2}/r_{w2}^2, a shift between +90° to around +69° for the third value of the inertia effect I_{w3}/r_{w3}^2, and a shift between +90° to around +82° for the fourth value of the inertia effect I_{w4}/r_{w4}^2. The experimental results align well with the simulated base impedance FRFs for all configurations except the last one. For the highest value of equivalent relative axial inertia effect I_{w4}/r_{w4}^2 (Figure 3.15f) the simulation result gives lower actuator resonance frequency compared to the experiment. Additionally, with the increase of the axial inertia effect the phase starts to drop compared to the simulation value, especially for the two configurations shown in Figure 3.15d and in Figure 3.15f. It is

assumed that this effect is linked to the backlash effect in the hinged joints of the rocker arm.

The base impedances for the second prototype of the flywheel inertial actuator shown in Figure 3.15g presents similar characteristics to the classical configuration and the first configuration, which is equipped with the rocker arm. Also in this case the flywheel element shifts the fundamental resonance peak to a lower value at about 14 Hz while the antiresonance low at about 20 Hz. The phase shown in the right hand side diagram of the Figure 3.15g shifts between +90° to around +15°. Compared to the classical configuration, the asymptotes below resonance frequency and above antiresonance low are slightly higher. This is due to the fact that, below the fundamental resonance frequency the flywheel element increments the total mass of the transducer to $M_a + m_b + m_w$, while above the antiresonance frequency the flywheel increase the seismic mass effect to $m_b + I_w/r_w^2$. The experimental results for the pinned configuration of the flywheel inertial actuator align very well with the simulated base impedance FRF and are better compared to the rocker arm configuration due to the use of the flexural bearings that minimise the backlash effects and provide smoother operation.

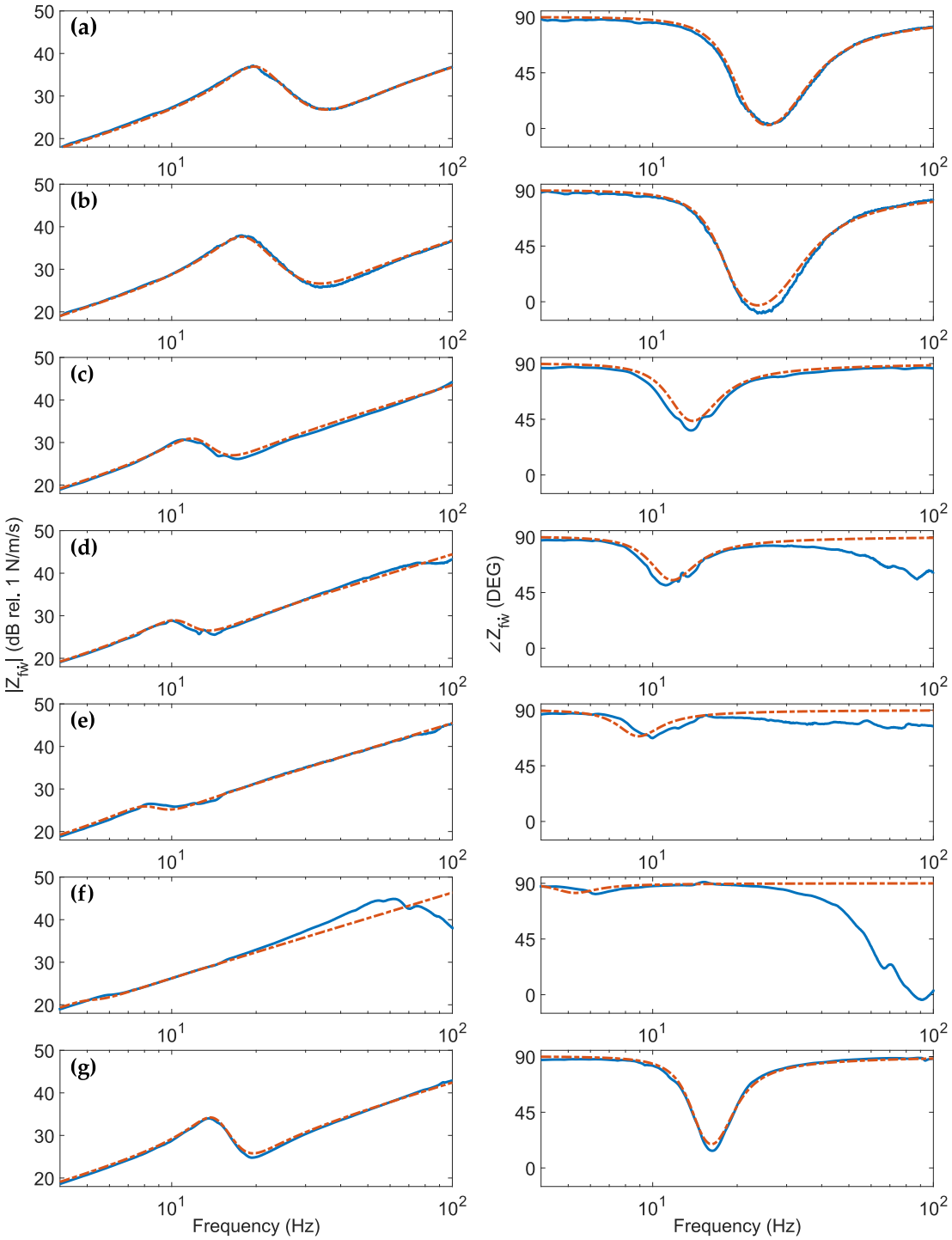

Figure 3.15. Actuator base impedance for the classical configuration (a), classical with the same inertial mass as that of the flywheel configuration (b), hinged flywheel element actuator with the increasing axial inertia values I_{w1}/r_{w1}^2 (c), I_{w2}/r_{w2}^2 (d), I_{w3}/r_{w3}^2 (e), I_{w4}/r_{w4}^2 (f) and pinned flywheel element (g). Comparison of the experimental results (solid blue lines) with the numerical simulations (dashed-dotted red lines).

Additional tests of the base impedances for the first prototype of the flywheel inertial actuator with the highest axial inertia value I_{w4}/r_{w4}^2 were performed. During these tests, it was observed that the angular position of the M2 screw (No. 7 shaft in Figure 3.4) plays an important influence on the resonance frequency of the actuator and additional modes that appears between 50Hz and 100Hz. Results presented in Figure 3.16 show the magnitude and phase of the actuator base impedance for four angular position of the M2 screw. Based on results it can be concluded that the dynamics of the hinged flywheel inertial actuator prototype with the rocker arm is strongly influenced by the backlash between the shaft and the bushing in the prototype.

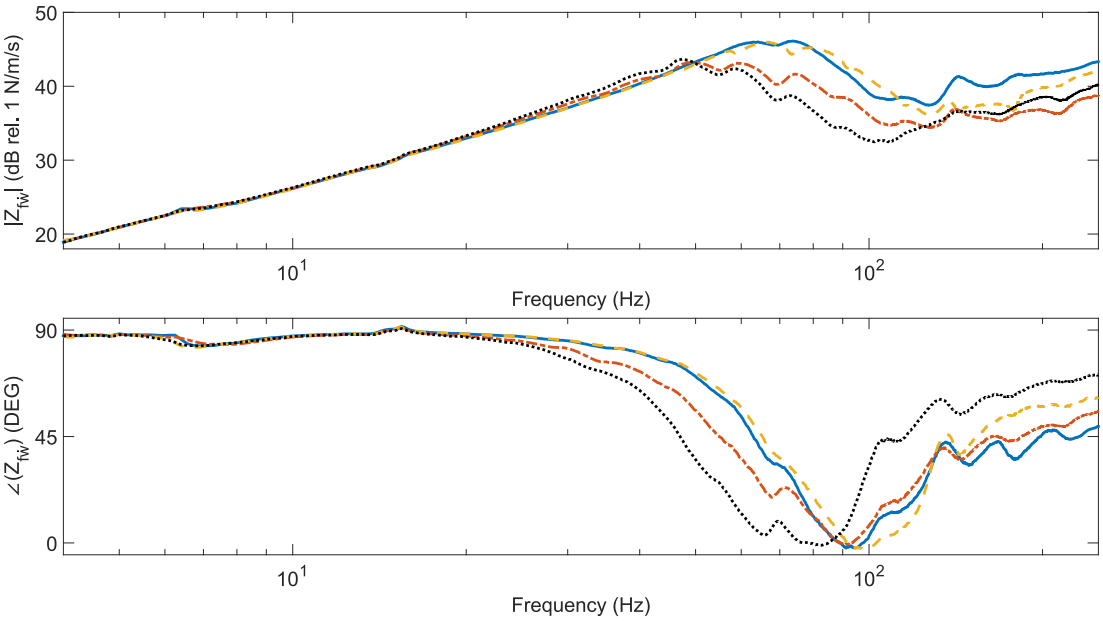

Figure 3.16. Actuator base impedance for hinged flywheel element with the highest axial inertia value I_{w4}/r_{w4}^2. Comparison of the M2 screw four different angle positions (0° solid blue lines, 90° dashed-dotted red lines, 180° dashed yellow lines, 270° dotted black lines).

3.4.4 Blocked force current driven

Figure 3.20 shows scheme (Figure 3.20a) and picture (Figure 3.20b) of the blocked force test setup for the current driven inertial actuator. During tests, the actuator was attached to a rigid base via a force cell as shown in Figure 3.20b. Two parameters were measured during tests using signal analyser. Channel input A measured force excreted to the actuator base while input B measured the current fed to the actuator. The quad amplifier was used to drive the EM actuators. Appendix D lists all the equipment used in the measurements of the transducer elecromechanical properties.

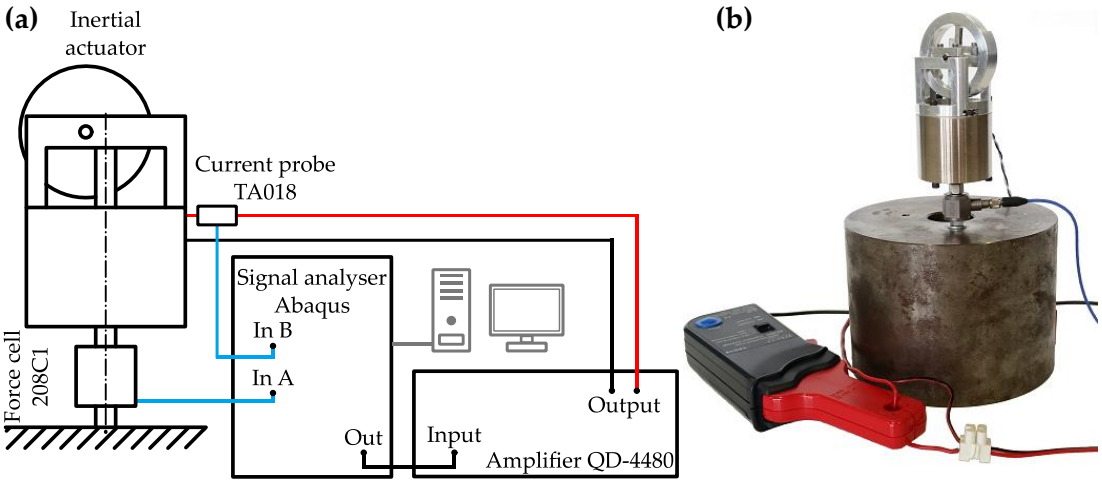

Figure 3.17. Scheme (a) and picture (b) of the blocked force per unit current fed to the actuator test setup.

The Bode plots in Figure 3.18 present the FRFs of the blocked force produced by the actuators per unit current fed to the classical, classical with the same inertial mass as the flywheel configuration, hinged and pinned configuration of the flywheel inertial actuators as given in Equation (2.52). The figure is organised in two columns where, the left column shows the modulus diagrams while the right column shows the phase diagrams of the actuator blocked force. The solid blue lines in the diagrams present the measurement results, while the dashed-dotted red lines present the simulation results. Plot (a) shows the blocked force of the classical actuator. Plot (b) shows the blocked force for the classical actuator with the same inertial mass as the flywheel configuration. Plots (c-f) show the blocked force of the hinged flywheel inertial actuator with increasing value of the equivalent axial inertia I_w / (r_w^2) effect

of the rocker arm ($I_{w1}/(r_{w1}^2) < I_{w2}/(r_{w2}^2) < I_{w3}/(r_{w3}^2)) < I_{w4}/(r_{w4}^2)$). Bottom plot (g) shows the blocked force for the pinned flywheel inertial actuator

The blocked force produced by the classical configuration of the inertial actuator is shown in Figure 3.18a. At low frequencies, the produced force rises proportionally to ω^2 and is out of phase with the driving current signal fed to the actuator coil, which is characterised by phase equal to 180°. Thus, the produced force is out of phase with the driving signal below fundamental resonance frequency of the actuator. The amplitude reaches a peak value at the resonance frequency of the actuator at about 21 Hz with the phase shift that undergoes a -180° lag such that it equal to 0°. At higher frequencies, the blocked force produced at the base of the actuator settles to a constant value that is equal to the actuator transduction coefficient ψ_a that is 27dB and is in phase with the driving current signal i_a. Thus, the investigated inertial actuator produces the desired constant force excitation effect, which is in phase with the driving signal at frequencies above its fundamental resonance frequency. The principal features of the measured blocked force for the classical configuration agree well those obtained from simulations.

The blocked force produced by the classical actuator with the same inertial mass as that of the flywheel configuration is shown in Figure 3.18b. The modulus and the phase diagram presents almost identical characteristic compared to the classical configuration. However, for this configuration the amplitude reaches a peak value at slightly lower frequency, which is at about 19 Hz. Also for this configuration, the measured blocked force agrees well with the simulation results.

The blocked force for the first prototype of the flywheel inertial actuator equipped with the rocker arm is shown in Figure 3.18c-f. The features found for the first prototype present similarity to the classical configuration, however with an increasingly smaller offset that is higher equivalent relative axial inertia effect of the rocking arm I_w/r_w^2, the resonance peak is progressively smoothened and brought down in frequency. Thus, the fundamental resonance frequency is moved to about 13 Hz (Figure 3.18c) for the first value of the inertia effect I_{w1}/r_{w1}^2, to about 11 Hz (Figure 3.18d) for the second value of the inertia effect I_{w2}/r_{w2}^2, to about 9 Hz (Figure 3.18e) for the third value of the inertia effect I_{w3}/r_{w3}^2 and to about 5 Hz (Figure 3.18f) for the fourth value of the inertia effect I_{w4}/r_{w4}^2. At higher frequencies, the produced blocked forces settle to progressively lower constant values. It settles at about 21 dB for the first value of the inertia effect, at about 18 dB for the second value of the inertia effect, at about 14 dB for the third value of the inertia effect and at about 5 dB for the fourth value of the inertia effect. The measured blocked force for the flywheel inertial

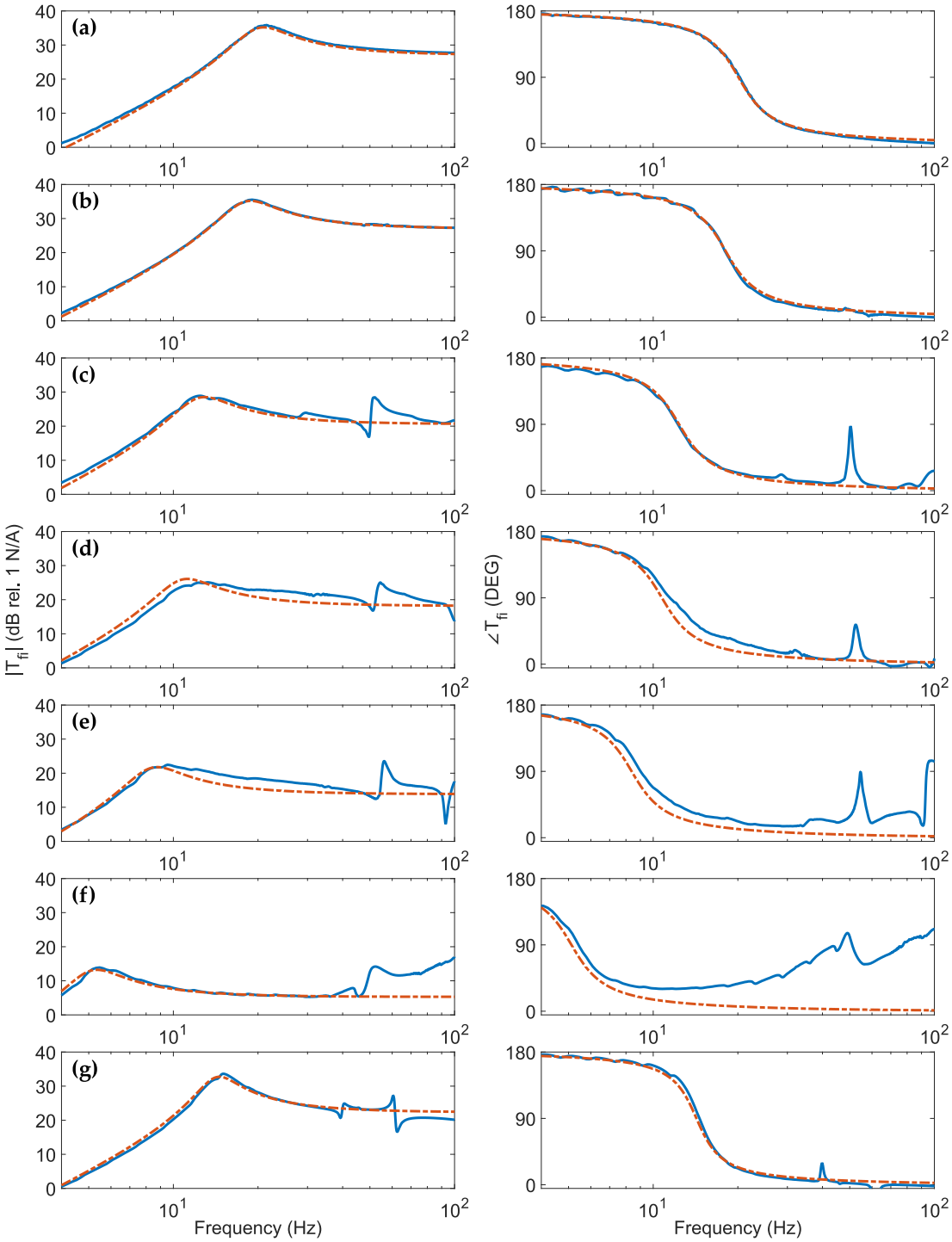

Figure 3.18. Blocked force per unit current fed to the actuator for the classical configuration (a), classical with the same inertial mass as that of the flywheel configuration (b), with the hinged flywheel element with the increasing axial inertia values I_{w1}/r_{w1}^2 (c), I_{w2}/r_{w2}^2 (d), I_{w3}/r_{w3}^2 (e), I_{w4}/r_{w4}^2 (f) and with the pinned flywheel element (g). Comparison of the experimental results (solid blue lines) with the numerical simulations (dashed-dotted red lines).

actuator equipped with the rocker arm agree well with that obtained with simulations. However, at about 50 Hz an additional peak appears for all four configurations, which should not depend on the axial inertia effect I_w/r_w^2. Most likely, it is a rocking effect of the suspended mass that was aggravated during measurements when the base mass of the actuator was rigidly fixed. For the third axial inertia effect I_{w3}/r_{w3}^2 value of the flywheel an additional through appears at about 90 Hz that could be caused by the dynamics of the rocker arm. At higher frequencies for the fourth axial inertia effect I_{w4}/r_{w4}^2 value (Figure 3.18f) the phase of the blocked force drifts causing the produced force to be out of phase with the driving current.

The blocked force for the second prototype of the inertial actuator equipped with the flywheel element is shown in Figure 3.18g. The blocked force is characterised by a similar FRF compared to the classical configuration except that the fundamental resonance peak occurs at lower frequency that is at about 14 Hz and that the amplitude at the peak is about 2.5 dB lower. The measured blocked force for the pinned flywheel inertial actuator agree with simulations compared to the hinged flywheel inertial actuator equipped with rocker arm. There two additional peaks that appear at 40 Hz and at 60 Hz, which could be due to the test setup used for the measurement and due to dynamics of flywheel mechanism.

3.4.5 Blocked force voltage driven

Figure 3.24 shows scheme (Figure 3.24a) and picture (Figure 3.24b) of the blocked force per unit voltage applied to the actuator test setup. During tests, the actuator was attached to a rigid base via a force cell as shown in Figure 3.24b. Two parameters were measured during tests using signal analyser. Input channel A measured force excreted to the actuator base while input channel B measured applied voltage to the actuator. The quad amplifier was used to drive the EM actuator. Appendix D lists all the equipment used in the measurements of the transducer elecromechanical properties.

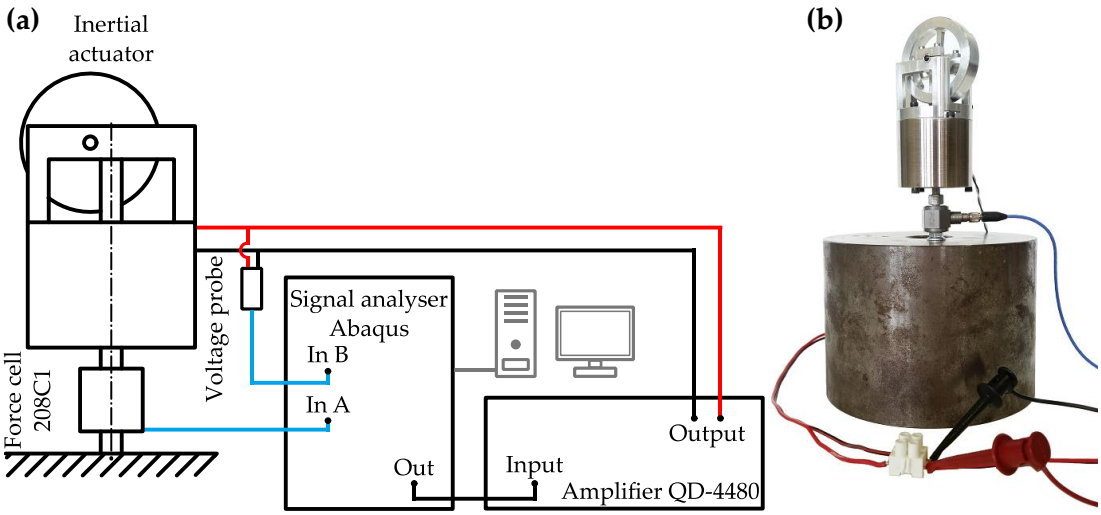

Figure 3.19. Scheme (a) and picture (b) of the blocked force per unit voltage applied to the actuator test setup.

The Bode plots in Figure 3.20 present the FRFs of the blocked force produced by the actuators per unit voltage applied to the classical, classical with the same inertial mass as the flywheel configuration, hinged and pinned configurations of the flywheel inertial actuators as given in Equation (2.54). The figure is organised in two columns where, the left column shows the modulus diagrams while the right column shows the phase diagrams of the blocked force. The solid blue lines in the diagrams present the measurement results, while the dashed-dotted red lines present the simulation results. Plot (a) shows the blocked force of the classical actuator. Plot (b) shows the blocked force for the classical actuator with the same inertial mass as the flywheel configuration. Plots (c-f) show the blocked force of the hinged flywheel inertial actuator with increasing value of the equivalent axial inertia I_w / (r_w^2) effect of the rocker arm $(I_{w1}/(r_{w1}^2) < I_{w2}/(r_{w2}^2) < I_{w3}/(r_{w3}^2) < I_{w4}/(r_{w4}^2))$. Bottom plot (g) shows the blocked force for the pinned flywheel inertial actuator.

The blocked force produced by the classical configuration of the inertial actuator is shown in Figure 3.20a. At low frequencies, the produced force rises proportionally to ω^2 and is out of phase with the voltage signal applied at the electrical terminals of the actuator coil, which is characterised by phase equal to 180°. Thus, the produced force is out of phase with the voltage signal below fundamental resonance frequency of the actuator, similarly as for the produced blocked force per unit current. Around the fundamental resonance frequency of the actuator, the blocked force passes a transient mode to reach constant value of around 0dB at higher frequencies. The well visible peak at the fundamental resonance frequency of the actuator observed for the

blocked force produced per unit current is rounded off for the voltage driven actuator. This behaviour is caused by the electrical properties of the transducer coil, mainly the resistance, which increases the internal damping effect. Additionally, at the fundamental resonance frequency the phase shifts and undergoes a -180° lag such that it equal 0° at higher frequencies. The classical inertial actuator can produce the constant force effect at frequencies above its fundamental resonance frequency that is in phase with the applied voltage signal. The measured blocked force for the classical configuration agrees well with simulations results, although the measured results are slightly higher in the amplitude compared to the simulation results.

The blocked force produced by the classical actuator with the same inertial mass as the flywheel configuration is shown in Figure 3.20b. The modulus and the phase diagram presents nearly identical characteristic compared to the classical configuration. For this configuration, the amplitude reaches a peak value at slightly lower frequency, which is at about 19 Hz. Also for this configuration, the measured blocked force agrees well with the simulation results.

The blocked force for the first prototype of the flywheel inertial actuator equipped with the rocker arm is shown in Figure 3.20c-f. The blocked force of the first prototype presents similar characteristic to the classical configuration. With higher equivalent relative axial inertia effect of the rocking arm I_w/r_w^2, the resonance peak is shifted down in frequency. The fundamental resonance frequency is moved to about 13 Hz (Figure 3.20c) for the first value of the inertia effect I_{w1}/r_{w1}^2, to about 11 Hz (Figure 3.20d) for the second value of the inertia effect I_{w2}/r_{w2}^2, to about 9 Hz (Figure 3.20e) for the third value of the inertia effect I_{w3}/r_{w3}^2 and to about 5 Hz (Figure 3.20f) for the fourth value of the inertia effect I_{w4}/r_{w4}^2. At higher frequencies, the produced blocked force settles to lowered values. It settles at about -6 dB for the first value of the inertia effect, at about -8 dB for the second value of the inertia effect, at about -13 dB for the third value of the inertia effect and at about -22 dB for the fourth value of the inertia effect. The measured blocked forces for the flywheel inertial actuator equipped with the rocker arm agree well with that obtained with simulations. A slight overshoot of the blocked force is observed above fundamental resonance frequency of the actuator for the higher axial inertia value of the flywheel element. For all four configurations, an additional peak appears at about 50 Hz and it can be assumed that it does not depend on the axial inertia effect I_w/r_w^2. Most probably, it is a rocking effect of the suspended mass that was aggravated during measurements when the base mass of the actuator was rigidly fixed. At higher frequencies for the fourth axial inertia effect

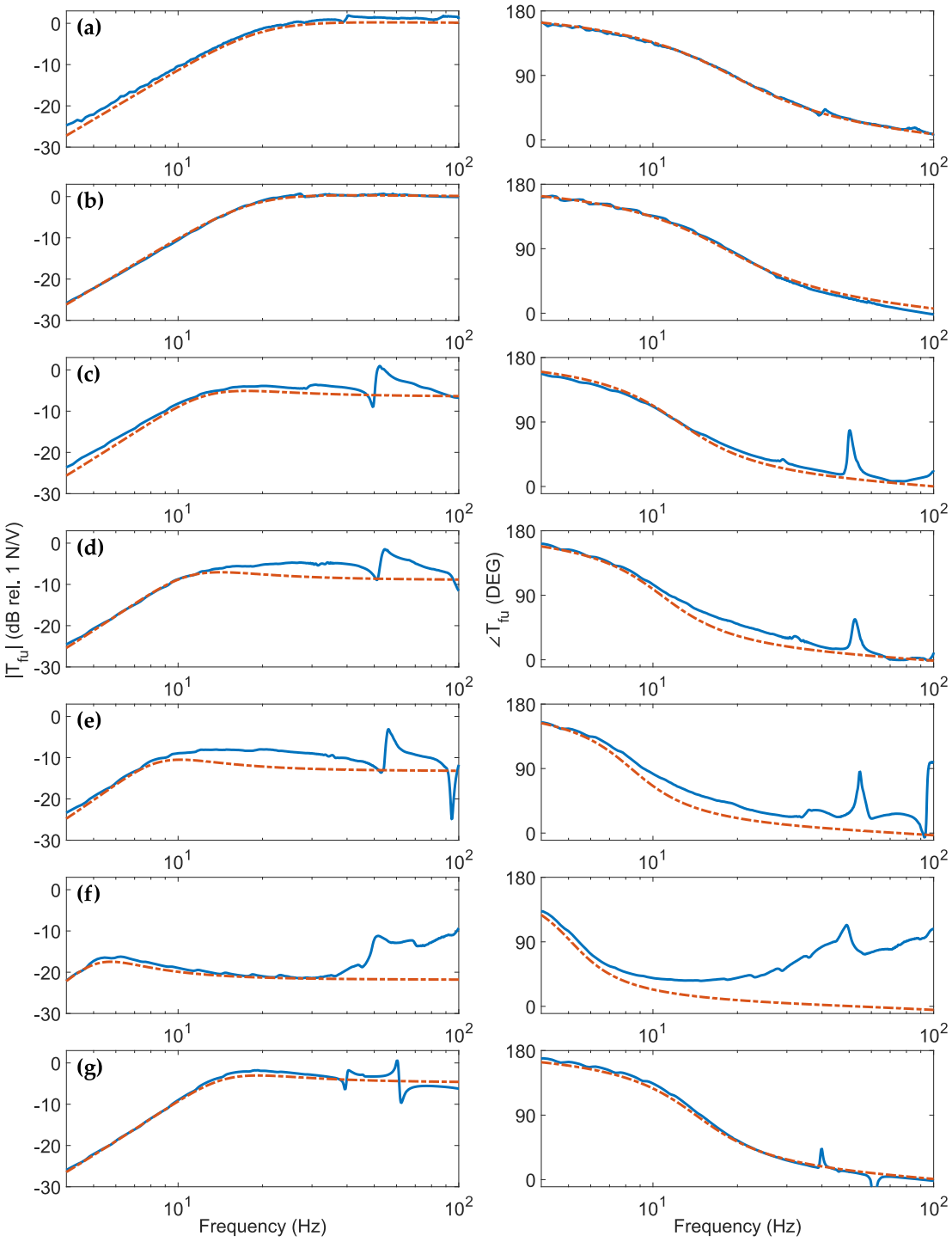

Figure 3.20. Blocked force per unit voltage applied to the actuator for the classical configuration (a), classical with the same inertial mass as that of the flywheel configuration (b), with the hinged flywheel element with the increasing axial inertia values I_{w1}/r_{w1}^2 (c), I_{w2}/r_{w2}^2 (d), I_{w3}/r_{w3}^2 (e), I_{w4}/r_{w4}^2 (f) and with the pinned flywheel element (g). Comparison of the experimental results (solid blue lines) with the numerical simulations (dashed-dotted red lines).

I_{w4}/r_{w4}^2 value (Figure 3.20f) the phase of the blocked force drifts causing the produced force to be out of phase with the applied voltage.

The blocked force for the second prototype of the inertial actuator equipped with the flywheel element is shown in Figure 3.20g. The produced blocked force is characterised by a similar FRF to the classical configuration except that the fundamental resonance of the actuator is shifted to a lower frequency that is at about 14 Hz. The produced blocked force settles at about -4 dB above fundamental resonance frequency of the actuator. The measured blocked force for the pinned flywheel inertial actuator agrees well with simulations compared to the hinged flywheel inertial actuator equipped with rocker arm. The two additional peaks that appear at 40 Hz and at 60 Hz may be due to the test setup used for the measurement and due to dynamics of flywheel mechanism.

3.4.6 Transduction FRF

Figure 3.21 shows the scheme (Figure 3.21a) and picture (Figure 3.21b) of the transduction FRF test setup. The tested transducers were mounted on the shaker. Two parameters were measured during tests using signal analyser. Input channel A measured voltage at the electrical terminals of the transducer, while input channel B measured the base acceleration. The shaker amplifier was used to drive the shaker with a sine logarithmic sweep excitation up to 100Hz. Appendix D lists all the equipment used in the measurements of the transducer elecromechanical properties.

The Bode plots in Figure 3.22 present the transduction coefficient FRFs of the classical, classical with the same inertial mass as the flywheel configuration, hinged and pinned flywheel configurations of the inertial actuators as given in Equation (2.53). According to Equation (2.53) the transduction coefficient should be equal to the blocked force T_{fi} produced by the actuators per unit current. The figure is organised in two columns where, the left column shows the modulus diagrams while the right column shows the phase diagrams of the transduction coefficient FRFs. The solid blue lines in the diagrams present the measurement results, while the dashed-dotted red lines present the simulation results. Plot (a) shows the transduction coefficient of the classical actuator. Plot (b) shows the blocked force for the classical actuator with the same inertial mass as the flywheel configuration. Plots (c-f) show the transduction coefficient FRFs of the hinged flywheel inertial actuator with increasing value of the equivalent axial inertia I_w / (r_w^2) effect of the rocker arm

$(I_{w1}/(r_{w1}^2) < I_{w2}/(r_{w2}^2) < I_{w3}/(r_{w3}^2) < I_{w4}/(r_{w4}^2))$. Bottom plot (g) shows the transduction coefficient FRF for the pinned flywheel inertial actuator.

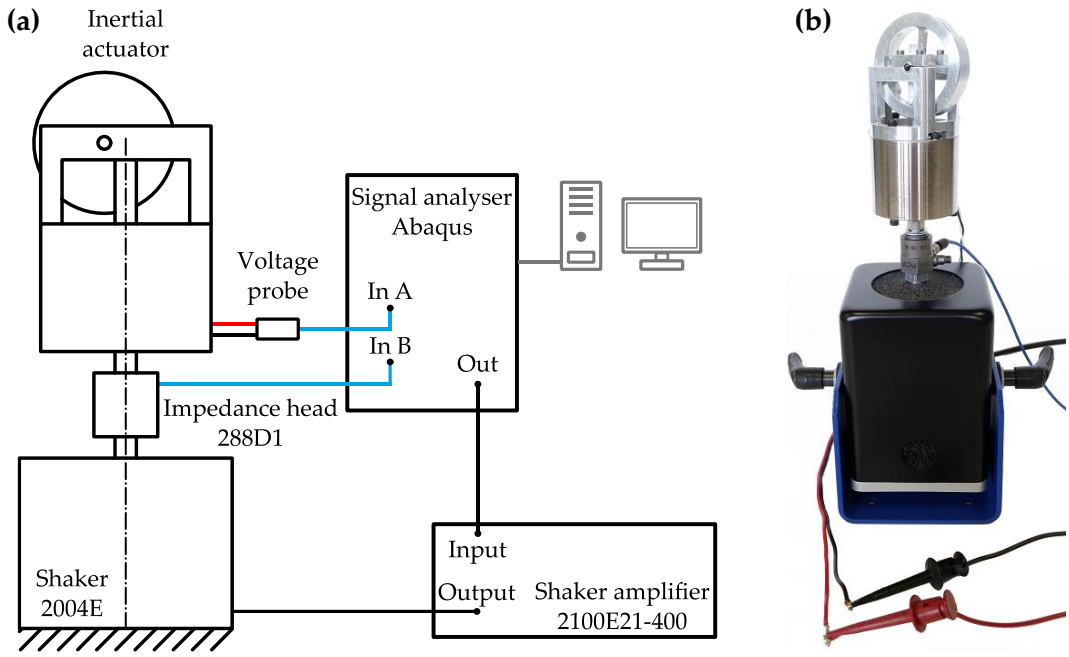

Figure 3.21. Scheme (a) and picture (b) of the transduction coefficient FRF test setup.

The transduction coefficient FRF of the classical inertial actuator shown in Figure 3.22a is almost identical to the results obtained for the blocked force produced per unit current fed to the actuator. At low frequency, the generated voltage rises proportionally to ω^2 and is out of phase with the unit velocity of excitation. The amplitude reaches a peak value at the resonance frequency of the actuator at about 21 Hz with the phase shift that undergoes a -180° lag. At higher frequencies, the generated voltage settles to a constant value that is equal to the actuator transduction coefficient ψ_a that is 27dB. The measured transduction coefficient FRF agrees well with the simulations.

The transduction coefficient FRF of the classical actuator with the same inertial mass as the flywheel configuration is shown in Figure 3.22b. The results present similar characteristic to the classical configuration with one difference. Compared to the classical configuration, the amplitude reaches a peak value at slightly lower frequency, which is at about 19 Hz. The measured transduction coefficient FRF agrees well with the simulation results.

The transduction coefficient FRFs for the first prototype of the inertial actuator equipped with the rocker arm are shown in Figure 3.22c-f. As expected the transduction FRF is similar to the blocked force FRF. Also in this case, with the smaller offset r_w, that is the higher equivalent relative axial inertia effect of the rocking arm I_w / (r_w^2), the resonance peak is progressively smoothened and brought down in frequency. The fundamental resonance frequency is moved to about 13 Hz (Figure 3.22c) for the first value of the inertia effect I_{w1}/r_{w1}^2, to about 11 Hz (Figure 3.22d) for the second value of the inertia effect I_{w2}/r_{w2}^2, to about 9 Hz (Figure 3.22e) for the third value of the inertia effect I_{w3}/r_{w3}^2 and to about 5 Hz (Figure 3.22f) for the fourth value of the inertia effect I_{w4}/r_{w4}^2. Furthermore, at higher frequencies the transduction coefficient FRFs settle to a progressively lowered constant value. It settles at about 21 dB for the first value of the inertia effect, at about 18 dB for the second value of the inertia effect, at about 14 dB for the third value of the inertia effect and at about 5 dB for the fourth value of the inertia effect. The measured transduction coefficients for the hinged flywheel inertial actuator equipped with the rocker arm agree well with the expected properties obtained with simulations. However for the third (Figure 3.22e) and fourth (Figure 3.22f) values of the inertia the transduction coefficient FRF does not settle to a constant value at higher frequencies. Above about 20 Hz the characteristics starts to rise in amplitude and settles to a value of the classical inertia actuator that is at about 27 dB. Most probably, this is due to the backlash in the hinged joints that is greater than the relative motion of the base and inertial mass of the actuator at higher frequencies. Above about 20 Hz the small relative movements start to be dissipated in the hinged joints rather than transferred via flywheel element, which means that the prototype starts to behave just like a classical configuration. The additional peak that appeared for all four configurations at about 50Hz in the blocked force measurements (Figure 3.18) is not visible with the transduction coefficient measurements because the actuator base mass is not rigidly fixed but excited.

The transduction coefficient FRF for the second prototype of the flywheel inertial actuator is shown in Figure 3.22g. The transduction coefficient FRF is characterised by a fundamental resonance frequency at about 14 Hz and with amplitude at the peak 2.5 dB lower compared to the classical configuration. The measured transduction coefficient FRF for the pinned flywheel inertial actuator agree well with simulations and align far better compared to the results obtained for the hinged configuration of the flywheel inertial actuator. The measurements show additional peak that appears at about 40 Hz, which most likely is caused by the dynamics of flywheel mechanism.

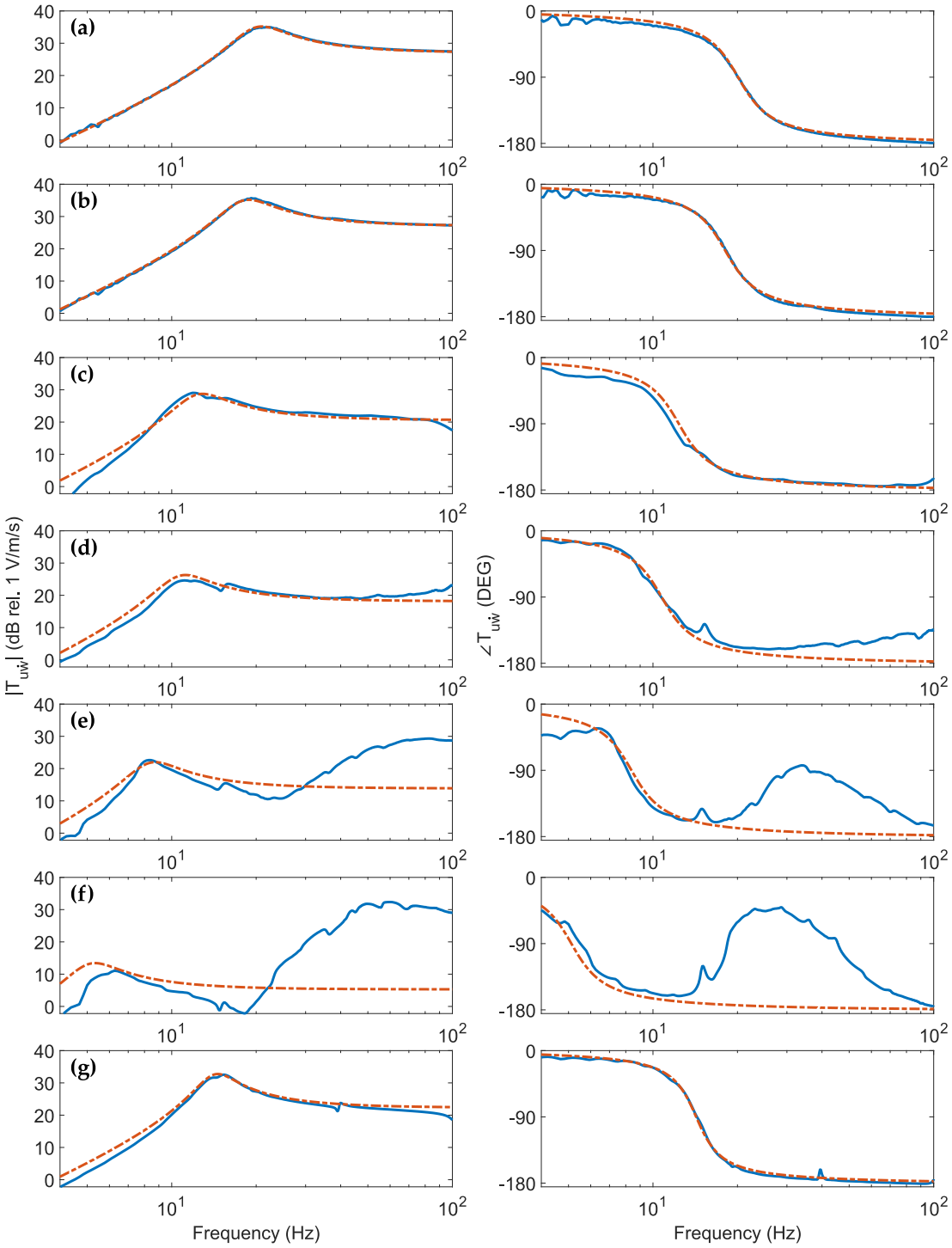

Figure 3.22. Actuator transduction coefficient for the classical configuration (a), classical with the same inertial mass as that of the flywheel configuration (b), with the hinged flywheel element with the increasing axial inertia values I_{w1}/r_{w1}^2 (c), I_{w2}/r_{w2}^2 (d), I_{w3}/r_{w3}^2 (e), I_{w4}/r_{w4}^2 (f) and with the pinned flywheel element (g). Comparison of the experimental results (solid blue lines) with the numerical simulations (dashed-dotted red lines).

3.4.7 *Electrical impedance*

Figure 3.23 shows the scheme (Figure 3.23a) and picture (Figure 3.23b) of the base impedance test setup. The tested actuators were attached to a rigid base. Two parameters were measured during tests using signal analyser. Input channel A measured voltage at the electrical terminals of the actuator while input B measured current fed to the actuator. The quad amplifier was used to drive the EM actuators. Appendix D lists all the equipment used in the measurements of the transducer elecromechanical properties.

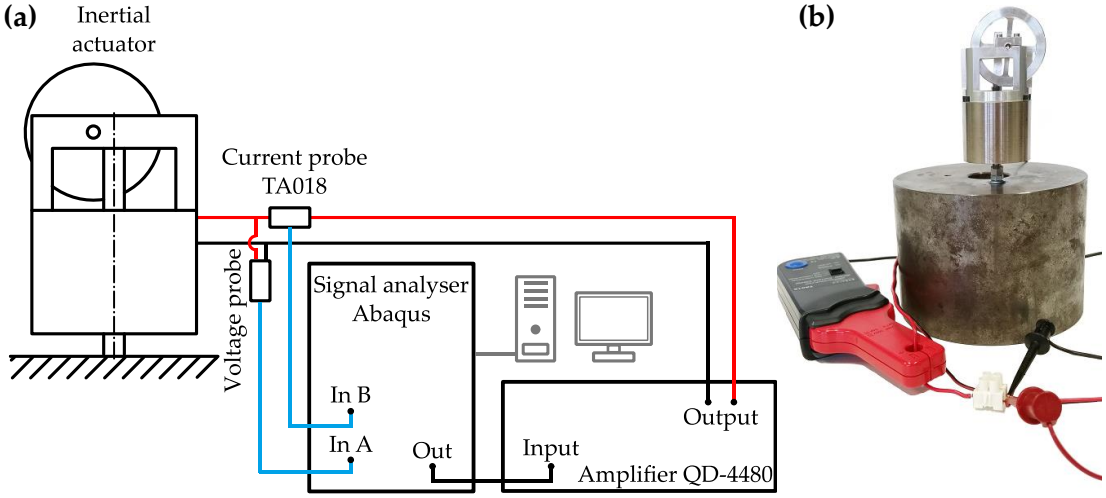

Figure 3.23. Scheme (a) and picture (b) of the electrical impedance test setup.

The Bode plots in Figure 3.24 present the electrical impedance FRFs of the classical, classical with the same inertial mass as the flywheel configuration, hinged and pinned flywheel configurations of the inertial actuators as given in Equation (2.55). The figure is organised in two columns where, the left column shows the modulus diagrams while the right column shows the phase diagrams. The solid blue lines in the diagrams present the measurement results, while the dashed-dotted red lines present the simulation results. Plot (a) shows the electrical impedance FRF of the classical actuator. Plot (b) shows the electrical impedance of the classical actuator with the same inertial mass as the flywheel configuration. Plots (c-f) show the electrical impedance FRFs of the hinged flywheel inertial actuator with increasing value of the equivalent axial inertia I_w / (r_w^2) effect of the rocker arm $(I_{w1}/(r_{w1}^2) < I_{w2}/(r_{w2}^2) < I_{w3}/(r_{w3}^2) < I_{w4}/(r_{w4}^2))$. Bottom plot (g) shows the electrical impedance FRF for the pinned flywheel inertial actuator.

The modulus of the electrical impedance for the classical configuration showed in left diagram of the Figure 3.24a is characterised by a low and high frequencies purely resistive behaviours separated by a resonance peak. The mechanical effect of the inertial mass is relevant only around the fundamental resonance frequency of the classical actuator that appears at about 20 Hz. At low frequencies, the spectrum is characterised by a constant value of about 27.5 dB that is equal to the coil resistance and the phase equal to zero meaning that the applied at the terminals of the actuator voltage is in phase with the driving current. At the fundamental resonance frequency the actuator electrical impedance reaches nearly 38 dB and the phase undergoes a shift from about +32° to -32°, which is due to the electro-mechanical effect of the inertial mass. Above the fundamental resonance frequency of the actuator the spectrum is still characterised by resistive behaviour of the coil. However, at higher frequencies the inductance of the coil starts to play more important role due to the frequency dependence of this parameter as shown in Equation (2.25). The measured electrical impedance for the classical configuration agree well with the previsioned properties obtained with simulations.

The electrical impedance FRF of the classical actuator with the same inertial mass as the flywheel configuration is shown in Figure 3.24b. The results present similar characteristic to the classical configuration with one difference. Compared to the classical configuration, the electrical impedance reaches amplitude peak at slightly lower frequency, which is at about 18 Hz. The measured electrical impedance FRF agrees well with the simulation results.

The electrical impedances for the first prototype of the flywheel inertial actuator shown in Figure 3.24c-f present similar characteristic to that of the classical configuration. The axial inertia effect produced by the hinged rocker arm shifts the fundamental resonance frequency to a lower value with progressively smaller offset values. Thus, the fundamental resonance frequency is moved to about 12 Hz (Figure 3.24c) for the first value of the inertia effect I_{w1}/r_{w1}^2, to about 10.5 Hz (Figure 3.24d) for the second value of the inertia effect I_{w2}/r_{w2}^2, to about 8.5 Hz (Figure 3.24e) for the third value of the inertia effect I_{w3}/r_{w3}^2 and to about 5 Hz (Figure 3.24f) for the fourth value of the inertia effect I_{w4}/r_{w4}^2. The internal damping effect is also increased, such that the resonance peaks are progressively rounded and the phase shifts between smaller values. For the first value of the inertia effect the modulus reaches about 35 dB with the phase shift from about +24° to -24°. For the second value of the inertia effect the modulus reaches about 34 dB with the phase shift from about +22° to -22°. For the third value of the inertia effect I_{w3}/r_{w3}^2 the modulus reaches about 33 dB with

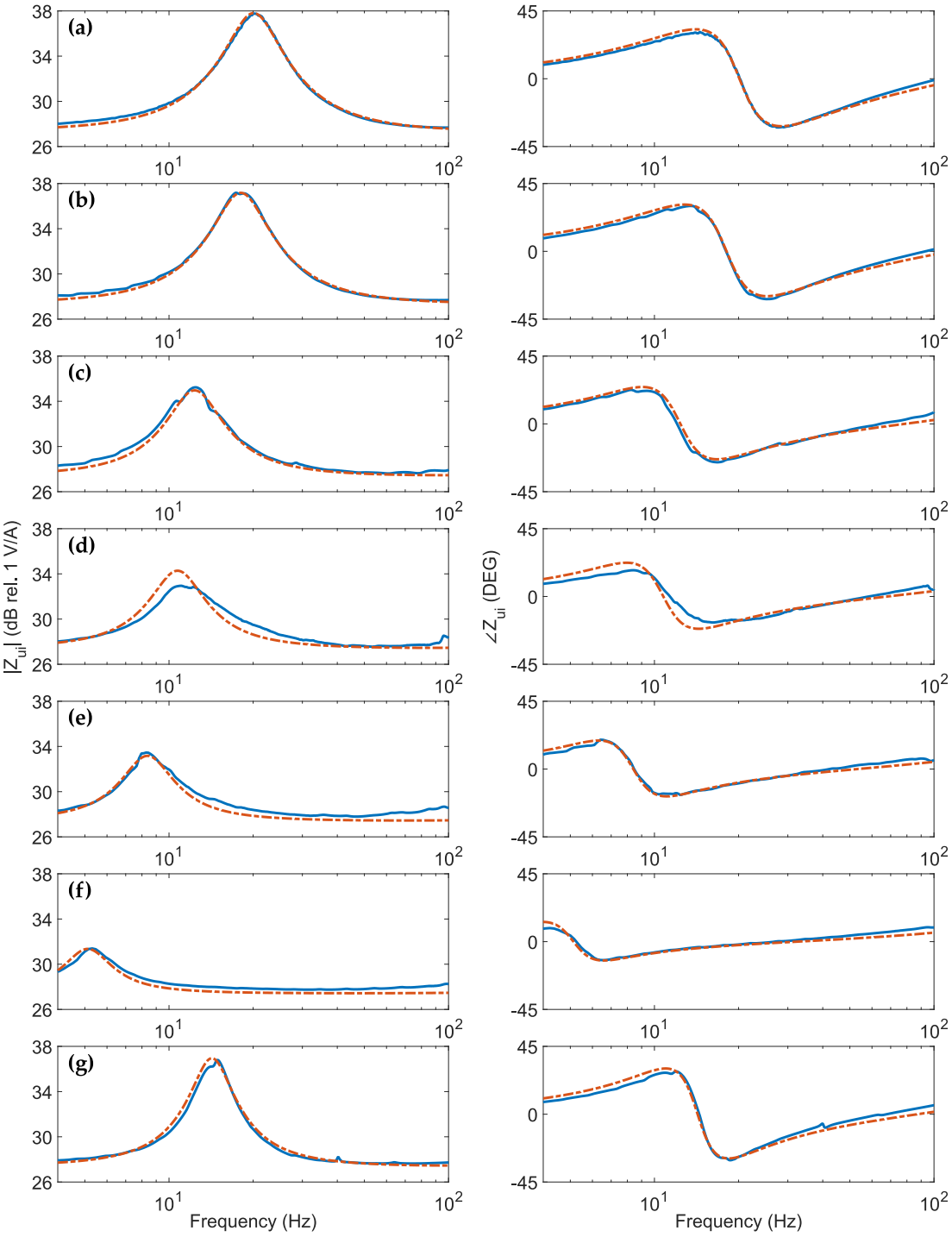

Figure 3.24. Actuator electrical impedance for the classical configuration (a), classical with the same inertial mass as that of the flywheel configuration (b), with the hinged flywheel element with the increasing axial inertia values I_{w1}/r_{w1}^2 (c), I_{w2}/r_{w2}^2 (d), I_{w3}/r_{w3}^2 (e), I_{w4}/r_{w4}^2 (f) and with the pinned flywheel element (g). Comparison of the experimental results (solid blue lines) with the numerical simulations (dashed-dotted red lines).

the phase shift from about +19° to -19°. For the fourth value of the inertia effect I_{w4}/r_{w4}^2 the modulus reaches about 31 dB with the phase shift from about +13° to -13°. The measured electrical impedance FRF for the flywheel inertial actuator equipped with the rocker arm agree well with the previsioned properties obtained with simulations. For the second value of the inertia effect (Figure 3.24d) the measured amplitude does not reaches the previsioned with simulations value.

The electrical impedances for the second prototype of the flywheel inertial actuator shown in Figure 3.24g presents similar characteristic to that of the classical configuration. The produced inertia effect of the flywheel element shifts the fundamental resonance peak to about 14 Hz with the maximum amplitude of about 37 dB. The phase shown in the right diagram of the Figure 3.24g shifts between +30° to around -30°. The experimental results for the pinned configuration of the flywheel inertial actuator align well with the numerical results. There is small additional peak that appears at about 40 Hz, which was also observed in the measurement results obtained with the other tests.

3.5 STATIC DEFLECTION STUDY

One of the key parameters used to characterise an inertial actuator for active vibration control is the static deflection. The static displacement of the springs-coil assembly defines the robustness of the actuator to shocks that may cause stability and control performance limitations. Figure 3.25 shows the comparison of the calculated static deflection of the classical actuator and two prototypes with previsioned simulation. The results are normalised to the static deflection of the classical configuration defined in Equation (2.58) with respect to its natural frequency for the classical actuator (blue dot), for the classical configuration with the same inertial mass as that of the flywheel configuration (magenta diamond), for the hinged flywheel inertial actuator with increasing value of the equivalent axial inertia effect I_w / (r_w^2) of the rocker arm (red crosses) and for the pinned flywheel inertial actuator (black square). The solid blue line shown in the Figure 3.25 presents the simulated static deflection of the classical configuration for the increasing weight of the inertial mass for the given stiffness value specified in Table 3.4.

The normalised static deflection of the classical inertial actuator is equal to one at its natural frequency that is at about 20 Hz. The solid blue line shows the simulated increase of the static deflection (inertial mass weight increase for given stiffness) with

reduction of the natural frequency for the classical inertial actuator. Thus, the static deflection for the classical actuator with the same inertial mass as the flywheel configuration shown in Figure 3.25 (magenta diamond) aligns with the previsioned solid blue line.

Considering the hinged configuration of the flywheel actuator, the normalised static deflection has increased to about 1.2 for all tree vales of the inertia effect I_w/r_w^2. In this case the increase of the static deflection does not depend on the flywheel inertia but is caused by the additional mass of flywheel itself and its support, which was attached to the inertial mass. The static deflection of the hinged flywheel actuator with the highest value of the inertia effect is nearly five times smaller compared to the classical configuration.

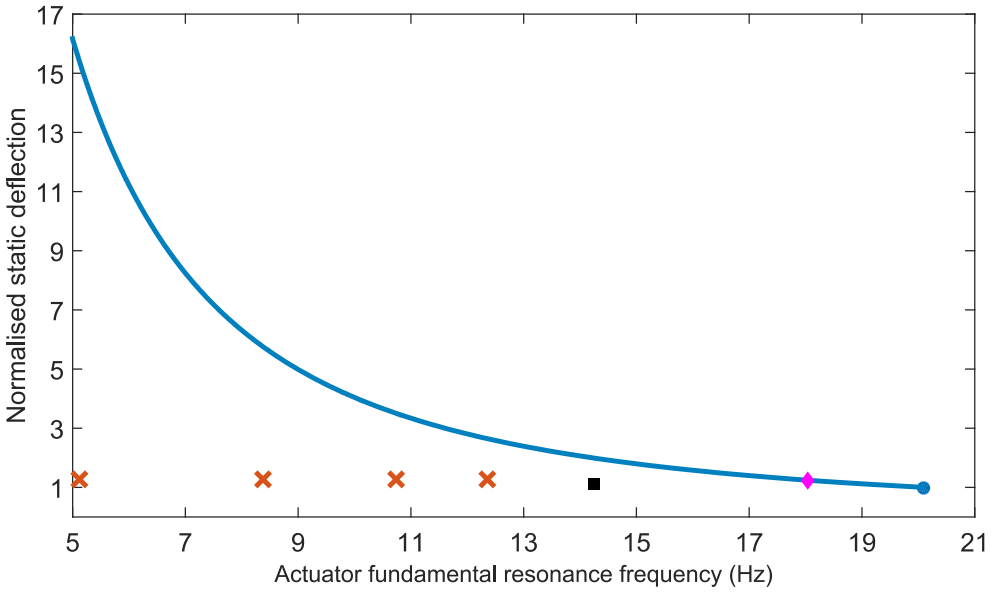

Figure 3.25. Normalised static deflection with respect to actuator natural frequency for the classical configuration (blue dot), classical configuration with the same inertial mass as that of the flywheel configuration (magenta diamond) with the hinged flywheel element (red crosses) and with the pinned flywheel element (black square). Solid blue line presents previsioned static deflection for diminishing natural frequency (increasing weight for given stiffness) of the inertial mass of the classical configuration.

The results for the pinned configuration of the flywheel inertial actuator show that the normalised static deflection has increased to 1.1. Although the flywheel element in the pinned configuration has the same mass as in the hinged configuration the static deflection is reduced due to the additional torsional bearings that increase the

stiffness of the actuator suspension system. Comparing the results with the simulations of the classical actuator the static deflection was reduced nearly twice with the pinned configuration of the flywheel inertial actuator.

The results shown in Figure 3.25 clearly demonstrate that the static deflection of the inertial actuators does not depend on the inertia effect I_w/r_w^2 produced by the flywheel element. Also, it shows that the flywheel configurations can increase the robustness to shocks of the active vibration control system by reducing the static deflection of the inertial actuators.

3.6 CHAPTER SUMMARY

This chapter has presented the EM actuator that was used as a base for designing two different flywheel prototypes. The first prototype was designed with hinged mechanism while the second prototype with the pinned flywheel element analogously to the theoretical study presented in the second chapter. The flywheel element of the hinged configuration was designed in a form of a rocker arm with four lumped masses. The rocker arm was designed with several holes that allowed changing the position of the lumped masses and thus changing the moment of inertia produced by the flywheel element. The pinned configuration was equipped with the flywheel element designed in a form of a wheel. The shape of the flywheel element was optimised to maximise the polar moment of inertia and minimise the total weight. The flexural bearings were used to minimise the backlash between the components and to avoid any nonlinear effects (stick-slip effect).

The first part of this chapter described in details both fabricated prototypes. The design and assembly process of each prototype was also described. A particular emphasis was given to the description of the mechanisms used to transform linear motion of the actuator into rotation of the flywheel element.

The second part of this chapter has presented experimental and simulation results on the FRFs that characterise the electromechanical response of the flywheel inertial actuators. The study has considered the actuators base impedance, the actuators blocked force per unit driving current, the actuators blocked force per unit applied voltage, the transduction FRF and the actuators electrical impedance. The measured FRFs were taken on a classical coil-magnet inertial actuator, classical inertial actuator with the same inertial mass as the flywheel configuration, on the hinged prototype inertial actuator equipped with a rocker arm designed to produce a variable flywheel

inertia effect and on the pinned prototype. The simulated FRFs were derived from a lumped parameter model defined in the theoretical study presented in the second chapter.

The experimental study has shown reasonably good agreement between the measured and simulated FRFs. In addition, it has confirmed that the rotational inertia effect of the flywheel element tends to reduce the resonance frequency and the amplitude of the fundamental resonance peak that characterise the response of the actuator. After testing various flywheel configurations of the hinged prototype it was observed that the surfaces of the shafts covered with the aluminium tape have visible wear effect. This wear effect on both shafts used in the hinged prototype is shown in the Figure 3.26. The experimental results of the hinged configuration showed that the play and backlash effect between the components introduces nonlinearities in the dynamics of the actuator. The hinged configuration does not fulfil the requirement of an inertial actuator to implement more stable and robust velocity feedback loops to control the vibration of flexible structures.

Figure 3.26. Screws used as shafts in the hinged prototype with visible wear effect.

The static deflection study has demonstrated that the flywheel element can be used to reduce the fundamental resonance frequency of the transducer without increasing the inertial mass. Thus, the flywheel element can improve stability and robustness to shocks of the implemented velocity feedback loops both by lowering the feedback control spillover effect at the fundamental resonance frequency of the actuator and without increasing the static deflection of the transducer.

The designed flywheel prototypes are much heavier compared to the configurations analysed in the theoretical study. Thus, to implement a velocity feedback loops with the fabricated inertial actuators a specific test structure need to be build. To compare the theoretical study with the experimental results it is required to design a new setup with a simply supported plate, in which the weight of the inertial actuators would be around 10% of the host structure mass.

4

FLYWHEEL PIEZOELECTRIC TRANSDUCER

This chapter presents the experimental tests carried out on a new proof mass piezoelectric actuator equipped with a flywheel element for the implementation of decentralised velocity feedback loops for vibration control of large flexible structures. The measured frequency response functions that characterise the electromechanical responses of the flywheel inertial actuator are contrasted with simulation results obtained from a simplified mathematical model and compared with those of a classical proof mass actuator.

The first part of this chapter presents the detailed design of the flywheel piezoelectric actuator. The selection of the components and assembly process is described in details. The second part of this chapter presents the classical and flywheel piezoelectric proof mass actuator that can be used in the active vibration control applications. A new mathematical formulation is used to derive the FRFs that characterise the electromechanical properties of both configurations. The simulated FRFs of actuator base impedance, blocked force and electrical admittance are contrasted with the experimental results.

4.1 PIEZOELECTRIC TRANSDUCER

The piezoelectric transducer presented in Figure 4.1, was used as a base for designing the flywheel inertial actuator. The amplified piezoelectric transducer produced by Cedrat Technologies (APA900M)[83] is built with piezoelectric stack actuators mounted in the oval shell. The transducer uses two 5x5x20mm^3 PZT (Lead Zirconate Titanate) stacks that are installed in the metal shell, which is used to mechanically amplify the produced displacement. When a voltage is applied to the transducer, the piezo stacks start to expand in the direction of the longest edge, proportionally to the applied signal. The expanding piezo stacks push on the longer sides of the shell causing the shell to contract in the direction of the shorter edge. Thus, the amplified piezoelectric transducer works as a pulling actuator. The ratio

between the shell deformation in longer axis to the deformation in shorter axis is called the transducer displacement amplification ratio and for the presented actuator is equal to 21. This type of transducer works with low voltage piezeoelectric stack actuators (-20V ÷ 150V) and can provide 850μm of stroke. The transducer can be used either for energy harvesting applications or as an actuator.

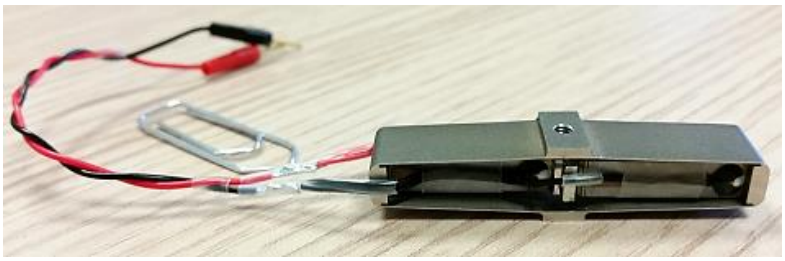

Figure 4.1. Amplified piezoelectric transducer.

The amplified piezoelectric transducer was used as a base for building a prototype flywheel actuator due to flat surfaces and M2.5 holes on the both mechanical terminals of the metal shell. The physical properties of the actuator are summarised in Table 4.1. The electromechanical properties of the amplified piezoelectric transducer were obtained from the producer datasheet [83].

Table 4.1. Physical properties of the transducer [83].

Parameter	Value
Stroke	850μm
Total Mass	18 g
Resonance frequency (free-free)	969 Hz
Resonance frequency (blocked-free)	225 Hz
Stiffness	25600 N/m
Blocked force	11.8 N
Capacitance	2.25 μF
High	10 mm
Length	49 mm
Width	10 mm

The amplified piezoelectric transducer presented in Figure 4.1 can be used to implement a velocity feedback loop to reduce the flexural vibration of flexible

structures. However, to produce a constant force effect at the control position in the low frequency range the actuator should be equipped with a large inertial mass. However, in case the actuator is exposed to shocks, the metal shell of the piezoelectric transducer undergoes large deformations, which may lead to cracks of the piezo stack and eventually to instability of the control system. Thus, it was decided to equip this actuator with the flywheel element that can improve the robustness of the control system to shocks and large disturbances by producing an apparent mass effect without increasing the inertial mass.

4.2 FLYWHEEL PIEZOELECTRIC INERTIAL ACTUATOR

The flywheel piezoelectric prototype was developed from the experience obtained during design of the two flywheel electromagnetic inertial actuators. The designed piezoelectric prototype is presented in Figure 4.2. Rendered view is shown in Figure 4.2a while the schematic view is shown in Figure 4.2b. The physical properties of the designed flywheel piezoelectric actuator are summarised in Table 4.2. The designed inertial actuator was based on the commercially available amplified piezoelectric transducer. In contrast to electromagnetic prototypes, the piezoelectric configuration was designed with the flywheel element attached to the base of the actuator. The flywheel element was designed in a form of a beam with lumped masses at both ends. A special yoke bracket is used to support the flywheel element and to connect it with the base of the piezoelectric actuator. The flywheel element was designed with a fixed value of the polar moment of inertia. Most of the fabricated components were made of aluminium. However, the lumped masses were made out of heavier brass to increase the moment of inertia produced by the flywheel element. The linear motion of the actuator is converted into a rotation of the flywheel by four pivot bearings. Two flexural bearings, one on each side, connect the flywheel element with the yoke bracket. Other two pivot bearings, also one on each side, connect the top output of the piezoelectric actuator via a special connector. The distance between the pair of the flexural bearings is the flywheel offset value. This parameter influences the axial inertia effect produced by the flywheel element and corresponds to a small radius defined with r_w symbol in the theoretical study. The technical drawings of the manufactured components for piezoelectric flywheel prototype are presented in appendix B.

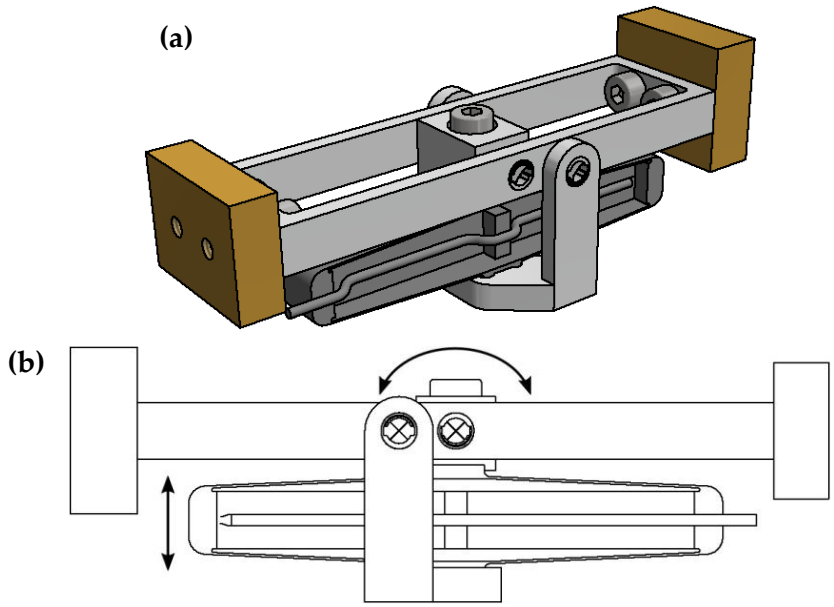

Figure 4.2. Design view of the flywheel piezoelectric inertial actuator. Rendered view (a) and schematic view (b).

Table 4.2. Physical properties of the piezoelectric flywheel inertial actuator.

Parameter	Value
Inertial mass	0.013 kg
Case mass	0.011 kg
Flywheel mass	0.024 kg
Torsional stiffness	$0.003\ \mathrm{Nmrad^{-1}}$
Flywheel inertia	$25.5 \cdot 10^{-6}\ \mathrm{kgm^2}$
Pushing pin offset	$r_w = 5$ mm
Axial flywheel mass effect	1.02 kg

4.2.1 Flywheel element

The designed flywheel element for the piezoelectric inertial actuator is shown in Figure 4.3. The flywheel element was composed of a beam with two lumped masses attached at both ends. The rectangular chassis was made out of aluminium, while the lumped masses were made out of heavier brass to increase the moment of inertia produced by the flywheel element. The lumped masses are attached to the rectangular chassis with four M2.5 socked head cap screws. The dimensions of the flywheel element were optimised in such a way as to maximise the polar moment of

inertia and to sustain the compact dimensions of the inertial actuator. Thus, the length of the flywheel element slightly exceeds the length of the amplified piezoelectric actuator. The weight of the lumped masses was chosen such that the axial inertia effect produced by the flywheel element could reduce the fundamental resonance frequency of the actuator to about 20Hz. This fundamental resonance frequency was chosen so that the piezoelectric inertial actuator could be compared with the electromagnetic configuration described in the previous chapter. Additionally, the dimensions and thus the weight of the lumped masses were chosen such that the centre of flywheel gravity would coincide with the axis defined by two holes where the supporting flexural bearings would be mounted. Figure 4.3 shows the flywheel centre of gravity offset from the axis defined by two holes (defined with the black-white circle) for each specific direction:

X = 0.006 mm (red arrow in the drawing)

Y = 0.000 mm (green arrow in the drawing)

Z =0.000 mm (blue arrow in the drawing)

The two holes that coincide with the flywheel centre of gravity are connected to the yoke bracket via two flexural bearings, while the yoke bracket is connected with the base of the piezoelectric actuator. Thus, in this configuration the mass of the flywheel element is attached to the base mass of the piezoelectric actuator. The other two holes are connected to the top part of the piezoelectric actuator via special connector and are distanced by 5mm from the holes used for flywheel support. The flywheel element was designed with the fixed value of the polar moment of inertia. With the total mass of 24 g, the axial inertia effect produced by the flywheel element is equal to 1.02 kg.

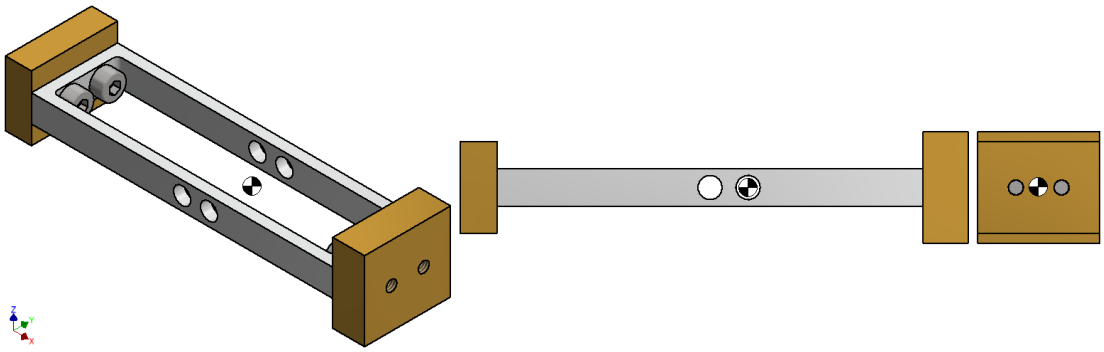

Figure 4.3. Flywheel element with marked centre of gravity.

4.2.2 Assembly process

The assembly process of the flywheel piezoelectric actuator is presented to clarify the development of the prototype. Figure 4.4 shows the exploded CAD view of an actuator with numbered parts. The assembly process of the flywheel piezoelectric actuator is performed in several steps.

Firstly, the APA900M actuator (No. 2) should be glued with the yoke bracket (No. 1). A small grove in the base of the yoke (No. 1) was machined to match exactly the flat surface of the actuator mechanical terminal (No. 2). After placing small amount of glue on the flat surface of the mechanical terminal (No. 2) the actuator can be placed in the grove of the yoke (No. 1). At the same time, the special connector (No. 3) can be glued to the top flat surface of the actuator mechanical terminal (No. 2). The special connector (No. 3) was also fabricated with the small grove on the bottom surfaces. The M2.5 screw (No. 6) should be used to position the connector (No. 3) on the top flat surface of the actuator mechanical terminal (No. 2). Before proceeding to the next phase, it is recommended to wait until the glue dries.

The second step is to attach the chassis (No. 7) to the yoke bracket (No. 1). In order to perform this operation the chassis should be placed between the yoke bracket (No. 1) and the connector (No. 3) so that the holes would coincide. A small amount of glue should be placed on the external, round surfaces of the flexural bearings (No. 4) and then both of them can be pushed through the holes of the yoke bracket (No. 1) and the chassis (No. 7). The flexural bearings (No. 4) that connect the chassis (No. 7) with the actuator connector (No. 3) should be installed exactly in the same way. It is recommended to take a particular care while gluing the components to prevent the situation when the glue might penetrate between the sleeves or leaf springs of the flexural bearings.

Finally, the two lumped masses can be attached to chassis. The heavier and bigger mass (No. 8) should be attached on the side where the flywheel is attached to the yoke brackets. The smaller and lighter mass (No. 9) should be attached closer to the side where the flywheel is attached to the actuator.

The bottom connector is only used to connect the actuator with the measurement equipment (No. 5).

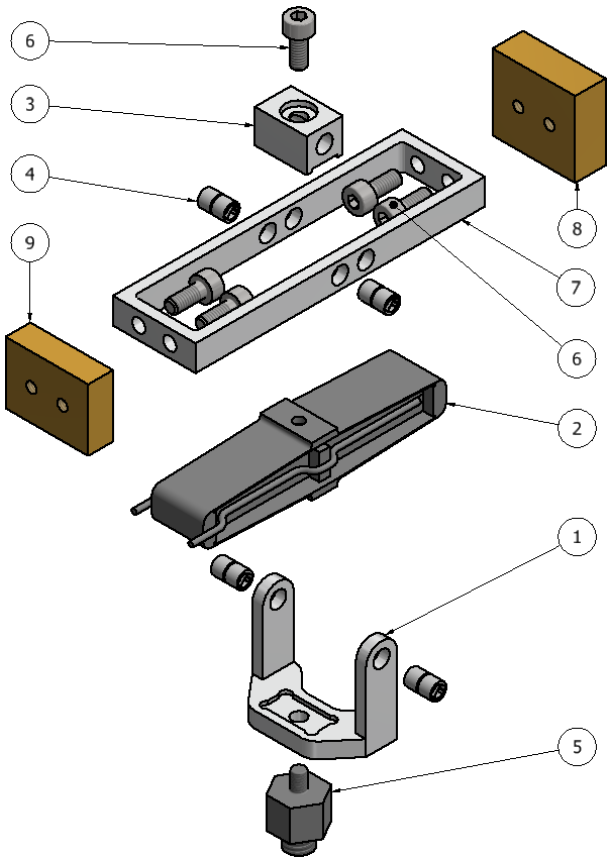

Figure 4.4. Exploded view of the designed flywheel piezoelectric inertial actuator.

4.3 ACTUATORS DESCRIPTION

This section describes the classical and the flywheel proof mass actuators equipped with the amplified piezoelectric stack actuators. Also, it presents the lumped parameter models used to derive the electromechanical frequency response functions that characterise the two actuators. The classical proof mass actuator considered in this study is made with the amplified piezoelectric transducer connected to an inertial mass. This reference proof mass actuator is shown in Figure 4.5a with the lumped element model shown in Figure 4.5c. The classical configuration shown in Figure 4.5a, was equipped with a square metal block that was attached to one end of the transducer to act as a inertial mass M_a. The bottom part of the shell with piezo stacks that is attached to the structure act as a base mass m_b. The stiffness k and damping c of the metal shell are modelled with the spring and dashpot as depicted schematically in Figure 4.5c. The electromechanical effect that produces a pair of reactive forces F_a between the base mass and proof mass of the actuator is modelled in terms of

transduction coefficient ψ_{pzt}, and voltage u_a applied at the electrical terminals of the actuator. The applied voltage u_a and the current i_a flowing in the circuit is proportional to the capacitance C_{pzt} of the piezo stacks. The direct piezoelectric effect produces a voltage u_{pzt}, which is proportional to the relative displacement w_m-w_b between the proof mass and the base mass of the actuator.

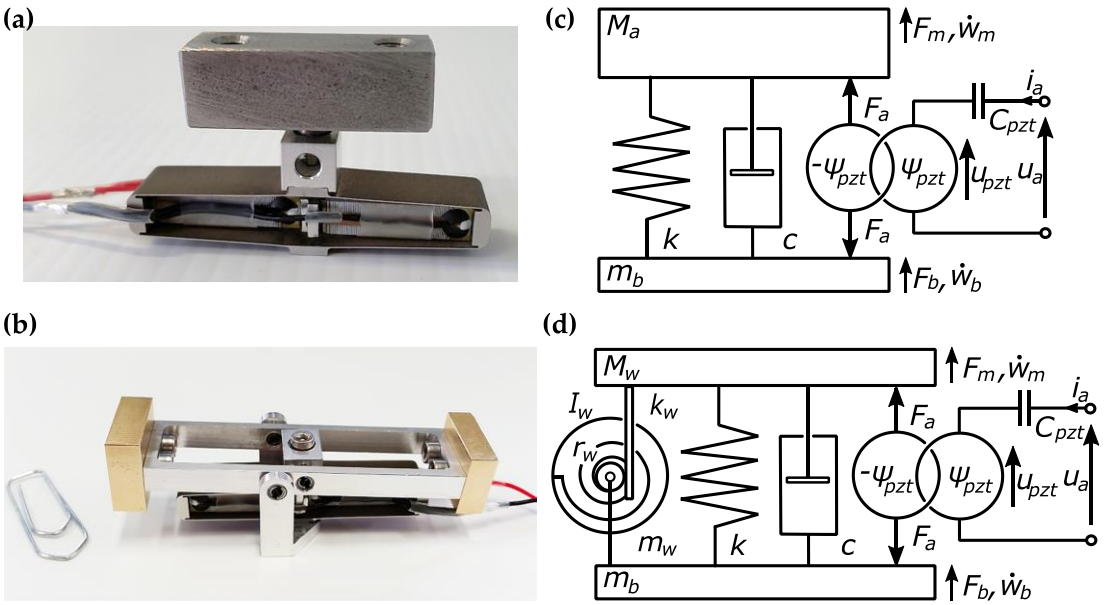

Figure 4.5. Pictures (a,b) and schemes (c,d) of the tested classical (a,c) and the flywheel inertial actuator (b,d).

The flywheel porotype is shown in Figure 4.5b, with the lumped parameter model shown in Figure 4.5d. The additional flywheel element was designed in the form of a beam with two ballasts placed at the far ends of the arm. As can be seen in Figure 4.5b, the shape and the dimensions of the flywheel element were optimised to minimise weight and to maximise the produced polar moment of inertia I_w. The ballasts were designed to ensure that the flywheel centre of gravity is in line with the axis of rotation in the designed bracket support and that the flywheel mass m_w adds to the base mass m_b of the actuator. The produced rotational inertial effect is proportional to the relative axial motion between the base mass m_b and proof mass M_w of the actuator and is transferred with four frictionless pivot bearings of torsional stiffness k_w to the flywheel element. The flywheel element is suspended with two flexural bearings to the designed bracket attached to the base. The other two frictionless pivot bearings connect flywheel element to the top end of the amplified

piezoelectric transducer. The distance between the bearing axis of rotation installed in the brackets and the bearing axis of rotation mounted to the top end of the transducer is the flywheel offset r_w as depicted in Figure 4.5d.

The physical properties of the classical piezoelectric actuator and the flywheel prototype are summarised in Table 4.3. The table specifies the axial inertia I_w / (r_w^2) effect that defines the equivalent inertial mass that would be required to reduce the fundamental resonance frequency of the actuator to the same value as in the flywheel prototype without using the flywheel element.

Table 4.3. Mechanical parameters of the piezoelectric inertial actuators.

Parameter	Value
Inertial mass of the classical actuator	$M_a = 0.039$ kg
Inertial mass of the flywheel actuator	$M_w = 0.013$ kg
Base mass	$m_b = 0.011$ kg
Flywheel mass	$m_w = 0.030$ kg
Total mass of the classical actuator	$M_a + m_b = 0.050$ kg
Total mass of the flywheel actuator	$M_w + m_w + m_b = 0.054$ kg
Axial stiffness	$k = 25600$ Nm^{-1}
Torsional stiffness	$k_w = 0.012$ Nmrad^{-1}
Damping ratio of the classical actuator	$\zeta = 0.0065$
Damping ratio of the flywheel actuator	$\zeta = 0.01$
Flywheel inertia value	$I_w = 2.55 \times 10^{-5}$ kgm^2
Flywheel offset value	$r_w = 0.005$ m
Axial mass effect of the flywheel	$I_w/r_w^2 = 1.02$ kg
Piezo stacks capacitance	$C_{pzt} = 2.25$ µF
Transduction coefficient	$\psi_{pzt} = 0.075$ NV^{-1}

4.4 MATHEMATICAL MODEL

This section presents the mathematical equations based on mobility–impedance formulation [136] used to derive the frequency response functions (FRFs) for the base impedance, electrical admittance and blocked force that characterise the electromechanical response of the classical (Figure 4.5a,c) and flywheel (Figure 4.5b,d) inertial actuators. The piezoelectric inertial actuator studied in this chapter has different electromechanical properties compared to the EM actuator. Thus, a slightly

different mathematical model was derived for the actuators investigated in this chapter.

Considering the lumped parameter models of the classical (Figure 4.5c) and flywheel (Figure 4.5d) inertial actuators, the complex force at the base of the transducer is given with the following impedance relation:

$$F_b = -Z_b \dot{w}_b - Z_a \dot{w}_b + Z_a \dot{w}_m - F_a \,, \tag{4.1}$$

where Z_b is the base mass impedance for the classical (Figure 4.5a) and for the flywheel inertial actuator (Figure 4.5b) given respectively by:

$$Z_b = j\omega m_b \quad , \quad Z_b = j\omega(m_b + m_w) \,. \tag{4.2}$$

Also Z_a are the transducer suspension system impedances for the classical and proposed flywheel inertial transducer given respectively by:

$$Z_a = c + \frac{k}{j\omega} \quad , \quad Z_a = c + \frac{k}{j\omega} + j\omega \frac{I_w}{r_w^2} + \frac{k_w}{j\omega r_w^2} \,, \tag{4.3}$$

where the damping is defined as $c = \zeta 2\sqrt{M_a k}$ for the classical actuator and $c = \zeta 2\sqrt{(M_a + I_w/r_w^2)(k + k_w/r_w^2)}$ for the flywheel actuator. The force generated by the piezoelectric stack is given by:

$$F_a = \psi_{pzt} Z_e i_a \,, \tag{4.4}$$

where Z_e is the electrical impedance of the piezoelectric stack given by:

$$Z_e = \frac{C_{pzt}}{j\omega} \,. \tag{4.5}$$

The complex force acting on the inertial mass of the transducers can be expressed with the following impedance relation:

$$F_m = Z_a \dot{w}_b - Z_a \dot{w}_m + F_a \,. \tag{4.6}$$

The complex velocity of the inertial mass is given by the following mobility relation:

$$\dot{w}_m = Y_m F_m \,, \tag{4.7}$$

where Y_m is the inertial mass mobility for the classical (Figure 4.5a) and for the flywheel inertial actuator (Figure 4.5b) given respectively by:

$$Y_m = \frac{1}{j\omega M_a} \quad , \quad Y_m = \frac{1}{j\omega(M_w)} \,. \tag{4.8}$$

Finally, the complex voltage at the terminals of the piezoelectric transducer is given by:

$$u_a = Z_e i_a + Z_e \psi_{pzt} \dot{w}_b - Z_e \psi_{pzt} \dot{w}_m \,. \tag{4.9}$$

Substituting Equation (4.4) into Equation (4.6) and then the resulting equation into Equation (4.7) the velocity of the inertial mass is given by:

$$\dot{w}_m = \frac{Y_m Z_a}{1 + Y_m Z_a} \dot{w}_b + \frac{Y_m Z_e \psi_{pzt}}{1 + Y_m Z_a} i_a \,. \tag{4.10}$$

Substituting Equation (4.4) and Equation (4.10) into Equation (4.1) the force acting at the base mass is given by:

$$F_b = -\frac{Z_b + Z_b Y_m Z_a + Z_a}{1 + Y_m Z_a} \dot{w}_b - \frac{Z_e \psi_{pzt}}{1 + Y_m Z_a} i_a \,, \tag{4.11}$$

where

$$Z_{f\dot{w}} = \left.\frac{-F_b}{\dot{w}_b}\right|_{i_a = 0} = Z_b + \frac{Z_a}{1 + Y_m Z_a} \tag{4.12}$$

is the mechanical impedance of the open circuit transducer and

$$T_{fi} = \left.\frac{F_b}{i_a}\right|_{\dot{w}_b = 0} = -\frac{Z_e \psi_{pzt}}{1 + Y_m Z_a} \tag{4.13}$$

is the electromechanical coupling coefficient, which gives the produced force per unit current for the transducer with the blocked base. Substituting Equation (4.10) into Equation (4.9) the driving current of the piezoelectric transducers is given by:

$$i_a = \frac{1 + Y_m Z_a}{Z_e + Z_e Y_m Z_a - Z_e \psi_{pzt} Y_m Z_e \psi_{pzt}} u_a - \frac{\psi_{pzt}}{1 + Y_m Z_a - \psi_{pzt} Y_m Z_e \psi_{pzt}} \dot{w}_b \,, \tag{4.14}$$

where

$$Y_{iu} = \left.\frac{i_a}{u_a}\right|_{\dot{w}_b = 0} = \frac{1 + Y_m Z_a}{Z_e + Z_e Y_m Z_a - Z_e \psi_{pzt} Y_m Z_e \psi_{pzt}} \tag{4.15}$$

is the electrical admittance of the transducer with the blocked base. Substituting Equation (4.14) into Equation (4.11)the force acting at the base mass is given by:

$$\begin{aligned} F_b = &\left(-Z_b - \frac{Z_a}{1 + Y_m Z_a} + \frac{Z_e \psi_{pzt} \psi_{pzt}}{(1 + Y_m Z_a)\left(1 + Y_m Z_a - \psi_{pzt} Y_m Z_a\right)}\right) \dot{w}_b \\ &- \frac{\psi_a}{1 + Y_m Z_a - \psi_{pzt} Y_m Z_e \psi_{pzt}} u_a \,, \end{aligned} \tag{4.16}$$

where

$$Z_{f\dot{w}} = \frac{-F_b}{\dot{w}_b}\bigg|_{u_a=0} = Z_b + \frac{Z_a}{1+Y_m Z_a} - \frac{Z_e \psi_{pzt} \psi_{pzt}}{(1+Y_m Z_a)\left(1+Y_m Z_a - \psi_{pzt} Y_m Z_a\right)} \quad (4.17)$$

is the mechanical impedance of the short circuit transducer and

$$T_{fi} = \frac{F_b}{u_a}\bigg|_{\dot{w}_b=0} = \frac{-\psi_{pzt}}{1+Y_m Z_a - \psi_{pzt} Y_m Z_e \psi_{pzt}} \quad (4.18)$$

is the electromechanical coupling coefficient, which gives the produced force per unit voltage applied to the transducer with the blocked base.

4.5 EXPERIMENTAL TESTS

The following subsections contrast the measured and simulated base impedance, blocked force and electrical admittance of the classical and flywheel piezoelectric actuators. The FRFs are depicted in form of matrix of plots where the left hand side plots show the measured (solid blue lines) and simulated (dash-dotted red lines) results of the classical actuators while the right hand side plots show the measured (solid blue lines) and simulated (dash-dotted red lines) results of the flywheel actuator.

4.5.1 Mechanical impedance of the open circuit transducer

Figure 4.6 shows scheme (Figure 4.6a) and picture (Figure 4.6b) of the base impedance test setup. The electrical terminals of the inertial actuators were in the open circuit configuration during tests. The tested actuators were mounted on a shaker as shown in Figure 4.6b. The shaker was excited with a sine logarithmic sweep signal up to 1kHz. Two parameters were measured during tests using signal analyser. Input channel A measured force excreted to the actuator base while input channel B measured the base acceleration. As shown in Figure 4.6b, the impedance head mounted between shaker and the actuator measured simultaneously force and acceleration. The shaker amplifier was used to drive the shaker with required excitation signal. Appendix D lists equipment used in the measurements of the transducer elecromechanical properties.

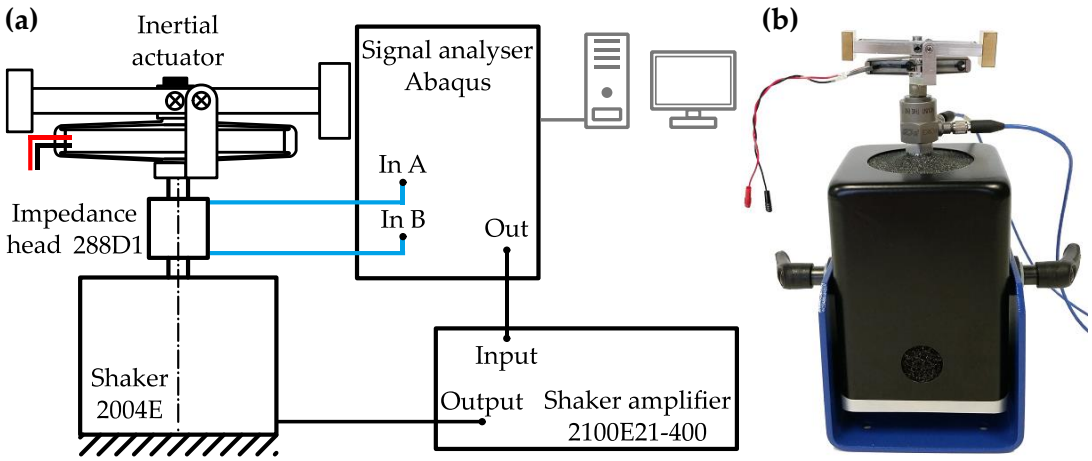

Figure 4.6. Scheme (a) and picture (b) of the base impedance test with the actuator electrical terminals in open circuit.

The Bode plots in Figure 4.7 show the base impedance FRFs of the open circuit classical and flywheel configurations of the proof mass actuators as given in Equation (4.12). The plots in Figure 4.7a show the results for the classical configuration while the plots in Figure 4.7b show the results for the flywheel configuration.

The base impedance of the open circuit classical actuator simulation shown in the modulus plot of Figure 4.7a is characterised by low and high frequency mass-laws separated by a resonance peak and an antiresonance low. The resonance peak of the classical actuator is at about 129Hz while the antiresonance low at about 275Hz. The low frequency asymptote is proportional to the total mass ($M_a + m_b$) while the high frequency asymptote is proportional to base mass (m_b) of the proof mass actuator. The phase of the base impedance shown in lower plot of Figure 4.7a is characterised by two shifts. At resonance frequency of about 129Hz, the base impedance phase shifts from +90° to -90° whereas at antiresonance frequency of about 275Hz, the phase shifts back from -90° to +90°. The full phase shift (+90° to -90°) and sharp resonance peak and antiresonance low indicates that the classical piezoelectric actuator is lightly dampened and thus is characterised by a high quality factor ($Q = 1/2\zeta$). The measured base impedances of the open circuit classical configuration agree well with the simulated value. However, the antiresonance low is pushed to lower value of 236 Hz due to the additional peak that appears at about 290 Hz. Most probably, the additional peak is caused by a higher flexible mode of the ceramics installed in the shell.

The base impedances of the open circuit flywheel prototype shown in Figure 4.7b presents similar characteristic to the classical configuration, apart from small

differences. Firstly, the flywheel axial inertia effect (I_w/r_w^2) shifts the fundamental resonance frequency to a lower value at about 25 Hz while the antiresonance low at about 25.5 Hz. The sky-hook stiffness effect in between the resonance and antiresonance frequency is nearly cancelled. Secondly, the amplitude of the higher frequency asymptotic mass behaviour is increased because of the additional axial inertia effect ($m_b + m_w + I_w/r_w^2$) produced by the flywheel element. However, the amplitude of the lower frequency asymptotic mass behaviour has not changed because the classical and flywheel actuators have nearly equal weight. Finally, the internal damping effect in the inertial actuator is also increased, such that the resonance peak and antiresonance through are rounded. The increase of the internal damping effect is also observed in the phase diagrams. The phase presented in the lower diagram of Figure 4.7b shifts only by couple of degrees between +90° to around +81°. The experimental results align well with the simulated open circuit base impedance FRF. Exactly as for the classical configuration, also for the flywheel prototype there is an additional peak that appears at about 290 Hz. In the experimental results there are two additional peaks that appear at 680 Hz and 780 Hz. Most probably, the dynamics of the flywheel mechanism causes these peaks.

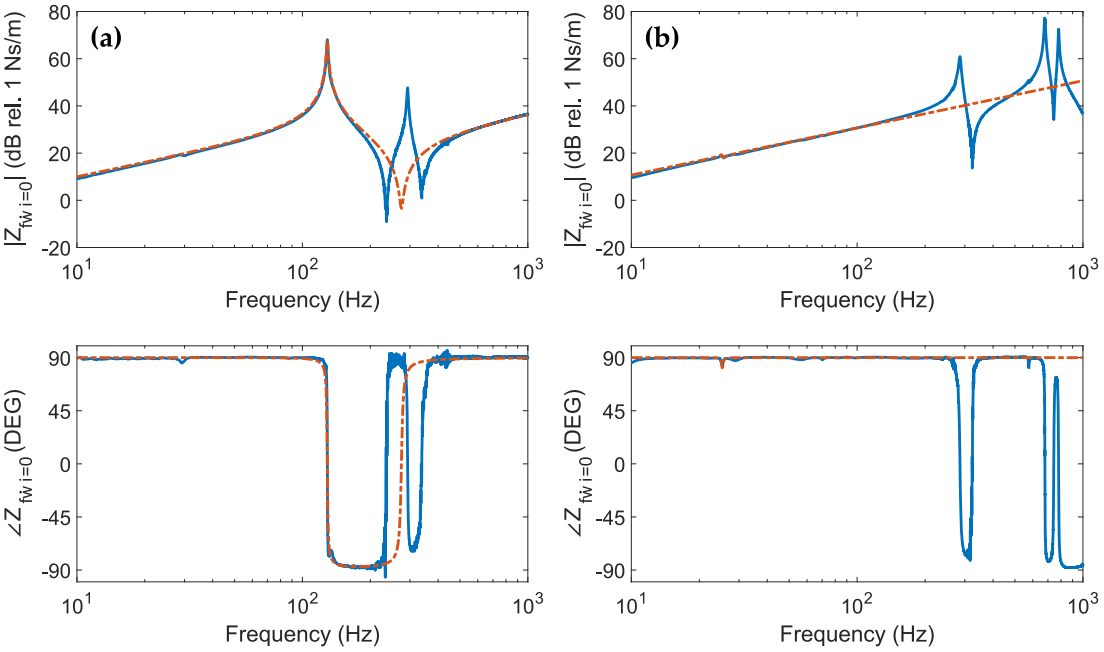

Figure 4.7. Base impedance of the actuators with the electrical terminals in open circuit: (a) classical configuration, (b) flywheel prototype. Experimental results (solid blue lines) and numerical simulations (dashed-dotted red lines).

4.5.2 Mechanical impedance of the short circuit transducer

Figure 4.8 shows scheme (Figure 4.8a) and picture (Figure 4.8b) of the base impedance test setup with the actuator electrical terminals in short circuit. The tested actuators were mounted on a shaker as shown in Figure 4.8b. The shaker was excited with a sine logarithmic sweep signal up to 1kHz. Two parameters were measured simultaneously during tests using signal analyser. As shown in Figure 4.8b, the impedance head mounted between shaker and the actuator measured simultaneously force and acceleration. Input channel A measured force excreted to the actuator base while input channel B measured the base acceleration. The shaker amplifier was used to drive the shaker with required excitation signal. Appendix D lists equipment used in the measurements of the transducer elecromechanical properties.

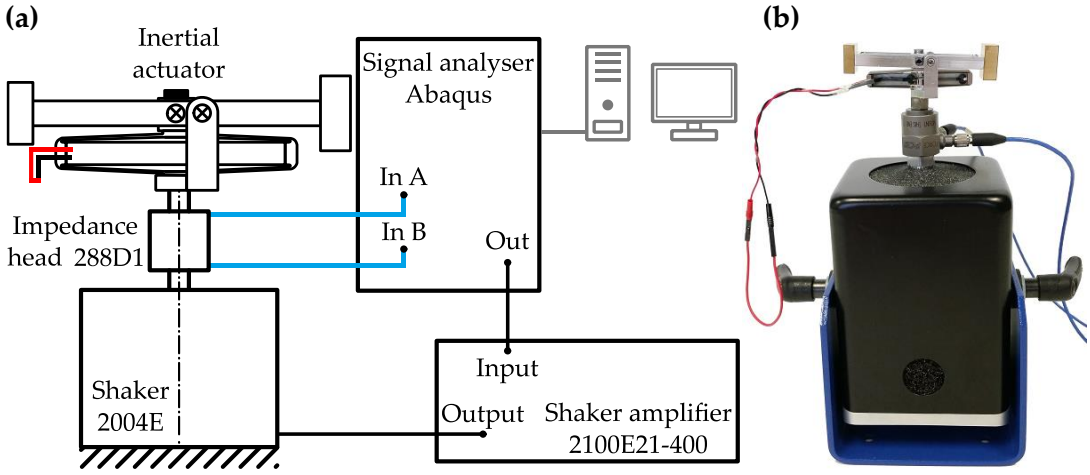

Figure 4.8. Scheme (a) and picture (b) of the base impedance test with the actuator electrical terminals in short circuit.

The Bode plots in Figure 4.9 show the base impedance FRFs of the short circuit classical and flywheel configuration of the proof mass actuators as given in Equation (4.17). The plots in Figure 4.9a show the results for the classical configuration while the plots in Figure 4.9b show the results for the flywheel configuration.

The base impedance of the short circuit classical actuator shown in Figure 4.9a presents similar characteristics to the results obtained for the open circuit transducer. The main difference is that the resonance peak and antiresonance low are shifted to lower frequencies. Since the piezo ceramics is a dielectric medium, the strains and stresses in the material are strongly related to the electrical field. The free flow of electrons and lack of the generated electrical field in the short circuit configuration

makes the ceramics slightly softer compared to the configuration with open circuit. The resonance peak of the classical actuator is at about the fundamental resonance frequency of 123 Hz while the antiresonance low at about 261 Hz. The phase of the base impedance shown in phase plot of Figure 4.9a is characterised by the shift from +90° to -90° at the resonance frequency and a shift from -90° to +90° at the antiresonance frequency. The measured base impedances of the closed circuit classical configuration agree well with the simulated value. As found for the base impedance with the open circuit transducer, also here the antiresonance low is pushed to a lower value of 224 Hz due to the additional peak that appears at about 290 Hz.

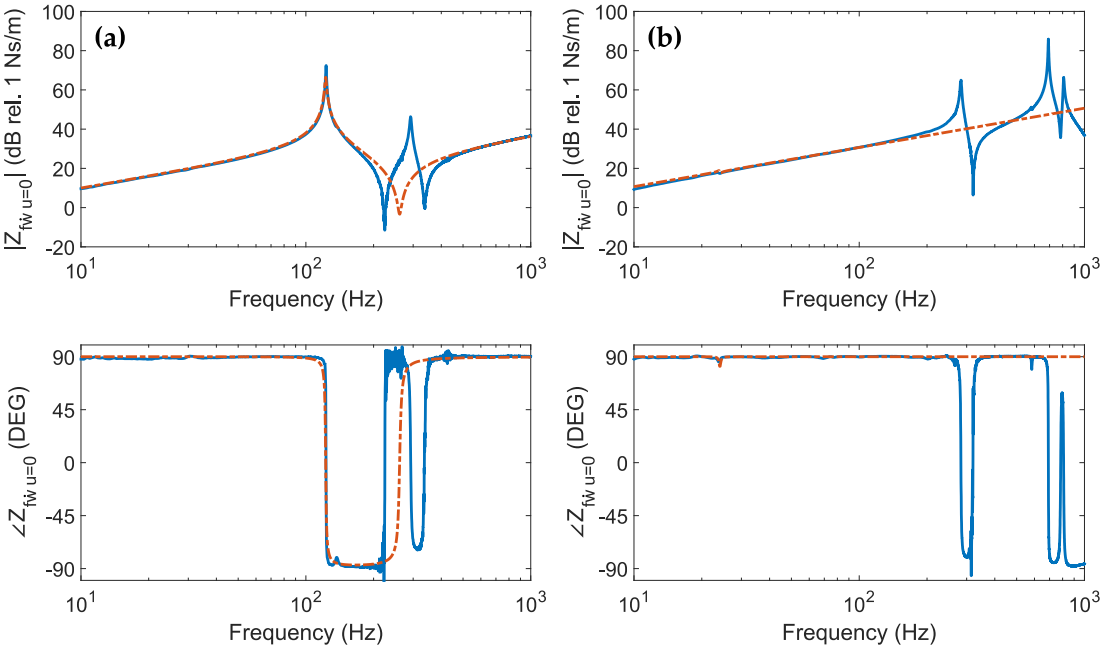

Figure 4.9. Base impedance of the actuators with the electrical terminals in short circuit: (a) classical configuration, (b) flywheel prototype. Experimental results (solid blue lines) and numerical simulations (dashed-dotted red lines).

The base impedances of the short circuit flywheel prototype shown in Figure 4.9b presents similar characteristics to those obtained for the transducer in open circuit. The flywheel axial inertia effect (I_w/r_w^2) shifts the fundamental resonance frequency to about 24 Hz and the antiresonance low to about 24.5Hz. The amplitude at the resonance peak is nearly the same as for the open circuit configuration with the shift form +90° to around +81° as shown in lower plot of Figure 2b. The experimental results align well with the simulated short circuit base impedance FRF. Also in this

case there is an additional peak that appears at about 290 Hz. The experimental results show two additional peaks that appear at about 690 Hz and 810 Hz caused by the higher dynamics of the flywheel mechanism.

4.5.3 Blocked force for current driven actuator

Figure 4.10 shows the scheme (Figure 4.10a) and picture (Figure 4.10b) of the blocked force test setup for the current driven inertial actuator. During tests, the actuator was attached to a rigid base via a force cell as shown in Figure 4.10b. Two parameters were measured during tests using signal analyser. Channel input A measured force excreted to the actuator base while input B measured the current fed to the actuator. The T-500 amplifier was used to drive the piezoelectric actuators. Appendix D lists all the equipment used in the measurements of the transducer elecromechanical properties.

(a)

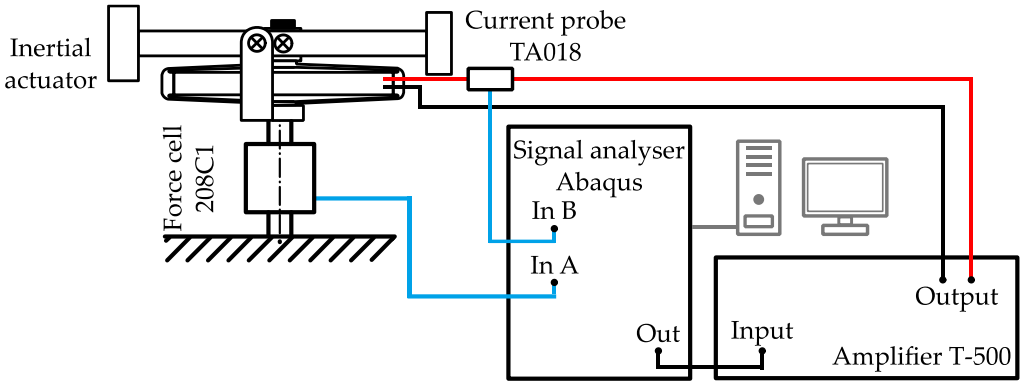

(b)

Figure 4.10. Scheme (a) and picture (b) of the blocked force per unit current fed to the actuator test setup.

The Bode plots in Figure 4.11 show the blocked force FRFs per unit current fed to the classical and flywheel configurations of the proof mass actuators as given in Equation (4.13). The plots in Figure 4.11a show the results for the classical configuration while the plots in Figure 4.11b show the results for the flywheel configuration.

Considering first the bode plot shown in Figure 4.11a for the classical transducer, at low frequencies the blocked force per unit current fed to the transducer rises proportionally with frequency and has phase -90°. At the resonance peak, the blocked force effect reaches maximum value and undergoes a -180° lag as show in the phase plot of Figure 4.11a. The resonance peak of the classical actuator is at about 129 Hz, as found for the base impedance measurement assuming open circuit transducer. At frequencies above the resonance peak, the blocked force drops proportionally with frequency. The measured blocked force per unit current fed to the actuator of the classical configuration agree well with the simulated value. Also with the blocked force measurements, an additional peak appears at about 290 Hz.

The blocked force per unit current fed to the flywheel prototype shown in Figure 4.11b presents similar characteristic to the classical configuration. The flywheel element axial inertia effect (I_w / (r_w^2)) shifts the fundamental resonance frequency to a lower value of about 25 Hz, similarly to the result for the base impedance assuming open circuit transducer. In comparison to the classical configuration, the blocked force is reduced by about 30 dB at the resonance peak and by about 40 dB at frequencies above the resonance peak. Because of this reduction, the additional peak that appears at 290 Hz seems to be much sharper compared to the results for the classical configuration. However, in both measurement the peak at 290 Hz has similar amplitude. The additional dynamics of the flywheel element appear at 680 Hz and at 740 Hz as for the base impedance measurements.

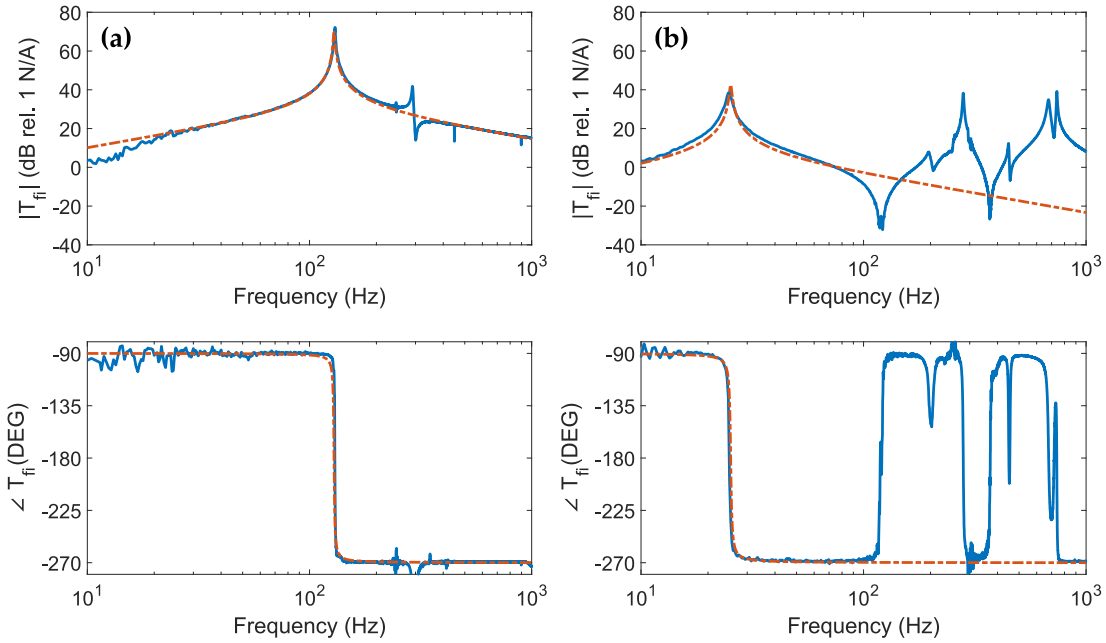

Figure 4.11. Blocked force for current driven actuators: (a) classical configuration, (b) flywheel prototype. Experimental results (solid blue lines) and numerical simulations (dashed-dotted red lines).

4.5.4 Blocked force for voltage driven actuator

Figure 4.12 shows scheme (Figure 4.12a) and picture (Figure 4.12b) of the blocked force per unit applied voltage applied to the actuator test setup. During tests, the actuator was attached to a rigid base via a force cell as shown in Figure 4.12b. Two parameters were measured during tests using signal analyser. Input channel A measured force excreted to the actuator base while input channel B measured applied voltage to the actuator. The T-500 amplifier was used to drive the piezoelectric actuators. Appendix D lists equipment used in the measurements of the transducer elecromechanical properties.

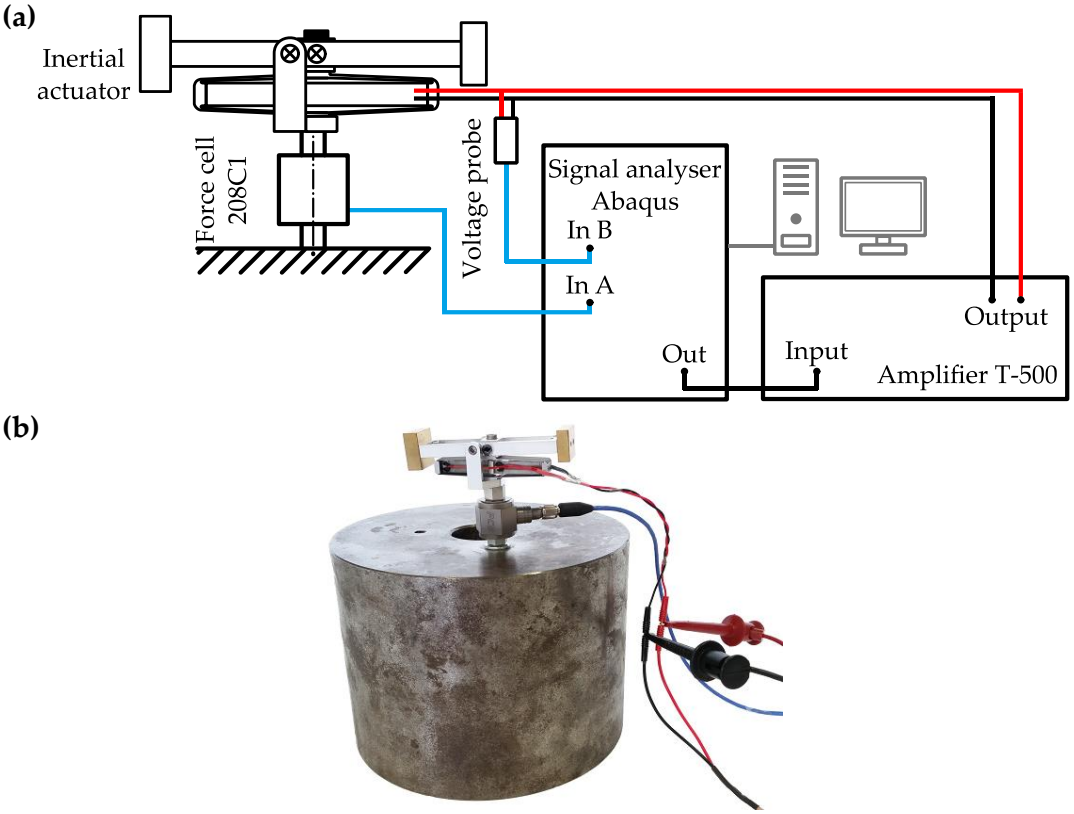

Figure 4.12. Scheme (a) and picture (b) of the blocked force per unit voltage applied to the actuator test setup.

The Bode plots in Figure 4.13 show the blocked force per unit voltage fed to the classical and flywheel configurations of the proof mass actuator as given in Equation (4.18). The plots in Figure 4.13a show the results for the classical configuration while the plots in Figure 4.13b show the results for the flywheel configuration.

Considering the plot for the classical transducer, at low frequencies the blocked force per unit voltage applied to the transducer rises proportionally with frequency and has phase at 0°. At the resonance peak, the blocked force effect reaches maximum value and undergoes a -180° lag. The fundamental resonance peak is at about 122 Hz, as found in the measured base impedance FRF for the short circuit transducer. At frequencies above the resonance peak, the blocked force approximates to a constant value equal to the transduction coefficient ψ_{pzt} of the transducer. As mentioned in the actuator description, the amplified piezoelectric transducer works as a pulling actuator thus the phase is opposite to the applied voltage signal. The measured blocked force per unit voltage applied to the actuator of the classical configuration agrees well with the simulation results. An additional peak appears at about 290 Hz as found in the measurements of the previous electromechanical properties.

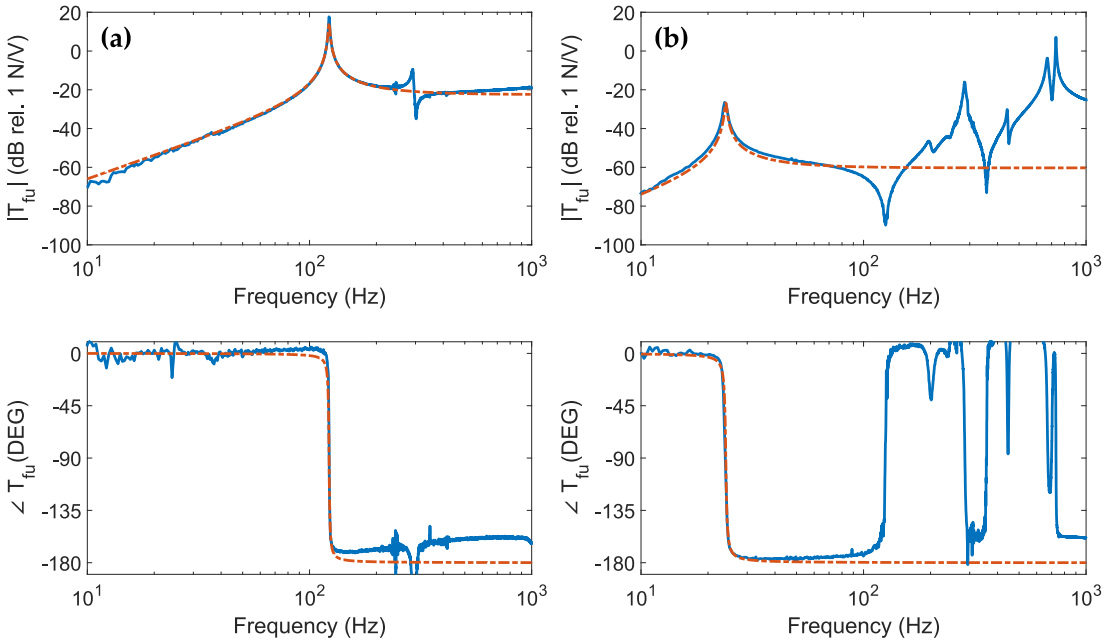

Figure 4.13. Blocked force for voltage driven actuators: (a) classical configuration, (b) flywheel prototype. Experimental results (solid blue lines) and numerical simulations (dashed-dotted red lines).

The blocked force per unit voltage fed to the flywheel prototype shown in Figure 4.13b presents similar characteristic to that of the classical configuration. The flywheel axial inertia effect (I_w / (r_w^2)) shifts the fundamental resonance frequency to a lower value at about 24 Hz, as found for the base impedance FRF of the short circuit transducer. Compared to that of the classical configuration, the blocked force is reduced also in amplitude by about 40 dB. The additional peak above the fundamental resonance frequency appears at about 290 Hz and has similar amplitude compared to that of the classical configuration. The higher order dynamic effects of the flywheel element appear at 670 Hz and 730 Hz. Thus, these effects limit the frequency range for the active vibration control system.

The FRFs presented in this and previous subsections suggest that when the actuator is driven with constant current, the point force produced above the fundamental resonance frequency of the actuator tends to decrease with frequency. In contrast, when the actuator is driven with constant voltage, the point force produced by the inertial actuator above the fundamental resonance frequency of the actuator remains constant with frequency. Thus, for the implementation of a uniform velocity feedback control, it is preferable to implement voltage driven control.

4.5.5 *Electrical admittance*

Figure 4.14 shows scheme (Figure 4.14a) and picture (Figure 4.14b) of the electrical admittance test setup. The tested actuators were attached to a rigid base. Two parameters were measured during tests using signal analyser. Input channel A measured voltage at the electrical terminals of the actuator while input B measured current fed to the actuator. The T-500 amplifier was used to drive the piezoelectric actuators. Appendix D lists all the equipment used in the measurements of the transducer elecromechanical properties.

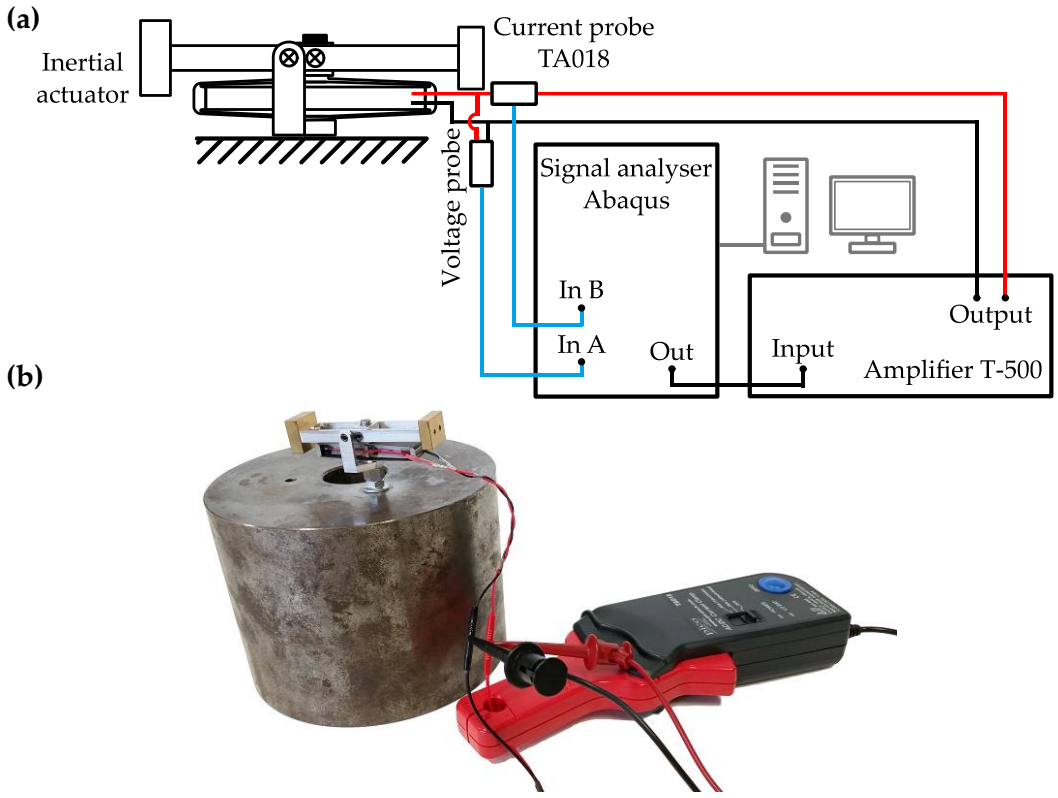

Figure 4.14. Scheme (a) and picture (b) of the electrical admittance test setup.

The Bode plots in Figure 4.15 show the electrical admittance of the classical and flywheel proof mass actuators as given in Equation (4.15). The plots in Figure 4.15a show the results for the classical configuration while the plots in Figure 4.15b show the results for the flywheel configuration

The Bode plot of the electrical admittance FRF for the classical configuration shown in Figure 4.15a is characterised by low and high frequency asymptotes with phase at +90° separated by a sharp peak and antiresonace low where the phase shifts

from +90° to about -70° and finally returns to +90°. The sharp resonance peak is at about 122 Hz that is resonance frequency of the short circuit transducer. The aniresonance low is at about 129 Hz that is the resonance frequency of the open circuit transducer. The low and high frequency asymptotes rise proportionally to the transducer piezo capacitance. At the resonance frequencies of the transducer, the electrical admittance has phase equal to 0°, that is the driving current is in phase with the voltage. The measured electrical admittance of the classical configuration agrees well with the simulation results.

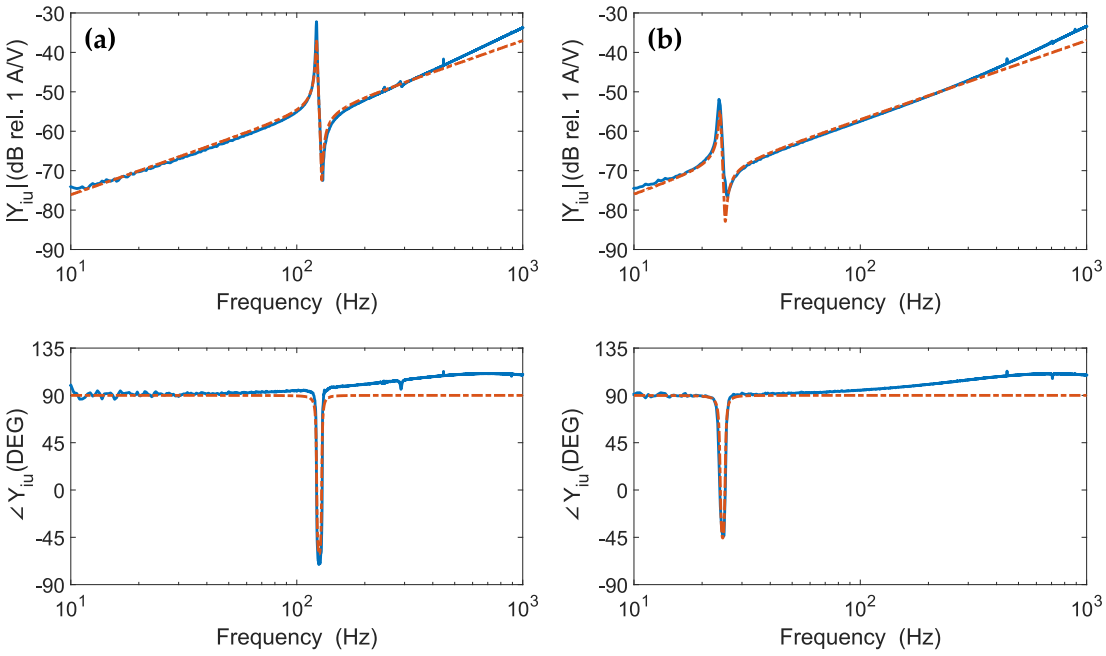

Figure 4.15. Electrical admittance of (a) classical configuration and (b) flywheel prototype. Experimental results (solid blue lines) and numerical simulations (dashed-dotted red lines).

The electrical admittance of the flywheel prototype shown in Figure 4.15b is very similar to the classical configuration, since the two transducers are made with identical piezo component. The principal difference remains in the lower resonance frequency due to the additional mass effect produced by the flywheel axial inertia effect (I_w / (r_w^2)). The sharp resonance peak at about 24 Hz is the resonance frequency of the short circuit transducer, while the aniresonance low at about 25 Hz is the resonance frequency of the open circuit transducer. The phase falls from +90° to about -45° at the resonance frequency and finally returns to +90° at the aniresonance frequency. The measured electrical admittance of the flywheel configuration agrees

well with the simulation results. The numerical and experimental results show that for the given driving voltage the transducers require higher currents at high frequencies. Thus to control the vibrations at high frequencies this type of inertial actuator requires amplifier that can provide large power.

4.6 CHAPTER CONCLUSIONS

This chapter has presented simulation and experimental results that characterise the electromechanical FRFs of a classical and flywheel piezoelectric proof mass actuator, which can be used to implement a velocity feedback loop to reduce the flexural vibration of large flexible structures. The study has considered the mechanical base impedance, the blocked force and the electrical admittance FRFs. The experimental testes were matched with numerical results derived from a new lumped parameter model, which included a dedicated flywheel element connected to the piezoelectric transducer. The results for the flywheel configuration were compared with those obtained for an amplified piezoelectric transducer equipped with additional inertial mass element.

The results have shown reasonably good agreement between the measured and simulated FRFs, both for the classical and the flywheel proof mass actuators. The results show that the flywheel element can be used to reduce the fundamental resonance frequency of the actuator without increasing the total weight of the suspended mass. Moreover, the flywheel element can be optimised to obtain compact shape and dimensions.

The blocked force study has shown that the piezoelectric actuators should not be used in velocity feedback system where the actuator is driven with a current signal. In this case, above the transducer fundamental resonance frequency, the produced blocked force per unit current fed to the actuator decrees causing the control system to be less effective at higher frequencies. Instead, the piezoelectric actuator should be driven with a voltage signal.

The electrical admittance study has shown that the actuators can be used in a wide frequency range. However, for the voltage driven actuator the required current rises proportionally to the piezo capacitance and driving frequency. Thus, to efficiently control the structure at higher frequencies the inertial actuators would require amplifiers that can provide high power.

This chapter has also presented the advantages of the piezoelectric proof mass actuator over the classical electromagnetic solution used in active vibration control systems. The piezoelectric actuators can be more compact and do not generate magnetic flux. Piezoelectric actuators with switching amplifiers present very high efficiency and use less power compared to the electromagnetic actuators. Additionally, the capacitive effect of the piezoelectric material can be used in power recovery systems of the switching amplifiers. This system could be easily reconfigured for the energy harvesting applications of the vibration structures. Compared to piezoelectric patches, the amplified piezoelectric transducer considered in this study provides higher displacements that can be efficiently used to produce large point forces via the oscillations of the inertial mass.

The experimental results obtained with the prototype actuator have shown that the flywheel element induces additional dynamic in the actuator. Thus, a velocity feedback loop with the proposed flywheel piezoelectric actuator could be implemented in narrow and low frequency band.

5

ACTIVE VIBRATION CONTROL

This section presents the test setup and models used to evaluate the stability and control performance of a velocity feedback loop implemented on thin rectangular plate using inertial EM actuators. The stability and control performance of the control system is assessed using the classical, classical with the same inertial mass as the flywheel configuration and the pinned configuration of the flywheel inertial actuator. The results presented in the previous chapters for the electromechanical properties of the inertial actuators showed that the flexural bearings used in the pinned configuration minimise the nonlinear effects and reduce the backlash effects that could introduce stability issues. Thus, the hinged configuration of the flywheel inertial actuator was excluded from this study.

5.1 EXPERIMENTAL SETUP

A special experimental setup was designed to test the velocity feedback loops with the inertial EM actuators. Figure 5.1 shows the fabricated test setup with a supported rectangular plate. The structure was designed for multipurpose use and can be adapted for measurements in horizontal and vertical orientations. The base of the test setup was fabricated out of concrete material sealed in a metal frame. Heavy base prevents the setup from any undesired oscillations during measurements by lowering the amplitude of the rigid body modes. A multipurpose aluminium profile was immersed in the concrete base and can be used to attach various equipment. The chassis attached to the concrete base was designed with triangle sidewalls to reduce the vibrations in parallel direction to the out-of-plane axis of the plate. The construction of the chassis allows to approach the plate from both sides. A T-slot support was mounted inside the chassis, which is used to attach the excitation shakers. The level at which the T-slot support is mounted can be easily changed allowing to define any excitation position over the surface of the plate. Finally, the investigated plate is mounted between top and bottom frames that are attached to the

chassis. A large number of M10 bolts guarantee that the clamping force is evenly distributed. A thin layer of soldering wire was distributed between the frame and the steel plate to mimic a simply supported boundary condition. However, the preliminary tests showed that the simulation results match better the experimental results when the natural frequencies of the plate are calculated for the clamped boundary condition as given in Equation (2.9). The technical drawings of the manufactured structure used for implementation of the active control system are presented in appendix C.

Figure 5.1. Test setup with a rectangular plate for the implementation of the velocity feedback loop system with inertial actuators.

The picture and schematic model of the velocity feedback loop system implemented on the rectangular plate is shown in the Figure 5.2. The tested actuator is attached on one side of the rectangular panel. The panel is excited by a point force produced by a shaker located on the other side of the panel. The error signal is measured with a small accelerometer sensor that is attached on the same side of the panel as the shaker, exactly underneath the actuator position. The mechanical properties of the rectangular panel and location of the actuator and primary force are specified in Table 5.1.

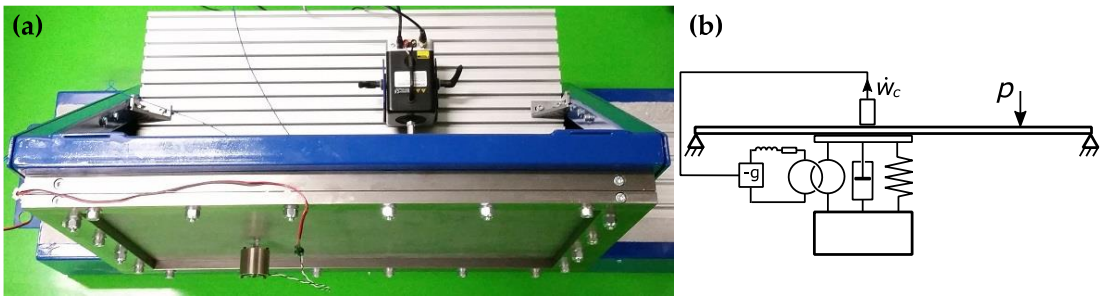

Figure 5.2. Picture (a) and scheme (b) of a rectangular plate with a velocity feedback control loop system using the inertial actuators. The picture clearly shows the shaker used to excite the plate with point force and the control inertial actuator attached to the plate. The small accelerometer sensor was installed on the shaker side as shown in the scheme (b).

Table 5.1. Mechanical parameters of the thin rectangular plate used for the inmplemantation of the velocity feedback control system.

Parameter	**Value**
Length	$l_x = 0.668$ m
Width	$l_y = 0.444$ m
Thickness	$h = 0.00137$ m
Mass density	$\rho = 8200\ \mathrm{kgm^{-3}}$
Elastic modulus	$E = 210 \times 10^9\ \mathrm{Nm^{-2}}$
Poisson ratio	$\nu = 0.31$
Damping ratio	$\zeta_s = 0.0035$
Position of the actuator	$(x_c, y_c) = (0.234\ \mathrm{m}, 0.178\ \mathrm{m})$
Position of the primary force	$(x_p, y_p) = (0.433\mathrm{m}, 0.157\ \mathrm{m})$

The velocity feedback control loop was implement with an analogue conditioner that filters and integrates the signal obtained from the accelerometer. The output velocity signal is send back to the actuator via a voltage operational amplifier that also increases the gain of the error signal. The stability of the velocity feedback loops using the classical configuration, the classical with the same inertial mass as the flywheel configuration and the pinned flywheel inertial actuator is assessed using the Nyquist criterion based on the open loop sensor – actuator frequency response function. The performance of the feedback loops has been assessed considering the velocity at the control position and the total flexural kinetic energy of the hosting plate. The experimental results are compared with numerical simulations obtained

from the lumped parameter model of the actuators located on the rectangular panel derived in chapter two of this thesis.

5.2 OPEN LOOP STABILITY ANALYSIS FOR THE CURRENT DRIVEN ACTUATOR

Figure 5.3 shows scheme (Figure 5.3a) and picture (Figure 5.3b) of the open loop sensor – actuator FRF test setup for the current driven inertial actuator. During tests, the actuator was attached to a rectangular plate as show in Figure 5.3b. Two parameters were measured during tests using signal analyser. Input channel A measured acceleration at the base footprint of the actuator while input channel B measured current fed to the actuator. The quad amplifier was used to drive the

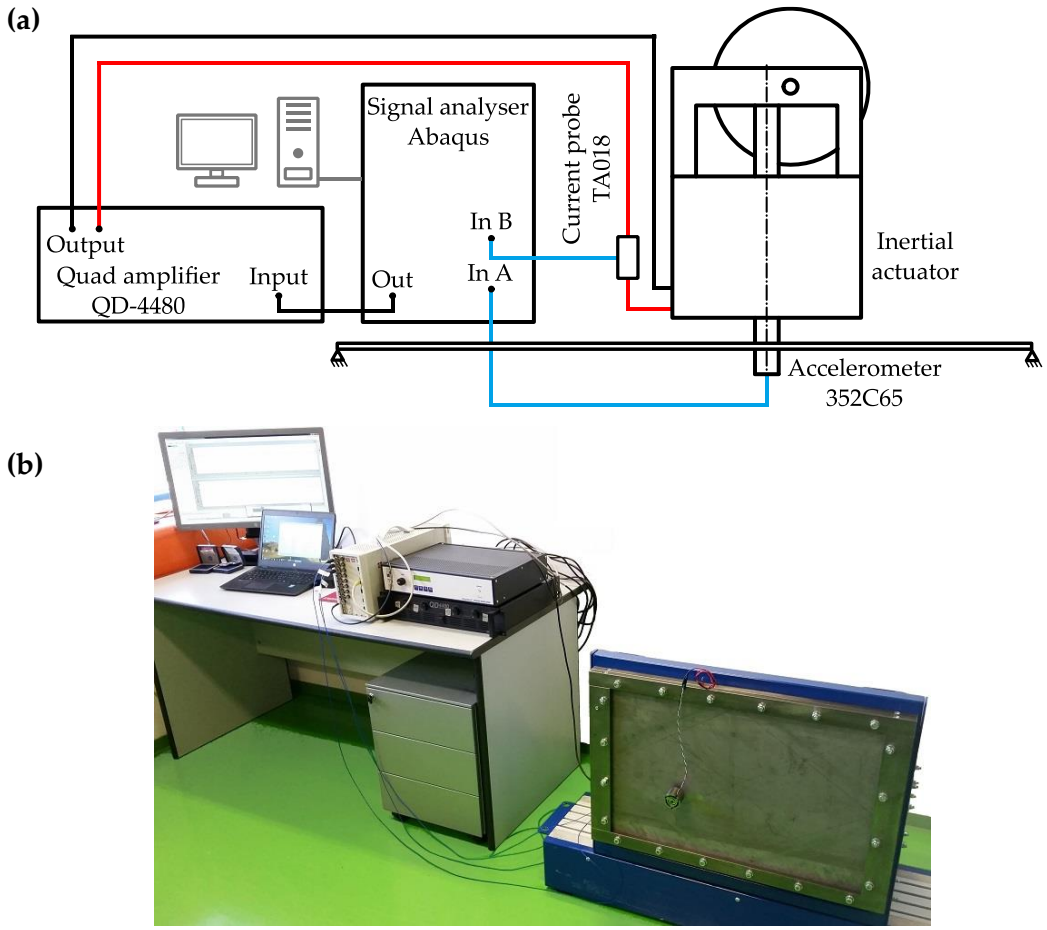

Figure 5.3. Scheme (a) and picture (b) of the open loop sensor – actuator FRF test setup for the current driven inertial actuator.

actuator with a 1kHz random excitation signal generated by the signal analyser. Appendix D lists all the equipment used in the measurements.

The stability of the velocity feedback loops using the classical, classical with the same inertial mass as the flywheel configuration and the pinned flywheel inertial actuator is assessed using the Nyquist criterion. Figure 5.4 shows the Bode diagram of the open loop sensor – actuator frequency response function for the classical actuator. The top plot in Figure 5.4 shows the modulus diagram while the bottom plot shows the phase diagram of the actuator open loop FRF for the current driven classical actuator. The solid blue lines in the plots present the measurement results, while the dashed-dotted red lines present the simulation results of the open loop sensor – actuator FRF which is given by G_{ca} as specified in Equation (2.32).

The modulus plot for the classical actuator is characterised by a resonance peak at about 19 Hz with amplitude of -15.7 dB, which is due to the fundamental resonance of the inertial actuator, and then a sequence of sharp resonance peaks and narrow antiresonance lows pairs. The phase plot is characterised by a -180° phase lag at the fundamental resonance frequency of the actuator and then a sequence of -180° phase lag and +180° phase lead for each resonance peak and antiresonance low pair due to the response of the plate. The experimental results (solid blue lines) for the classical configuration of the inertial actuator align well with the numerical results (dashed-dotted red lines). The mathematical model predicts well the resonance peak and the phase shift due to dynamics of the inertial actuator. Furthermore, most of the resonance peaks and antiresonance lows pairs due to dynamics of the plate aligns well with the measurement. A small difference in the amplitude and frequency can be observed at higher frequencies, mainly between 400 Hz and 600 Hz. The simulated phase of the open loop sensor–actuator FRF for the current driven classical actuator aligns well with measurement. However, the measured phase starts slowly to decay at higher frequencies. Most probably, this is caused by the electrical properties of the measurement setup that were neglected in the simulations.

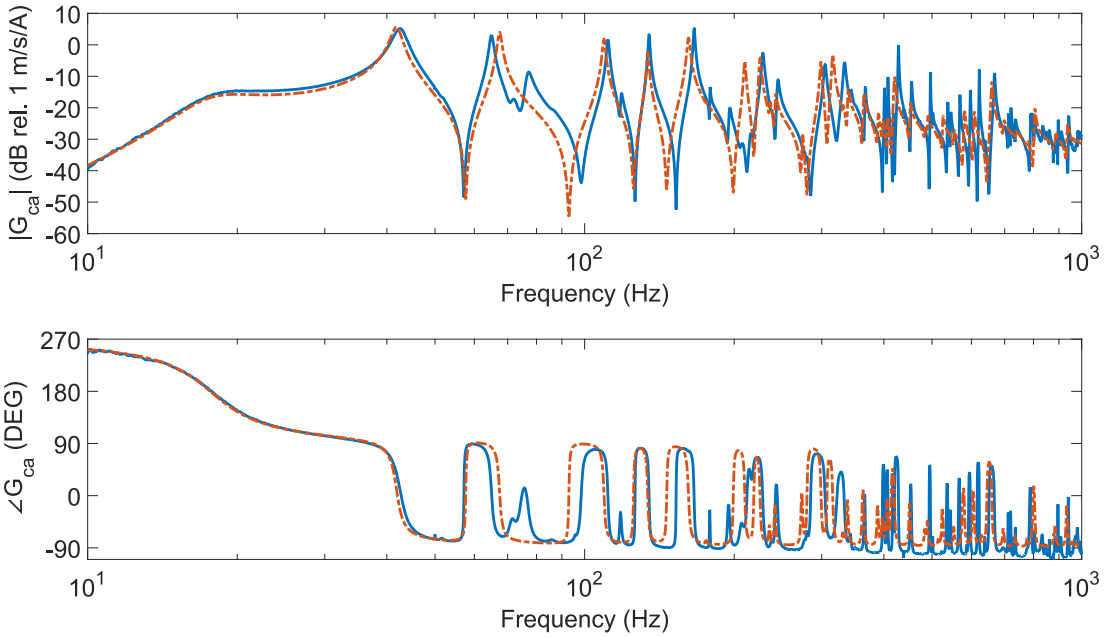

Figure 5.4. Open loop sensor–actuator FRFs for the current driven classical inertial actuator. Experimental results (solid blue lines) and numerical simulations (dashed-dotted red lines).

Figure 5.5 shows the Bode diagram of the open loop sensor – actuator FRF for the current driven classical actuator with the same inertial mass as the flywheel configuration. The modulus and phase diagrams present almost identical characteristic to those of the classical configuration. However, due to the heavier inertial mass, the resonance peak at the fundamental resonance of the inertial actuator appears at slightly lower frequency of about 17 Hz and has slightly lower amplitude of -16.3 dB. The sequence of sharp resonance peaks and narrow antiresonance lows pairs in the modulus diagram with the sequence of -180° phase lag and +180° phase lead in the phase diagram is almost identical as for the classical configuration. The experimental results (solid blue lines) align well with the numerical results (dashed-dotted red lines) also for this configuration of the inertial actuator. The additional peaks in the modulus diagram between 50 Hz and 60 Hz in measurements are caused by the increased mass attached to the inertial actuator. Most probably, due to the heavier inertial mass the higher order mode that appeared at 70 Hz for the classical inertial actuator (Figure 5.4) is shifted to lower frequency. Also for the classical actuator with the same inertial mass as the flywheel configuration a small difference in the amplitude and frequency can be observed between 400 Hz and 600 Hz. The simulated phase of the open loop sensor–actuator FRF aligns well with the measured

one. The measured phase starts slowly to decay at higher frequencies also for open loop sensor–actuator FRF of the classical actuator with the same inertial mass as the flywheel configuration.

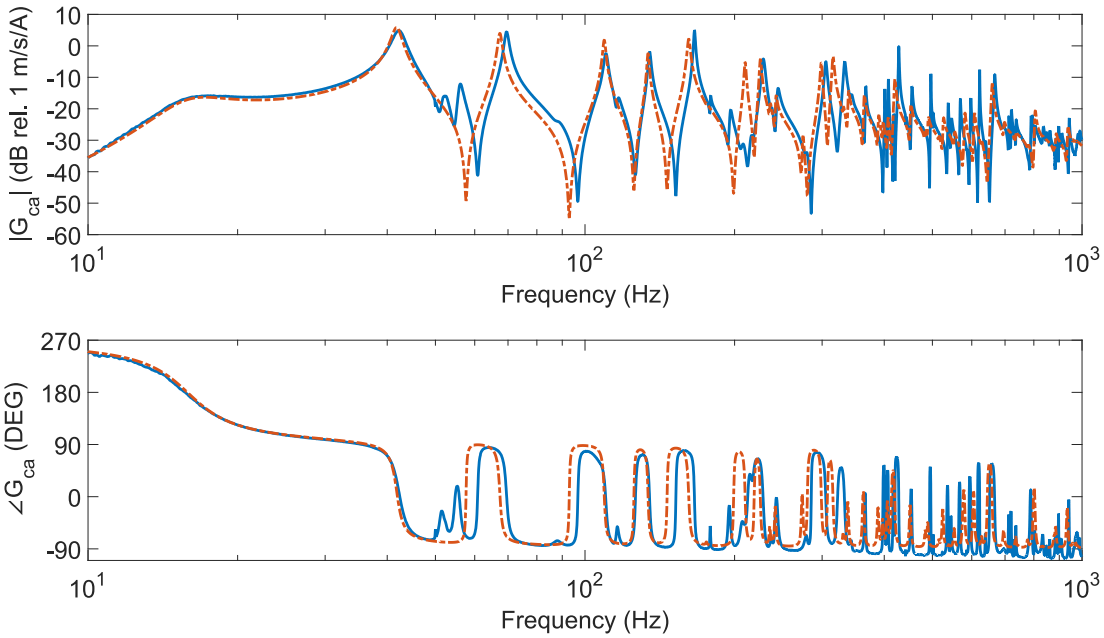

Figure 5.5. Open loop sensor–actuator FRFs for the current driven classical configuration with the same inertial mass as that of the flywheel configurations. Experimental results (solid blue lines) and numerical simulations (dashed-dotted red lines).

Figure 5.6 shows the open loop sensor – actuator FRF for the pinned configuration of the flywheel inertial actuator. The modulus and phase diagrams clearly show that the inertia effect of the flywheel element shifts the resonance peak of the fundamental resonance of the inertial actuator to lower frequency of about 13 Hz and to lower amplitude of -22.1 dB. The experimental results (solid blue lines) for the flywheel configuration of the inertial actuator align with the numerical results (dashed-dotted red lines) mainly at lower frequenices. The additional resonance of the actuator at about 210 Hz causes the phase shift from 90° to about 190°. Although additional dynamics of the actuator can cause instability in the velocity feedback loop, this resonance has much lower amplitude of -28 dB compared to the fundamental resonance of the inertial actuator. Thus, the stability limit of the feedback control system can be considered based on the fundamental resonance frequency of the flywheel inertial actuator. Another mayor difference between the measurement and

simulation results are the rapidly smoothen resonance peaks and antiresonance lows above 300 Hz, both in modulus and phase diagrams. The measured resonance peaks and antiresonance lows show similar amplitudes compared to those found in the other configurations of the inertial actuators. Thus, it can be assumed that the influence of the inertia effect of the flywheel element is diminished at higher frequencies or that the dynamics of the plate is slightly different from the one predicted with simulations. Considering the phase diagram, the measured phase starts to decay at higher frequencies due to the electrical properties of the measurement setup that were neglected in the simulations.

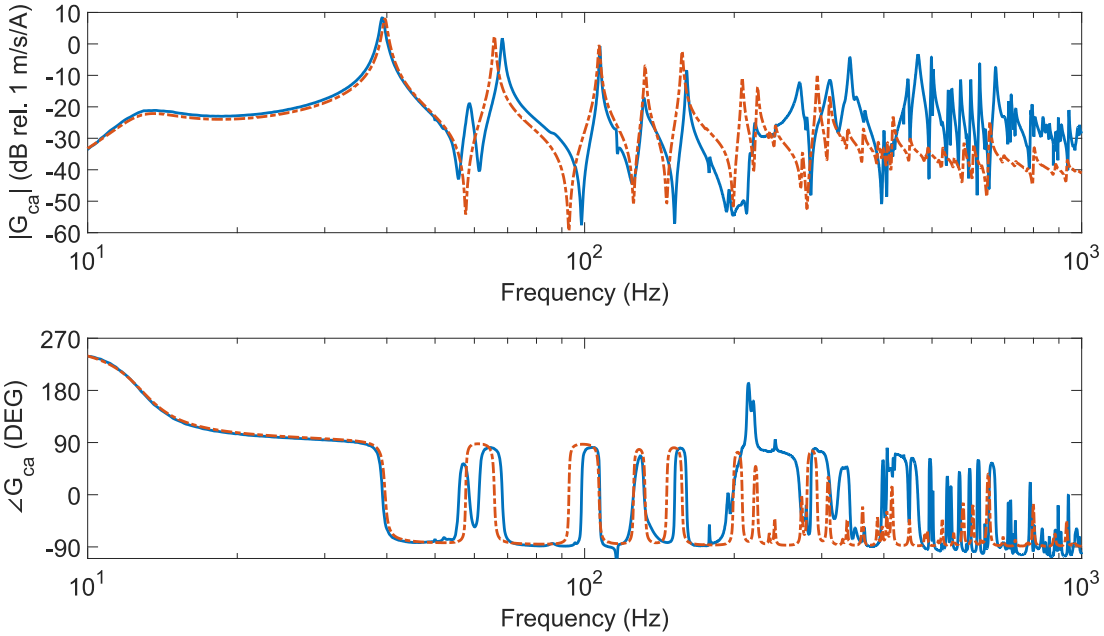

Figure 5.6. Open loop sensor–actuator FRFs for the current driven pinned configuration of the flywheel inertial actuator. Experimental results (solid blue lines) and numerical simulations (dashed-dotted red lines).

The stability of the velocity feedback loops using the classical and the pinned flywheel inertial actuator is assessed using the Nyquist criterion. Figure 5.7 shows the Nyquist plots of the open loop sensor – actuator FRF for the three configurations of the inertial actuator. Figure 5.7a shows the results for the classical configuration. Figure 5.7b shows the results for the classical actuator with the same inertial mass as the flywheel configuration. Finally, Figure 5.7c shows the results for the pinned configuration of the flywheel inertial actuator. The solid blue lines in the plots present

the measurement results, while the dashed-dotted red lines present the simulation results.

The Nyquist diagram for the open loop FRF with the current driven classical inertial actuator is characterised by a circle in the real negative quadrants, which is due to the resonance peak of the fundamental natural frequency, whereas the progressively smaller circles in the real positive quadrants are due to the resonance peaks and antiresonance lows of the plate. The circles in the real negative and positive quadrants are not centred along the axis due to high damping ratio of the inertial actuator that slightly shifts the pattern. The circle in the left hand side quadrants indicates that the feedback loop is only conditionally stable with maximum signal gain margin of about 16 dB. The experimental results (solid blue lines) align well with the numerical results (dashed-dotted red lines) mainly for the first and second resonance peaks. Thus, the performance of the velocity feedback loops for the current driven inertial actuator can be assessed with following approximation $20\log_{10}(1+\delta_n/\delta_a)$, proposed by Aoki et al. [147]–[149], where the δ_n and δ_a are the real values of the open loop sensor-actuator FRF for the n^{th} resonance peak of the plate and resonance peak at the fundamental resonance of the inertial actuator as shown in Figure 5.7. Therefore, the maximum reduction of the first resonance peak of the plate with the classical inertial actuator can reach 23 dB.

The Nyquist plot for the classical actuator with the same inertial mass as the flywheel configuration shown in Figure 5.7b presents similar characteristic to the classical configuration. The circle in the left hand side quadrants indicates that stability gain margin is about 17 dB. The experimental results (solid blue lines) align well with the numerical results (dashed-dotted red lines) also for this configuration of the inertial actuator. This analysis shows that the maximum reduction of the first resonance peak of the plate with this configuartion of the inertial actuator can reach 23.4 dB.

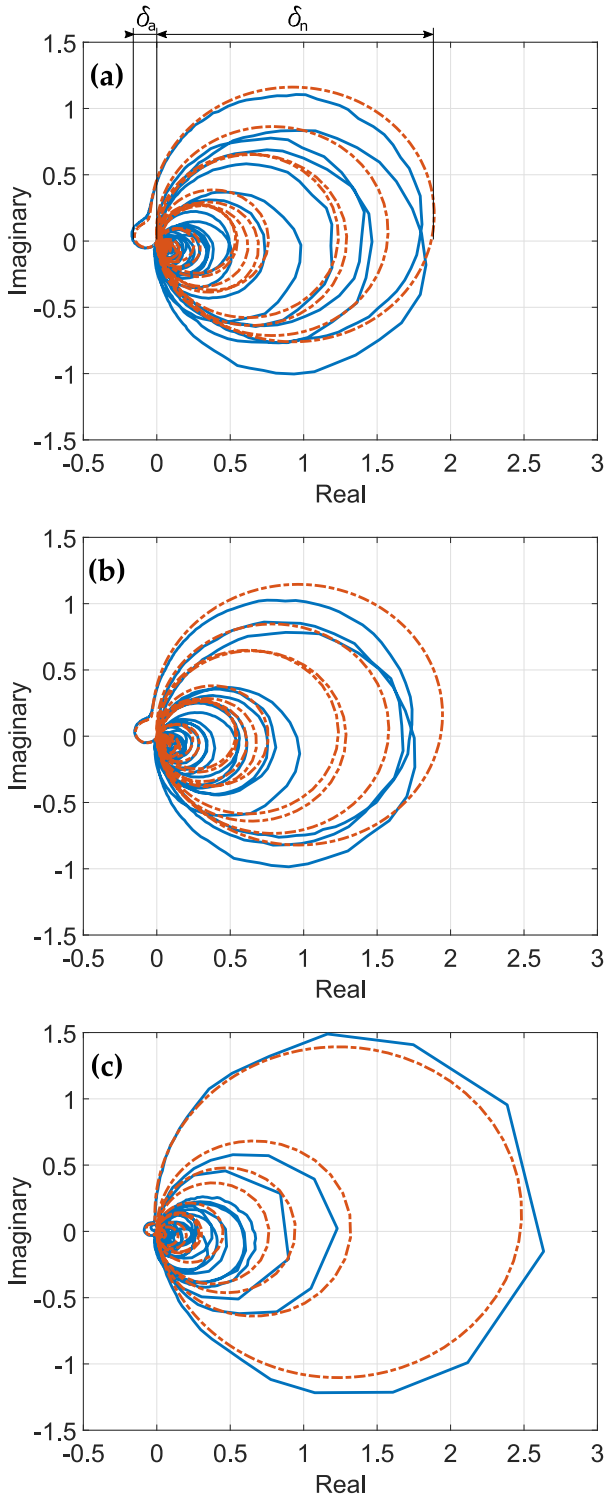

Figure 5.7. Nyquist plots of the open loop sensor – actuator FRFs for the current driven actuators. (a) Classical actuator, (b) classical configuration with the same inertial mass as the flywheel configuration, (c) pinned configuration of the flywheel inertial actuator. Experimental results (solid blue lines) and numerical simulations (dashed-dotted red lines).

The Nyquist plot for the pinned configuration of the flywheel inertial actuator shown in Figure 5.7c presents similar characteristic to the previous two configurations. However, the inertia effect produced by the flywheel element has significantly increased the stability of the feedback loop. Thus, the stability gain margin is about 21.5 dB. The experimental results (solid blue lines) align well with the numerical results (dashed-dotted red lines). As shown in Figure 5.6 for the open loop sensor – actuator FRF, an additional resonance of the actuator creates a second circle in the left hand quadrants. The second circle is much smaller compared to the one for the resonance peak of the actuator fundamental natural frequency and does not threaten stability of the velocity feedback loop. The assesed performance for the flywheel inertial actuator shows that the maximum reduction of the first resonance peak of the plate can reach up to 30.7 dB.

5.3 OPEN LOOP STABILITY ANALYSIS FOR THE VOLTAGE DRIVEN ACTUATOR

Although electromagnetic actuators are typically driven with current amplifiers, they can also be used with voltage amplifiers that are generally more easily available. The results presented in paragraph 3 show that the inertial actuators used in the experiments can produce constant force effect while being driven either with current or voltage signals. Therefore, the stability of the velocity feedback loops is assessed also for the voltage driven inertial actuators.

Figure 5.8 shows scheme (Figure 5.8a) and picture (Figure 5.8b) of the open loop sensor – actuator FRF test setup for the voltage driven inertial actuator. During tests, the actuator was attached to a rectangular plate as show in Figure 5.8b. Two parameters were measured during tests using signal analyser. Input channel A measured acceleration at the base footprint of the actuator while input channel B measured voltage applied to the inertial actuator. The quad amplifier was used to drive the actuator with a 1kHz random excitation signal generated by the signal analyser. Appendix D lists all the equipment used in the measurements.

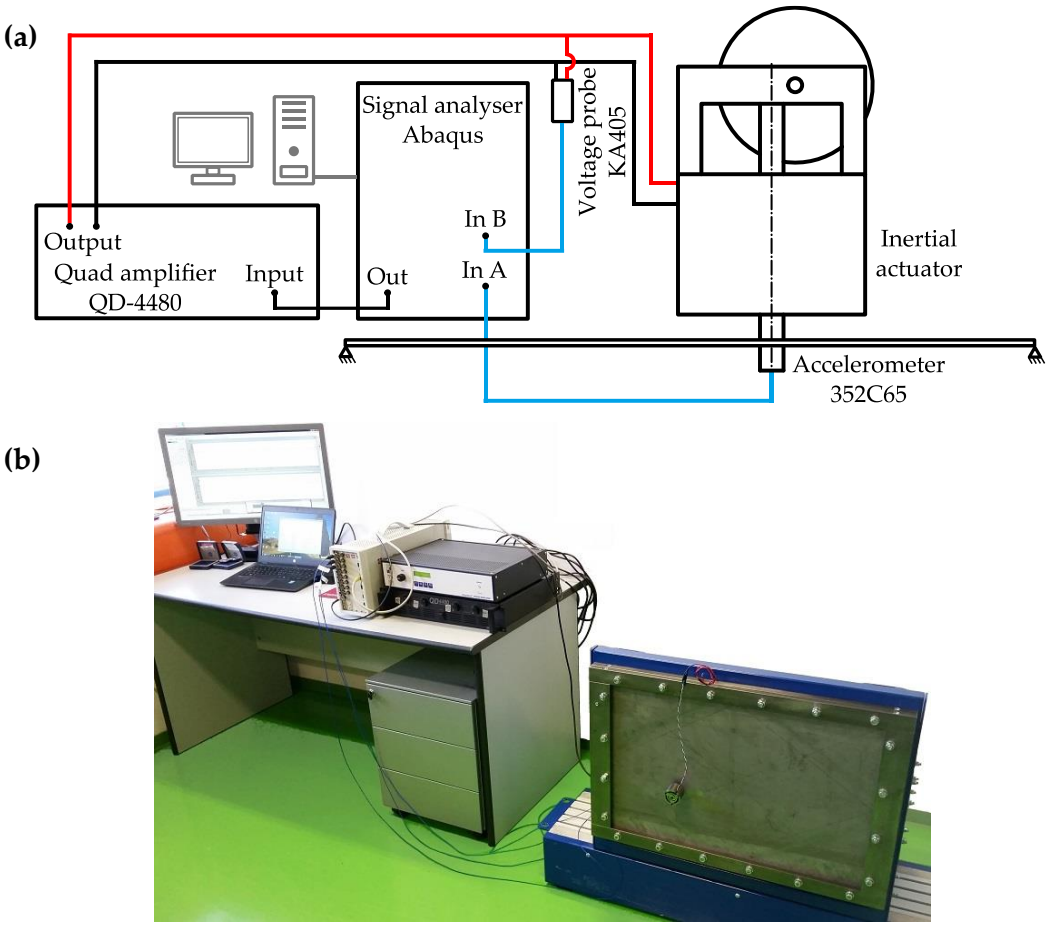

Figure 5.8. Scheme (a) and picture (b) of the open loop sensor – actuator FRF test setup for the voltage driven inertial actuator.

Figure 5.9 shows the Bode diagram of the open loop sensor – actuator FRF for the voltage driven classical inertial actuator. The solid blue lines in the plots present the measurement results, while the dashed-dotted red lines present the simulation results of the open loop sensor – actuator FRF which is given by G_{cu} as specified in Equation (2.34). The modulus plot is characterised by a heavily damped resonance peak at the fundamental resonance of the inertial actuator and then a sequence of rounded resonance peaks and antiresonance lows pairs. The resonance peaks are rounded off by the resistive effect in the transducer coil as specified in Equation (2.24). The phase plot is characterised by a -180° phase lag at the fundamental resonance frequency of the actuator and then a sequence of -180° phase lag and +180° phase lead for each resonance peak and antiresonance low pair of the plate. The experimental result (solid blue lines) for the classical configuration of the inertial actuator aligns with the numerical result (dashed-dotted red lines). The mathematical model predicts well the

resonance peak with the phase shift of the inertial actuator and most of the resonance peaks and antiresonance lows pairs due to dynamics of the plate. A small difference in amplitude and frequency between the numerical and measurement results can be observed between 400 Hz and 600 Hz, as noticed with the open loop sensor-actuator FRF for the current driven actuator. The simulated phase of the open loop sensor–actuator FRF for the voltage driven classical actuator aligns well with the measured one. The measured phase starts to decay at higher frequencies due to the electrical inductance of actuator coil, as predicted in numerical results.

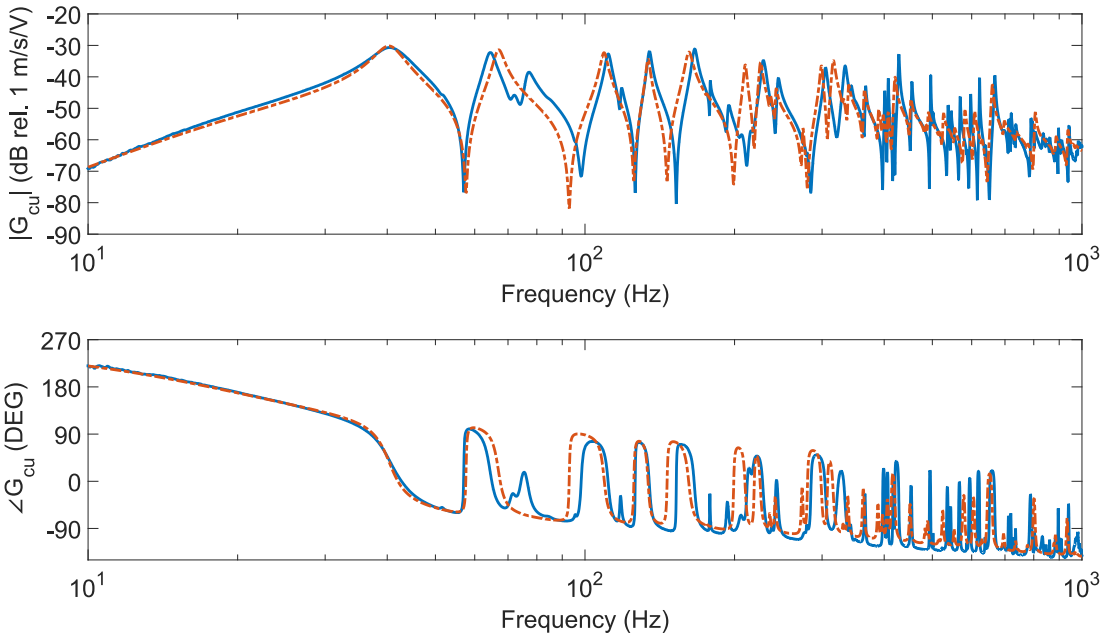

Figure 5.9. Open loop sensor–actuator FRFs for the voltage driven classical inertial actuator. Experimental results (solid blue lines) and numerical simulations (dashed-dotted red lines).

Figure 5.10 shows the Bode diagram of open loop sensor–actuator FRFs for the voltage driven classical actuator with the same inertial mass as the flywheel configuration. The modulus and phase diagrams present almost identical characteristics to the classical configuration. Slightly heavier inertial mass shifts the fundamental resonance of the inertial actuator to a hardly noticeable lower frequency. The sequence of rounded off resonance peaks and narrow antiresonance lows pairs in the modulus diagram with the sequence of -180° phase lag and +180° phase lead in the phase diagram is almost identical as for the classical configuration. The experimental results (solid blue lines) align well with the numerical results (dashed-

dotted red lines) also for this configuration of the inertial actuator. The classical actuator with the same inertial mass as the flywheel configuration presents a small difference in the amplitude and frequency between 400 Hz and 600 Hz. The simulated phase of the open loop sensor–actuator FRF aligns well with the measured one.

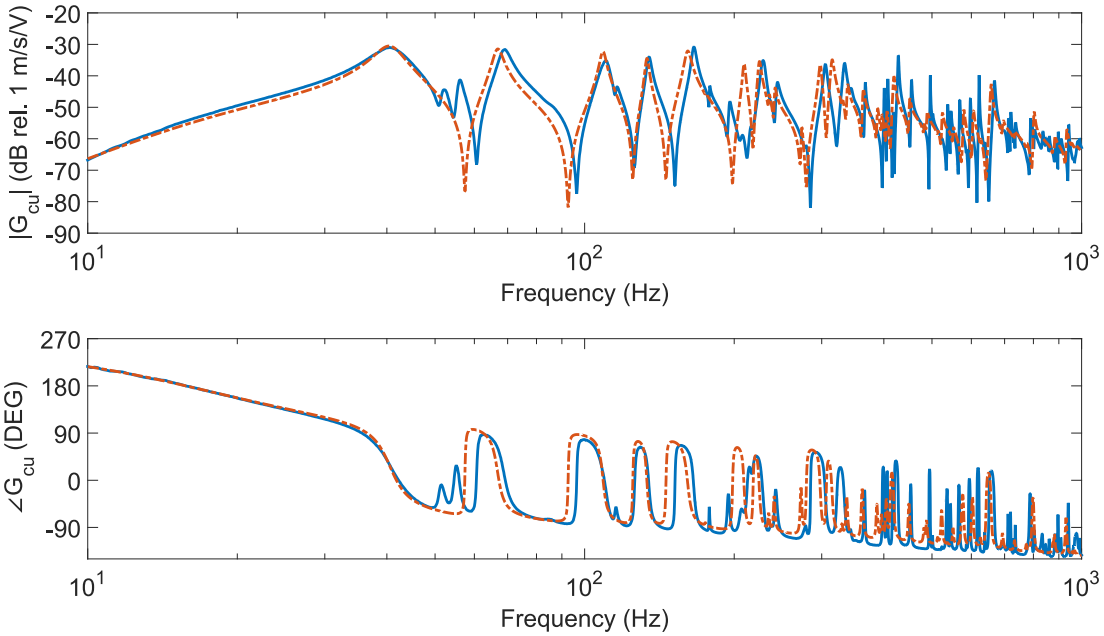

Figure 5.10. Open loop sensor–actuator FRFs for the voltage driven classical configuration with the same inertial mass as that of the flywheel configuration. Experimental results (solid blue lines) and numerical simulations (dashed-dotted red lines).

Figure 5.11 shows the results for the pinned configuration of the flywheel inertial actuator. The inertia effect of the flywheel element shifts the resonance peak at the fundamental resonance of the inertial actuator to lower frequency. The experimental results (solid blue lines) for the flywheel configuration of the inertial actuator align well with the numerical results (dashed-dotted red lines) mainly at lower frequenices. Similarly to the open loop sensor-actuator for the current driven actuator there is an additional resonance of the actuator at about 210 Hz that causes the phase to shift from 70° to about 170°. However, the actuator additional dynamics produces lower fundamental resonance peak compared to the peak of fundamental resonance frequency of the inertial actuator. Another mayor difference between the measurement and simulation results are the rapidly smoothen resonance peaks and antiresonance lows above 300 Hz, both visible in the modulus and the phase

diagrams. This effect is very similar to the one visible for the open loop sensor-actuator for the current driven actuator. Considering the phase diagram, the measured phase starts to decay at higher frequencies due to the electrical properties of the actuator coil that were predicted in the simulations.

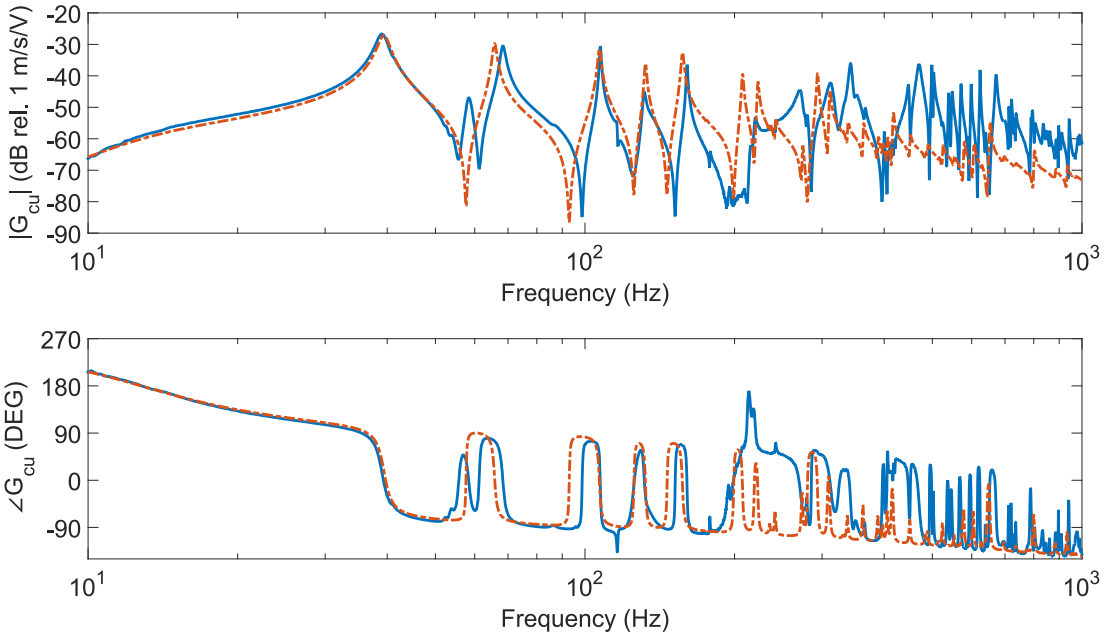

Figure 5.11. Open loop sensor–actuator FRFs for the voltage driven pinned configuration of the flywheel inertial actuator. Experimental results (solid blue lines) and numerical simulations (dashed-dotted red lines).

The stability of the velocity feedback loops using the classical, classical configuration with the same inertial mass as the flywheel configuration and the pinned flywheel inertial actuator is assessed using the Nyquist criterion. Figure 5.12 shows the Nyquist plots of the open loop sensor – actuator FRF for the three configurations of the inertial actuator. Figure 5.12a shows the results for the classical configuration. Figure 5.12b shows the results for the classical actuator with the same inertial mass as the flywheel configuration. Figure 5.12c shows the results for the pinned configuration of the flywheel inertial actuator. The solid blue lines in the plots present the measurement results, while the dashed-dotted red lines present the simulation results.

The Nyquist diagram for the open loop sensor-actuator FRF with the voltage driven classical inertial actuator is characterised by a small circle in the real negative quadrants, which is due to the fundamental resonance frequency of the actuator,

while the progressively smaller circles in the real positive quadrants are due to the resonance peaks and antiresonance lows of the plate. The circles are not centred along the axis due to high damping ratio of the inertial actuator that shifts the pattern. The small circle in the left hand side quadrants indicates that the feedback loop is only conditionally stable with maximum signal gain margin of about 54 dB. The experimental results (solid blue lines) align well with the numerical results (dashed-dotted red lines). As done for the current driven actuator, the performance of the velocity feedback loops with the voltage driven inertial actuator can be assessed with the approximation $20\log_{10}(1+\delta_n/\delta_a)$ [147]–[149], where the δ_n and δ_a are the real values of the open loop sensor-actuator FRF for the n^{th} resonance peak of the plate and resonance peak at the fundamental resonance of the inertial actuator as shown in Figure 5.12. In this case, the maximum reduction of the first resonance peak of the plate with the classical inertial actuator can reach 23.8 dB.

The Nyquist plot for the classical actuator with the same inertial mass as the flywheel configuration shown in Figure 5.12b presents similar characteristic to the classical configuration. The circle in the left hand quadrants indicates that the stability gain margin is about 55 dB. The experimental results (solid blue lines) align well with the numerical results (dashed-dotted red lines) also for this configuration of the inertial actuator. The assesed performance shows that the maximum reduction of the first resonance peak of the plate with this configuartion of the inertial actuator can reach 24.3 dB.

The Nyquist plot for the pinned inertial actuator shown in Figure 5.12c presents similar characteristic to the previous two configurations. However, the inertia effect produced by the flywheel element has significantly increased the stability of the feedback loop. Indeed, the stability gain margin is now about 59 dB. The experimental results (solid blue lines) obtained for the flywheel inertial actuator align well with the numerical results (dashed-dotted red lines). As shown in Figure 5.11 of the open loop sensor – actuator FRF, an additional resonance effect of the actuator creates a second circle in the left hand quadrants. The second circle is much smaller compared to the one for the resonance peak of the fundamental resonance frequency of the actuator and does not threaten the stability of the velocity feedback loop. The assesed performance for the flywheel inertial actuator shows that the maximum reduction of the first resonance peak of the plate can reach up to 32.8 dB.

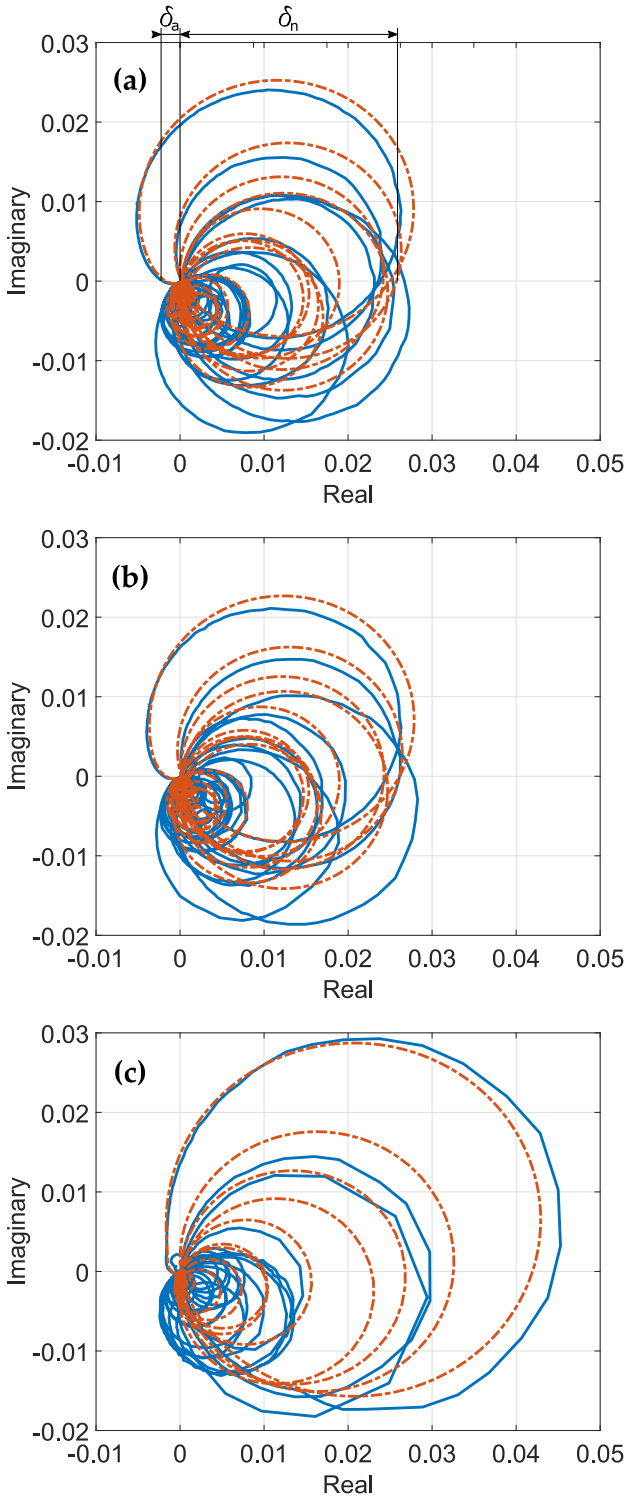

Figure 5.12. Nyquist plots of the open loop sensor – actuator FRFs for the voltage driven actuators. (a) Classical actuator, (b) classical configuration with the same inertial mass as the flywheel configuration, (c) pinned configuration of the flywheel inertial actuator. Experimental results (solid blue lines) and numerical simulations (dashed-dotted red lines).

5.4 PERFORMANCE

The control performance of the velocity feedback loops with the classical, classical configuration with the same inertial mass as the flywheel configuration and the pinned configuration of the flywheel inertial actuator is assessed by plotting the velocity reductions generated at the control position and the total flexural kinetic energy of the rectangular plate.

Figure 5.13 shows the scheme (Figure 5.13a) and the picture (Figure 5.13b) of the closed loop sensor – actuator test setup for the voltage driven inertial actuator. During tests, the actuator was attached to a thin rectangular plate as shown in Figure 5.13b. Two parameters were measured during tests using signal analyser. Input channel A measured excitation force while input channel B measured acceleration at the base footprint of the inertial actuator. A dedicated shaker amplifier was used to drive the shaker with a 1kHz random excitation signal generated by the signal analyser. The quad amplifier was used to drive the actuator with a velocity signal obtained from the accelerometer mounted at the base footprint of the inertial actuator. A signal conditioner was used to integrate the acceleration and to obtain the velocity signal. Appendix D lists all the equipment used in the measurements.

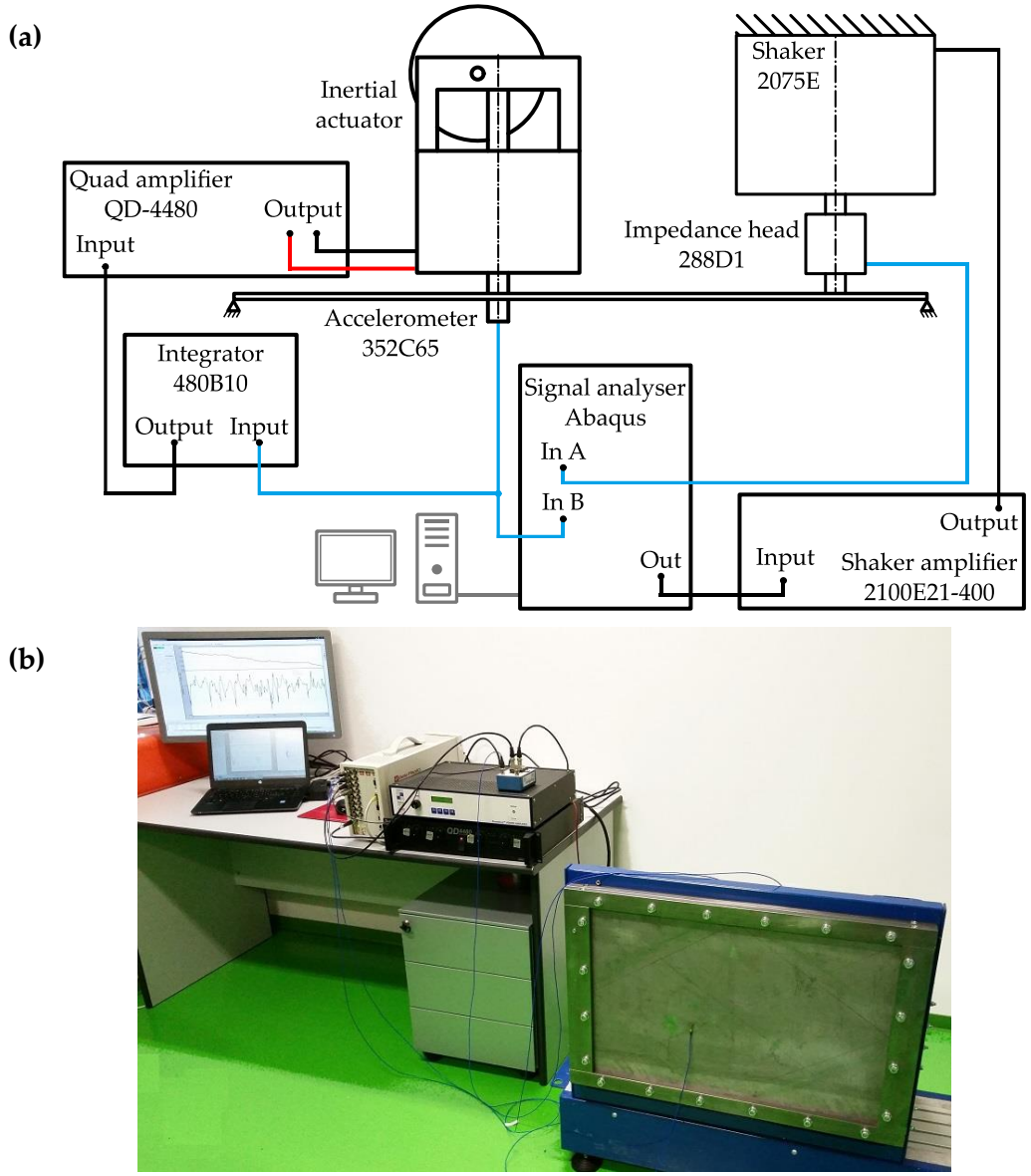

Figure 5.13. Scheme (a) and picture (b) of the closed loop sensor – actuator test setup for the voltage driven inertial actuator.

Figure 5.14 shows the control performance of the velocity feedback loops at the control position of the rectangular plate per unit force excitation for different control gains applied to the actuators. The figure is organised in two columns where, the left column shows the simulation results (plots a-c) given by Equation (2.39) while the right column shows the measurement results (plots d-f).

Figure 5.14 shows the control velocity signal per unit primary force excitation considering the plain plate (dotted green lines), the plate equipped with open loop inertial actuator (dashed brown lines) the plate equipped with the feedback loop using voltage driven inertial actuator with 10 dB signal gain margin (dashed-dotted magenta lines) and the plate equipped with the feedback loop with maximum signal gain that guarantee stability applied to the control actuator (solid lines). To extinguish three configurations of the inertial actuators shown in Figure 5.14, the blue lines present the classical inertial actuator, the black lines present the classical configuration with the same inertial mass as the flywheel configuration and the red lines present the pinned flywheel inertial actuator.

The spectrum of the plane plate flexural response at the control position (dotted green lines) is characterised by fundamental resonance peak at about 43 Hz and then a sequence of progressively smaller in amplitude sharp resonance peaks. The numerical results for the plain plate shown in left hand plots of Figure 5.14 correspond quite well to the experimental results shown in right hand plots of Figure 5.14. The amplitude of the plate resonance peak starts to diminish with the increase of the frequency with numerical results (plots a-c), while in the experimental results (plots d-f), the amplitude of the plate resonance peaks stay relatively equal in entire measured band.

When the classical inertial actuator (plots a, d), classical configuration with the same inertial mass as the flywheel configuration (plots b, e) or flywheel inertial actuator (plots c, f) is mounted to the plate (dashed brown lines), the amplitudes of the sharp resonance peaks are rounded off. The mass of the inertial actuators shifts the fundamental resonance peak of the plate to a slightly lower frequency. The numerical results (plots a, b, c) for the plate equipped with open loop inertial actuators present slightly higher reductions of the plate fundamental resonance peak compared to measurements (plots d, e, f). The experimental results show that the fundamental resonance peak of the plate is rounded off by about 11.9 dB with the classical inertial actuator, by about 12 dB with the classical configuration with the same inertial mass as the flywheel configuration and by about 6.4 dB with the flywheel configuration.

When the velocity feedback loops are implemented with 10 dB control gain margins (dashed-dotted magenta lines), to ensure stability and robustness in case of shocks of the hosting structure, the control loops produce higher vibration reductions. Experimental results show that when the feedback loops with 10 dB control gain margins are implemented the plate fundamental resonance peak is rounded off by

about 32.1 dB with the classical inertial actuator, by about 33.6 dB with the classical configuration with the same inertial mass as the flywheel configuration and by about 31.3 dB with the flywheel configuration. The numerical (plots a, b, c) and experimental (plots d, e, f) results show that the velocity feedback loops also generate small control spillover effect around the fundamental resonance frequency of the actuators. The control spillover for the classical inertial actuator has amplitude of about -45.7 dB, for the classical configuration with the same inertial mass as the flywheel configuration has amplitude of about -48.8 dB while for the flywheel configuration has amplitude of about -53.3 dB.

When the velocity feedback loops are implemented with maximum control gain that guarantee stability (solid lines) the control loops produce high vibration reductions. Experimental results show that when the feedback loops with maximum signal gain that guarantee stability are implemented the plate fundamental resonance peak is rounded off by about 40.6 dB with the classical inertial actuator, by about 40.4 dB with the classical configuration with the same inertial mass as the flywheel configuration and by about 39.8 dB with the flywheel configuration. The numerical (plots a, b, c) and experimental (plots d, e, f) results show that the velocity feedback loops also generate high control spillover effect at the fundamental resonance frequency of the actuators.

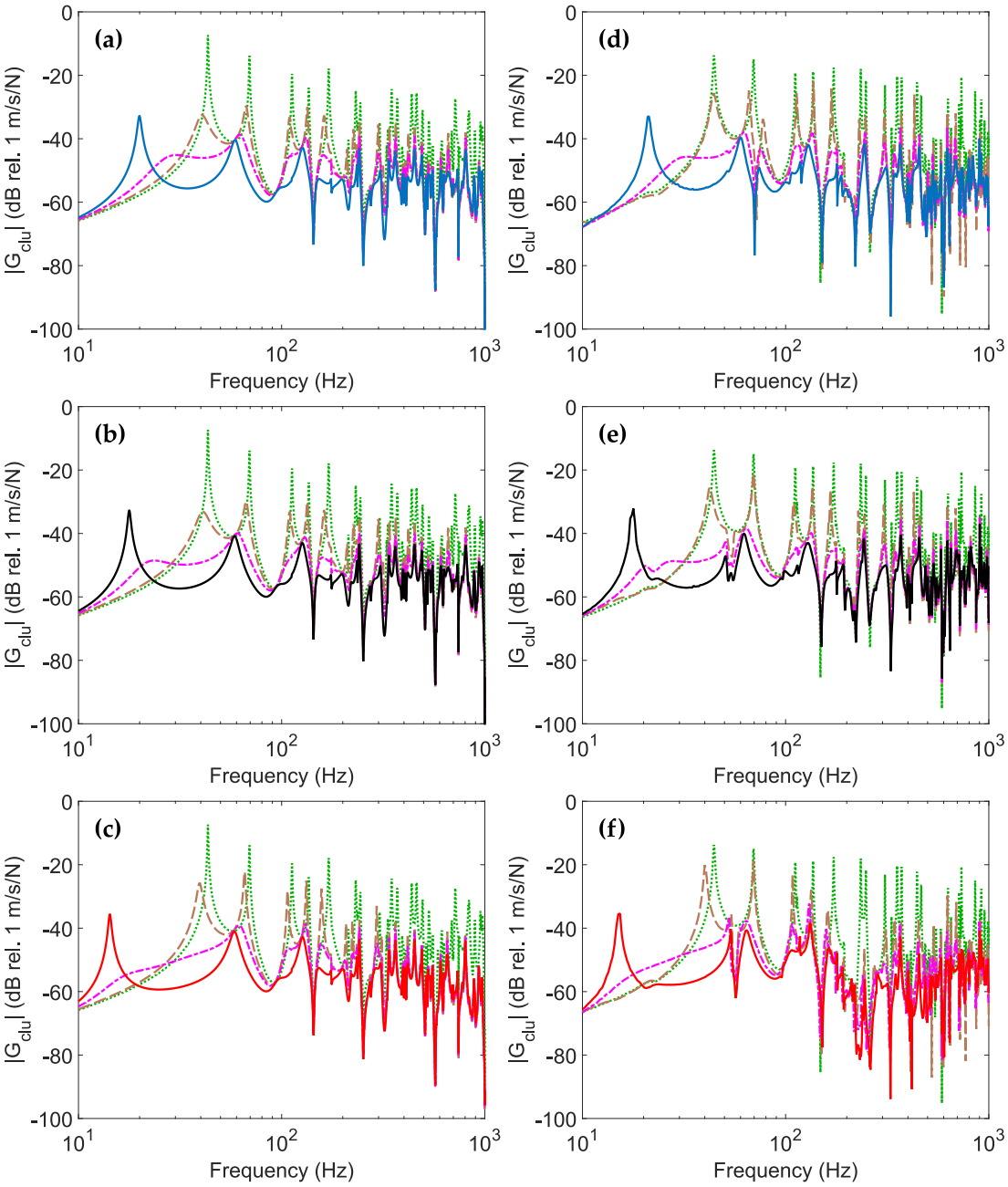

Figure 5.14. Velocity at the control position per unit force excitation of the plate with different signal gains applied to the actuators. Simulation results (plots a, b, c) compared with measurements (plots d, e, f). Plate without inertial actuator (dotted green lines). Plate with the feedback control loop using voltage driven classical inertial actuator (plots a, d), classical configuration with the same inertial mass as the flywheel configuration (plots b, e) and flywheel inertial actuator (plots c, f). Plate with open loop inertial actuator (dashed brown lines). Plate with the feedback control systems using voltage driven inertial actuator with 10 dB signal gain margin (dashed-dotted magenta lines) and with maximum signal gain that guarantee stability applied to the control actuators (solid lines).

Figure 5.15 shows the control velocity signal per unit primary force excitation considering the plain plate (dotted green lines) and the plate equipped with the feedback loop with maximum signal gain that guarantee stability using classical actuator (solid blue line), classical configuration with the same inertial mass as the flywheel configuration (dashed black lines) and the pinned flywheel inertial actuator (dashed-dotted red lines). The simulation results (Figure 5.15a) are compared with the measurements (Figure 5.15b). The velocity feedback loops are implemented with maximum signal gains that guarantee stability, which were defined using open loop FRFs presented in paragraph 5.3.

When the velocity feedback loops are implemented with maximum control gains that ensure stability using the inertial actuators the response at the control position is characterised by rounded off plate resonance peaks. However, both plots show that the velocity feedback loops also generate quite high control spillover effect around the fundamental resonance frequency of the actuators. Thus, for the classical configuration of the inertial actuator the spillover effect appears at about 20 Hz, for the classical configuration with the same inertial mass as the flywheel configuration at about 18 Hz, while for the pinned flywheel inertial actuator at about 15 Hz. The spillover effect produced by the flywheel configuration has lower amplitude by about 3 dB compared to the other two configurations. The simulation results show that all three configurations produce similar vibration control performance at low frequencies and round off the fundamental resonance peak of the plate by about 48 dB. However, above around 500 Hz the flywheel configuration produces higher reductions compared to other two configurations. The measurement results present similar characteristic to the numerical results given by Equation (2.39). The fundamental resonance frequency of the plate is rounded off by about 40 dB by all three configurations. Measurement results also show that the flywheel configuration produces much smaller control effect at lower frequencies compared to other two configurations. However, between 200 Hz and 800 Hz the control performance of the flywheel configuration is much greater compared to the other two configurations. Additionally, both plots clearly show the pinning effect of the plate at the control position due to the high feedback gains applied to the actuators. The first pinning effect appears at about 60 Hz, while the second at about 130 Hz, which as discussed in chapter 2.6 may limit the control performance of the velocity feedback control loop.

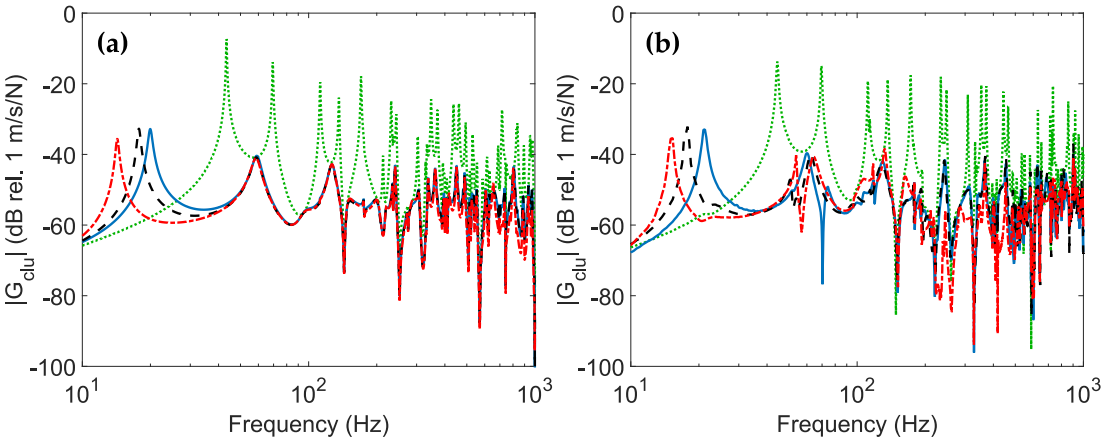

Figure 5.15. Velocity at the control position per unit force excitation of the plate with maximum signal gain that guarantee stability applied to the control actuators. Plate without inertial actuator (dotted green lines) and for the plate with the feedback control systems using voltage driven classical inertial actuator (solid blue lines), classical configuration with the same inertial mass as the flywheel configuration (dashed black lines) and with the flywheel inertial actuator (dashed-dotted red lines). Simulation results (plot a) compared with measurements (plot b).

The performance of the velocity feedback loops with the classical, classical configuration with the same inertial mass as the flywheel configuration and the pinned configuration of the flywheel inertial actuator is also assessed considering the total flexural kinetic energy of the rectangular plate.

Figure 5.16 shows the scheme (Figure 5.16a) and the picture (Figure 5.16b) of the laser vibrometer closed loop sensor – actuator test setup. During tests, the actuator was attached to a thin rectangular plate as shown in Figure 5.16b. The velocity of the panel was measured at 186 (17x11 grid mesh) evenly distributed points using laser vibrometer. The reference input channel measured the excitation force generated by the shaker. The shaker amplifier was used to drive the shaker with a 1kHz pseudo random excitation signal generated by the laser vibrometer. The quad amplifier was used to drive the actuator with a velocity signal obtained from the accelerometer mounted at the base footprint of the inertial actuator. A signal conditioner was used to integrate the acceleration and to obtain the velocity signal. Appendix D lists all the equipment used in the measurements.

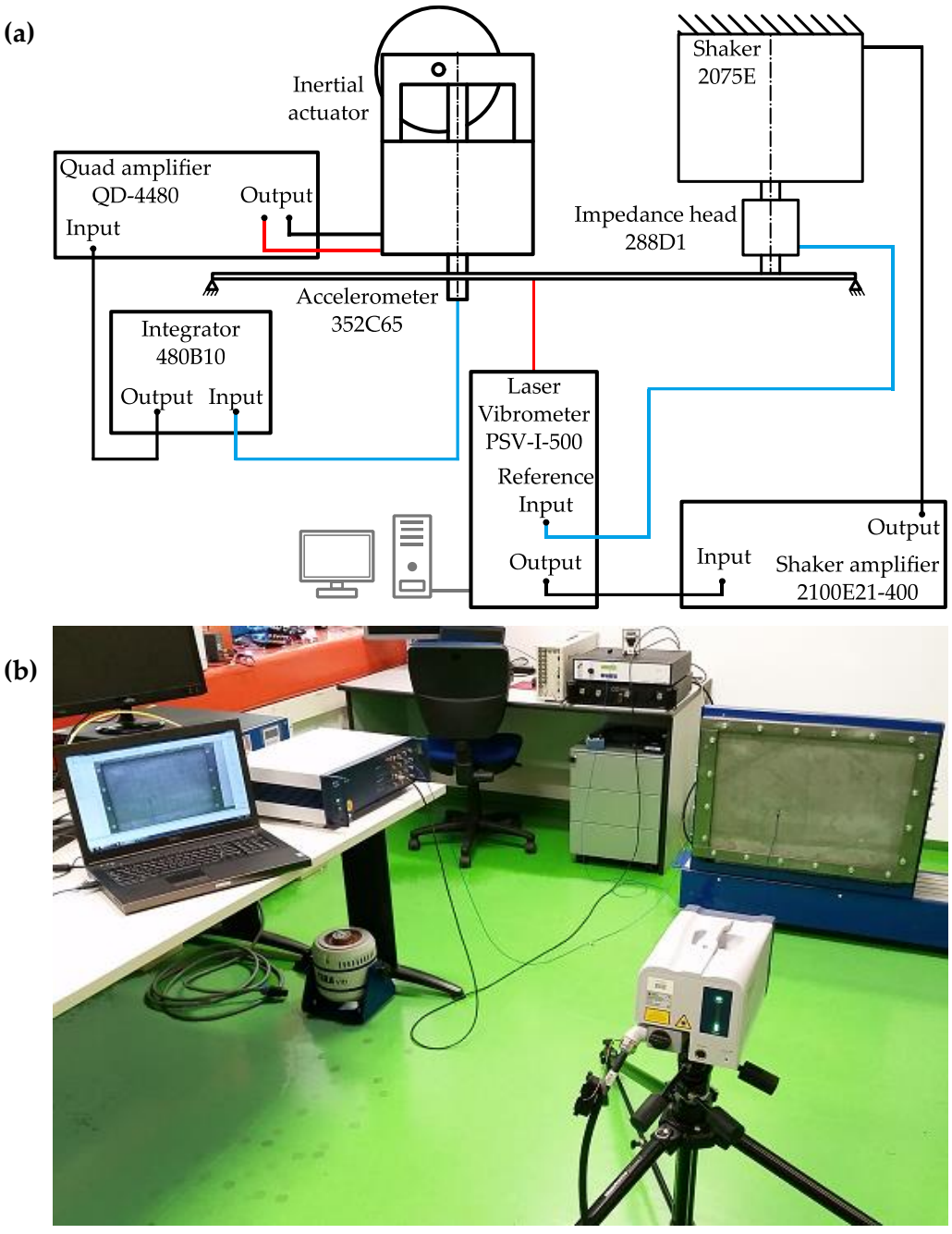

Figure 5.16. Scheme (a) and picture (b) of the laser vibrometer closed loop sensor – actuator test setup.

Figure 5.17 shows the total flexural kinetic energy of the plate per unit force excitation for different control gains applied to the actuators. The figure is organised in two columns where, the left column shows the simulation results (plots a-c) given by Equation (2.50) while the right column shows the measurement results (plots d-f).

Figure 5.17 shows the total flexural kinetic energy per unit primary force excitation considering the plain plate (dotted green lines), the plate equipped with open loop inertial actuator (dashed brown lines) the plate equipped with the feedback loop using voltage driven inertial actuator with 10 dB signal gain margin (dashed-dotted magenta lines) and the plate equipped with the feedback loop with maximum signal gain that guarantee stability applied to the control actuator (solid lines).

The spectrum of the total flexural kinetic energy of the plain plate (dotted green lines) is characterised by a sharp resonance peak at about 44 Hz, which is due to the fundamental natural mode of the plate followed by other peaks due to flexural modes of the plate. The numerical results for the plate shown in left hand plots of Figure 5.17 correspond quite well to the experimental results shown in right hand plots of Figure 5.17. However, the measurement results show that up to 200 Hz the amplitude of the plate resonance peaks stay relatively equal.

When the classical inertial actuator (plots a, d), classical configuration with the same inertial mass as the flywheel configuration (plots b, e) or flywheel inertial actuator (plots c, f) is mounted to the plate (dashed brown lines), the amplitudes of the sharp resonance peaks are rounded off. Similarly to the results obtained at the control position, the mass of the inertial actuators shifts the fundamental resonance peak of the plate to a slightly lower frequency. Also, the numerical results (plots a, b, c) for the plate equipped with open loop inertial actuators present slightly higher reductions compared to the experimental results (plots d, e, f). The experimental results show that the fundamental resonance peak of the plate is rounded off by about 41.2 dB with the classical inertial actuator, by about 42.2 dB with the classical configuration with the same inertial mass as the flywheel configuration and by about 33.3 dB with the flywheel configuration.

When the velocity feedback loops are implemented with 10 dB control gain margins (dashed-dotted magenta lines), to ensure stability and robustness in case of shock of the hosting structure, the control loops produce higher vibration reductions. Experimental results show that when the feedback loops with 10 dB control gain margins are implemented the plate fundamental resonance peak is rounded off by about 79.3 dB with the classical inertial actuator, by about 78 dB with the classical configuration with the same inertial mass as the flywheel configuration and by about 79.5 dB with the flywheel configuration. The numerical (plots a, b, c) and experimental (plots d, e, f) results show that the velocity feedback loops also generate small control spillover effect around the fundamental resonance frequency of the actuators.

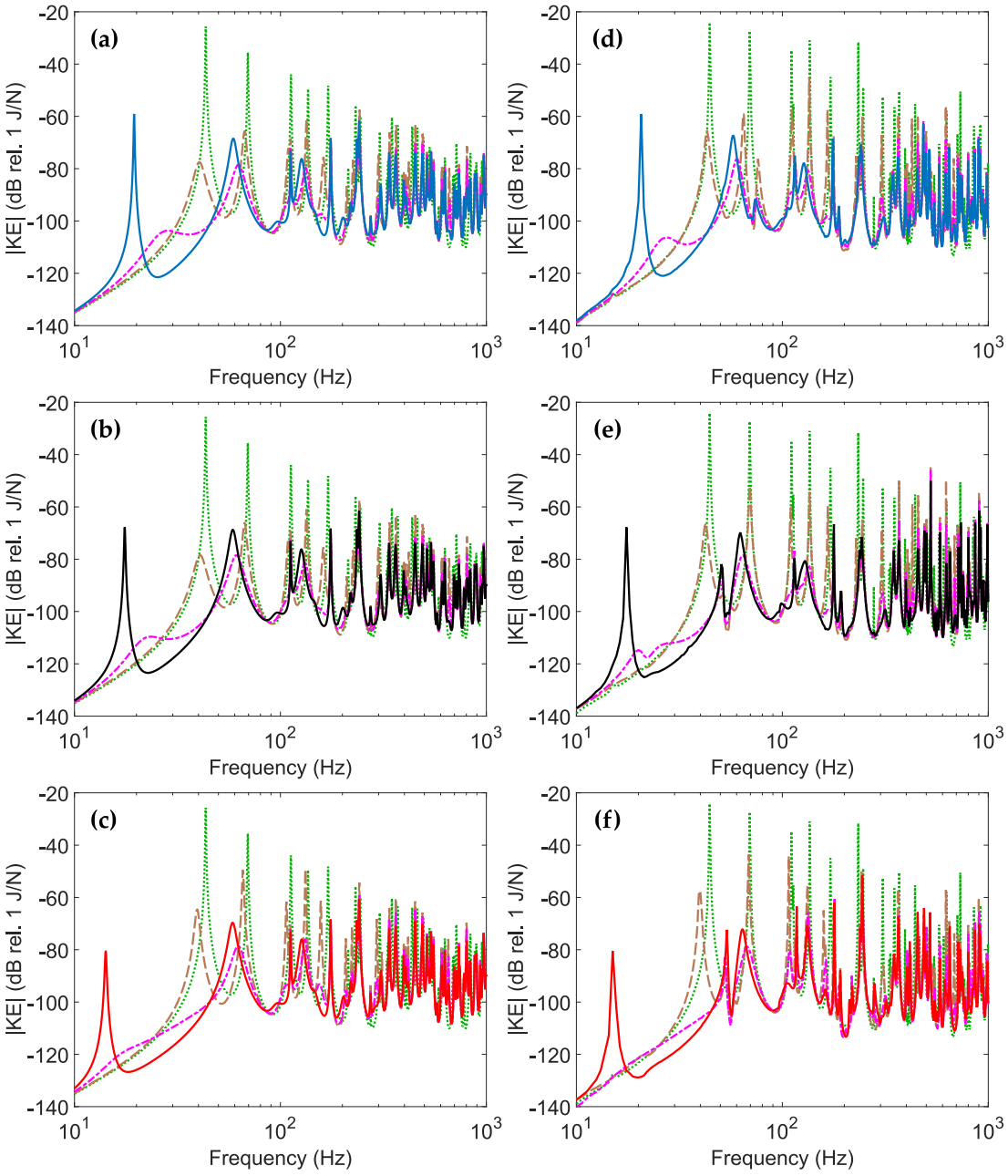

Figure 5.17. Total flexural kinetic energy per unit force excitation of the plate with different signal gains applied to the actuators. Simulation results (plots a, b, c) compared with measurements (plots d, e, f). Plate without inertial actuator (dotted green lines). Plate with the feedback control loop using voltage driven classical inertial actuator (plots a, d), classical configuration with the same inertial mass as the flywheel configuration (plots b, e) and flywheel inertial actuator (plots c, f). Plate with open loop inertial actuator (dashed brown lines). Plate with the feedback control systems using voltage driven inertial actuator with 10 dB signal gain margin (dashed-dotted magenta lines) and with maximum signal gain that guarantee stability applied to the control actuators (solid lines).

When the velocity feedback loops are implemented with maximum control gain that guarantee stability (solid lines) the control loops produce higher vibration reductions. The numerical (plots a, b, c) and experimental (plots d, e, f) results show that the velocity feedback loops also generate high control spillover effect at the fundamental resonance frequency of the actuators. Results show that the velocity feedback loops with the maximum control gains and with 10 dB control gain margins produce similar reductions of the plate fundamental resonance peak. Similarly to the results obtained at the control position, the high feedback gains applied to the control actuators cause the pinning effect of the plate that can be observed with a peak at about 70 Hz , which as discussed in chapter 2.6 may limit the control performance of the velocity feedback control loop.

Figure 5.18 shows the total flexural kinetic energy of the panel per unit force excitation considering the plain plate (dotted green lines) and the plate equipped with the feedback loop with maximum signal gain that guarantee stability using classical actuator (solid blue line), classical configuration with the same inertial mass as the flywheel configuration (dashed black lines) and the pinned flywheel inertial actuator (dashed-dotted red lines). The simulation results (Figure 5.18a) are compared with the measurements (Figure 5.18b). The velocity feedback loops are implemented with maximum signal gains that guarantee stability, which were defined using open loop FRFs presented in paragraph 5.3.

Considering the kinetic energy of the plate when the velocity feedback loops are implemented with maximum control gains that ensure stability using the inertial actuators the spectra are characterised by rounded off plate resonance peaks. The spectra also show that the velocity feedback loops generate high control spillover effects around the fundamental resonance frequency of the actuators, as observed in Figure 5.15. However, the kinetic energy spectrum shows that when the feedback loops with flywheel configuration is implemented the spillover effect is about 20 dB lower compared to classical configuration and about 13 dB lower compared to the classical configuration with the same inertial mass as the flywheel actuator. The simulation results show that all three velocity feedback loops produce similar vibration control performance in the entire frequency band. The feedback loops round off the two resonance peaks of plate by about 77 dB and by about 57 dB (Figure 5.18a). The measured spectra of the total flexural kinetic energy present slightly different characteristics to the simulated ones. For instance, the first two resonance peaks are rounded off by about 79 dB and by about 60 dB (Figure 5.18b). Similarly to the results obtained at the control position, the measured performance of the velocity

feedback loops with flywheel actuator is worse at lower frequencies compared to other two configurations. However, the control performance of the flywheel configuration is much greater compared to other configurations above 500 Hz.

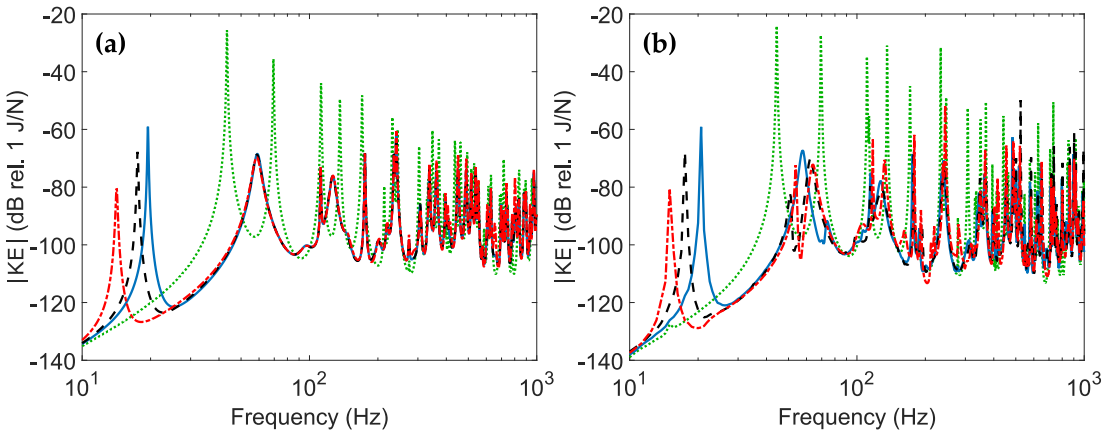

Figure 5.18. Total flexural kinetic energy per unit force excitation of the plate with maximum signal gain. Without inertial actuator (dotted green lines) and for the plate with the closed loop feedback control systems using voltage driven classical inertial actuator without flywheel (solid blue lines), classical configuration with the same inertial mass as the flywheel configuration (dashed black lines) and with the flywheel inertial actuator (dashed-dotted red lines). Simulation results (plot a) compared with measurements (plot b).

5.5 FREQUENCY AVERAGED ANALYSIS

The plate flexural kinetic energy vibration control effect presented in the previous paragraph showed the velocity feedback loops implemented only with maximum control gains that ensure stability. To better asses the effectiveness of the proposed control systems, the 10 Hz to 1 kHz frequency averaged plate kinetic energy reduction is considered with reference to increasingly higher feedback control gains. The reductions of the frequency averaged flexural kinetic energy of the plate equipped with the feedback control units are normalised with reference to the frequency averaged kinetic energy of the plain rectangular plate. Figure 5.19 shows reduction of the frequency average kinetic energy when the feedback loops are implemented using the classical (solid blue line), classical configuration that have the same inertial mass as the flywheel configuration (dashed black line) and the flywheel inertial actuator (dashed-dotted red line). The results show the frequency averaged plate kinetic

energy reduction with increasing feedback control gains up to maximum control gain that guarantees stability. Figure 5.19 shows point with performance for the 10 dB signal margin that should be used in practical applications to improve stability and robustness of the feedback loops in case of shocks of the hosting structure. Figure 5.19 shows only experimental results due to the slight variation between the measured and numerical results as discussed for the results shown in Figure 5.15 and Figure 5.18 .

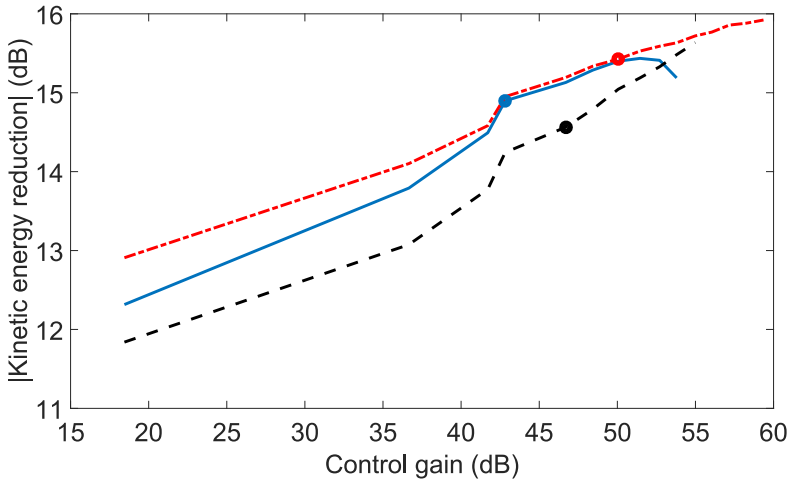

Figure 5.19. Reductions of the 10 Hz – 1 kHz frequency averaged kinetic energy produced by the feedback loops using either the voltage driven classical inertial actuator without flywheel (solid blue lines), classical configuration with the same inertial mass as the flywheel configuration (dashed black lines) and with the flywheel inertial actuator (dashed-dotted red lines).

Considering first the classical configuration (solid blue line), the results show that the feedback loop with the inertial actuator produces up to 15.4 dB reduction of the frequency averaged kinetic energy with a maximum control gain of 54 dB. However, the maximum stable gain does not produces maximum control performance, which as discussed in chapter 2.6 is due to the pinning effect produced by the velocity feedback control loop. When the velocity feedback loop is implemented with a 10 dB signal gain margin the classical inertial actuator produces up to 14.9 dB reduction.

The performance of the velocity feedback loop is slightly better when the classical configuration that has the same inertial mass as the flywheel configuration is used. Considering the dashed black line, when the velocity feedback loop is implemented the inertial actuator produces up to 15.6 dB reduction. Then, when the velocity

feedback loop is implemented with a 10 dB signal gain margin this inertial actuator produces 14.5 dB reduction. Finally, the feedback loop with the flywheel inertial actuator (dashed-dotted red lines) can implement much larger feedback control gains (up to 59dB) such that the frequency averaged kinetic energy of the plate is reduced by up to 15.9 dB. Similarly to the previous configurations, when the velocity feedback loop is implemented with a 10 dB signal gain margin the flywheel configuration of the inertial actuator produces about 15.4 dB reduction. The improved control performance are obtained thanks to the possibility of implementing about 5.6 dB higher control gains.

5.6 CHAPTER CONCLUSIONS

This chapter has investigated the use of flywheel inertial actuator for the implementation of velocity feedback loop independent units that can be used to control the broadband vibration of thin structures. Experimental results were obtained based on the tests carried out on a rectangular panel test rig and have been contrasted with simulations. The stability and control performance of velocity feedback loops were considered using classical inertial actuator, classical inertial actuator with the same inertial mass as the flywheel actuator and pinned flywheel inertial actuator.

The stability of the velocity feedback loops has been assessed using the Nyquist criterion based on the open loop sensor – actuator FRFs for the current and voltage driven transducers. The stability analysis has shown that the actuator with additional flywheel element has much higher gain margin of the feedback loop with the classical configurations. Moreover, comparing the classical actuator with the same inertial mass as the flywheel configuration and the pinned flywheel prototype, the gain margin results increased without any increment of the actuator proof mass. The actuators driven with a current signal have reached maximum signal gain margin of 16 dB for the reference configuration, 17 dB for the classical actuator with the same inertial mass as the flywheel configuration and 21.5 dB for the flywheel prototype. Instead, the actuators driven with the voltage signal have reached the maximum signal gain margin of 54 dB for the classical inertial actuator, 55 dB for the classical actuator with the same inertial mass as the flywheel configuration and 59 dB for the flywheel prototype. Both for the current and voltage driven inertial actuators, the experimental testes matched well the numerical results.

The performance of the feedback loops has been assessed considering the velocity at the control position and the total flexural kinetic energy of the hosting structure. The experimental results have been compared with the numerical simulations obtained from the lumped parameter model of the actuators located on the rectangular panel derived in chapter two of this thesis. Result showed that the feedback loops using the flywheel inertial actuators are characterised by a slightly better control performance thanks to increased signal gain margins.

The experimental results presented in this chapter confirmed the simulation study. The flywheel inertial actuators can improve the control performance of the velocity feedback loops to reduce the broadband vibration of thin plate.

6

ENERGY HARVESTING

This chapter presents the study on the energy harvesting with the inertial EM transducers. The mathematical formulation for the power harvested per unit base excitation is derived for a classical, classical with the same inertial mass as the flywheel configuration and flywheel inertial transducer. Finally, both simulation and experimental results of the energy harvesting effects are presented for three inertial transducers connected to a purely resistive load.

This chapter introduces a new flywheel coil–magnet proof mass transducer for vibration energy harvesting. The seismic transducer includes an additional flywheel element that produces three effects on the elastically suspended proof mass: firstly, it lowers the fundamental resonance frequency, secondly it lowers the static displacement and thirdly it lowers the mechanical damping effect. The combination of all three effects is beneficial for vibration energy harvesting applications. In fact, having a low resonance frequency transducer facilitates the tuning of the harvester to a low frequency band where ambient vibration energy is normally higher. Also, having a low static displacement of the proof mass element allows the construction of a device robust to shocks and fast movements despite it has a low fundamental resonance frequency. Finally, having a low internal mechanical damping leaves more energy for the conversion to electrical energy. The chapter presents both simulations and experimental results that contrast the principal electro-mechanical properties and the energy harvesting effects of classical and proposed flywheel coil–magnet proof mass transducers connected to a purely resistive load.

Simulated frequency response functions (FRFs) are contrasted with measured FRFs taken on a classical coil-magnet proof mass transducer and on a prototype coil-magnet proof mass transducer equipped with a flywheel element.

6.1 MATHEMATICAL MODEL FOR ENERGY HARVESTING

This section presents the mathematical formulation used to derive the power harvested per unit base excitation with the classical, with the classical having the same inertial mass as the flywheel configuration and with the proposed flywheel inertial transducer. The frequency domain formulations presented in this section consider the complex amplitudes of time–harmonic functions as defined in chapter two.

To harvest vibration energy, the EM transducers presented in Figure 3.13 are connected to an electrical impedance Z_h at the terminals of the coil. Considering the lumped parameter models shown in Figure 3.13e, f, h, the voltage across two terminals u_a is equal to:

$$u_a = -Z_H i_a \,, \tag{6.1}$$

since i_a is defined to flow onto the transducer. The complex velocity at the proof mass can be derived from Equation (2.4) and is given by:

$$\dot{w}_m = Y_m F_m \,, \tag{6.2}$$

while the complex force at the proof mass can be derived from Equation (2.20) and is given by:

$$F_m = Z_a \dot{w}_c - Z_a \dot{w}_m + \psi_a i_a \,. \tag{6.3}$$

After substitution of Equation (6.2) into Equation (6.3), the complex velocity at the proof mass for the current driven actuator results:

$$\dot{w}_m = \frac{Y_m Z_a}{1 + Y_m Z_a} \dot{w}_c - \frac{Y_m \psi_a}{1 + Y_m Z_a} i_a \,. \tag{6.4}$$

Substituting Equation (6.4) into Equation (2.24), the complex voltage at the terminals of the coil is given by:

$$u_a = -T_{u\dot{w}} \dot{w}_c + Z_{ui} i_a \,, \tag{6.5}$$

where $T_{u\dot{w}}$ is the actuators transduction FRF given in Equation (2.53) while the Z_{ui} is the actuators electrical impedance given in Equation (2.55). Substituting Equation (6.1) into Equation (6.7), the generated current at the terminals of the coil is given:

$$i_a = \frac{T_{u\dot{w}}}{Z_h + Z_{ui}} \dot{w}_c \,. \tag{6.6}$$

When the electromagnetic transducer is exposed to harmonic vibrations, the time averaged harvested power is given by:

$$\bar{P}_H = \frac{1}{2} Re\{i_a^* u_a\} \tag{6.7}$$

and using Equation (6.1) and Equation (6.10) the harvested power results:

$$\bar{P}_H = \frac{1}{2} \mathrm{Re}(Z_H) \left| \frac{T_{u\dot{w}}}{Z_H + Z_{ui}} \dot{w}_c \right|^2 . \tag{6.8}$$

Now, assuming a purely resistive electrical load, i.e. $Z_H = R_H$, and recalling the expressions given in Equation (2.53) and Equation (2.55) the harvested power can be rewritten in the following form:

$$\bar{P}_H = \frac{1}{2} R_H \left| \frac{\psi_a}{R_H + Z_e + (R_H + Z_e) Y_m Z_a + Y_m \psi_a^2} \right|^2 |\dot{w}_c|^2 . \tag{6.9}$$

This equation indicates how both the electrical and mechanical parameters of the harvester influence the energy harvesting with either the classical or the proposed flywheel proof mass transducer. This study is indeed focused on the use of the additional flywheel element in the proof mass transducer to increase the energy harvesting of classical proof mass actuators.

6.2 ENERGY HARVESTING COMPARISON

A key factor that determines the harvested power from a coil–magnet proof mass transducer connected to a purely resistive load is the internal losses in the transducer, which is mechanical damping and electrical dissipation. The mechanical damping is primarily due to the eddy current effect between the magnet and the steel coil armature. The electrical losses are instead generated by the resistive effect of the coil. While the electrical losses can be easily modelled considering the resistance of the coil, the mechanical dissipation is somewhat more complex to handle. This is particularly the case with the proposed proof mass transducer comprising the flywheel element, which is both pinned to the case and connected to the moving coil-armature component via flexural bearings. Thus, a preliminary experimental study was put in place to identify the most appropriate expression for the critical damping to be used in a classical viscous damping model. The power harvested per unit base acceleration was therefore measured with the pinned flywheel proof mass transducer connected to a purely resistive load Z_H=68 Ω.

Figure 6.1 shows the scheme (Figure 6.1a) and the picture (Figure 6.1b) of the energy harvesting test setup. The actuator mounted on the shaker was excited with a

random excitation signal up to 40 Hz. Two parameters were measured during tests using signal analyser. Input channel A measured base acceleration measured, input channel B current flowing in the variable resistor while input channel C measured voltage generated by the actuator at the terminals of the variable resistor. The shaker amplifier was used to drive the shaker with required excitation signal generated by the signal analyser. Appendix D lists all the equipment used in the measurements.

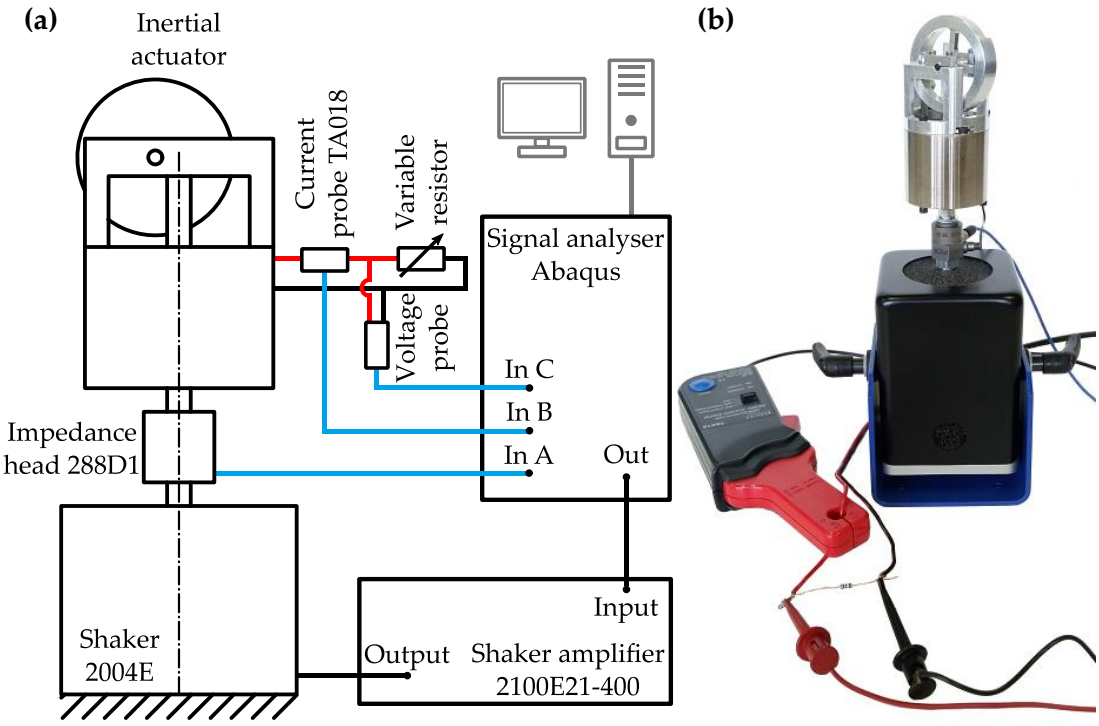

Figure 6.1. Scheme (a) and picture (b) of the energy harvesting test setup.

The solid blue lines in plots a-c of Figure 6.2 show the spectra of the measured power harvested. The dash-dotted red lines in the same plots a-c of Figure 6.2 show the power harvested simulated using Equation (6.9), where the damping term c in the mechanical impedance Z_a has been taken equal to:

$$c = \zeta c_c \tag{6.10}$$

considering a damping ratio equal to ζ=0.2. Plot a shows the simulated power harvested assuming the critical damping is derived from the classical definition given for the inerter transducers:

$$c_c = 2\sqrt{\left(k + \frac{k_w}{r_w^2}\right)\left(M_a + \frac{I_w}{r_w^2} + m_w\right)}\,. \tag{6.11}$$

Alternatively, plot b shows the simulated power harvested assuming the critical damping is equal to that for the proof mass transducer without flywheel:

$$c_c = 2\sqrt{kM_a}\,. \tag{6.12}$$

Finally, plot c shows the simulated power harvested assuming the critical damping is given by:

$$c_c = 2\sqrt{\left(k + \frac{k_w}{r_w^2}\right)(M_a + m_w)}\,. \tag{6.13}$$

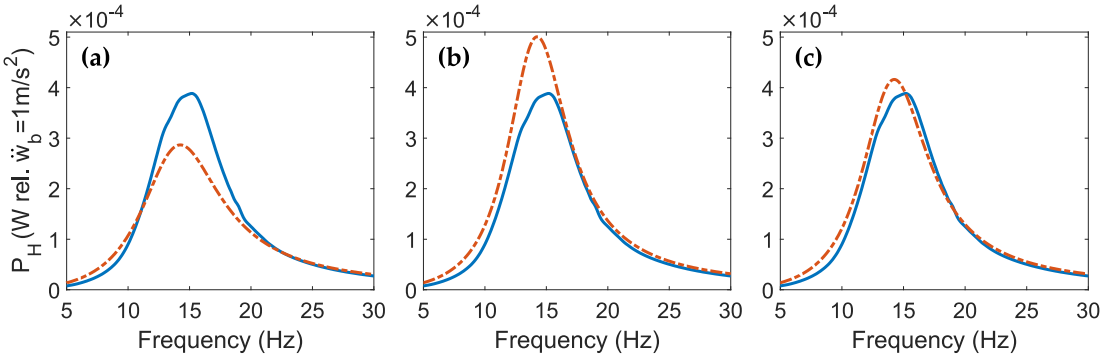

Figure 6.2. Frequency response function of the harvested power to a resistive load $Z_H = 68\Omega$ for the flywheel proof mass transducer with the constant damping ratio (a), with the constant damping coefficient (b), with the optimal damping (c). Experimental results (blue lines). Simulations (dashed-dotted red lines).

Contrasting the results plotted in Figure 6.2a-c it is noted that the expression for the critical damping given in Equation (6.13) is the most appropriate to derive the damping factor to be used in the calculus of the mechanical impedance Z_a in order to derive correctly the energy harvested with Equation (6.9). This result indicates that, although the axial inertia effect produced by the flywheel element (I_w / (r_w^2)) reduces the fundamental resonance frequency of the transducer, it does not influence the mechanical damping, which, as discussed above, plays a key role in the disposal of the absorbed mechanical vibration energy to electrical energy, which is then harvested.

Having established the correct model for the mechanical damping, the measured results (solid blue lines) of energy harvested is contrasted with the simulated (dash-dotted red lines). The energy harvested with the classical inertial transducer (Figure 3.13a), classical with the same inertial mass as the flywheel configuration (Figure 3.13b) and with the proposed flywheel inertial transducer (Figure 3.13c) are shown respectively in Figure 6.3. Since the three transducers are characterised by different mechanical damping factors, the maximum energy harvesting at the resonance frequency is obtained with different resistive loads. The result in Figure 6.3a shows that maximum power can be harvested by applying to the classical proof mass transducer a resistive load of $R_H = 75\ \Omega$. Alternatively, the result in Figure 6.3c shows that maximum power can be harvested by applying to the proposed flywheel proof mass transducer a resistive load of $R_H = 68\ \Omega$.

The two plots clearly show that the simulation results agree well with the experimental tests carried out either with the classical configuration (Figure 6.3a), classical with the same inertial mass as the flywheel configuration (Figure 6.3b) and with the pinned flywheel inertial transducer (Figure 6.3c).

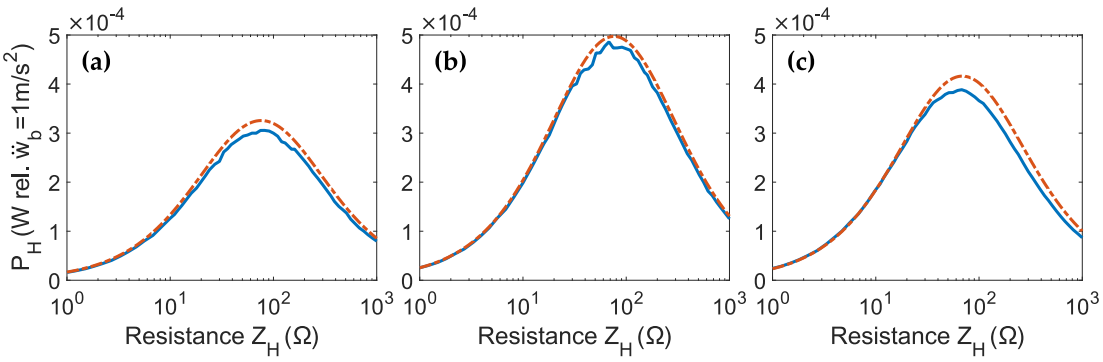

Figure 6.3. Maximum harvested power at the resonance frequency with varying resistive load Z_h for the classical transducer (a), and classical with the same inertial mass as the flywheel configuration (b) and pinned flywheel prototype (c). Experimental results (solid blue lines). Simulations (dashed-dotted red lines).

6.3 CHAPTER CONCLUSIONS

This chapter has investigated the use of the inertial EM transducers for energy harvesting applications. The experimental testes were successfully matched with numerical results obtained from a lumped parameter scheme, which included a

specific model for the damping coefficient of the flywheel inertial transducer. The results for the new configuration were compared with those obtained with a classical coil-magnet proof mass transducer and a classical transducer with the same inertial mass as the flywheel configuration.

The results of the energy harvesting have shown that the flywheel element reduces the fundamental resonance frequency of the actuator without significantly increasing the total mass of the transducer and without increasing the damping coefficient of the transducer. Moreover, the simulation and experimental results have shown that the flywheel transducer increases the harvested energy by about 30% compared to the reference configuration. However, compared to the classical transducer with the same inertial mass as the flywheel configuration the fabricated prototype presented lower energy harvesting performance by about 25%. It is worth to emphasise that transducers used in this study are characterised with high damping, which is disadvantageous for the energy harvesting applications. Thus, it may be possible that a proper design of the new transducer may lead to a device with even higher energy harvesting capabilities.

7

SUMMARY

This chapter summarises the work presented in this thesis and gives suggestions for the future work.

7.1 CONCLUSIONS

The objective of this study was to investigate and develop a new inertial electromechanical transducer for the implementation of velocity feedback loops that control the broadband vibration of distributed structures. The idea for the new transducers was based on the inerter element that has been used to augment the inertia effect by using a rotational mass element. A comprehensive theoretical study has been performed to assess the benefits of using the proposed actuators for the velocity feedback control applications. Three new prototypes with the flywheel element have been designed and fabricated. The prototypes were analysed based on typical electromechanical FRFs of inertial actuators. Finally, the stability and performance of the velocity feedback loops with the fabricated prototype has been assessed. The experimental results have been compared with the these obtained for a classical inertial actuator used for the active vibration control applications.

Chapter two has presented simulation results for the new inertial electrodynamic actuator with a flywheel element for velocity feedback control loops on flexible structures. Four different configurations have been considered where the flywheel is either hinged or pinned to either the proof mass or the case of the actuator. The study has introduced a lumped parameter model and an impedance – mobility electromechanical formulation for the operation of the feedback loop. The kinetic and kinematic response of the classical and four proposed flywheel proof mass actuators were first investigated considering spectra of six electromechanical FRFs. The stability and control performance of velocity feedback loops using the classical and four proposed flywheel actuator was considered assuming the control loops operate

on a thin rectangular panel excited by an acoustic plane wave. The performance of the point velocity feedback loops have been assessed based on the total flexural kinetic energy of the panel. Finally, a parametric and scaling study was introduced to give basic guidelines for designing flywheel prototypes.

The theoretical study presented in this chapter has shown that the inertial transducers could be equipped with the flywheel element that has one mechanical terminal attached to the base mass while to other mechanical terminal to the proof mass of the inertial transducer. The simulated electromechanical FRFs of the proposed flywheel inertial actuators have shown that the fundamental resonance frequency of the transducer can be lowered with the axial inertia effect produced by the flywheel element. The simulated blocked force FRFs per unit current fed to the proposed flywheel actuators has shown that with the increase of the axial inertia effect produced by the flywheel element the constant force effect at frequencies above the fundamental resonance frequency of the actuator diminishes. Thus to obtain the same vale of control force as the classical inertial actuator, the proposed flywheel inertial actuators need to be fed with much higher control signals. This result showed that it is important to scale the electromechanical components of the actuator that could withstand the high current signals that would be fed to the coil when the maximum feedback control gains are implemented. The stability analysis has shown that for all configurations of the actuator, the addition of the flywheel element increases the gain margin of the feedback loop without any increase of a total mass of the actuator. As a result the feedback loops using the proposed proof mass actuators with the flywheel element were characterised by improved control performance thanks to the possibility of implementing higher control gains. Results showed that the actuators equipped with the flywheel element attached either to base or to proof mass present similar control performance. However, slightly higher reductions were obtained when the flywheel was attached to the proof mass. The control performance study has highlighted that when the actuator with the flywheel element is used to implement a velocity feedback, the additional inertia effect produced by the flywheel element tends to lower the low frequency range where the destabilising positive feedback effect occurs. The parametric and scaling study presented in this chapter has shown that the control performance and rebusteness to shocks of the velocity feedback control loops can be improved when the inertial mass is shifted twoards the flywheel element. Also the static deflection of the inertial actuator can be improved when the radius of the gear mechanism that transforms the axial oscillations of the proof mass into angular oscillations of the flywheel is reduced. Finally, the scaling

study has shown that the proposed flywheel element could be used to effectively reduce the fundamental natural frequency of the actuator allowing then the use of small scale devices.

Chapter three has presented the design of two flywheel electromagnetic inertial actuators. The prototypes were designed based on a commercially available linear electromagnetic actuator. The first prototype was designed with a hinged while the second prototype with the pinned flywheel element analogously to the theoretical study presented in chapter two. The flywheel element of the hinged configuration was designed in a form of a rocker arm with four lumped masses. The pinned configuration was equipped with the flywheel element designed in a form of a wheel. The shape of the flywheel element was optimised to maximise the polar moment of inertia and minimise the total weight. The flexural bearings were used to minimise the backlash between the components and to avoid any nonlinear effects caused by stick-slip effect. The dynamic response of the classical and two flywheel prototypes were investigated considering spectra of electromechanical FRFs. The properties of the classical and flywheel configurations were also compared with the mathematical simulation obtained from the simplified lumped parameter model.

The study presented in this chapter has shown that it is vitally important for a flywheel inertial actuator to design a proper mechanism that can transform the axial oscillations of the inertial mass into angular oscillations of the flywheel. Also the suspension system of the flywheel element should be designed with soft torsional spring that has comparatively much higher axial stiffness. The design of both elements should be done with flexural hinges to minimise the nonlinear effects caused by the backlash or stick-slip effect. The experimental test results of both prototypes have confirmed the expected dynamics of the flywheel element that were previsioned in chapter two. The electromechanical properties of the flywheel prototypes assessed based on simulation and experimental results have shown that the fundamental resonance frequency of transducers can be reduced with the axial inertia effect produced by the flywheel element. The experimental results of the hinged configuration showed that the play and backlash effect between the components introduces nonlinearities in the dynamics of the transducer. Hence, the hinged configuration did not fulfil the requirement of an inertial actuator to implement more stable and robust velocity feedback loop. Finally, the static deflection study has demonstrated that the flywheel element can be used to reduce the fundamental resonance frequency of the transducer without increasing the inertial mass. Thus, the

flywheel element can improve stability and robustness to shocks of the implemented velocity feedback loops by lowering the spillover effect at the fundamental resonance frequency of the actuator without increasing the static deflection of the actuator.

Chapter four has presented a new piezoelectric actuator that can be used to implement a velocity feedback loop to reduce the flexural vibration of large flexible structures. The new actuator was designed with a long beam flywheel element suspended with flexural bearings. The developed control unit was more compact and lightweight than ordinary unit with axial inertial mass. The electromechanical properties of a classical and flywheel prototype were assessed based on the simulation and experimental results of the actuators FRFs. The study has considered the mechanical base impedance, the blocked force and the electrical admittance FRFs. The experimental testes were matched with numerical results derived from a new lumped parameter model for the piezoelectric inertial actuator.

The study presented in this chapter has confirmed that the axial inertia effect produced by the flywheel element can be used to reduce the fundamental resonance frequency of the actuator without increasing the inertial mass. However, the flywheel element with high axial inertia effect can also reduce the higher resonance frequencies of the inertial actuators and induce additional dynamics. The study has also showed that the flywheel piezoelectric stack actuator could be a good alternative to electromagnetic actuators or piezo patches in the active vibration control applications. The electromechanical properties of the flywheel prototype assessed based on simulation and experimental results have shown that when the actuator is driven with constant current, the point force produced by the inertial actuator above the fundamental resonance frequency of the actuator tends to decrease with frequency. In contrast, when the actuator is driven with constant voltage, the point force produced by the inertial actuator above the fundamental resonance frequency of the actuator remains constant with frequency. Thus, for the implementation of a uniform velocity feedback control with the flywheel piezoelectric actuator it is preferable to implement voltage driven control, contrary to the current driven control for the electromagnetic actuator. The study has also shown that for the voltage driven piezoelectric actuator the required current rises proportionally to the piezo capacitance and driving frequency. Thus, to efficiently control the structure at higher frequencies the inertial actuators would require amplifiers that can provide high power. The switching topology of the amplifiers would be more preferable compared

to the linear amplifiers because of their high efficient thanks to the power recovery system when driving piezoelectric actuators.

Chapter five has presented the test setup with a supported plate to implement the velocity feedback loops with the proposed flywheel inertial actuators. The setup has been used to evaluate the stability and control performance of the velocity feedback loop implemented on thin rectangular plate using electromagnetic inertial actuators. The stability and control performance has been assessed for the feedback loops using the classical, classical with the same inertial mass as the flywheel configuration and the pinned configuration of the flywheel inertial actuator. The stability of the velocity feedback loops has been assessed both for voltage and current driven inertial actuators. The performance of the feedback loops has been assessed considering the velocity at the control position and the total flexural kinetic energy of the hosting structure. Finally, the performance of the velocity feedback loops using three configurations of the inertial actuator have been compared based on the frequency averaged plate kinetic energy reduction.

The experimental results presented in this chapter confirmed the that the flywheel inertial actuators can improve the control performance of the velocity feedback loops to reduce the broadband vibration of thin plate. The experimental tests of the velocity feedback loop stability and control performance have confirmed the expected results previsioned in the theoretical study presented in chapter two. The stability study presented in this chapter has shown that the actuator with additional flywheel element has much higher gain margin of the feedback loop compared to the classical configurations. The performance study has shown that the feedback loops using the flywheel inertial actuators are characterised by a slightly better control performance thanks to increased signal gain margins. This is a rather important results, particularly in view of the fact that the proposed flywheel actuator is characterised by much smaller static displacements and thus can be also used in presence of large shock effects due to undesired persistent excitations.

Chapter six has investigated the possibility of using the proposed flywheel inertial transducer for energy harvesting applications. Both simulation and experimental results of energy harvesting with the classical, classical with the same inertial mass as the flywheel configuration and proposed pinned flywheel electromagnetic transducer connected to a purely resistive load have been presented.

The experimental results presented in this chapter have shown that the flywheel element reduces the fundamental resonance frequency of the actuator without significantly increasing the total mass of the transducer and without increasing the damping coefficient of the transducer. Although, the flywheel element reduces the fundamental resonance frequency of the transducer where ambient vibration amplitudes are normally higher and more preferable for the energy harvesting applications, the tested prototype presented lower energy harvesting performance compared to the classical configuration with the same inertial mass as the flywheel prototype. Experimental results have shown that the pinned flywheel prototype presented lower energy harvesting performance by about 25% compared to the classical transducer with the same inertial mass as the flywheel configuration. It is worth to point out that the electromagnetic transducer used in this study was characterised by high damping value which is disadvantageous for the energy harvesting applications. Thus, a proper design of the new transducer could lead to a device with even higher energy harvesting capabilities.

Results presented in this thesis suggest that the future flywheel prototype for active vibration control and energy harvesting applications could be designed with much lower damping coefficient of the inertial mass suspension system. The axial inertia effect produced by the flywheel element would maintain good performance of the velocity feedback loop thanks to high signal gain margin and at the same time, the flywheel inertial prototype would be characterised with much higher energy harvesting performance thanks to low damping coefficient compared to the classical inertial transducer.

Based on the experimental results of the tree flywheel inertial actuators a list of advantages and disadvantages of the flywheel inertial configuration compared to the classical inertial transducer is shown in Table 7.1. The advantages are concentrated around the improved performance and stability of the velocity feedback loops, while the disadvantages are focused on the complexity and price of the flywheel components. Some of the described disadvantages could by avoided by designing new flywheel inertial transducer.

Table 7.1. Advantages and disadvantages of the flywheel inertial configuration compared to the classical inertial transducer.

Advantages	Disadvantages
Reduces the fundamental resonance frequency of the actuator.	Reduces the constant force effect at the frequencies above fundamental resonance frequency of the actuator.
Does not increase the static deflection of the inertial mass.	Increases the impedance of the proof mass suspension system.
Maintains low weight of the inertial mass.	Lowers the energy harvesting capabilities compared to the transducer with the same inertial mass.
Lowers the feedback control spillover effect at the fundamental resonance frequency of the actuator.	Increases the complexity of the inertial transducer, which leads to the additional dynamics.
Increases signal gain margin of the velocity feedback control loop.	Increases the costs due to additional components.
Improves actuator robustness in case of shocks and high accelerations.	

7.2 FUTURE WORK

The future work could be carried in the following topics listed below.

- Development of a mechanism that can transform the linear motion of the transducer into constant spinning motion, instead of oscillatory, of the flywheel element to reduce the nonlinear effects (e.g. stick-slip).
- Development of a device without flexural bearings that are relatively expensive and have limited angular range.
- Development of a device that is equipped just with flywheel element instead of the proof mass.
- Development of a device that would have the main axis of flywheel rotation perpendicular to the surfaces of the structure.
- Further miniaturisation of the actuators and the controller units. Although the used actuators are quite small-scale, the cumulative mass added to the structure could to be reduced.

- A full integration of the control system components into the smart panel, which should provide further savings in space and weight.
- A study on the MIMO velocity feedback control system with flywheel inertial actuators.
- A future research could be focused on the design of a control unit dedicated for energy harvesting applications.

LIST OF PUBLICATIONS

1. A. Kras and P. Gardonio, "Velocity feedback control with a flywheel proof mass actuator," *Journal of Sound and Vibration*, vol. 402, pp. 31–50, 2017.

2. A. Kras and P. Gardonio, "Flywheel proof mass actuator for velocity feedback control," in *Proceedings of the International Conference on Motion and Vibration Control (MoViC) and of the International Conference on Recent Advances in Structural Dynamics (RASD)*, 2016, pp. 1–14.

3. A. Kras and P. Gardonio, "Flywheel inertial actuator for velocity feedback control: parametric study," in *Proceedings of the international conference on noise and vibration engineering ISMA2016*, 2016, pp. 1217–1231.

4. A. Kras and P. Gardonio, "Flywheel proof mass transducer for energy harvesting applications," in *Proceedings of the VIII ECCOMAS Thematic Conference on Smart Structures and Materials, SMART 2017*, 2017, pp. 642–653.

5. A. Kras and P. Gardonio, "Experimental tests of a flywheel inertial actuator," in *Proceedings of the 24th International Congress on Sound and Vibration, ICSV 2017*, 2017, pp. 1–8.

6. A. Kras and P. Gardonio, "Flywheel piezoelectric actuator for active vibration control applications," in *Proceedings of SPIE 10595, Active and Passive Smart Structures and Integrated Systems XII, 105951T*, 2018, pp. 1–12.

7. A. Kras and P. Gardonio, "Experimental tests of a flywheel proof mass actuator for velocity feedback control," in *Proceedings of the international conference on noise and vibration engineering ISMA2018*, 2018, (submitted).

8. A. Kras and P. Gardonio, "Flywheel inertial actuator for velocity feedback control: experimental implementation," *Journal of Sound and Vibration*, (in preparation).

9. A. Kras and P. Gardonio, “Flywheel inertial actuator for velocity feedback and vibration control,” in *“ANTARES”Advanced Training and Research in Energy efficient Smart Structures*, W. Desmet, B. Pluymers, S. Ophem, P. Becht, Ed. KU Leuven, 2018.

A

TECHNICAL DRAWINGS OF THE EM PROTOTYPES

The following appendix consists technical drawings of the manufactured components for two EM flywheel prototypes. The assembly drawings are followed by the exploded view drawings and by the detailed drawings of each component.

The ANT16100 and ANT16103 drawings in edition A present the pinned flywheel prototype with the fabricated pushing pin that did not demonstrate the required flexibility. The ANT16100 and ANT16103 drawings in edition B present the pinned flywheel prototype with the fabricated pushing pin that uses the third flexural bearing to transmit the linear motion of the actuator into rotation of the flywheel.

The ANT162 drawings present the hinged flywheel prototype.

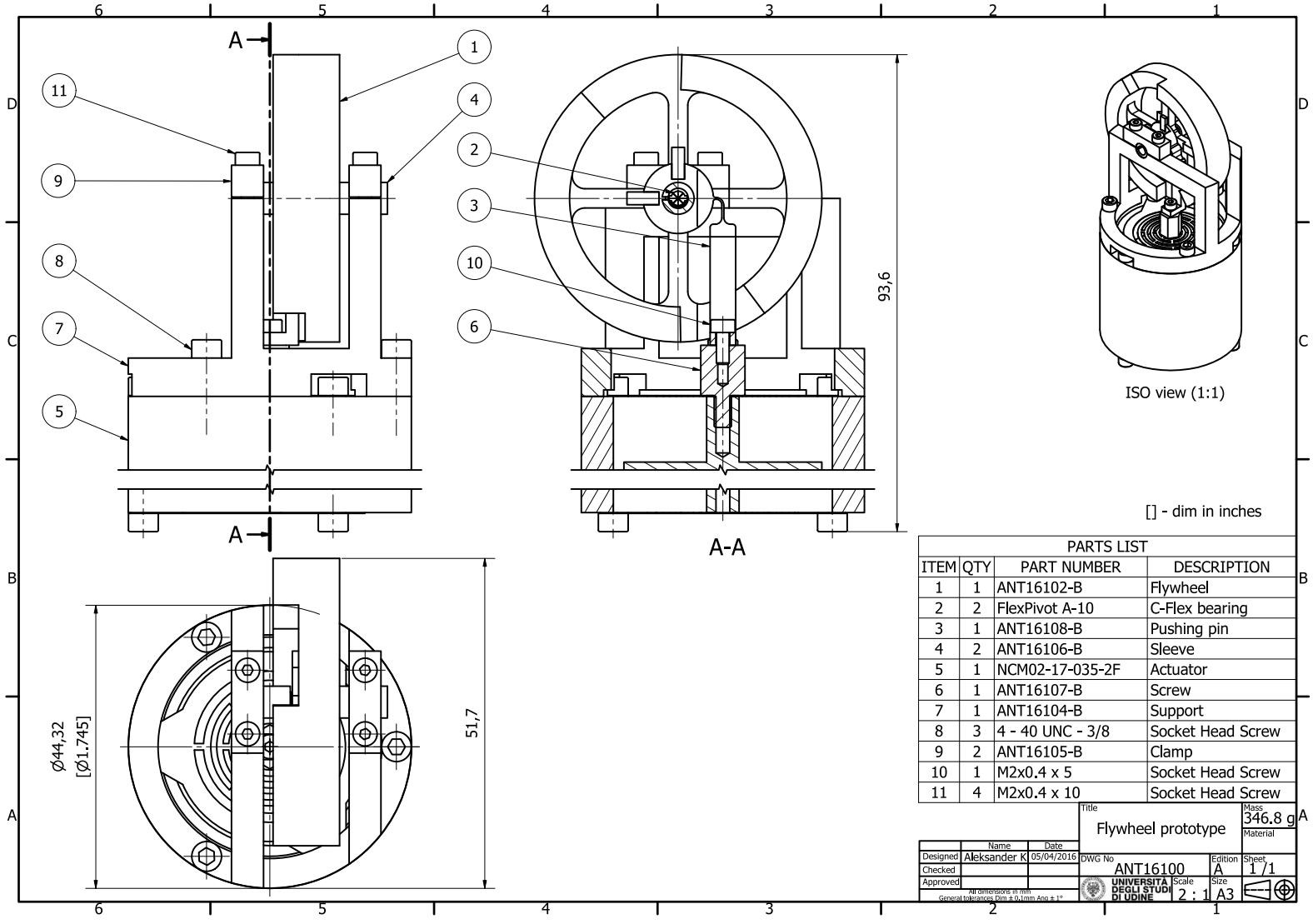

PARTS LIST			
ITEM	QTY	PART NUMBER	DESCRIPTION
1	1	ANT16102-B	Flywheel
2	2	FlexPivot A-10	C-Flex bearing
3	1	ANT16108-B	Pushing pin
4	2	ANT16106-B	Sleeve
5	1	NCM02-17-035-2F	Actuator
6	1	ANT16107-B	Screw
7	1	ANT16104-B	Support
8	3	4 - 40 UNC - 3/8	Socket Head Screw
9	2	ANT16105-B	Clamp
10	1	M2x0.4 x 5	Socket Head Screw
11	4	M2x0.4 x 10	Socket Head Screw

	Name	Date
Designed	Aleksander K	05/04/2016
Checked		
Approved		

All dimensions in mm
General tolerances Dim ± 0,1mm Ang ± 1°

Title: Flywheel prototype
Mass: 346.8 g
Material:
DWG No: ANT16100
Edition: A
Sheet: 1 /1
UNIVERSITÀ DEGLI STUDI DI UDINE
Scale: 2 : 1
Size: A3

PARTS LIST

ITEM	QTY	PART NUMBER	DESCRIPTION
1	1	ANT16102-B_ Flywheel	Flywheel
2	1	ANT16104-B_ Support	Support
3	2	ANT16105-B_ Clamp	Clamp
4	2	ANT16106-B_ Sleeve	Sleeve
5	1	ANT16107-C_ Screw	Screw
6	1	ANT16108-B_ Pushing_pin	Pushing pin
7	2	Flex Pivot A-10	C-Flex bearing
8	1	NCM02-17-03 5-2F	Actuator
9	3	4 - 40 UNC - 3/8 HS HCS	Socket Head Cap Screw
10	1	M2x0.4 x 5 A2	Socket Head Cap Screw
11	4	M2x0.4 x 10 A2	Socket Head Cap Screw

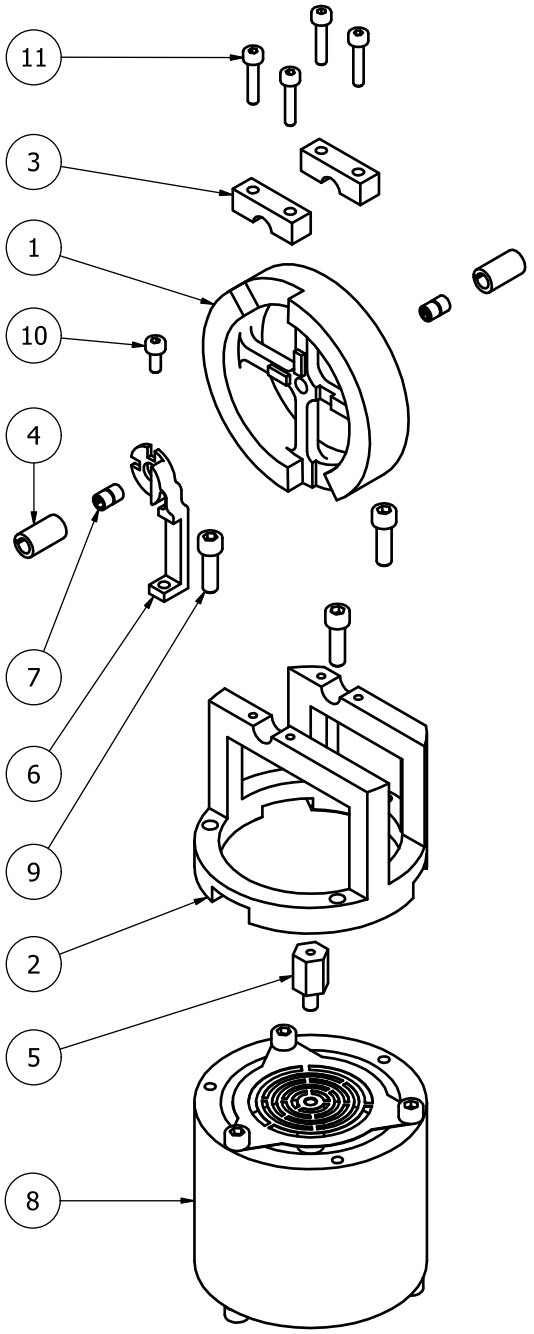

	Name	Date
Designed	Aleksander K	22/03/2016
Checked		
Approved		

All dimensions in mm
General tolerances Dim ± 0.1 mm Ang ± 1°

Title: Flywheel assembly exploded
Mass: 346.8 g
Material:
DWG No: ANT16103
Edition: A
Sheet: 1 /1
UNIVERSITÀ DEGLI STUDI DI UDINE
Scale: 1 : 1
Size: A4

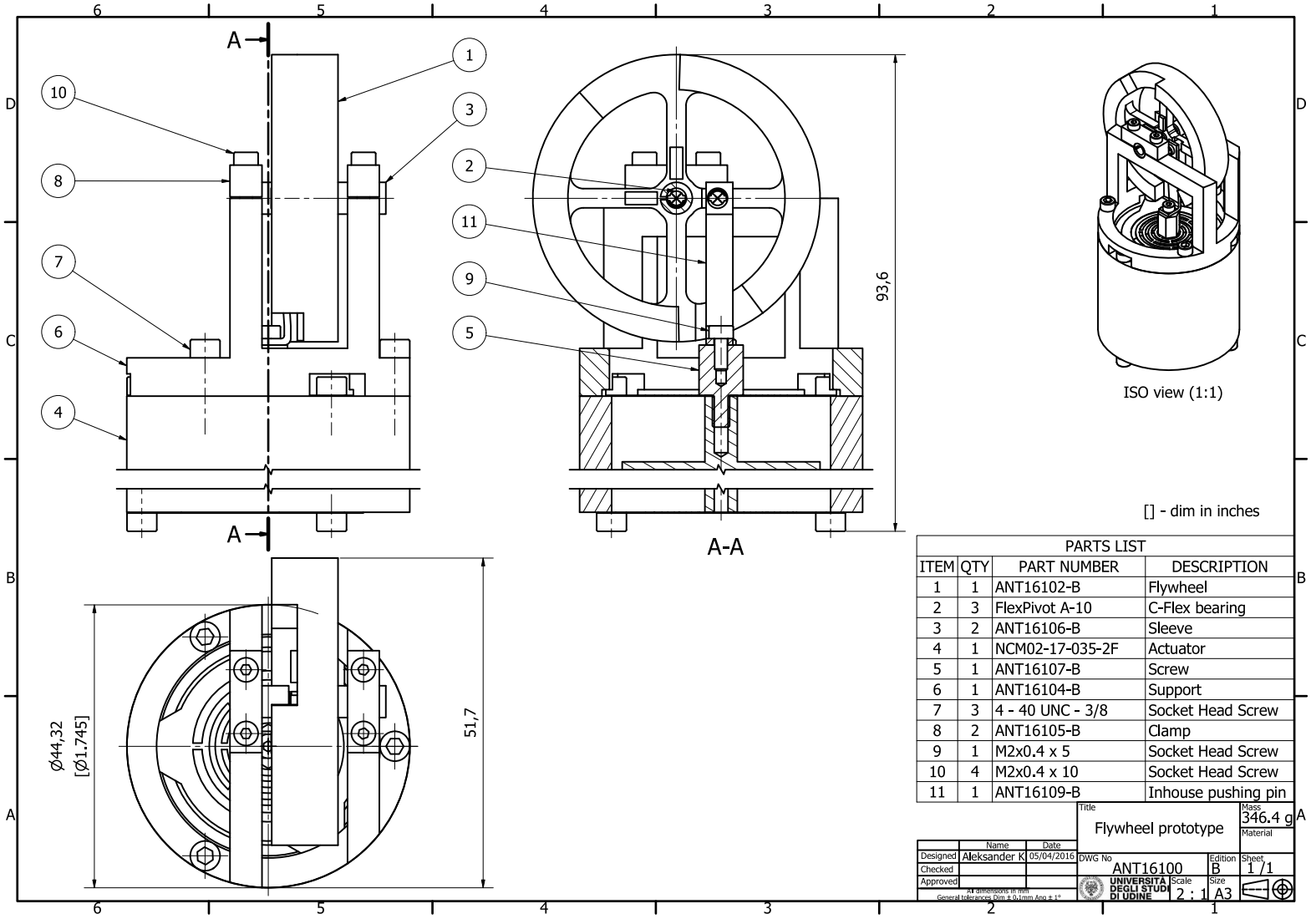

PARTS LIST			
ITEM	QTY	PART NUMBER	DESCRIPTION
1	1	ANT16102-B	Flywheel
2	3	FlexPivot A-10	C-Flex bearing
3	2	ANT16106-B	Sleeve
4	1	NCM02-17-035-2F	Actuator
5	1	ANT16107-B	Screw
6	1	ANT16104-B	Support
7	3	4 - 40 UNC - 3/8	Socket Head Screw
8	2	ANT16105-B	Clamp
9	1	M2x0.4 x 5	Socket Head Screw
10	4	M2x0.4 x 10	Socket Head Screw
11	1	ANT16109-B	Inhouse pushing pin

	Name	Date
Designed	Aleksander K	05/04/2016
Checked		
Approved		

All dimensions in mm
General tolerances Dim ± 0.1mm Ang ± 1°

Title: Flywheel prototype
Mass: 346.4 g
Material:
DWG No: ANT16100
Edition: B
Sheet: 1 /1
UNIVERSITÀ DEGLI STUDI DI UDINE
Scale: 2 : 1
Size: A3

PARTS LIST			
ITEM	QTY	PART NUMBER	DESCRIPTION
1	1	ANT16102-B_ Flywheel	Flywheel
2	2	Flex Pivot A-10	C-Flex bearing
3	2	ANT16105-B_ Clamp	Clamp
4	2	ANT16106-B_ Sleeve	Sleeve
5	1	ANT16107-C_ Screw	Screw
6	1	ANT16109-A_Inhouse_pushing_pin	Pushing pin
7	1	ANT16104-B_ Support	Support
8	1	NCM02-17-035-2F	Actuator
9	3	4 - 40 UNC - 3/8 HS HCS	Socket Head Cap Screw
10	1	M2x0.4 x 5 A2	Socket Head Cap Screw
11	4	M2x0.4 x 10 A2	Socket Head Cap Screw

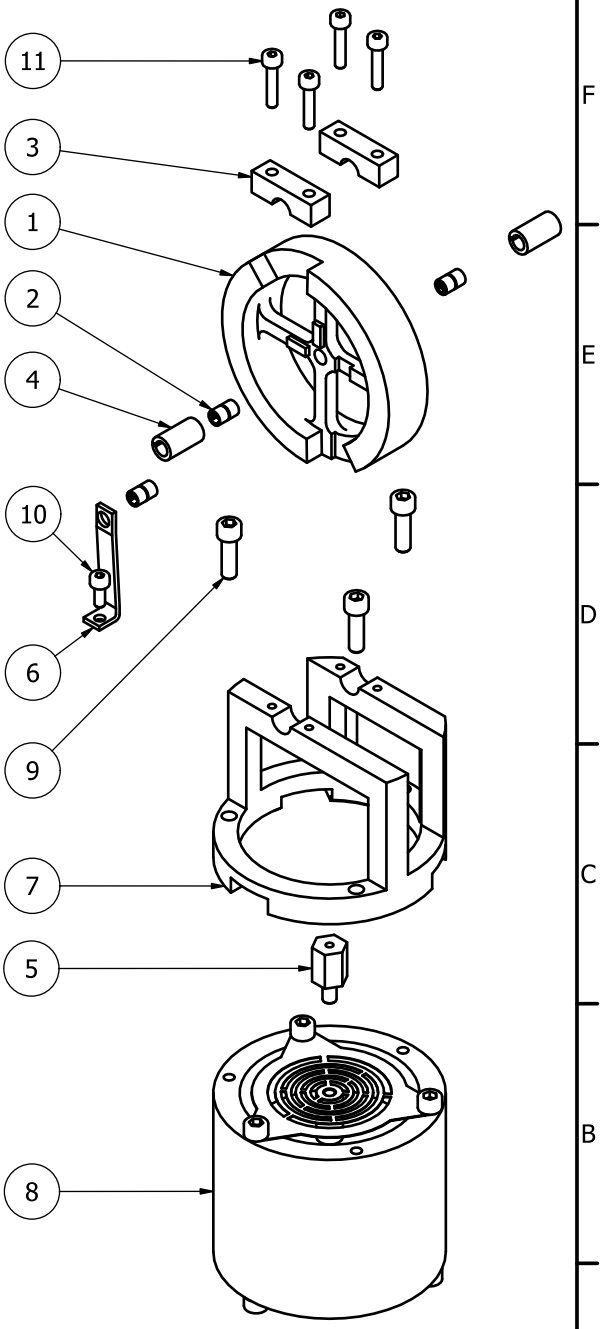

	Name	Date
Designed	Aleksander K	22/03/2016
Checked		
Approved		

All dimensions in mm
General tolerances Dim ± 0.1 mm Ang ± 1°

Title: Flywheel assembly exploded
Mass: 346.4 g
Material:
DWG No: ANT16103
Edition: B
Sheet: 1 /1
UNIVERSITÀ DEGLI STUDI DI UDINE
Scale: 1 : 1
Size: A4

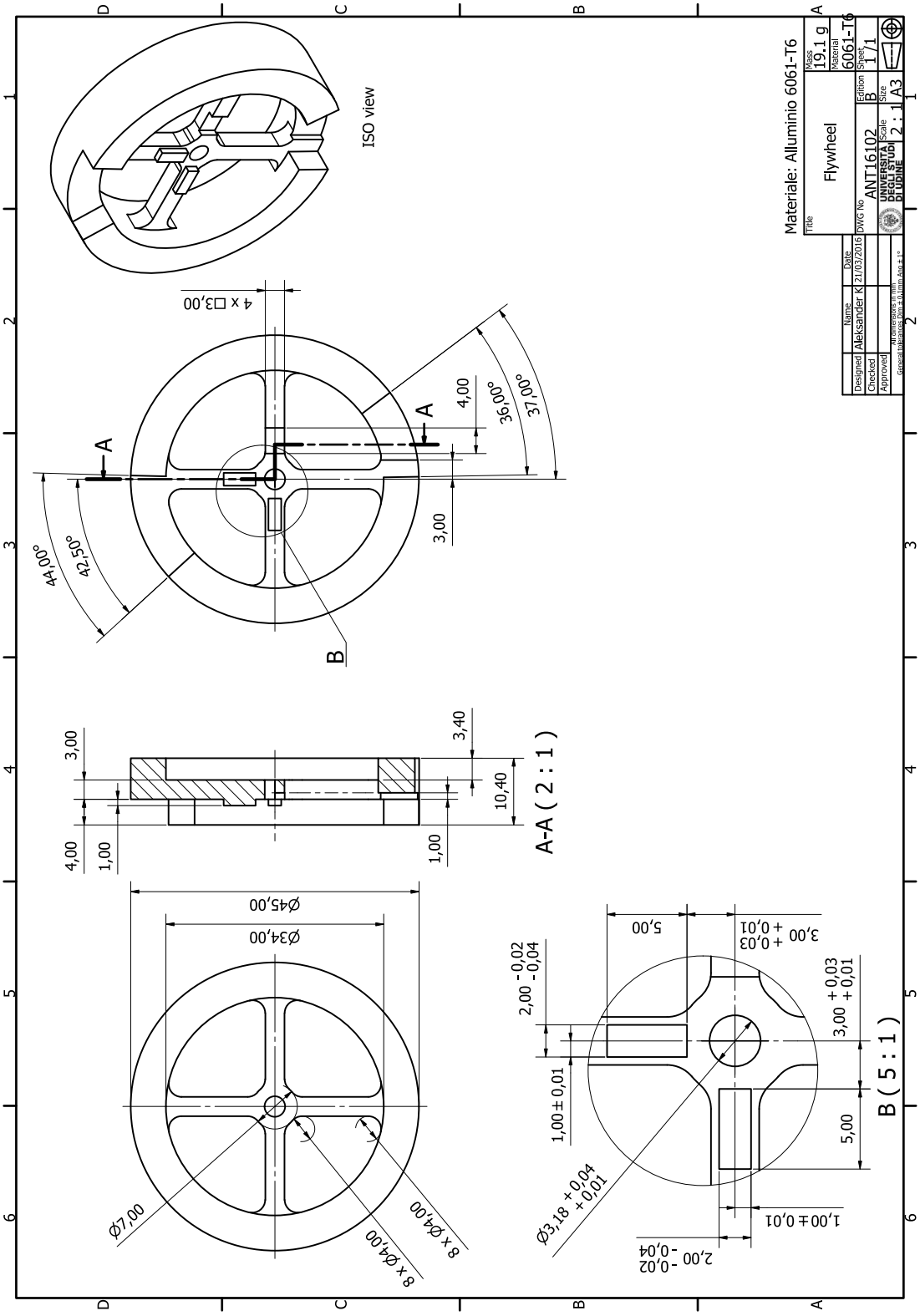
Materiale: Alluminio 6061-T6
Title
Flywheel
Mass
19,1 g
Material
6061-T6
Sheet
1/1
Edition
B
Size
A3
Scale
2 : 1
DWG No.
ANT16102
UNIVERSITÀ DEGLI STUDI DI UDINE
Name
Date
Designed
Aleksander K
21/03/2016
Checked
Approved
All dimensions in mm
General tolerances Dim ± 0,1mm Ang ± 1°
ISO view
4 x □3,00
A
B
44,00°
42,50°
36,00°
37,00°
4,00
3,00
A-A (2 : 1)
3,00
4,00
1,00
3,40
10,40
1,00
Ø45,00
Ø34,00
Ø7,00
8 x Ø4,00
8 x Ø4,00
B (5 : 1)
5,00
3,00 +0,03 +0,01
2,00 -0,02 -0,04
1,00 ± 0,01
3,00 +0,03 +0,01
5,00
Ø3,18 +0,04 +0,01
1,00 ± 0,01
2,00 -0,02 -0,04

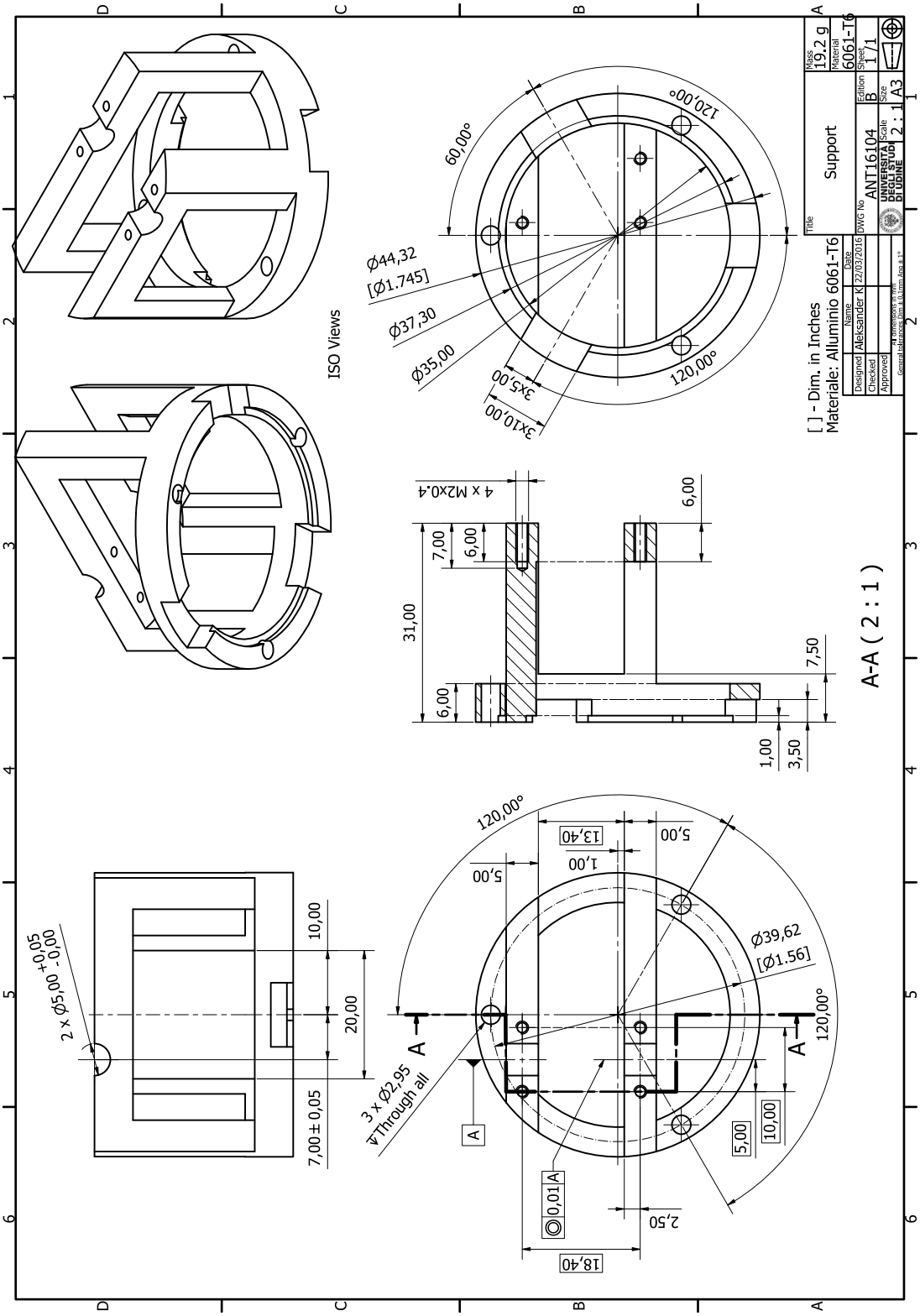
ISO Views
A-A (2 : 1)
[ ] - Dim. in Inches
Materiale: Alluminio 6061-T6
Support
ANT16104
UNIVERSITÀ DEGLI STUDI DI UDINE
Mass 19.2 g
Material 6061-T6
Sheet 1 / 1
Edition B
Size A3
Scale 2 : 1
Designed Aleksander K 22/03/2016
Checked
Approved
Ø44,32 [Ø1.745]
Ø37,30
Ø35,00
3x10,00
3x5,00
60,00°
120,00°
4 x M2x0.4
31,00
7,00
6,00
6,00
6,00
7,50
1,00
3,50
2 x Ø5,00 +0,05 -0,00
10,00
20,00
7,00 ± 0,05
3 x Ø2,95 Through all
13,40
5,00
1,00
Ø39,62 [Ø1.56]
0,01 A
2,50
18,40
5,00
10,00

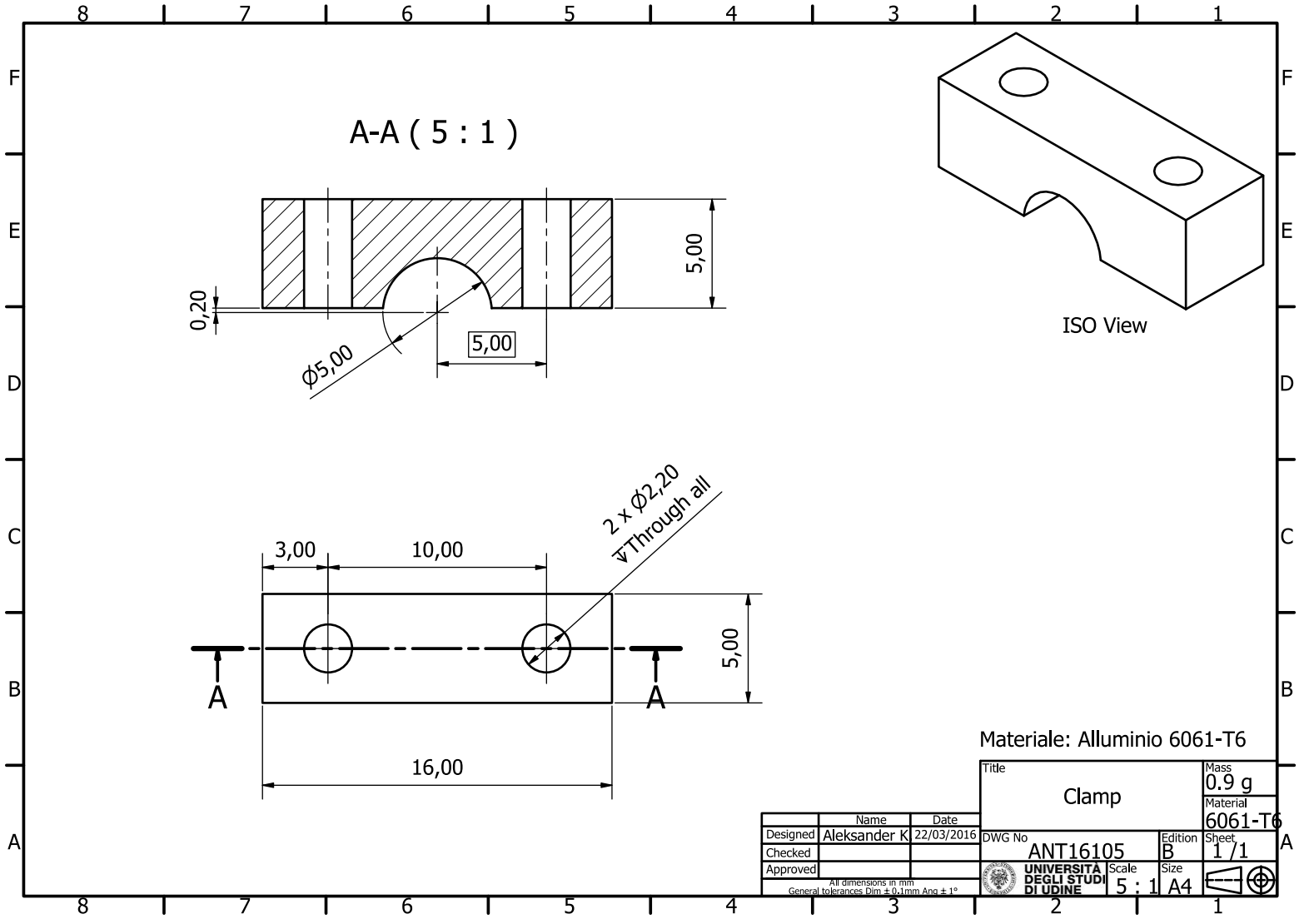
A-A (5 : 1)
0,20
5,00
ϕ5,00
5,00
ISO View
2 x ϕ2,20
Through all
3,00
10,00
5,00
A
A
16,00
Materiale: Alluminio 6061-T6
Name
Date
Designed
Aleksander K
22/03/2016
Checked
Approved
All dimensions in mm
General tolerances Dim ± 0,1mm Ang ± 1°
Title
Clamp
Mass
0.9 g
Material
6061-T6
DWG No
ANT16105
Edition
B
Sheet
1 /1
UNIVERSITÀ DEGLI STUDI DI UDINE
Scale
5 : 1
Size
A4

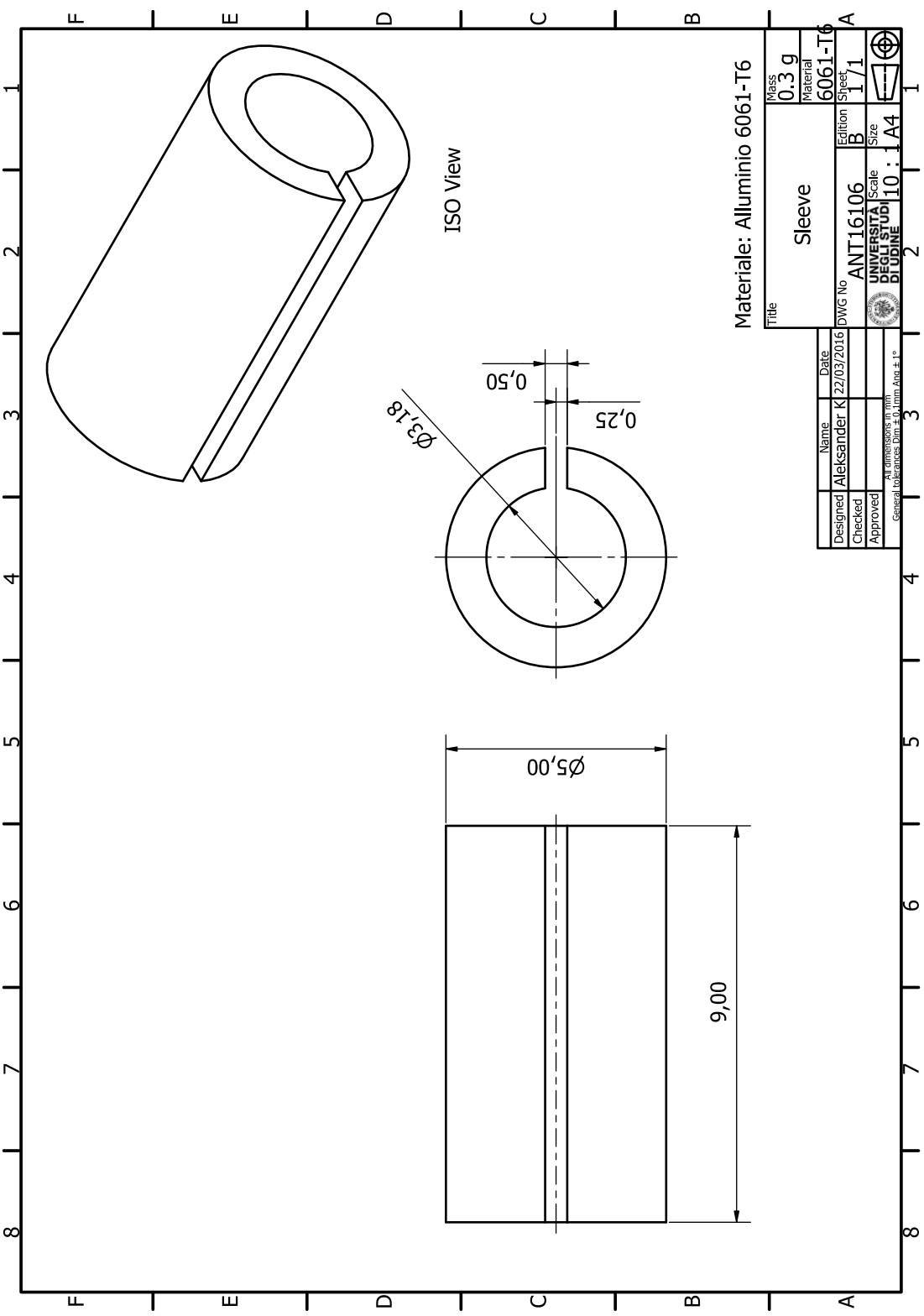
ISO View
Ø3,18
0,50
0,25
Ø5,00
9,00
Materiale: Alluminio 6061-T6
Mass 0.3 g
Material 6061-T6
Sheet 1/1
Edition B
Size A4
Scale 10 : 1
Title Sleeve
DWG No ANT16106
UNIVERSITÀ DEGLI STUDI DI UDINE
Designed Aleksander K 22/03/2016
Checked
Approved
Name Date
All dimensions in mm
General tolerances Dim ± 0.1mm Ang ± 1°

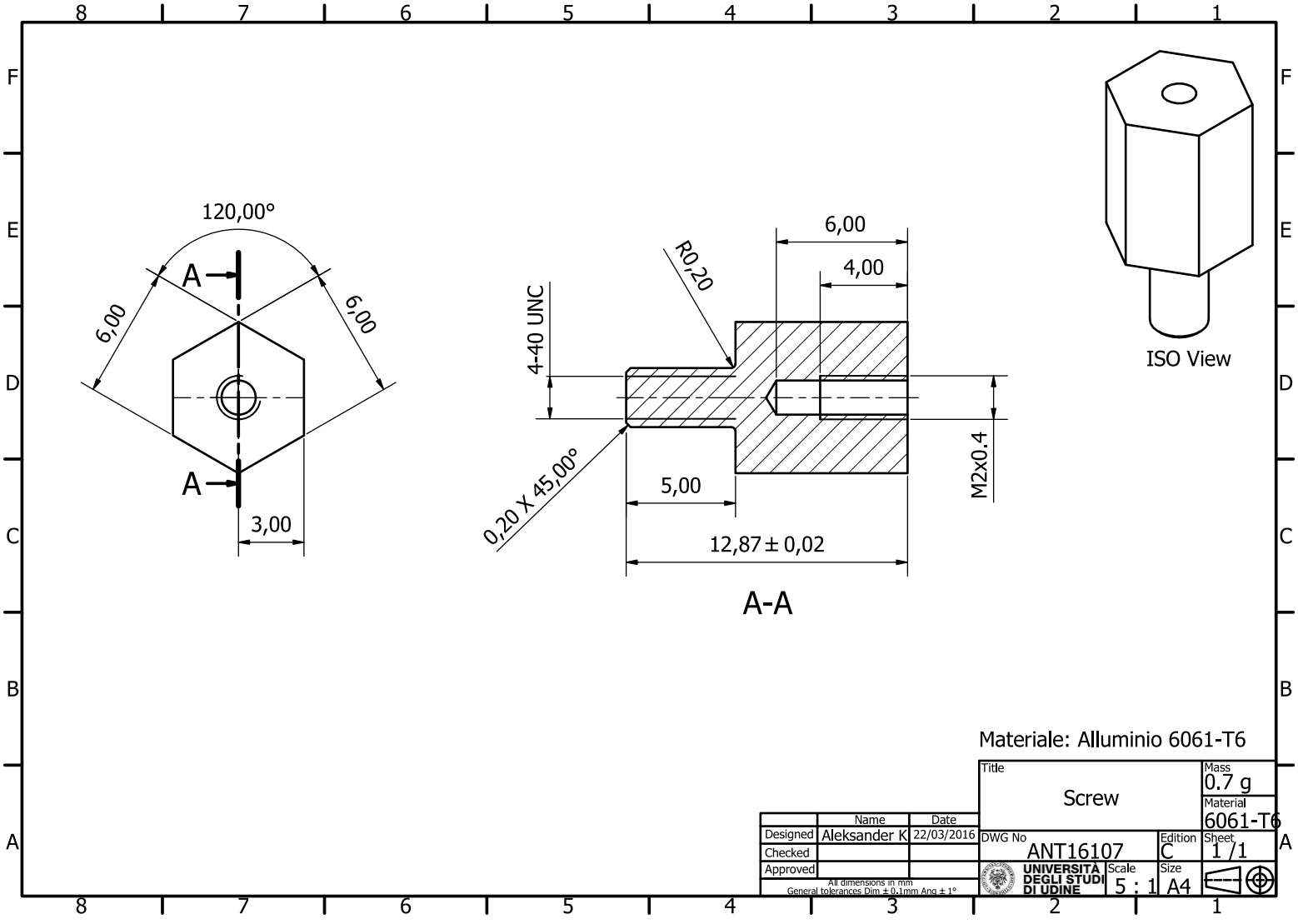
120,00°
A
A
6,00
6,00
3,00
6,00
4,00
R0,20
4-40 UNC
M2x0.4
0,20 X 45,00°
5,00
12,87 ± 0,02
A-A
ISO View
Materiale: Alluminio 6061-T6
Title
Screw
Mass
0.7 g
Material
6061-T6
Name
Date
Designed
Aleksander K
22/03/2016
Checked
Approved
All dimensions in mm
General tolerances Dim ± 0,1mm Ang ± 1°
DWG No
ANT16107
Edition
C
Sheet
1 /1
UNIVERSITÀ DEGLI STUDI DI UDINE
Scale
5 : 1
Size
A4

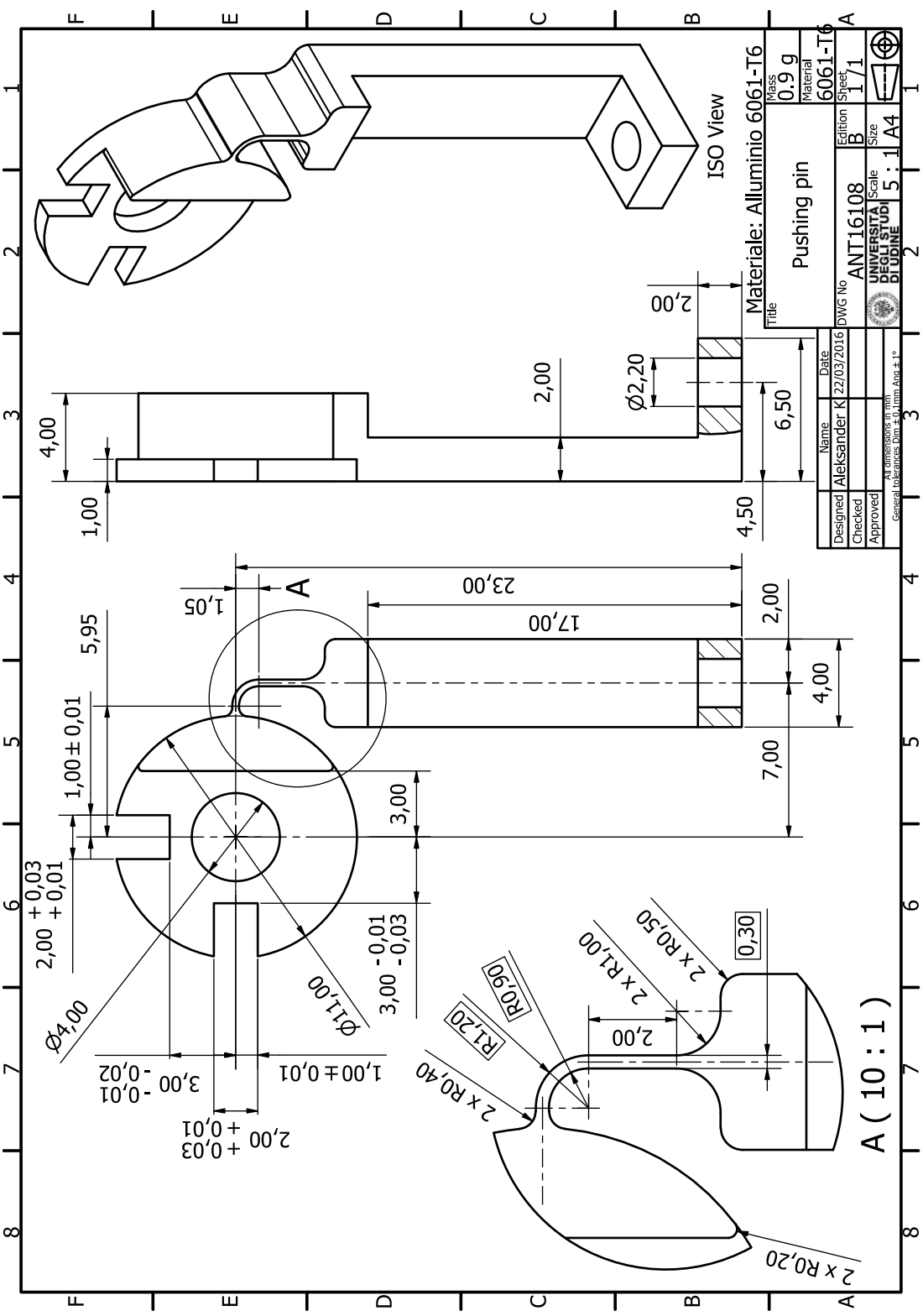
ISO View
Materiale: Alluminio 6061-T6
Pushing pin
ANT16108
UNIVERSITÀ DEGLI STUDI DI UDINE
Mass 0.9 g
Material 6061-T6
Sheet 1/1
Edition B
Scale 5 : 1
Size A4
Designed Aleksander K
Checked
Approved
Name
Date 22/03/2016
DWG No
Title
All dimensions in mm
General tolerances Dim ± 0,1mm Ang ± 1°
A (10 : 1)
2 x R0,20
2 x R0,40
2 x R0,50
2 x R1,00
R0,90
R1,20
0,30
2,00
1,00 ± 0,01
3,00 -0,01 -0,02
2,00 +0,03 +0,01
Ø4,00
Ø11,00
3,00 -0,01 -0,03
2,00 +0,03 +0,01
1,00 ± 0,01
5,95
1,05
A
23,00
17,00
2,00
4,00
7,00
3,00
4,00
1,00
2,00
Ø2,20
2,00
6,50
4,50

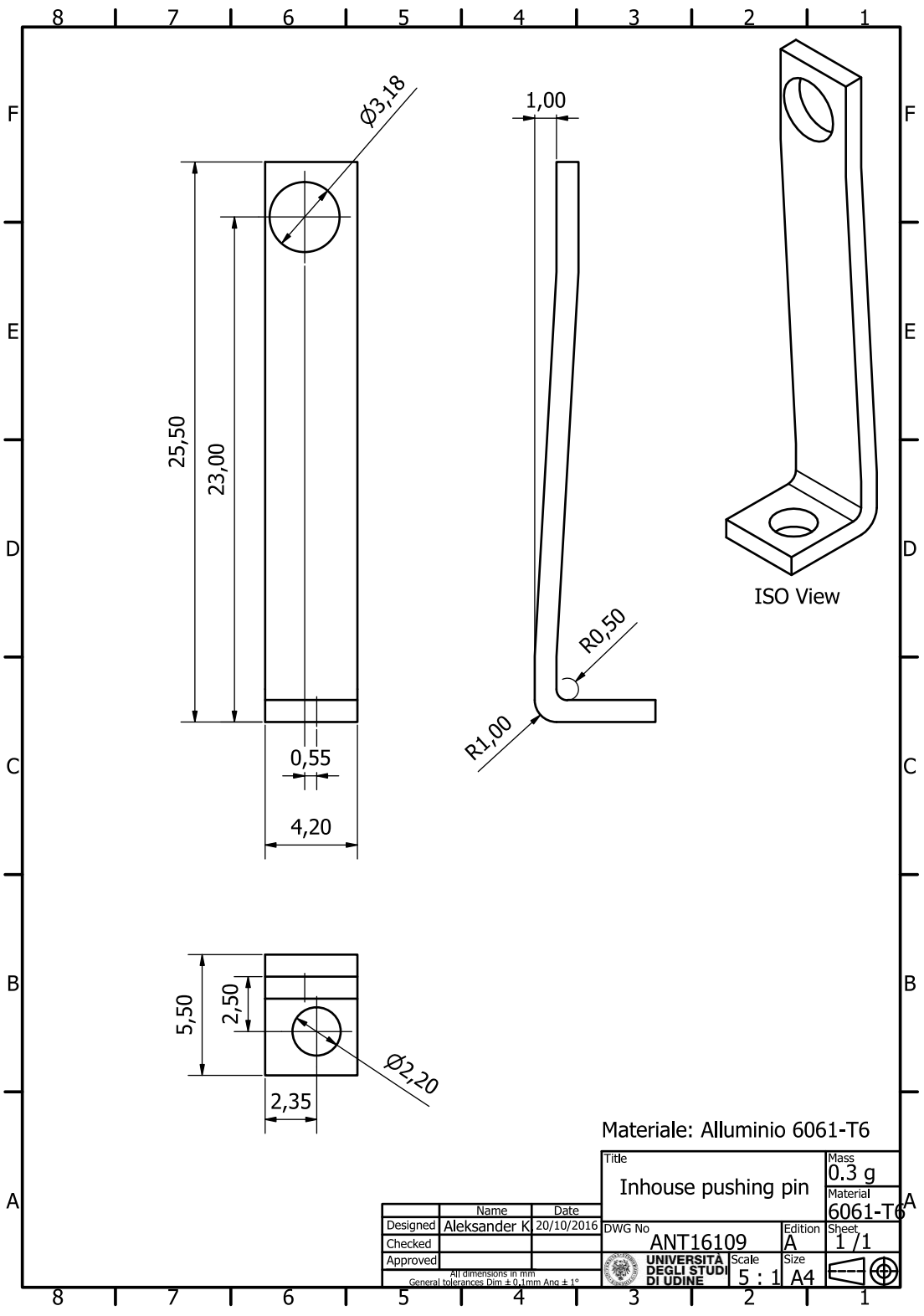
Ø3,18
1,00
25,50
23,00
0,55
4,20
R0,50
R1,00
ISO View
5,50
2,50
Ø2,20
2,35
Materiale: Alluminio 6061-T6
Title
Inhouse pushing pin
Mass
0.3 g
Material
6061-T6
Name
Date
Designed
Aleksander K
20/10/2016
Checked
Approved
DWG No
ANT16109
Edition
A
Sheet
1 /1
UNIVERSITÀ DEGLI STUDI DI UDINE
Scale
5 : 1
Size
A4
All dimensions in mm
General tolerances Dim ± 0,1mm Ang ± 1°

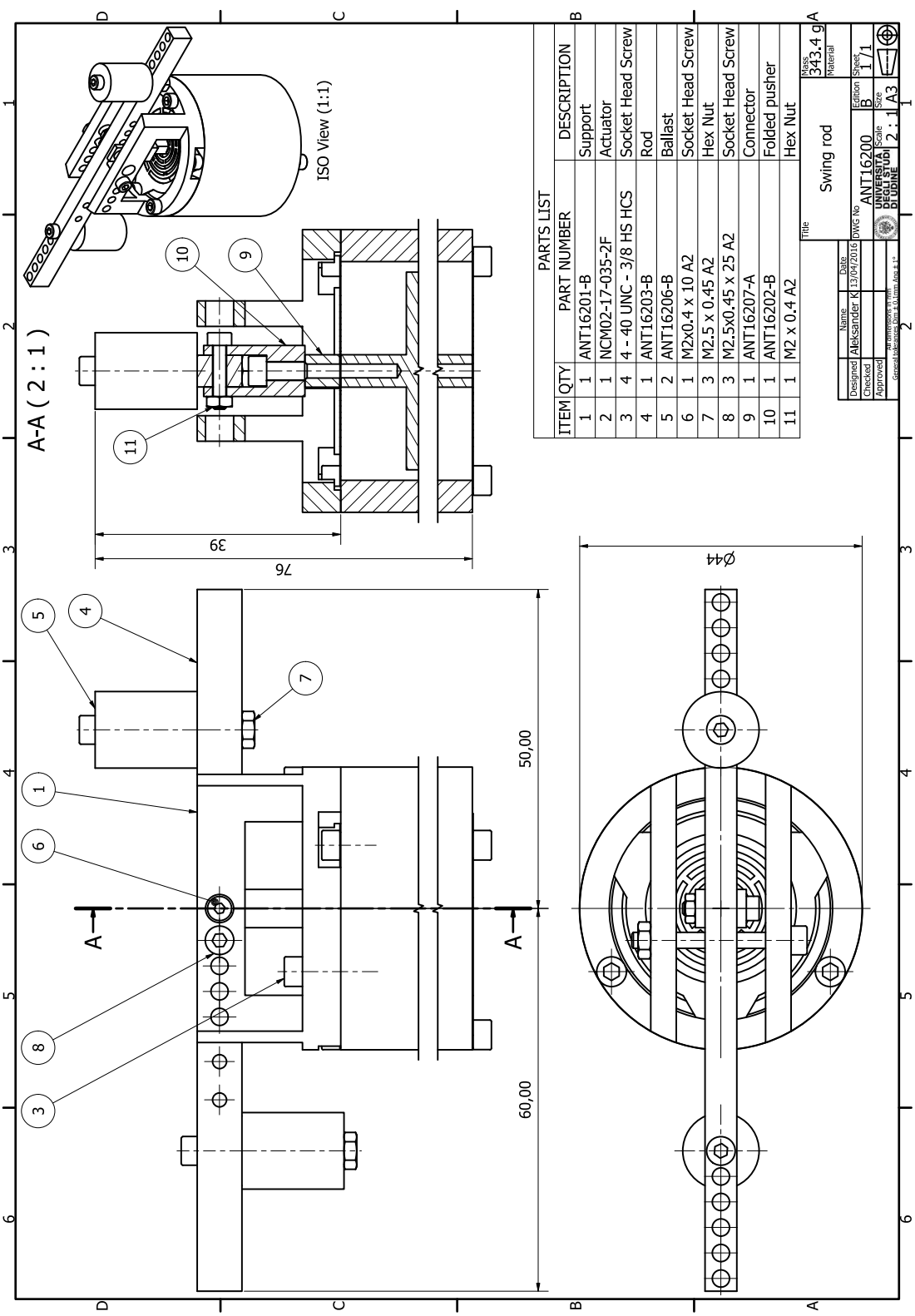
ISO View (1:1)
A-A (2 : 1)
PARTS LIST
ITEM QTY PART NUMBER DESCRIPTION
1 1 ANT16201-B Support
2 1 NCM02-17-035-2F Actuator
3 4 4 - 40 UNC - 3/8 HS HCS Socket Head Screw
4 1 ANT16203-B Rod
5 2 ANT16206-B Ballast
6 1 M2x0.4 x 10 A2 Socket Head Screw
7 3 M2.5 x 0.45 A2 Hex Nut
8 3 M2.5x0.45 x 25 A2 Socket Head Screw
9 1 ANT16207-A Connector
10 1 ANT16202-B Folded pusher
11 1 M2 x 0.4 A2 Hex Nut
Swing rod
Mass 343.4 g
Material
Name Date
Designed Aleksander K 13/04/2016
Checked
Approved
DWG No ANT16200
Edition B
Sheet 1/1
Scale 2 : 1
Size A3
UNIVERSITÀ DEGLI STUDI DI UDINE
All dimensions in mm
General tolerances Dim ± 0.1mm Ang ± 1°
50,00
60,00
39
76
Ø44

PARTS LIST

ITEM	QTY	PART NUMBER	DESCRIPTION
1	1	ANT16201-B_ Support	Support
2	1	NCM02-17-03 5-2F	Actuator
3	1	ANT16203-B_ Rod	Rod
4	2	ANT16206-B_ Ballast	Ballast
5	1	ANT16207-A_ Connector	Connector
6	1	ANT16202-B_ Folded_pusher	Folded pusher
7	3	M2.5x0.45 x 25	Screw
8	3	4 - 40 UNC - 3/8 HS HCS	Socket Head Cap Screw
9	1	4 - 40 UNC - 1/4 HS HCS	Socket Head Cap Screw
10	1	M2x0.4 x 10	Socket Head Cap Screw
11	3	M2.5 x 0.45	Hex Nut
12	1	M2 x 0.4	Hex Nut

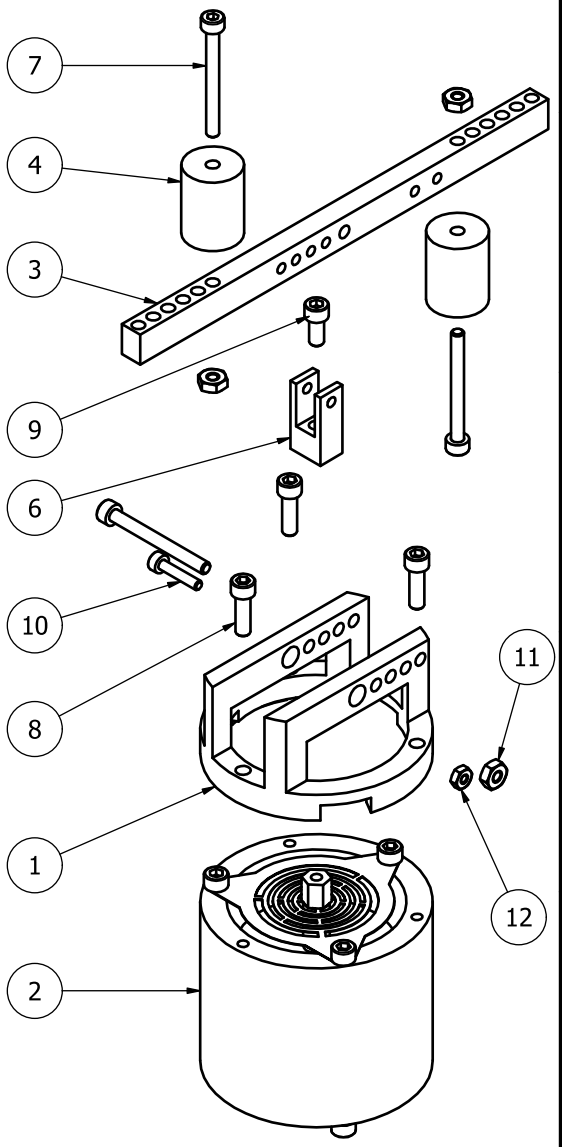

	Name	Date
Designed	Aleksander K	13/04/2016
Checked		
Approved		

All dimensions in mm
General tolerances Dim ± 0.1mm Ang ± 1°

Title: Swing rod assembly exploded

Mass: 343.4 g

Material:

DWG No: ANT16200

Edition: B

Sheet: 1 /1

UNIVERSITÀ DEGLI STUDI DI UDINE

Scale: 1:1

Size: A4

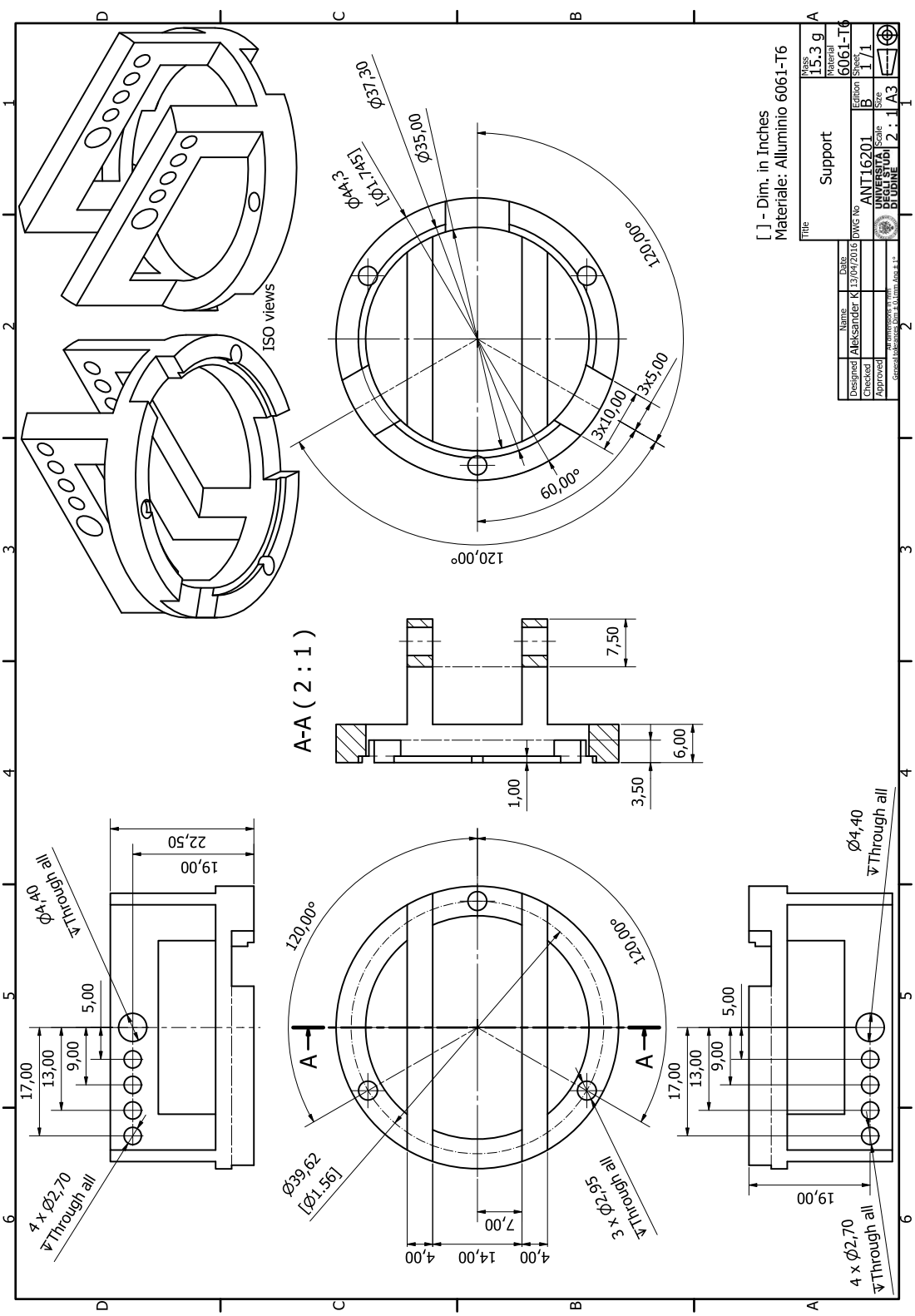
[ ] - Dim. in Inches
Materiale: Alluminio 6061-T6
Support
ANT16201
UNIVERSITÀ DEGLI STUDI DI UDINE
ISO views
A-A (2 : 1)
Ø37,30
Ø35,00
Ø4,40 [Ø1.74]
120,00°
60,00°
3x10,00
3x5,00
7,50
6,00
1,00
3,50
22,50
19,00
Ø4,40 ↧Through all
5,00
17,00
13,00
9,00
4 x Ø2,70 ↧Through all
Ø39,62 [Ø1.56]
7,00
4,00
14,00
4,00
3 x Ø2,95 ↧Through all

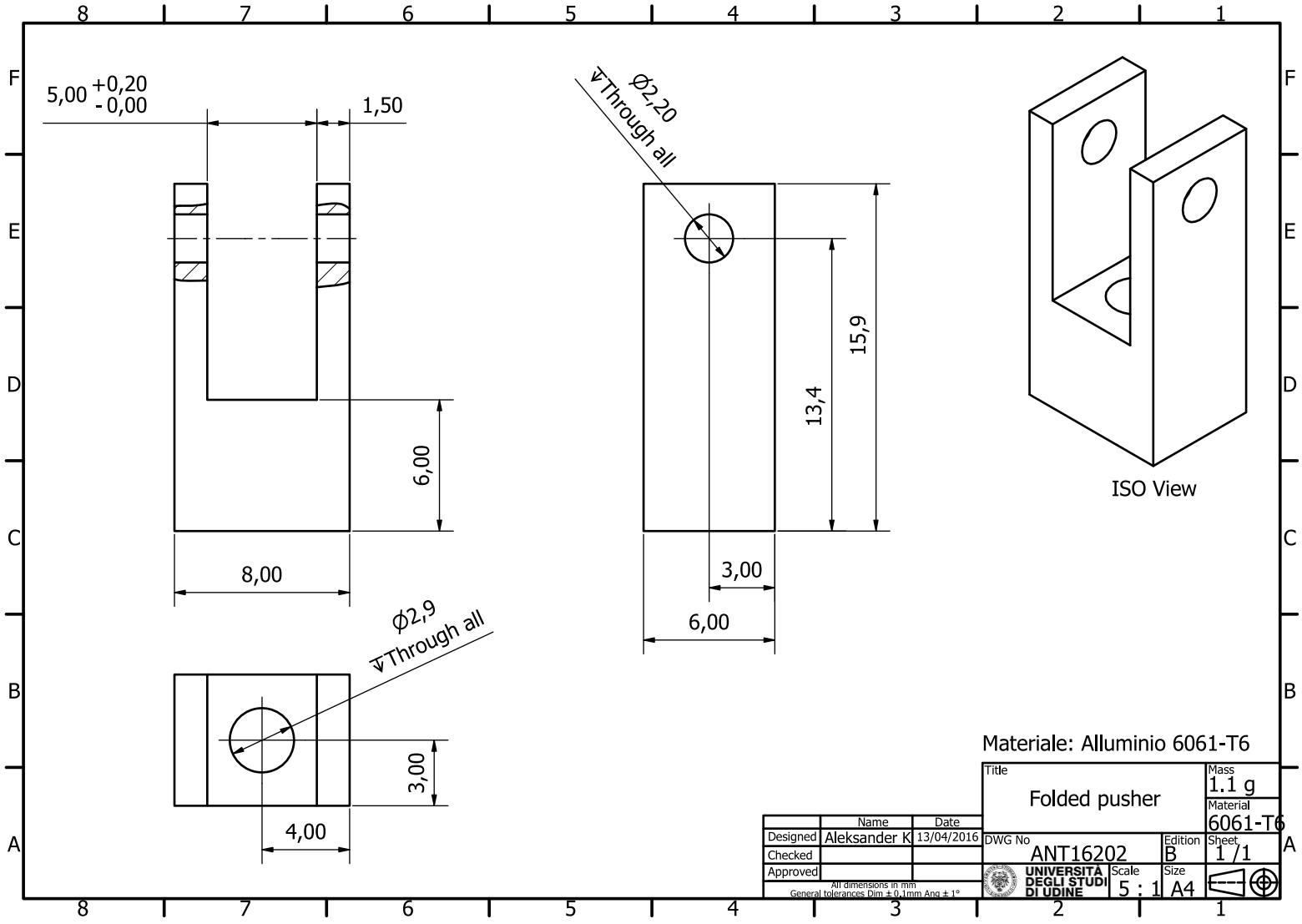
5,00 +0,20 -0,00
1,50
6,00
8,00
⌀2,20
Through all
15,9
13,4
3,00
6,00
⌀2,9
Through all
3,00
4,00
ISO View
Materiale: Alluminio 6061-T6
Title
Folded pusher
Mass
1.1 g
Material
6061-T6
Name
Date
Designed
Aleksander K
13/04/2016
Checked
Approved
DWG No
ANT16202
Edition
B
Sheet
1 /1
UNIVERSITÀ DEGLI STUDI DI UDINE
Scale
5 : 1
Size
A4
All dimensions in mm
General tolerances Dim ± 0,1mm Ang ± 1°

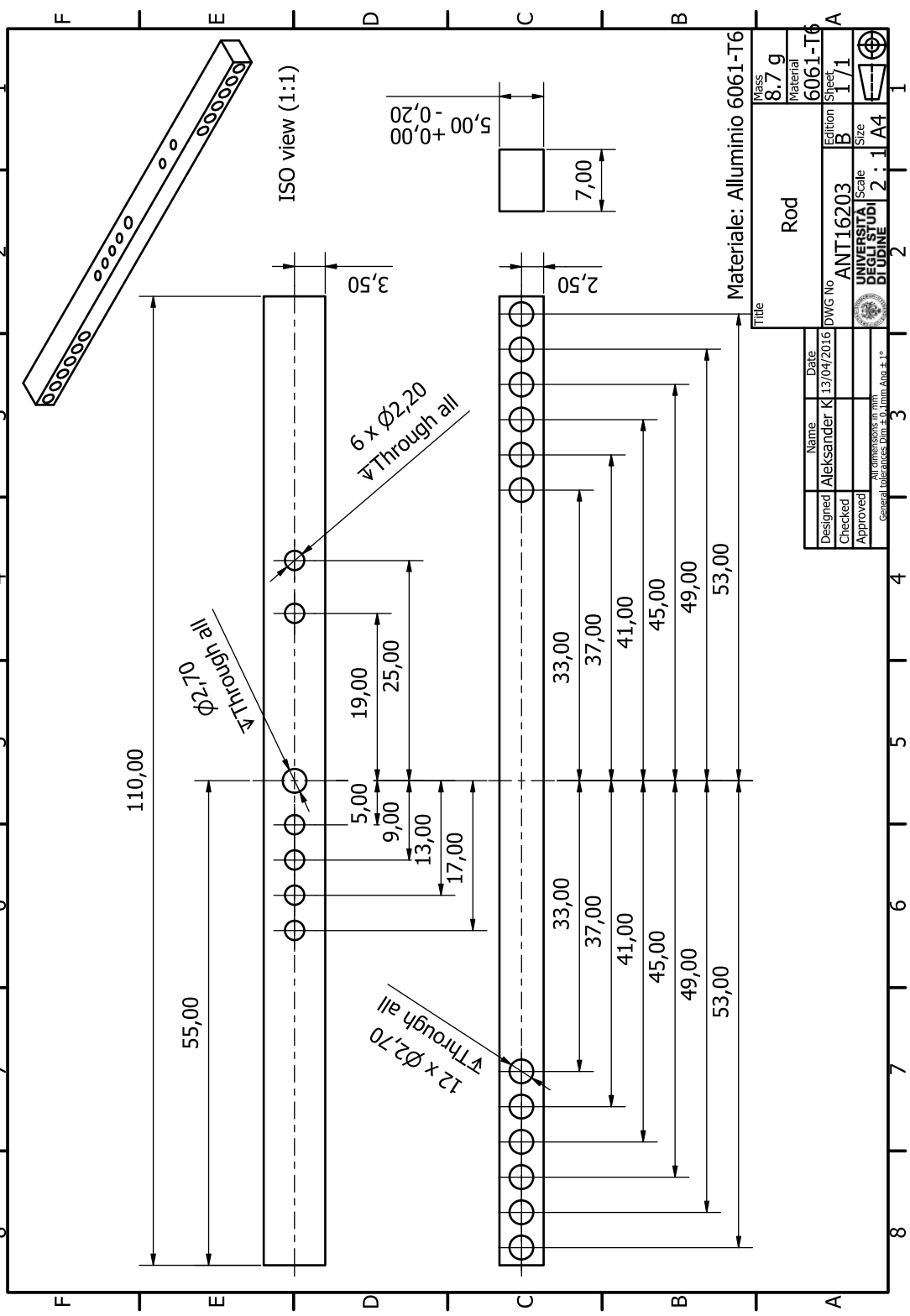
ISO view (1:1)
Materiale: Alluminio 6061-T6
Rod
Mass 8.7 g
Material 6061-T6
Sheet 1/1
Edition B
Size A4
Scale 2 : 1
DWG No ANT16203
UNIVERSITÀ DEGLI STUDI DI UDINE
Designed Aleksander K 13/04/2016
Checked
Approved
All dimensions in mm
General tolerances Dim ± 0,1mm Ang ± 1°
5,00 +0,00 -0,20
7,00
3,50
2,50
6 x Ø2,20 Through all
Ø2,70 Through all
12 x Ø2,70 Through all
110,00
55,00
19,00
25,00
5,00
9,00
13,00
17,00
33,00
37,00
41,00
45,00
49,00
53,00

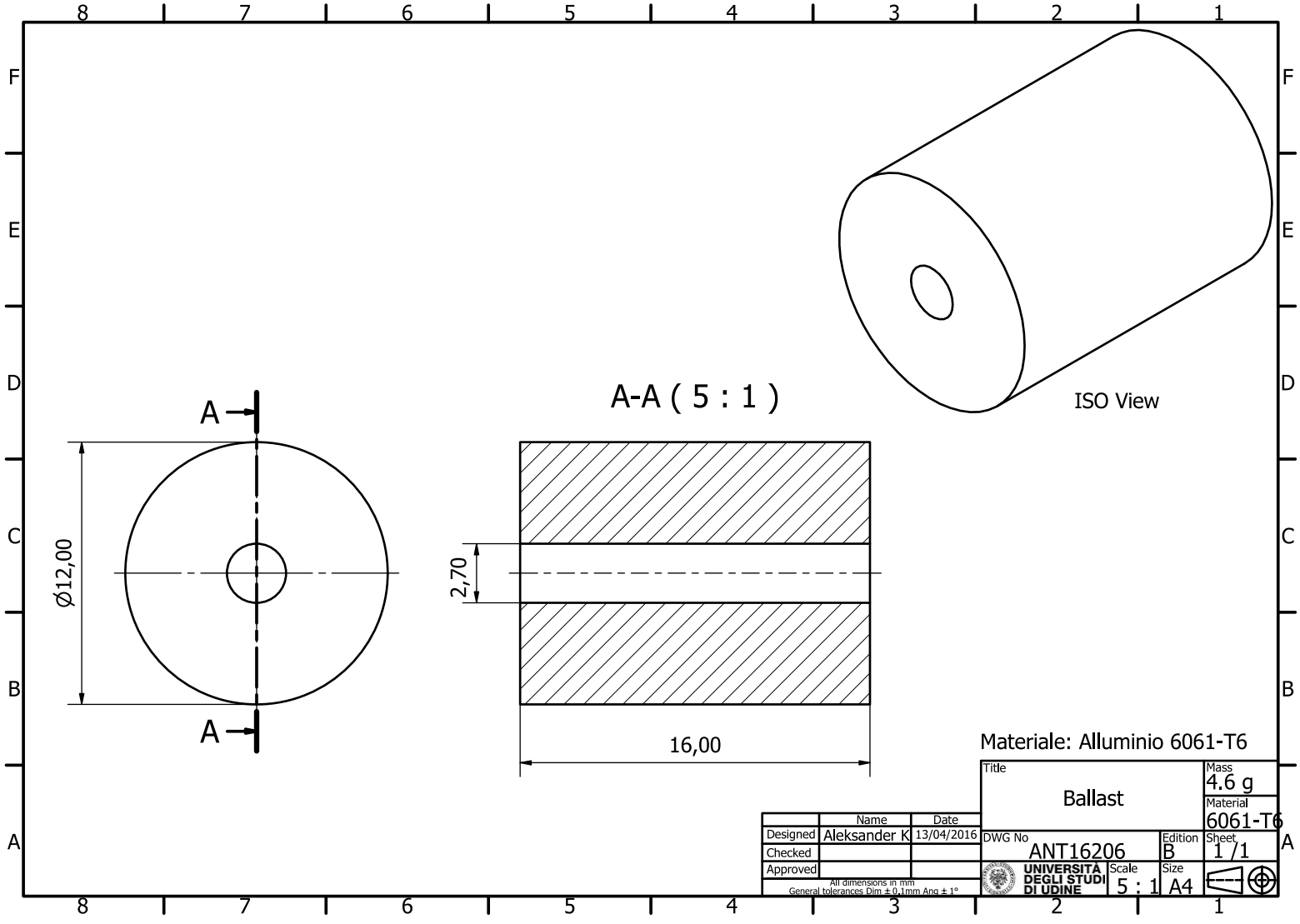
ISO View
A-A (5 : 1)
A
A
Ø12,00
2,70
16,00
Materiale: Alluminio 6061-T6
Title
Ballast
Mass
4.6 g
Material
6061-T6
Name
Date
Designed
Aleksander K
13/04/2016
Checked
Approved
DWG No
ANT16206
Edition
B
Sheet
1 /1
UNIVERSITÀ DEGLI STUDI DI UDINE
Scale
5 : 1
Size
A4
All dimensions in mm
General tolerances Dim ± 0,1mm Ang ± 1°

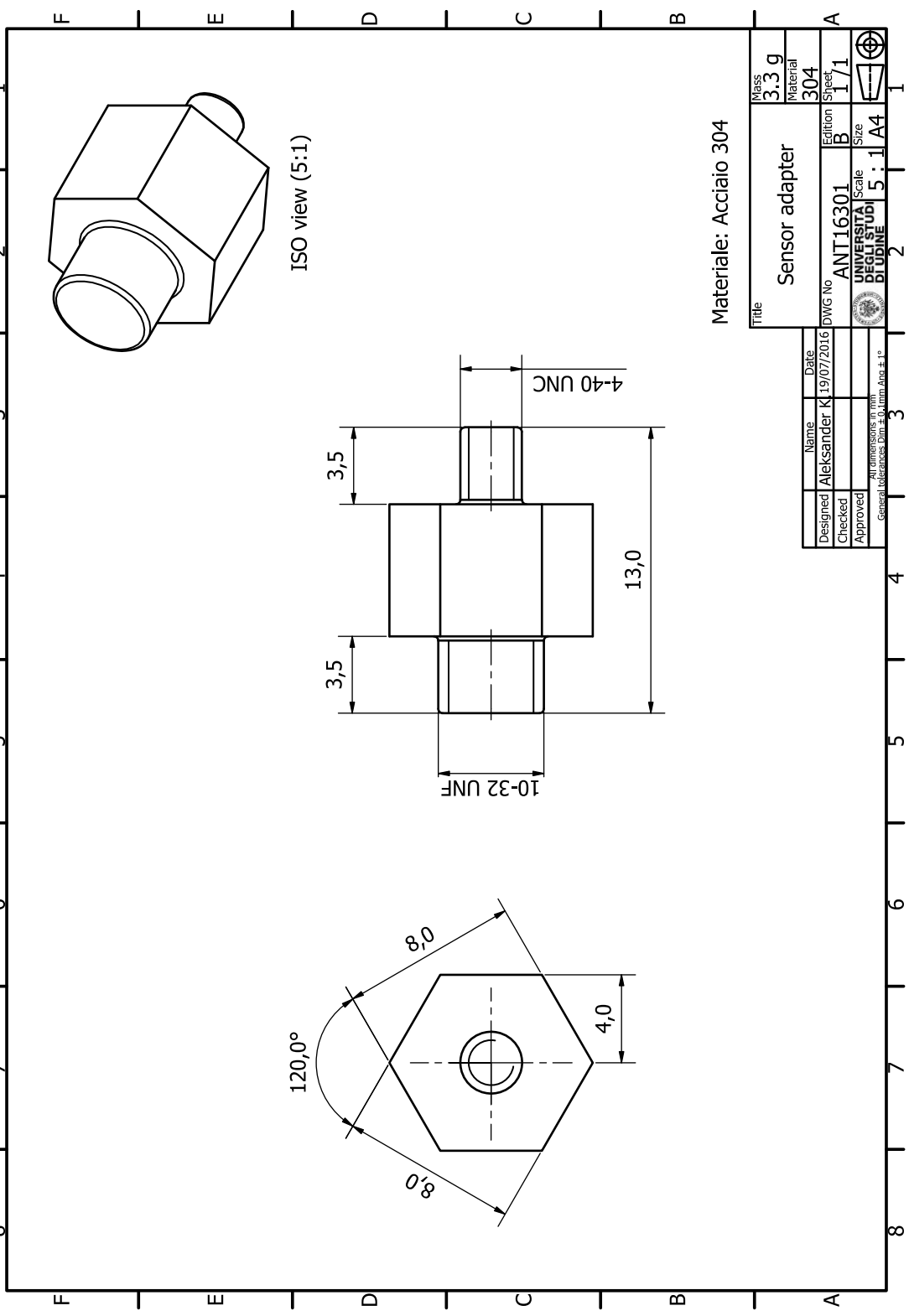
ISO view (5:1)
Materiale: Acciaio 304
4-40 UNC
10-32 UNF
3,5
3,5
13,0
8,0
8,0
4,0
120,0°
Mass
3.3 g
Material
304
Sheet
1/1
Edition
B
Size
A4
Scale
5 : 1
DWG No
ANT16301
Title
Sensor adapter
UNIVERSITÀ DEGLI STUDI DI UDINE
Designed
Checked
Approved
Name
Aleksander K
Date
19/07/2016
All dimensions in mm
General tolerances Dim ± 0.1mm Ang ± 1°

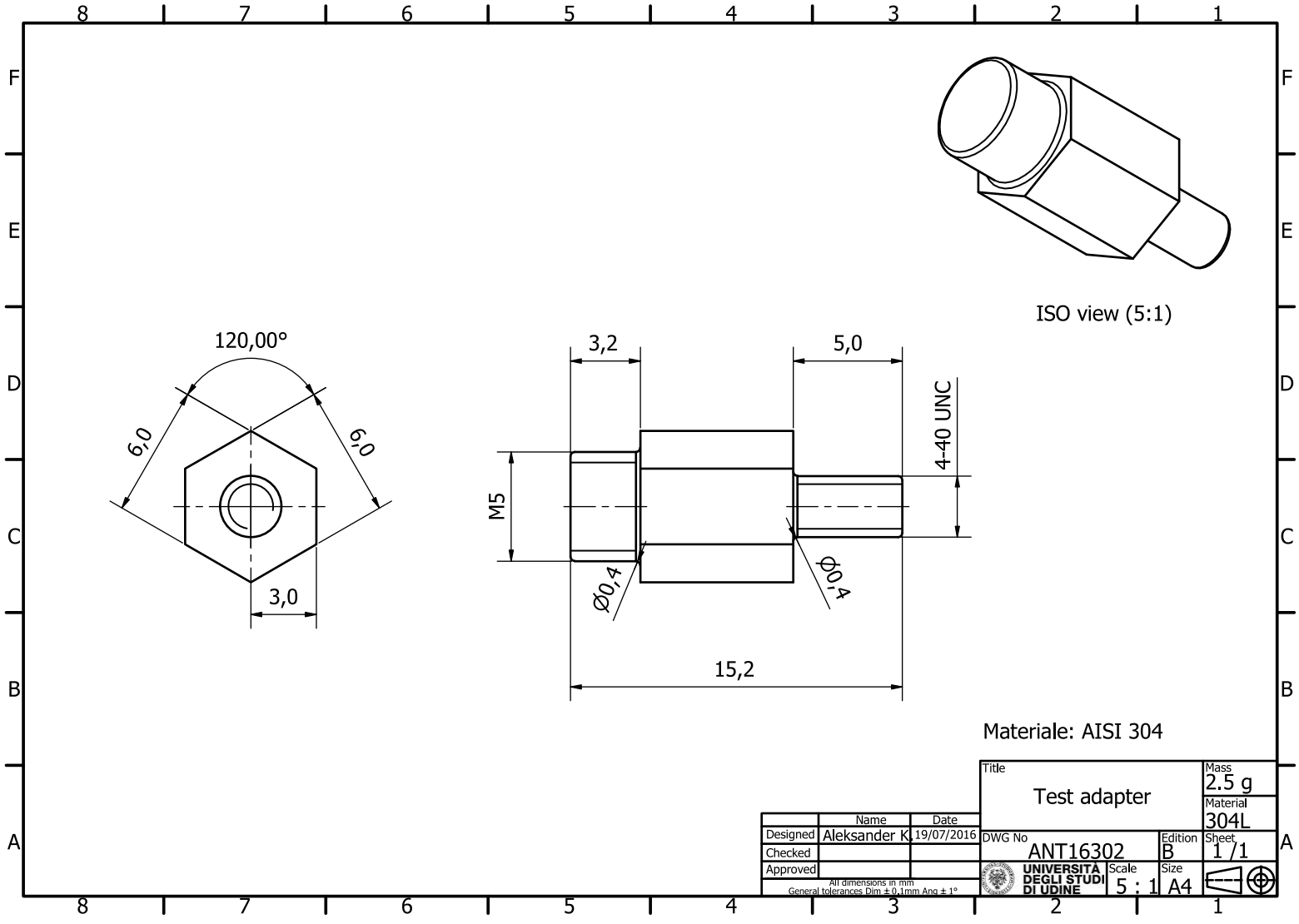
ISO view (5:1)
120,00°
6,0
6,0
3,0
3,2
5,0
4-40 UNC
M5
Ø0,4
Ø0,4
15,2
Materiale: AISI 304
Title
Test adapter
Mass
2.5 g
Material
304L
Name
Date
Designed
Aleksander K.
19/07/2016
Checked
Approved
All dimensions in mm
General tolerances Dim ± 0,1mm Ang ± 1°
DWG No
ANT16302
Edition
B
Sheet
1 /1
UNIVERSITÀ DEGLI STUDI DI UDINE
Scale
5 : 1
Size
A4

B

TECHNICAL DRAWINGS OF THE PIEZOELECTRIC PROTOTYPE

The following annex consists technical drawings of the manufactured components for the piezoelectric flywheel prototype. The assembly drawings are followed by the exploded view drawings and by the detailed drawings of each component.

PARTS LIST					
ITEM	QTY	PART NUMBER	REVISION	DESCRIPTION	MATERIAL
1	1	ANT17201-A_APA900M	ANY	STEP AP203	
2	1	ANT17202	C	Bearing connector	6061-T6
3	1	ANT17204	B	Support	6061-T6
4	1	ANT17205	A	Sensor adapter	304
5	1	ANT17206	A	Flywheel frame	6061-T6
6	1	ANT17207	B	Ballast1	Brass
7	1	ANT17208	B	Ballast2	Brass
8	4	Mod. A10	A	C-Flex	
9	5	M2.5x0.45 x 6		Socket Head Cap Screw	Steel

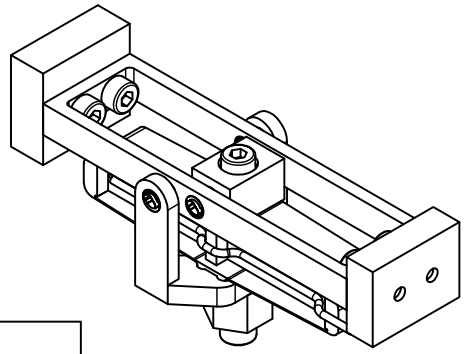

ISO View 2:1

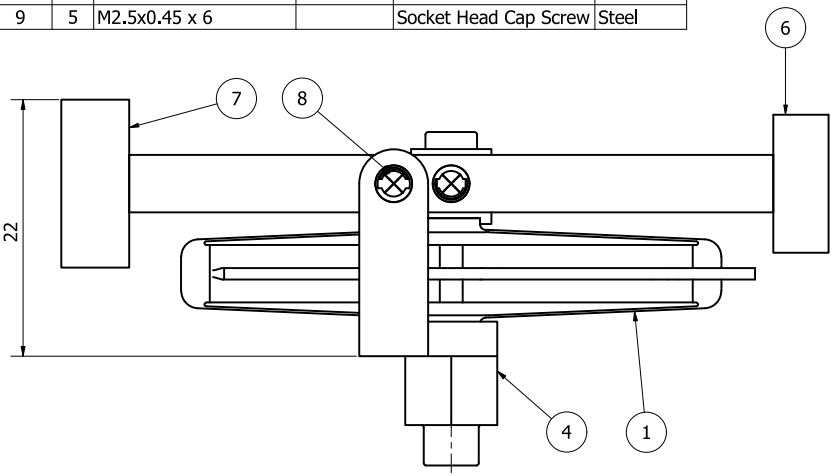

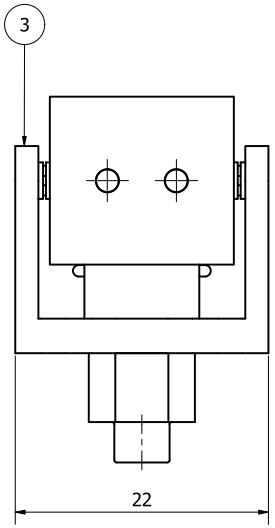

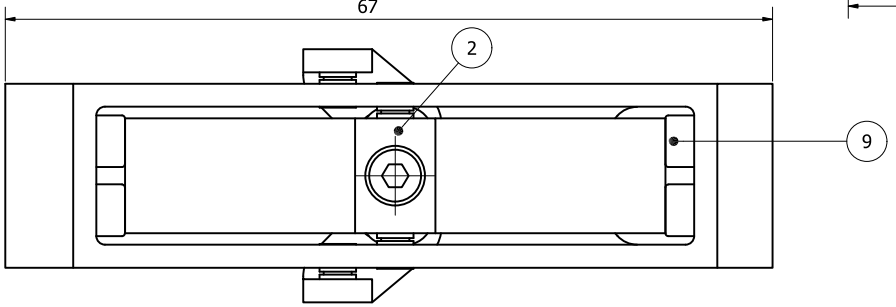

	Name	Date
Designed	Aleksander K.	12/01/2017
Checked		
Approved		

All dimensions in mm
General tolerances Dim ± 0,1mm Ang ± 1°

Title	APA Flywheel actuator
Mass	46.8 g
Material	
DWG No	ANT17200
Edition	C
Sheet	1 /1
Scale	3 : 1
Size	A3

UNIVERSITÀ DEGLI STUDI DI UDINE

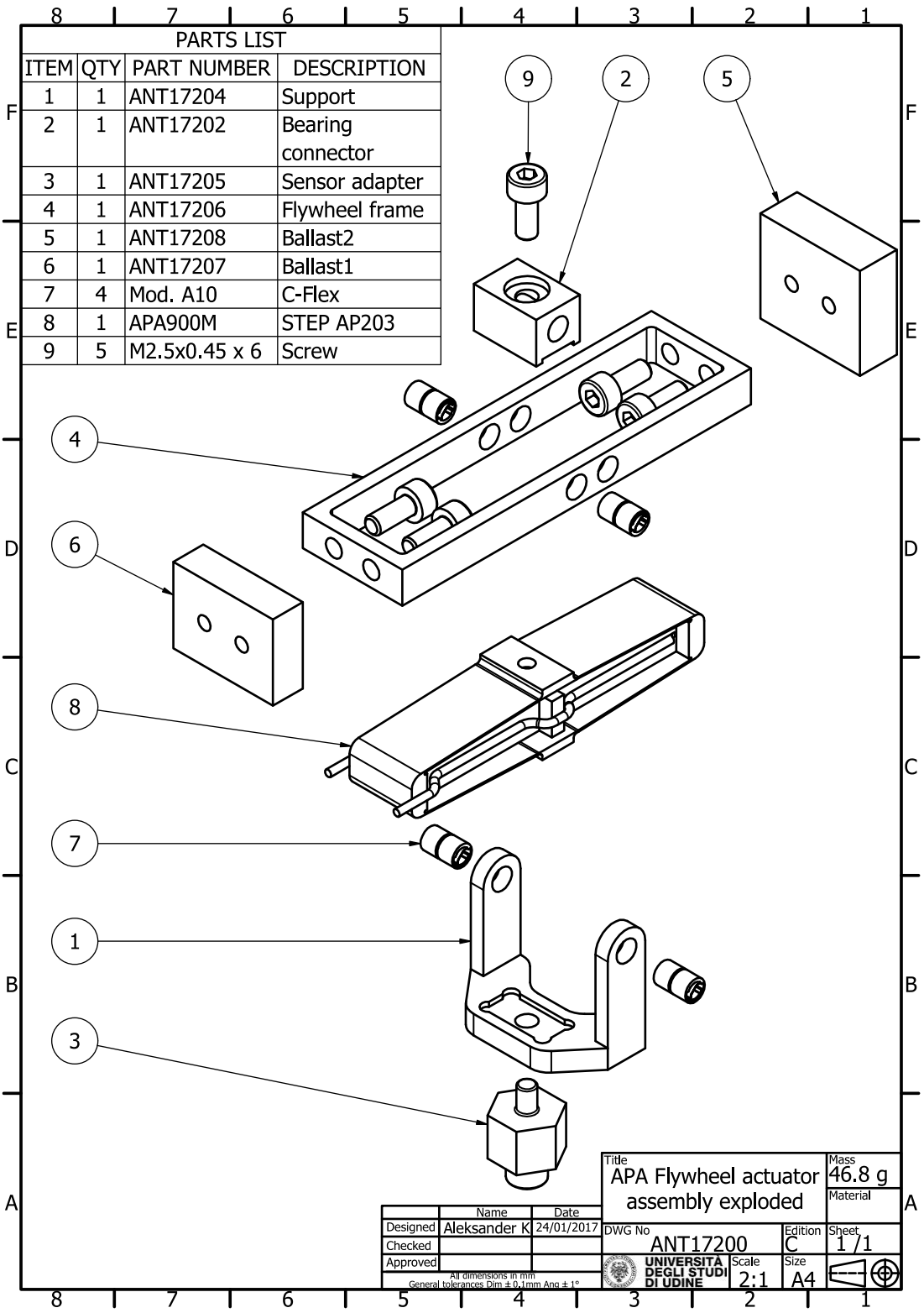
PARTS LIST
ITEM | QTY | PART NUMBER | DESCRIPTION
1 | 1 | ANT17204 | Support
2 | 1 | ANT17202 | Bearing connector
3 | 1 | ANT17205 | Sensor adapter
4 | 1 | ANT17206 | Flywheel frame
5 | 1 | ANT17208 | Ballast2
6 | 1 | ANT17207 | Ballast1
7 | 4 | Mod. A10 | C-Flex
8 | 1 | APA900M | STEP AP203
9 | 5 | M2.5x0.45 x 6 | Screw
Title
APA Flywheel actuator assembly exploded
Mass
46.8 g
Material
Name
Date
Designed
Aleksander K
24/01/2017
Checked
Approved
DWG No
ANT17200
Edition
C
Sheet
1 /1
UNIVERSITÀ DEGLI STUDI DI UDINE
Scale
2:1
Size
A4
All dimensions in mm
General tolerances Dim ± 0.1mm Ang ± 1°

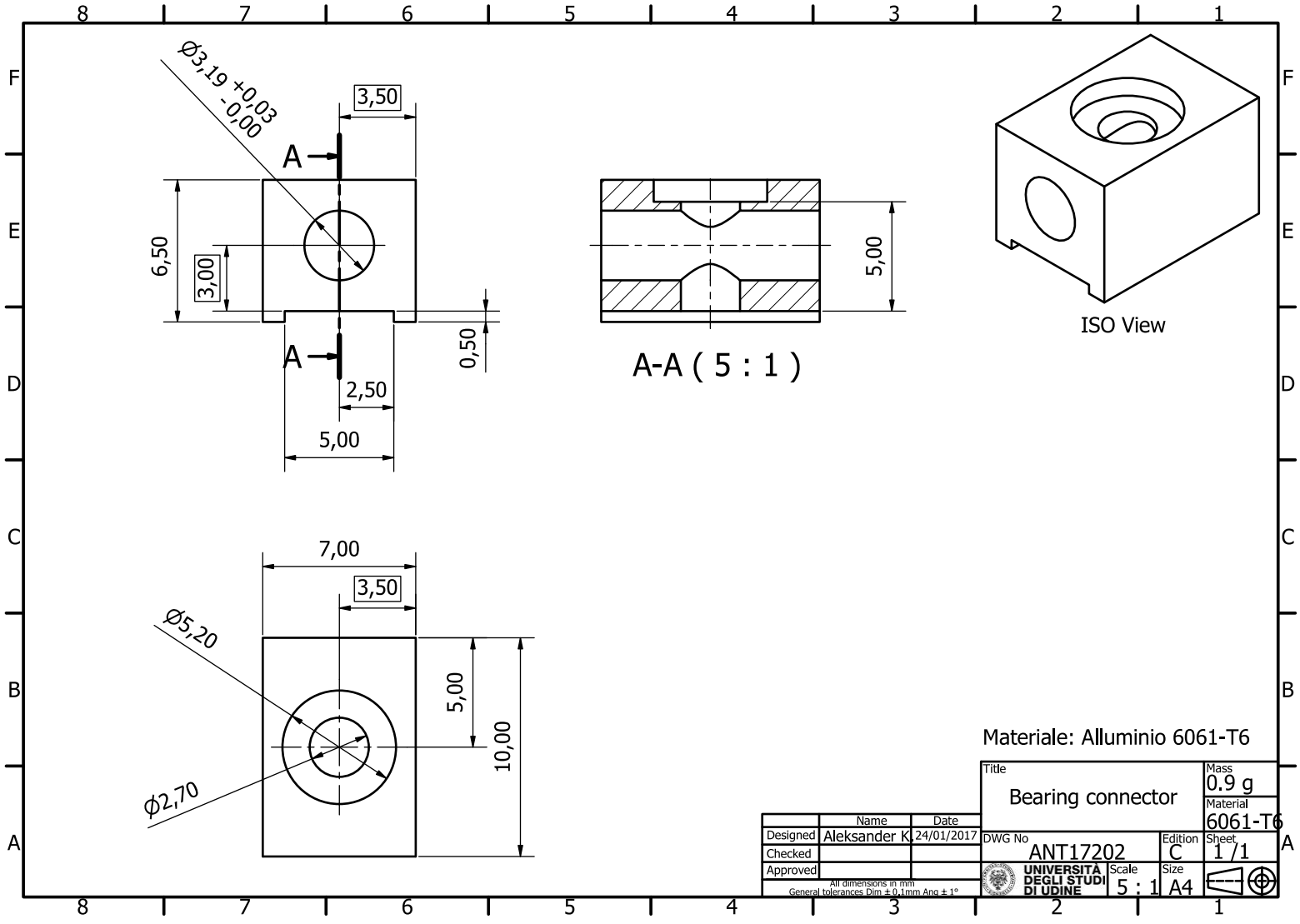
Ø3,19 +0,03 -0,00
3,50
A
6,50
3,00
A
0,50
2,50
5,00
A-A (5 : 1)
5,00
ISO View
7,00
3,50
Ø5,20
5,00
10,00
Ø2,70
Materiale: Alluminio 6061-T6
Name
Date
Designed
Aleksander K.
24/01/2017
Checked
Approved
All dimensions in mm
General tolerances Dim ± 0,1mm Ang ± 1°
Title
Bearing connector
Mass
0.9 g
Material
6061-T6
DWG No
ANT17202
Edition
C
Sheet
1 /1
UNIVERSITÀ DEGLI STUDI DI UDINE
Scale
5 : 1
Size
A4

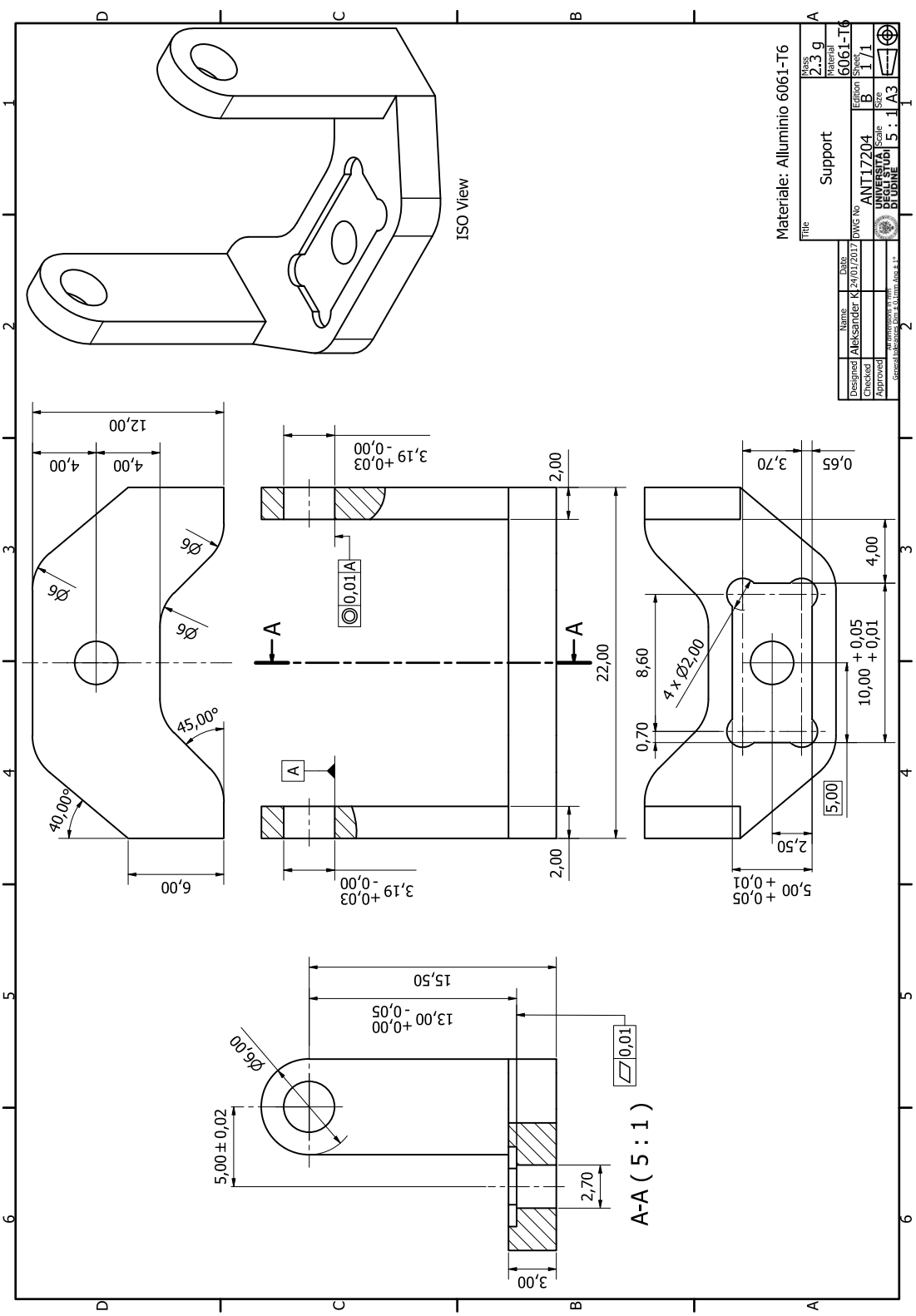
ISO View
Materiale: Alluminio 6061-T6
Support
ANT17204
UNIVERSITÀ DEGLI STUDI DI UDINE
Aleksander K.
24/01/2017
Mass 2.3 g
Material 6061-T6
Edition B
Sheet 1/1
Size A3
Scale 5 : 1
A-A (5 : 1)
4 x Ø2,00
0,01 A
0,01
5,00
12,00
4,00
6,00
45,00°
40,00°
22,00
2,00
8,60
0,70
4,00
3,70
0,65
2,50
15,50
13,00 +0,00 -0,05
Ø6,00
5,00 ± 0,02
2,70
3,00

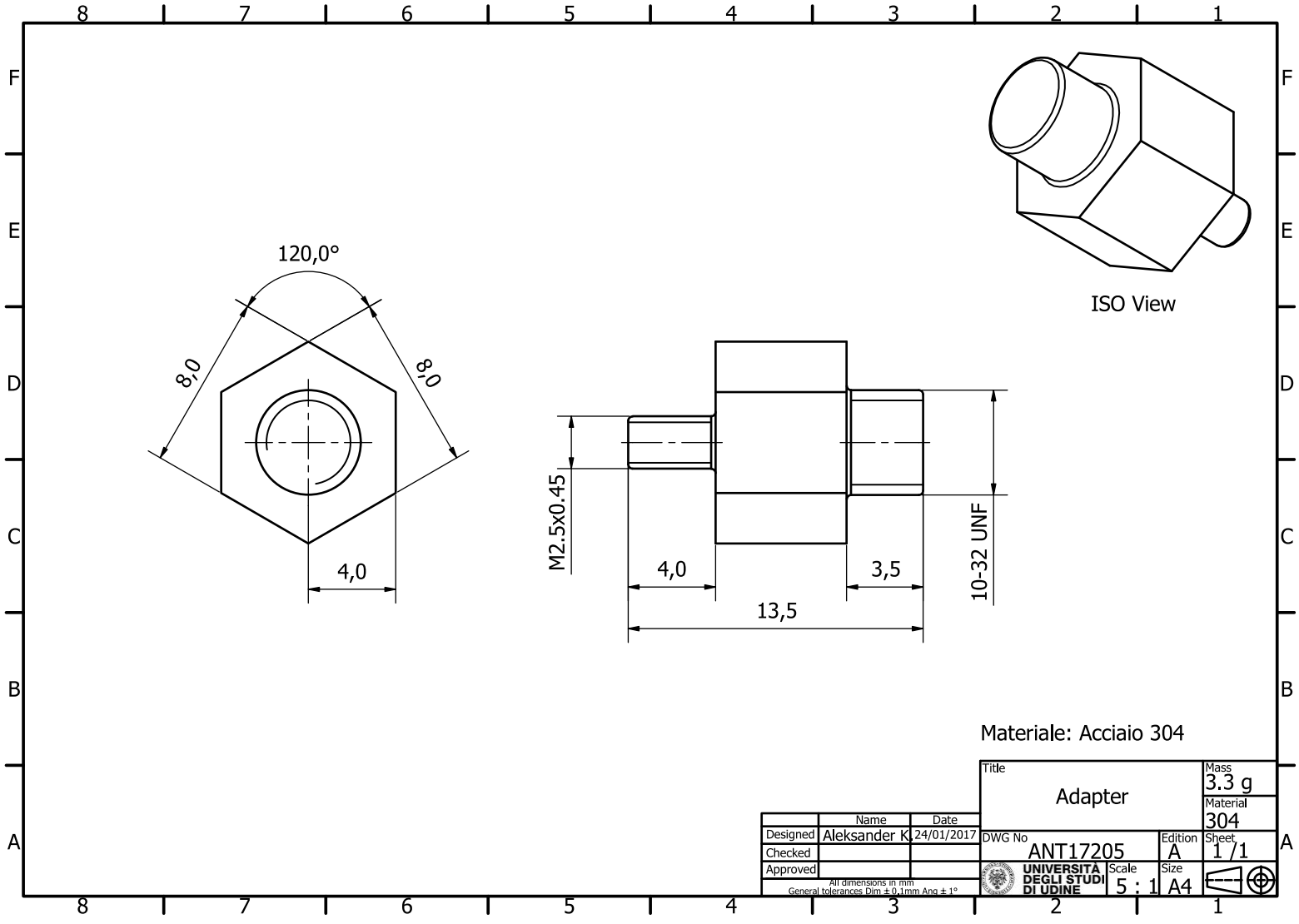
ISO View
120,0°
8,0
8,0
4,0
M2.5x0.45
4,0
3,5
13,5
10-32 UNF
Materiale: Acciaio 304
Title
Adapter
Mass
3.3 g
Material
304
Name
Date
Designed
Aleksander K.
24/01/2017
Checked
Approved
DWG No
ANT17205
Edition
A
Sheet
1 /1
UNIVERSITÀ DEGLI STUDI DI UDINE
Scale
5 : 1
Size
A4
All dimensions in mm
General tolerances Dim ± 0,1mm Ang ± 1°

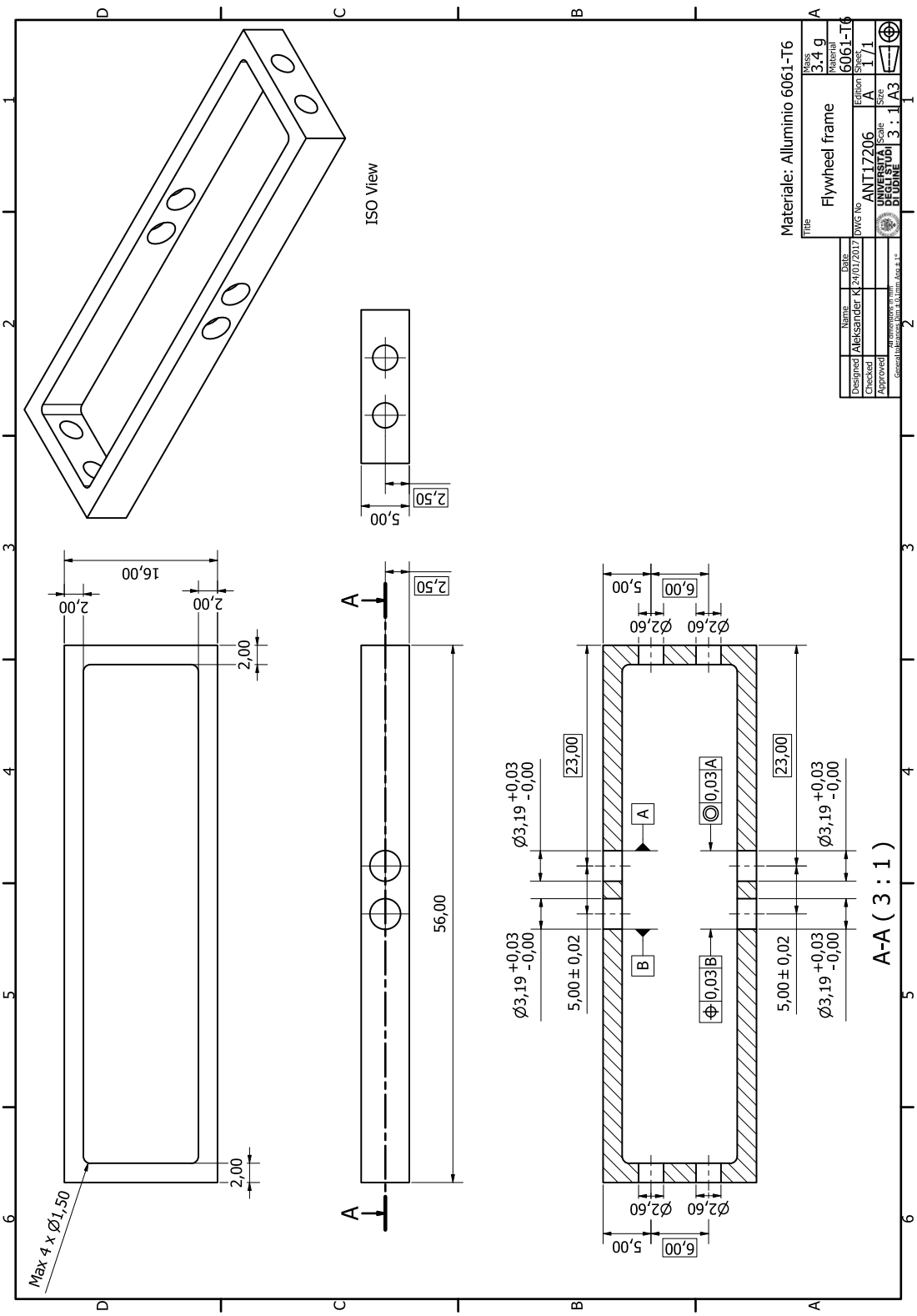
Materiale: Alluminio 6061-T6
Title
Flywheel frame
Mass
3.4 g
Material
6061-T6
Sheet
1/1
Edition
A
Size
A3
Scale
3 : 1
DWG No
ANT17206
UNIVERSITÀ DEGLI STUDI DI UDINE
Name
Date
Designed
Aleksander K.
24/01/2017
Checked
Approved
All dimensions in mm
General tolerances Dim ± 0.1mm Ang ± 1°
ISO View
A-A (3 : 1)
Max 4 x Ø1,50
16,00
2,00
2,00
2,00
2,00
2,50
5,00
56,00
23,00
23,00
5,00 ± 0,02
5,00 ± 0,02
Ø3,19 +0,03 -0,00
Ø3,19 +0,03 -0,00
Ø3,19 +0,03 -0,00
Ø3,19 +0,03 -0,00
Ø2,60
Ø2,60
Ø2,60
Ø2,60
5,00
6,00
5,00
6,00
0,03 A
0,03 B
A
B

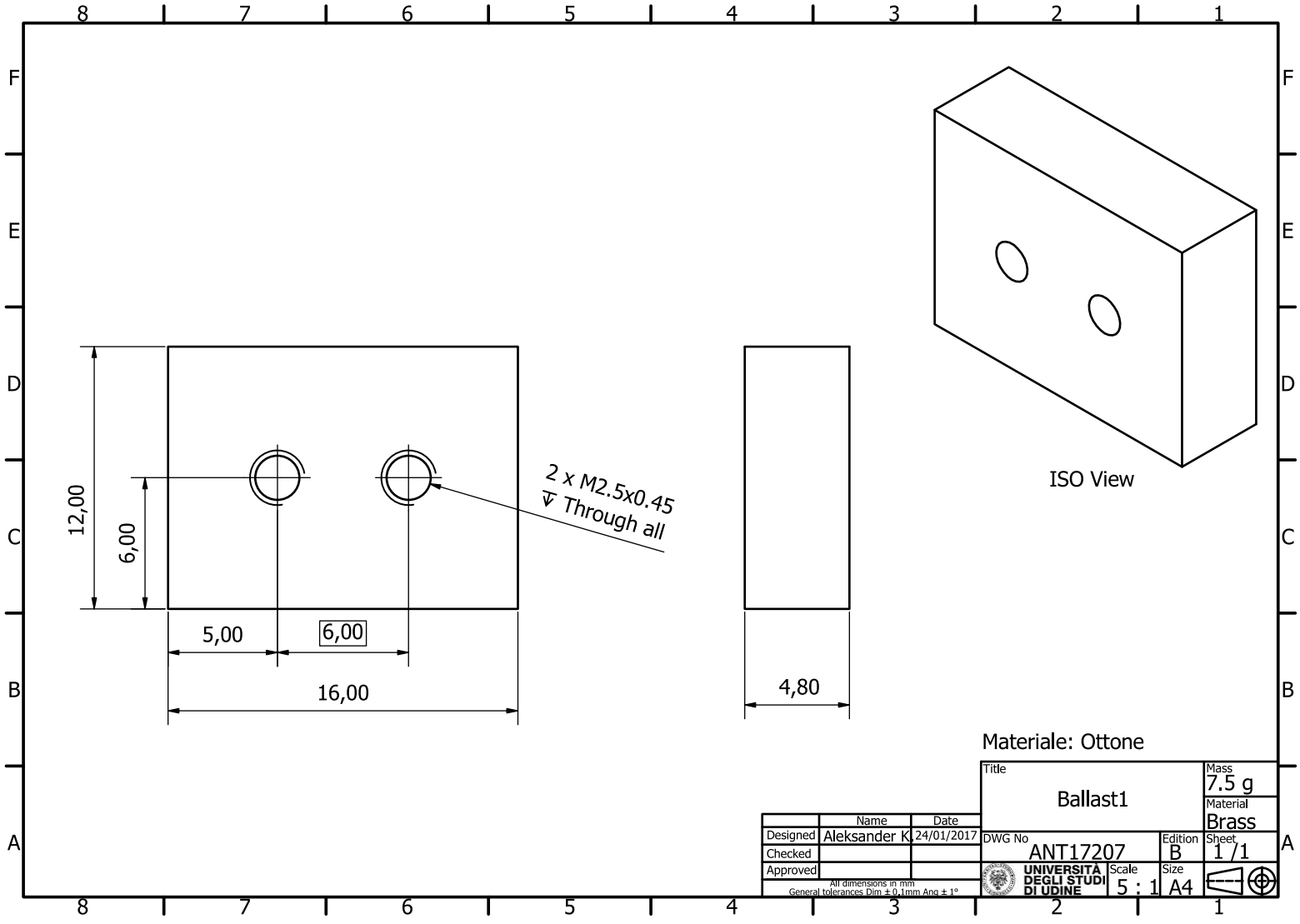
12,00
6,00
5,00
6,00
16,00
2 x M2.5x0.45
↧ Through all
4,80
ISO View
Materiale: Ottone
Title
Ballast1
Mass
7.5 g
Material
Brass
Name
Date
Designed
Aleksander K.
24/01/2017
Checked
Approved
All dimensions in mm
General tolerances Dim ± 0,1mm Ang ± 1°
DWG No
ANT17207
Edition
B
Sheet
1 /1
UNIVERSITÀ DEGLI STUDI DI UDINE
Scale
5 : 1
Size
A4

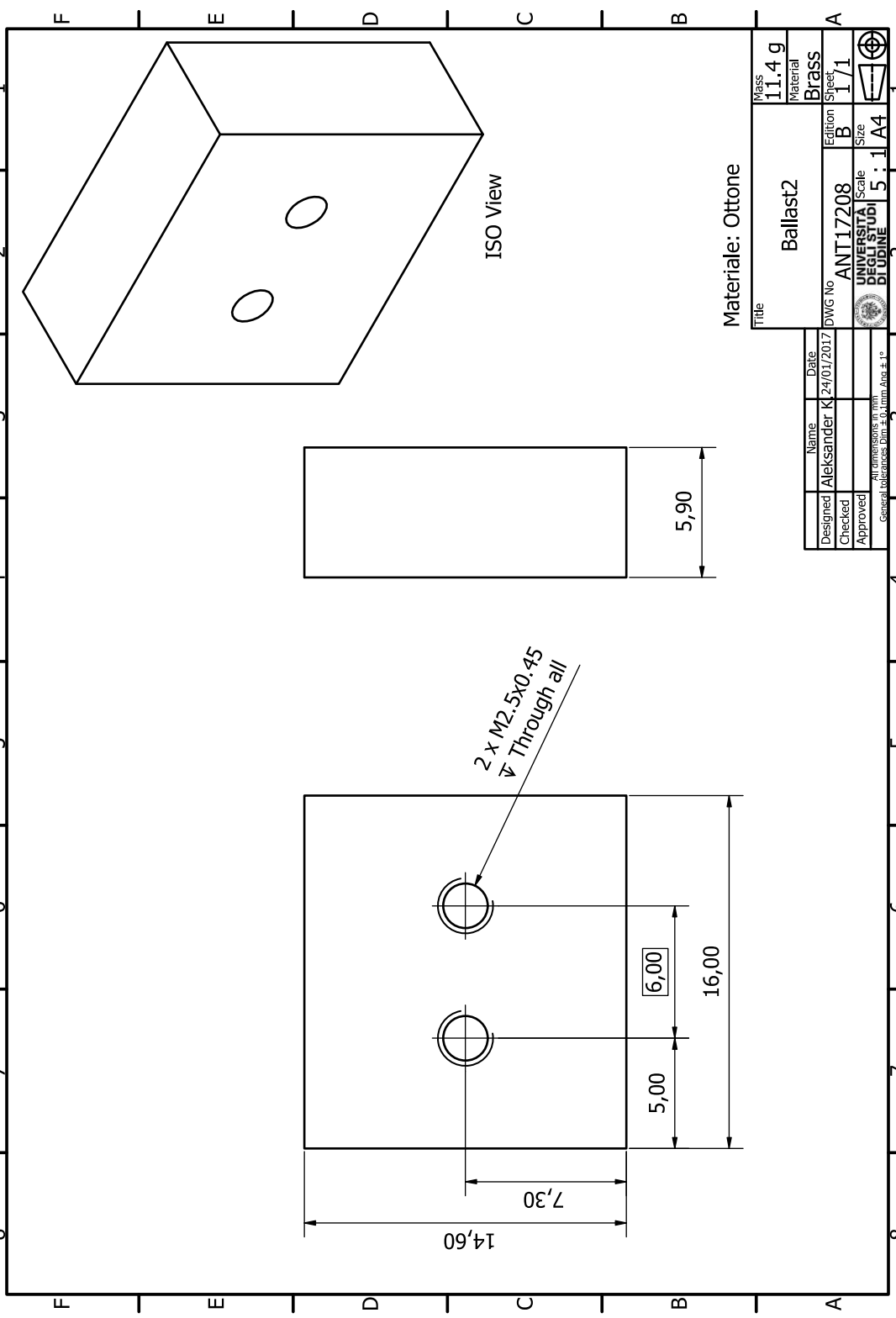
ISO View
Materiale: Ottone
5,90
2 x M2.5x0.45
Through all
6,00
16,00
5,00
7,30
14,60
Mass
11.4 g
Material
Brass
Sheet
1/1
Edition
B
Size
A4
Scale
5 : 1
DWG No
ANT17208
Title
Ballast2
UNIVERSITÀ DEGLI STUDI DI UDINE
Designed
Checked
Approved
Name
Aleksander K
Date
24/01/2017
All dimensions in mm
General tolerances Dim ± 0.1mm Ang ± 1°

C

TECHNICAL DRAWINGS OF THE PLATE SETUP

The following appendix consists technical drawings of the manufactured structure used for implementation of the active control system.

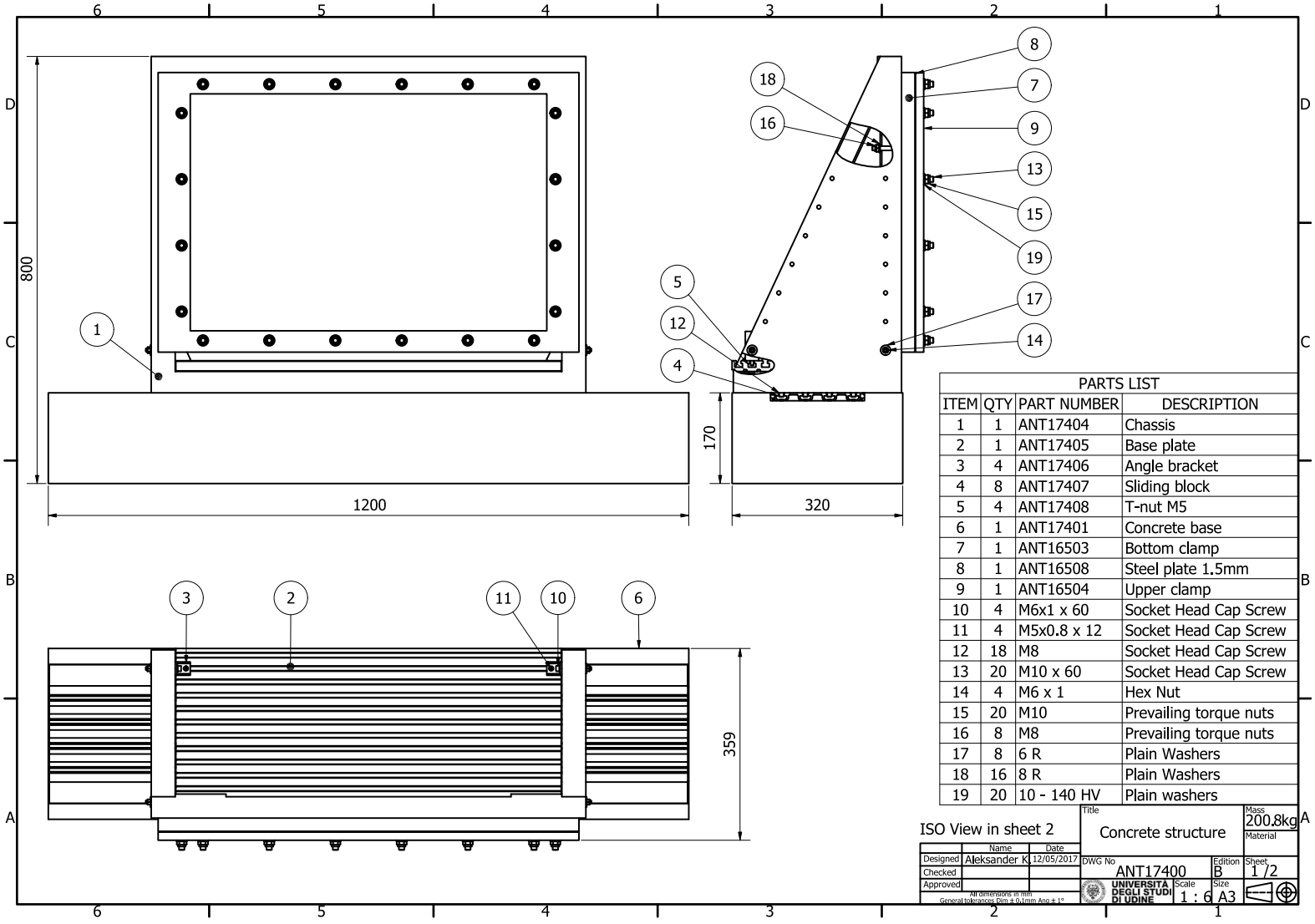

PARTS LIST			
ITEM	QTY	PART NUMBER	DESCRIPTION
1	1	ANT17404	Chassis
2	1	ANT17405	Base plate
3	4	ANT17406	Angle bracket
4	8	ANT17407	Sliding block
5	4	ANT17408	T-nut M5
6	1	ANT17401	Concrete base
7	1	ANT16503	Bottom clamp
8	1	ANT16508	Steel plate 1.5mm
9	1	ANT16504	Upper clamp
10	4	M6x1 x 60	Socket Head Cap Screw
11	4	M5x0.8 x 12	Socket Head Cap Screw
12	18	M8	Socket Head Cap Screw
13	20	M10 x 60	Socket Head Cap Screw
14	4	M6 x 1	Hex Nut
15	20	M10	Prevailing torque nuts
16	8	M8	Prevailing torque nuts
17	8	6 R	Plain Washers
18	16	8 R	Plain Washers
19	20	10 - 140 HV	Plain washers

	Name	Date
Designed	Aleksander K.	12/05/2017
Checked		
Approved		

All dimensions in mm
General tolerances Dim ± 0.1mm Ang ± 1°

Title: Concrete structure
Mass: 200.8kg
Material:
DWG No: ANT17400
Edition: B
Sheet: 1 /2
UNIVERSITÀ DEGLI STUDI DI UDINE
Scale: 1 : 6
Size: A3

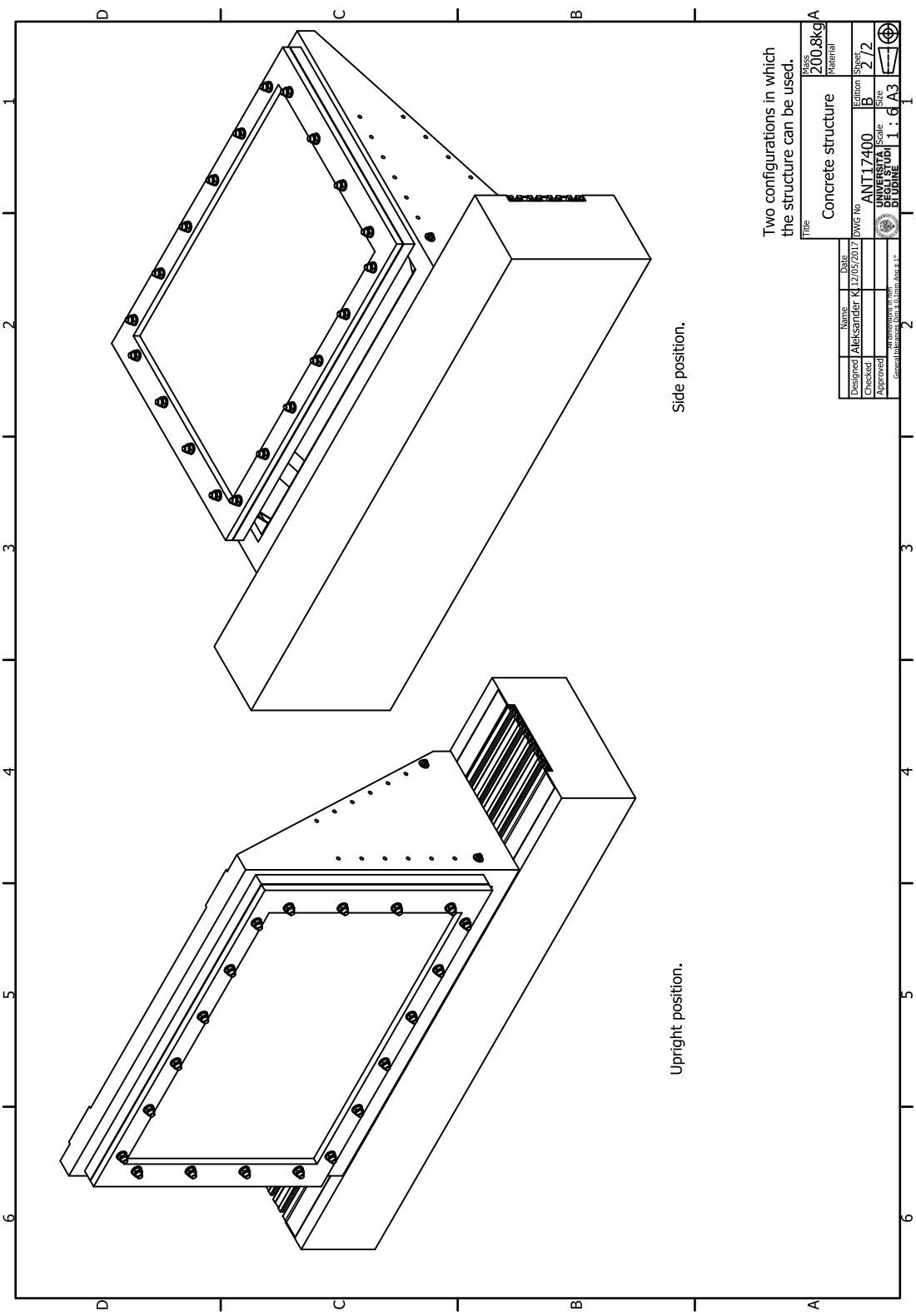
Side position.
Upright position.
Two configurations in which the structure can be used.
Title
Concrete structure
Mass
200.8kg
Material
Name
Date
Designed
Aleksander K.
12/05/2017
Checked
Approved
DWG No
ANT17400
Edition
B
Sheet
2/2
Scale
1 : 6
Size
A3
UNIVERSITÀ DEGLI STUDI DI UDINE

PARTS LIST			
ITEM	QTY	PART NUMBER	DESCRIPTION
1	1	ANT17402	Concrete block
2	1	ANT17409	Profilo 90x180
3	1	ANT17411	Cradle

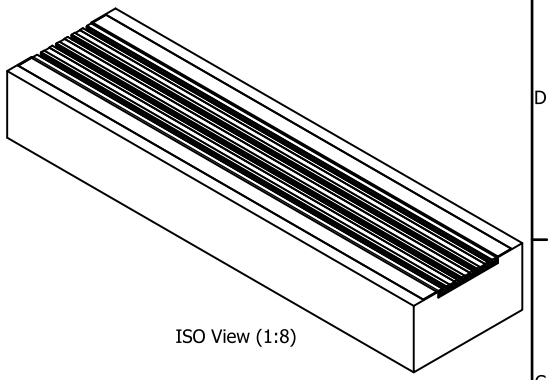

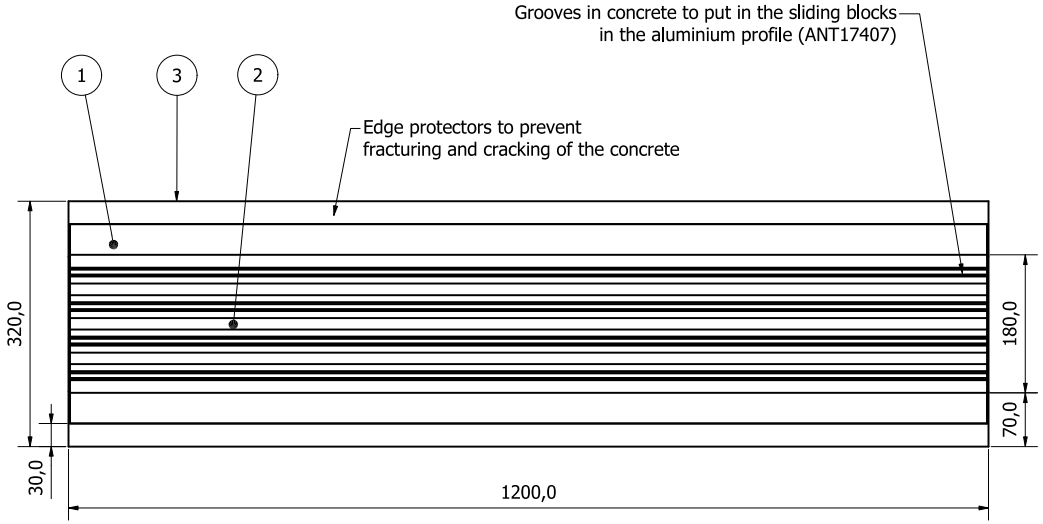

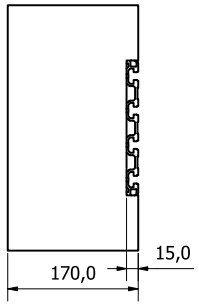

1. Handles or grips can be added to the structure for easier transportation.
2. The concrete must be reinforced with steel reinforcement bars (rebar).
3. The reinforcement must be connected with the cradle.
4. The inside of the aluminum profile can be filled up with the concrete.

	Name	Date
Designed	Aleksander K.	15/05/2017
Checked		
Approved		

All dimensions in mm
General tolerances Dim ± 0,1mm Ang ± 1°

Title: Concrete base
Mass: 121.5kg
Material:
DWG No: ANT17401
Edition: B
Sheet: 1 /1
UNIVERSITÀ DEGLI STUDI DI UDINE
Scale: 1 : 5
Size: A3

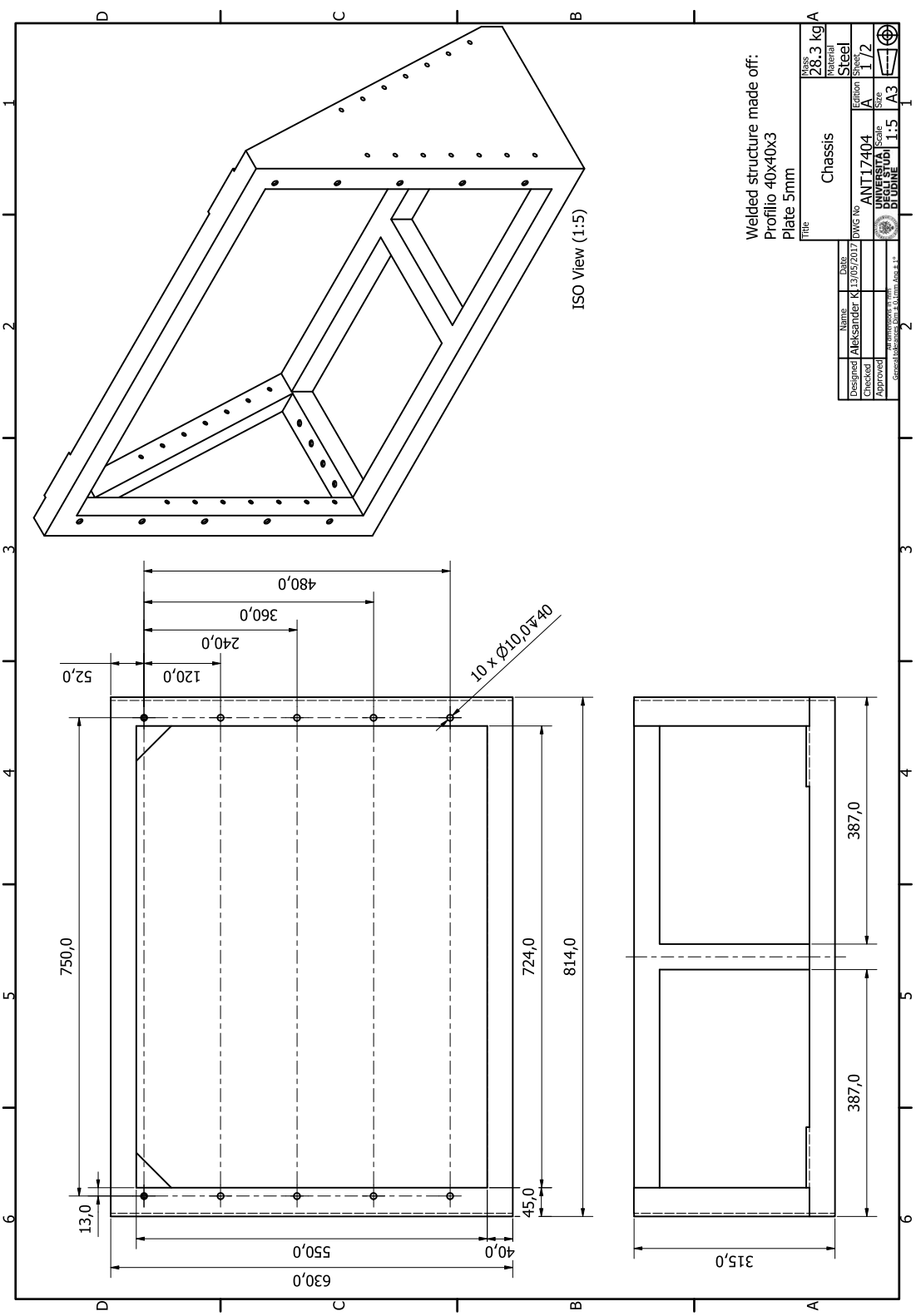
ISO View (1:5)
Welded structure made off:
Profilio 40x40x3
Plate 5mm
Chassis
ANT17404
UNIVERSITÀ DEGLI STUDI DI UDINE
Mass 28.3 kg
Material Steel
Sheet 1/2
Edition A
Size A3
Scale 1:5
Designed
Checked
Approved
Name
Aleksander K.
Date
13/05/2017
480,0
360,0
240,0
120,0
52,0
10 x Ø10,0▼40
750,0
724,0
814,0
45,0
13,0
550,0
40,0
630,0
387,0
387,0
315,0

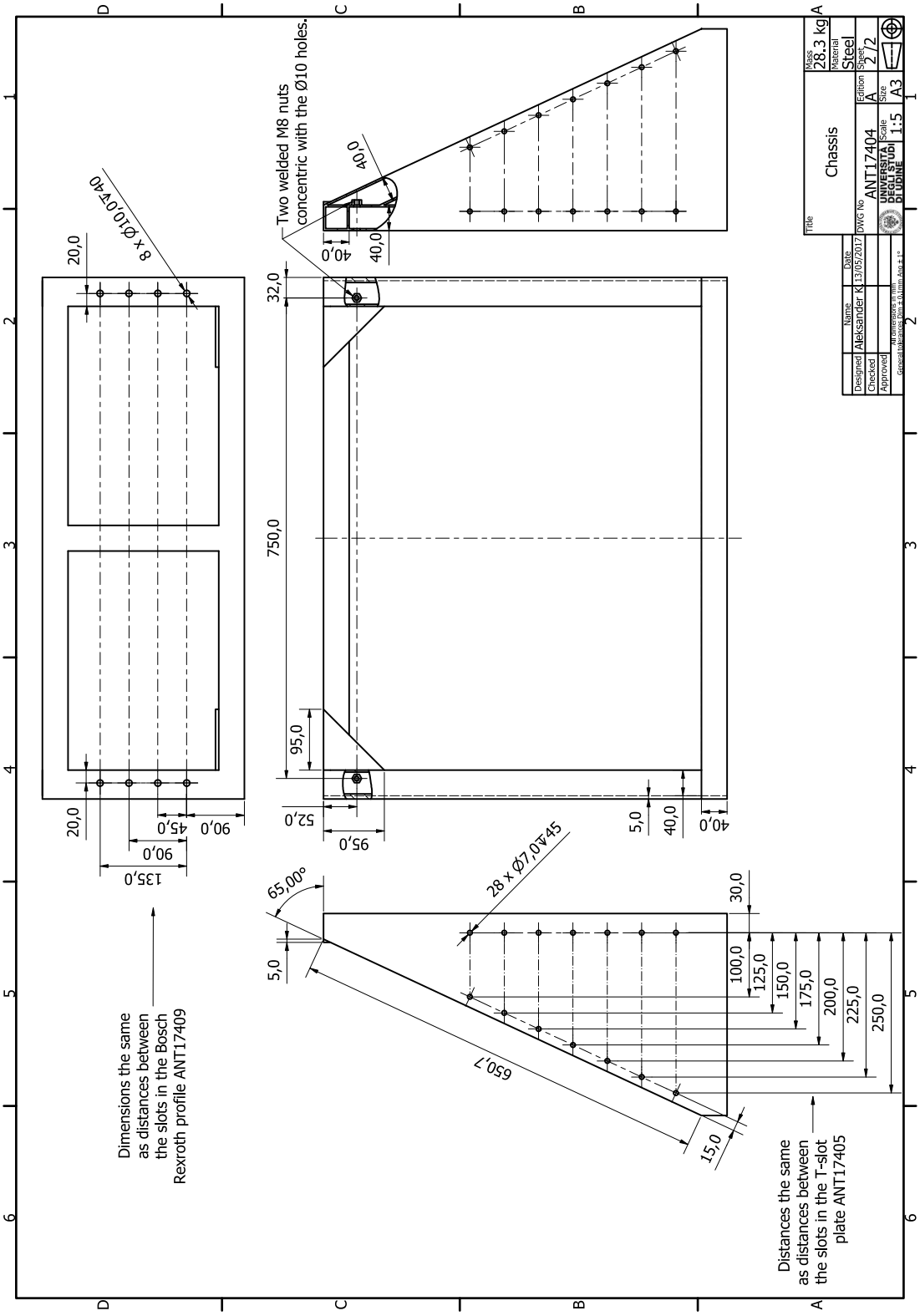
Two welded M8 nuts
concentric with the Ø10 holes.
8 x Ø10,0▽40
Dimensions the same
as distances between
the slots in the Bosch
Rexroth profile ANT17409
28 x Ø7,0▽45
Distances the same
as distances between
the slots in the T-slot
plate ANT17405
Chassis
ANT17404
28.3 kg
Steel
A3
1:5
2/2
A
13/05/2017
Aleksander K.
UNIVERSITÀ DEGLI STUDI DI UDINE

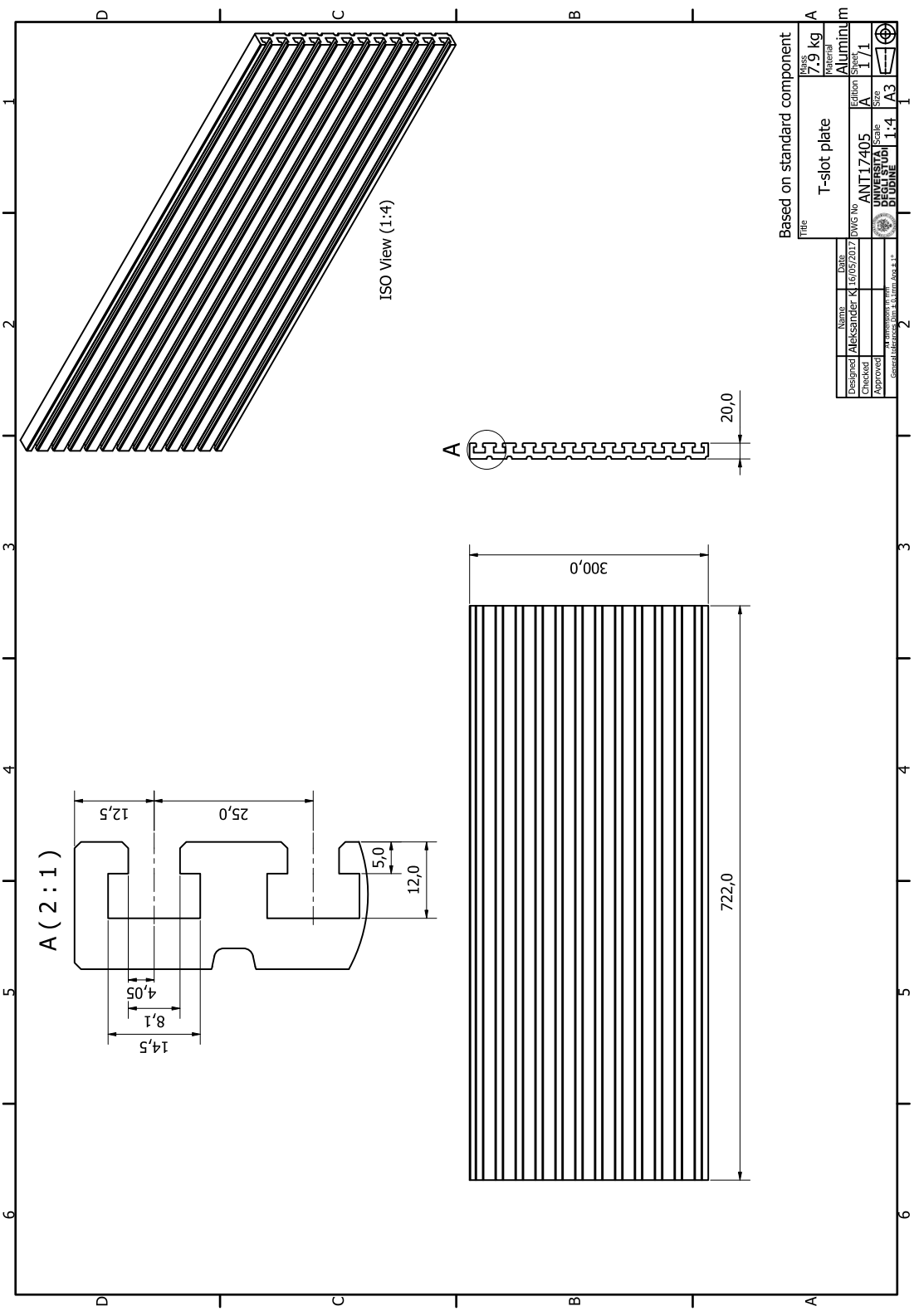
ISO View (1:4)
A
20,0
300,0
722,0
A (2 : 1)
12,5
25,0
5,0
12,0
4,05
8,1
14,5
Based on standard component
Title
T-slot plate
Mass
7.9 kg
Material
Aluminum
Sheet
1/1
Edition
A
Size
A3
DWG No
ANT17405
Scale
1:4
UNIVERSITÀ DEGLI STUDI DI UDINE
Designed
Checked
Approved
Name
Aleksander K
Date
16/05/2017

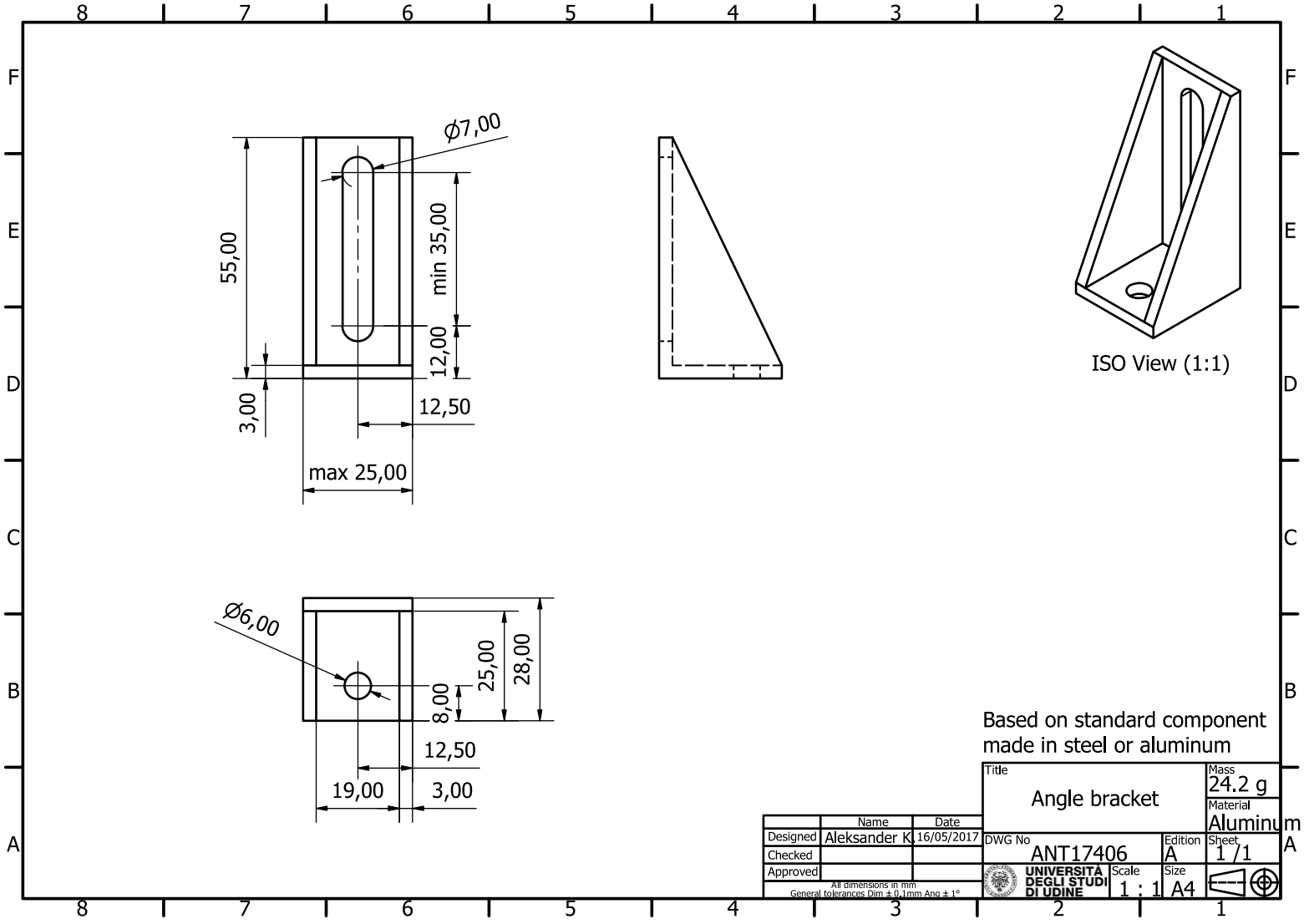
ϕ7,00
55,00
min 35,00
12,00
3,00
12,50
max 25,00
Ø6,00
25,00
28,00
8,00
12,50
19,00
3,00
ISO View (1:1)
Based on standard component
made in steel or aluminum
Name
Date
Designed
Aleksander K.
16/05/2017
Checked
Approved
All dimensions in mm
General tolerances Dim ± 0,1mm Ang ± 1°
Title
Angle bracket
Mass
24.2 g
Material
Aluminum
DWG No
ANT17406
Edition
A
Sheet
1 /1
UNIVERSITÀ DEGLI STUDI DI UDINE
Scale
1 : 1
Size
A4

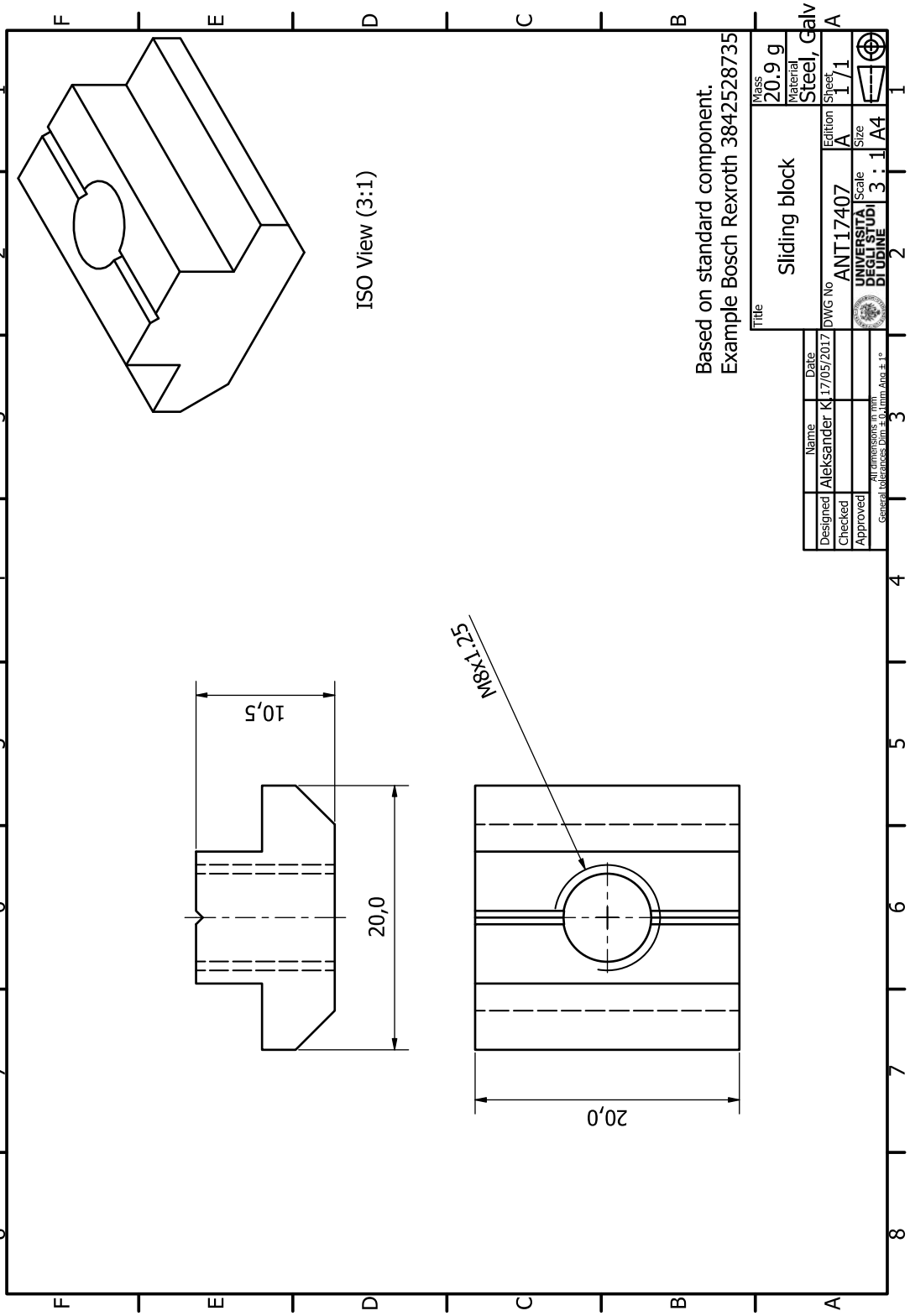
ISO View (3:1)
Based on standard component.
Example Bosch Rexroth 3842528735
Mass 20.9 g
Material Steel, Galv
Sheet 1 / 1
Edition A
Size A4
Scale 3 : 1
Title Sliding block
DWG No ANT17407
UNIVERSITÀ DEGLI STUDI DI UDINE
Designed Aleksander K 17/05/2017
Checked
Approved
All dimensions in mm
General tolerances Dim ± 0.1mm Ang ± 1°
M8x1.25
10,5
20,0
20,0

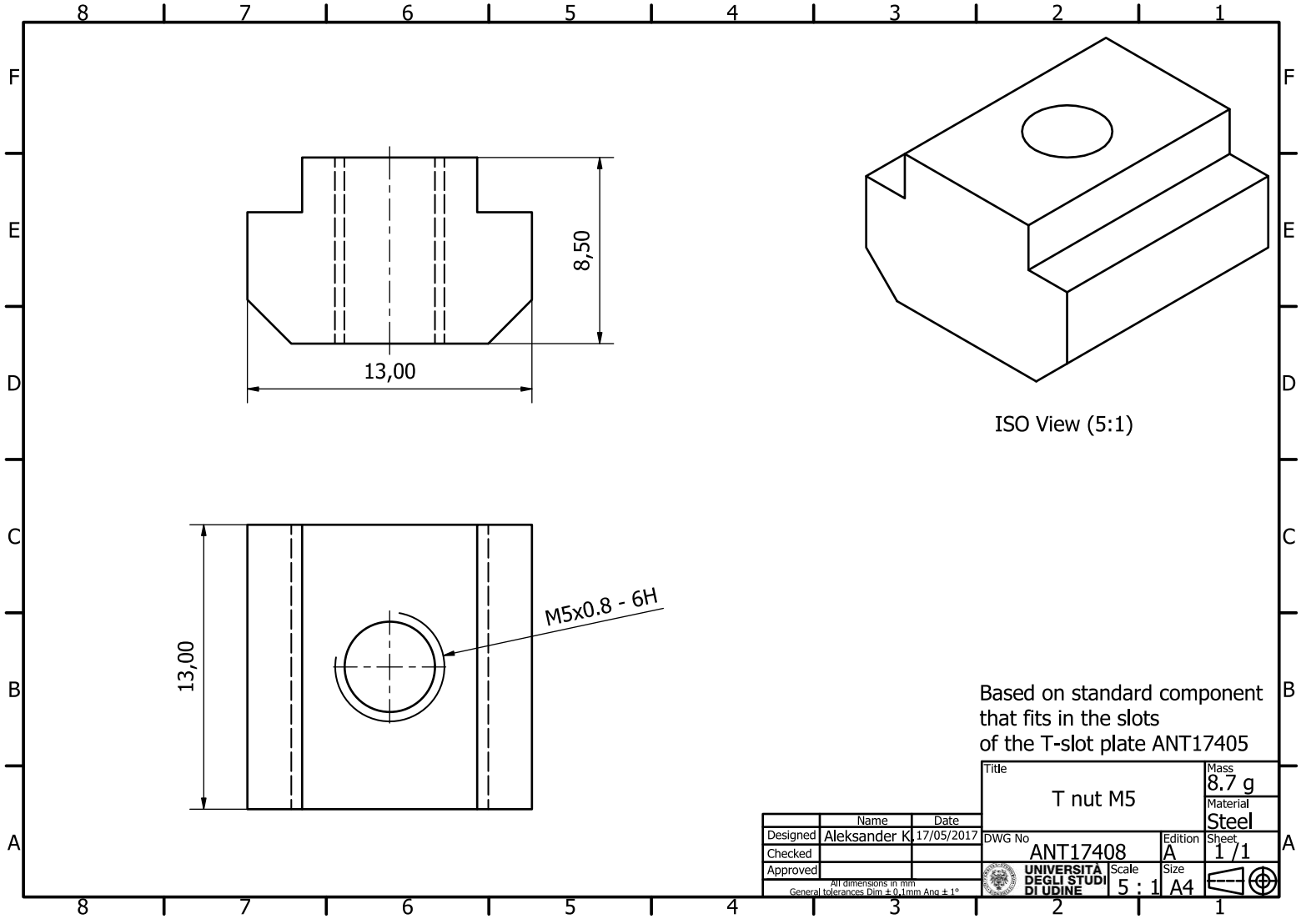
8,50
13,00
ISO View (5:1)
13,00
M5x0.8 - 6H
Based on standard component
that fits in the slots
of the T-slot plate ANT17405
Name
Date
Designed
Aleksander K.
17/05/2017
Checked
Approved
All dimensions in mm
General tolerances Dim ± 0,1mm Ang ± 1°
Title
T nut M5
Mass
8.7 g
Material
Steel
DWG No
ANT17408
Edition
A
Sheet
1 /1
UNIVERSITÀ DEGLI STUDI DI UDINE
Scale
5 : 1
Size
A4

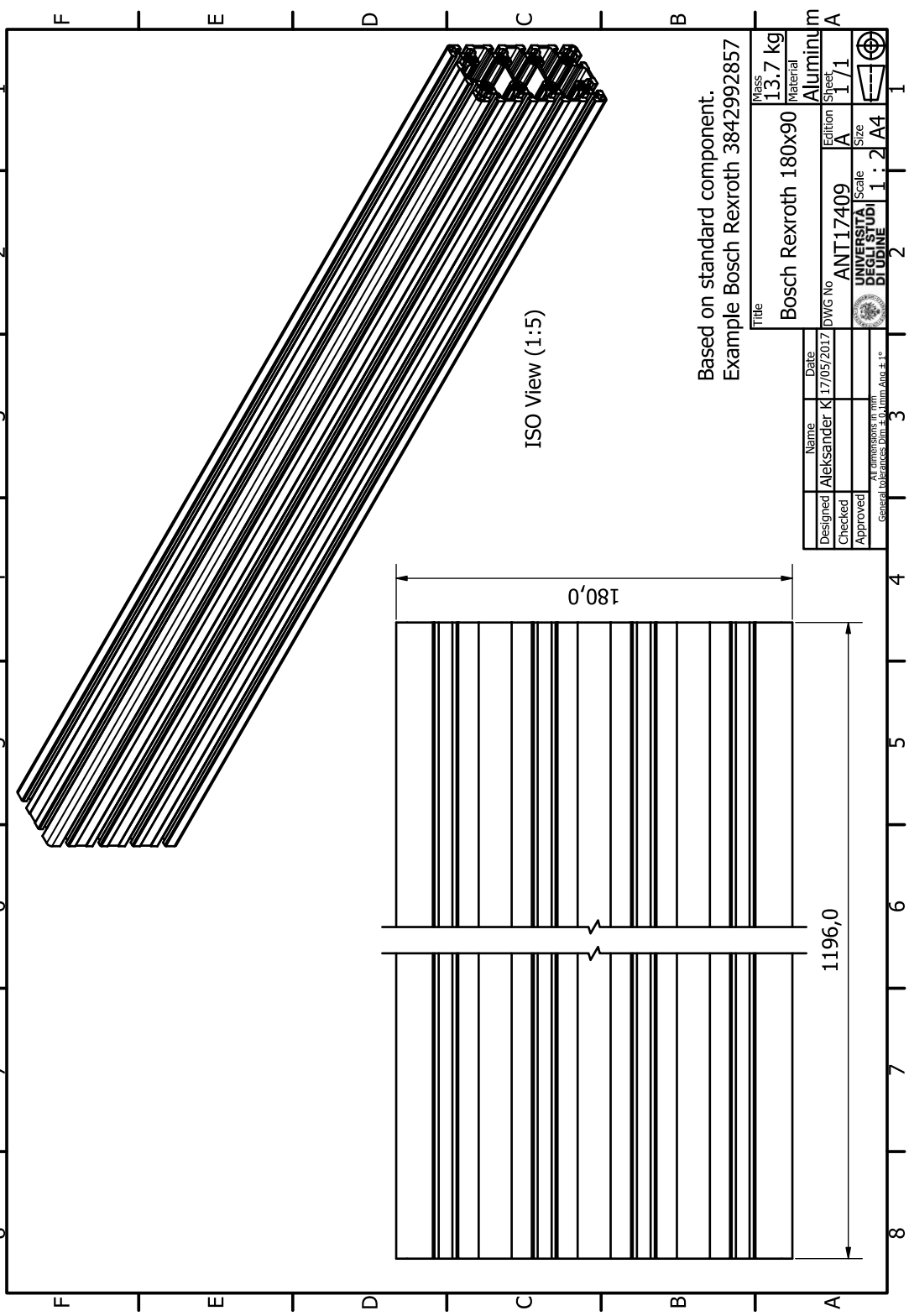
ISO View (1:5)
Based on standard component.
Example Bosch Rexroth 3842992857
180,0
1196,0
Bosch Rexroth 180x90
Mass 13.7 kg
Material Aluminum
Edition A
Sheet 1/1
DWG No ANT17409
Scale 1 : 2
Size A4
Designed Aleksander K 17/05/2017
Checked
Approved
All dimensions in mm
General tolerances Dim ±0.1mm Ang ±1°
UNIVERSITÀ DEGLI STUDI DI UDINE

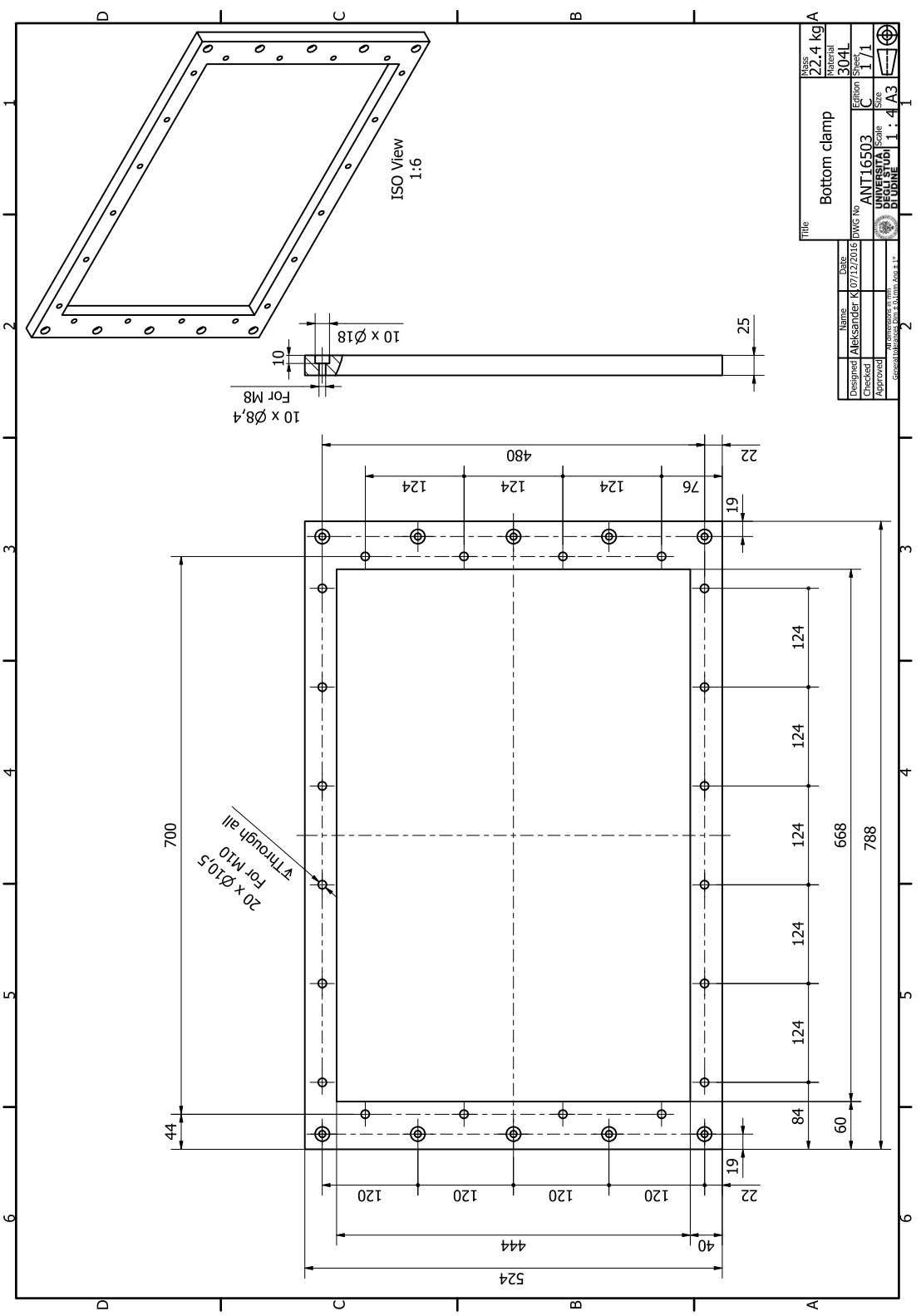
ISO View
1:6
10 x Ø18
10
25
10 x Ø8,4
For M8
480
22
124
124
124
76
19
700
20 x Ø10,5
For M10
Through all
124
124
124
124
124
668
788
44
84
60
19
120
120
120
120
22
444
40
524
Mass
22.4 kg
Material
304L
Sheet
1/1
Edition
C
Size
A3
Scale
1 : 4
Title
Bottom clamp
DWG No.
ANT16503
UNIVERSITÀ DEGLI STUDI DI UDINE
Name
Date
Designed
Aleksander K
07/12/2016
Checked
Approved
All dimensions in mm
General tolerances: Dim ± 0,1mm Ang ± 1°

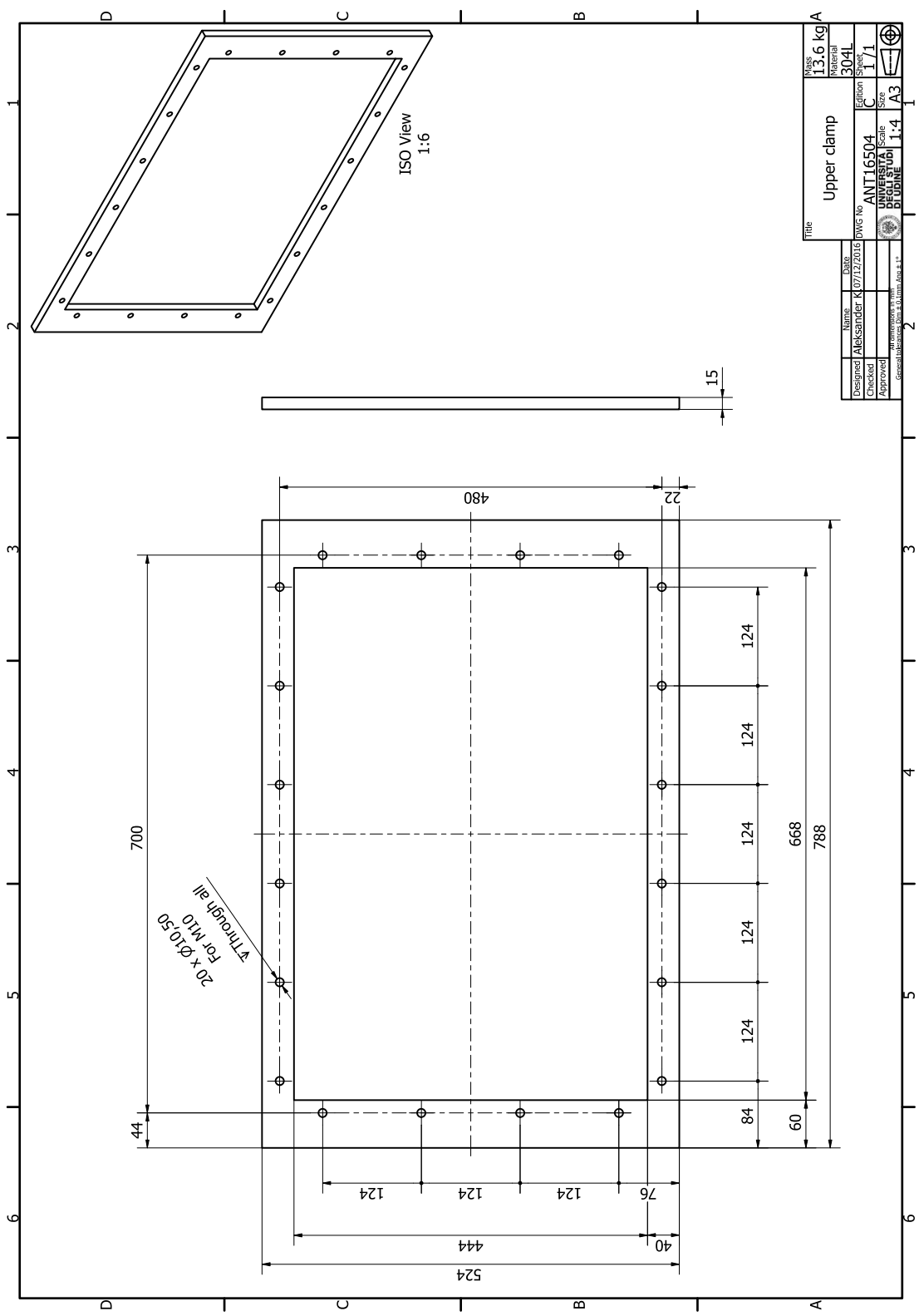
ISO View
1:6
15
480
22
700
668
788
124
124
124
124
124
84
60
44
20 x Ø10.50
For M10
Through all
524
444
40
76
124
124
124
Upper clamp
ANT16504
Mass
13.6 kg
Material
304L
Sheet
1/1
Edition
C
Size
A3
Scale
1:4
Name
Date
Designed
Aleksander K
07/12/2016
Checked
Approved
UNIVERSITÀ DEGLI STUDI DI UDINE

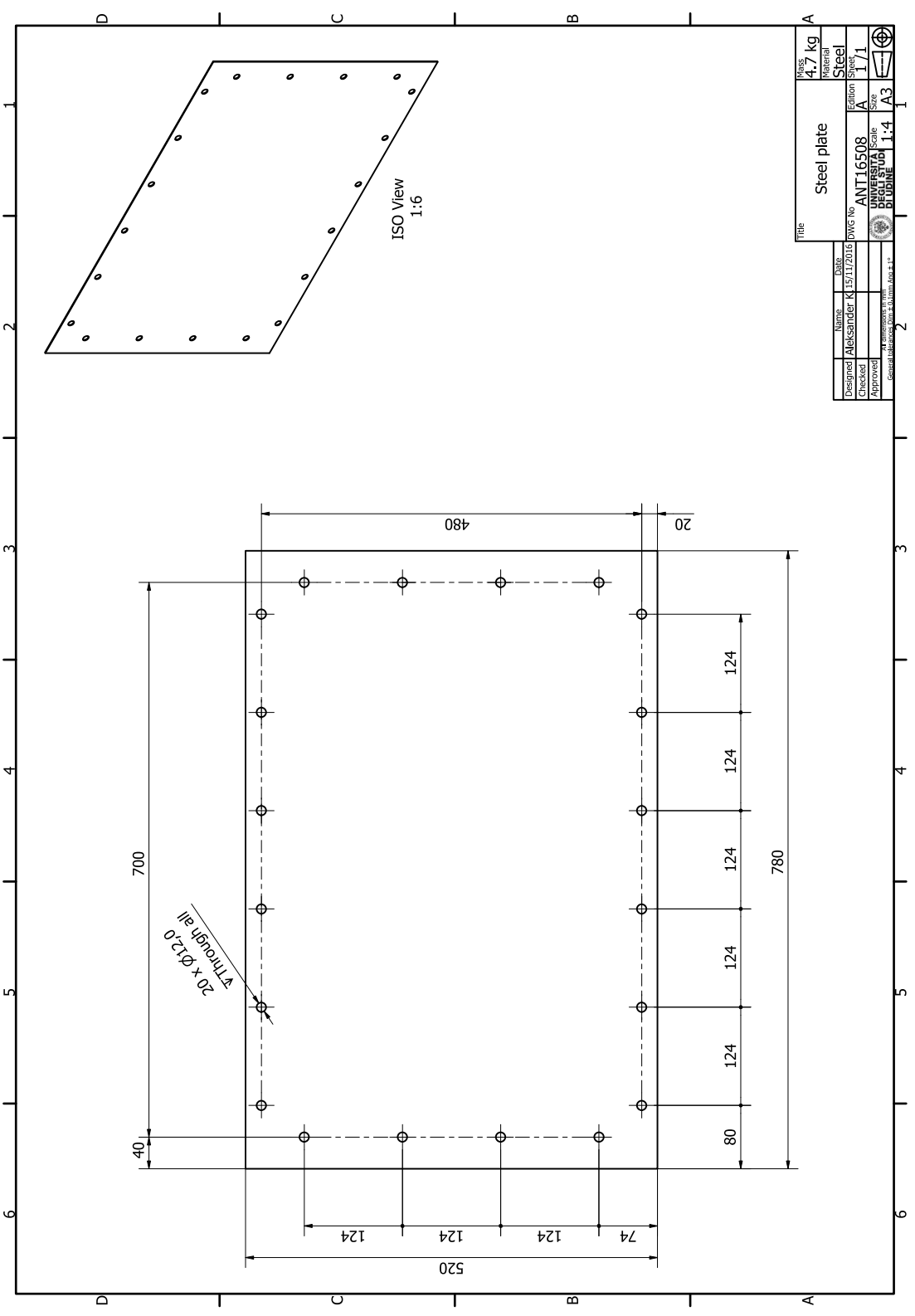
ISO View
1:6
480
20
700
780
40
124
124
124
124
124
80
520
124
124
124
74
20 x Ø12,0
Through all
Mass
4.7 kg
Material
Steel
Sheet
1/1
Edition
A
Size
A3
Title
Steel plate
DWG No
ANT16508
Scale
1:4
UNIVERSITÀ DEGLI STUDI DI UDINE
Designed
Checked
Approved
Name
Aleksander K
Date
15/11/2016
All dimensions in mm
General tolerance ISO 2768-mK

D

LIST OF EQUIPMENT

The following appendix presents list of equipment used in the measurements of transducers elecromechanical properties and in the implementation of the velocity feedback control loops on a rectangular plate with an EM actuators. The equipment used in the measurements is listed in Table D.1

Table D.1. List of the equipment used in the measurements.

No.	Equipment	Manufacturer	Model
1	ICP Impedance head	PCB	288D01
2	ICP Force cell	PCB	208C01
3	ICP Accelerometer	PCB	352C65
4	Shaker 1	PCB	2004E
6	Shaker 2	PCB	2075E
7	Shaker amplifier	PCB	2100E21-400
8	ICP Integrator	PCB	480B10
9	Voltage probe	Pico Technology	KA405
10	Current probe	Pico Technology	TA018
11	Quad amplifier	InterM	QD-4480
12	Piezo amplifier	ElbaTech	T-500
13	Signal analyser	DP Data Physics	Abacus
14	Laser vibrometer	Polytec	PSV-I-500

BIBLIOGRAPHY

[1] W. T. Thomson and M. D. Dahleh, *Theory of vibrations with applications, fifth edition*. Prentice hall, 2005.

[2] L. Meirovitch, *Fundamentals of vibrations*. Mcgraw-Hill international edition, 2001.

[3] D. J. Inman, *Vibration with Control*. John Wiley & Sons, 2006.

[4] A. Pagès, F. Claeyssen, M. Hihoud, and M. Bagot, "Rotation Free Linear Actuator," in *Proceedings of the 13th International Conference on New Actuators, ACTUATOR 2012*, 2012, pp. 72–75.

[5] Cedrat Technologies, "A new 3m-long ultrasonic reactor," 2015.

[6] M. Ruzzene, "Frequency-wavenumber domain filtering for improved damage visualization," *Smart Materials and Structures*, vol. 16, no. 6, pp. 2116–2129, 2007.

[7] P. Becht, E. Deckers, C. Claeys, B. Pluymers, and W. Desmet, "Defect detection in pipes based on the measurement of surface displacements," in *Proceedings of the 8th European Workshop on Structural Health Monitoring, EWSHM 2016*, 2016, vol. 2, pp. 7–11.

[8] C. Moutinho, A. Cunha, and E. Caetano, "Implementation of an Active Mass Damper To Control Vibrations in a ' Lively ' Footbridge," *Proceedings of the III ECCOMAS Thematic Conference on Smart Structures and Materials*, pp. 1–18, 2007.

[9] J. Simpson and J. Schweiger, "Industrial approach to piezoelectric damping of large fighter aircraft components," in *Proceedings of the SPIE 3326, Smart Structures and Materials: Industrial and Commercial Applications of Smart Structures Technologies*, 1998, pp. 34–46.

[10] S. Wu, T. L. Turner, and S. A. Rizzi, "Piezoelectric shunt vibration damping of an F-15 panel under high-acoustic excitation," in *Proceedings of the SPIE 3989, Smart Structures and Materials: Damping and Isolation*, 2018, vol. 3989, pp. 1–11.

[11] E. Zumelzu, R. Pereira, J. P. Arenas, F. Rull, and R. Silva, "Influence of vibrations on interface delamination in metal–polymer composites," *Journal of Applied Polymer Science*, vol. 125, pp. 97–103, 2011.

[12] F. Ripamonti, G. Cazzulani, S. Cinquemani, F. Resta, and A. Torti, "Adaptive active vibration control to improve the fatigue life of a carbon-epoxy smart structure," in *Proceedings of the SPIE Active and Passive Smart Structures and Integrated Systems*, 2015, vol. 9431.

[13] P. Gardonio, "Review of Active Techniques for Aerospace Vibro-Acoustic Control," *Journal of Aircraft*, vol. 39, no. 2. pp. 206–214, 2002.

[14] J. F. Wilby, "Aircraft interior noise," *Journal of Sound and Vibration*, vol. 190, no. 3, pp. 545–564, 1996.

[15] C. R. Fuller, S. J. Elliott, and P. A. Nelson, *Active Control of Vibration*. London: Academic Press, 1997.

[16] J. E. Mottershead, M. Ghandchi Tehrani, S. James, and P. Court, "Active vibration control experiments on an Augusta Westland W30 helicopter airframe," *Journal of Mechanical Engineering Science*, vol. 226, no. 6, pp. 1504–1516, 2011.

[17] H. Rottmayr, W. Popp, R. Mehlhose, and E. D. Gmbh, "Application of modern vibration control techniques on EC135 and future trends," in *The 23rd European Rotorcraft Forum*, 1997, pp. 1–17.

[18] J. Rohlfing and P. Gardonio, "Ventilation duct with concurrent acoustic feed-forward and decentralised structural feedback active control," *Journal of Sound and Vibration*, vol. 333, no. 3, pp. 630–645, 2014.

[19] M. P. Norton and D. G. Karczub, *Fundamentals of Noise and Vibration Analysis for Engineers, 2nd Edition*. Cambridge University Press, 2003.

[20] M. Griffin, *Handbook of human vibration*. London: Academic press, 1990.

[21] F. Fahy and D. Thompson, *Fundamentals of Sound and Vibration, Second Edition*. CRC Press, 2015.

[22] W. Bachta, P. Renaud, E. Laroche, J. Gangloff, and A. Forgione, "Cardiolock: an active cardiac stabilizer first in vivo experiments using a new robotized device," *Computer Aided Surgery*, vol. 4791, no. 10, pp. 78–85, 2007.

[23] A. Preumont, *Vibration Control of Active Structures, An Introduction 3rd Edition*, vol. 179. Springer, 2011.

[24] C. Collette, D. Tshilumba, F. Nassif, R. Furn, S. Janssens, and K. Artoos, "Vibration isolation of an extended object," in *Proceedings of the 15th International Conference & Exhibition, euspen*, 2015, pp. 8–9.

[25] A. Kras, F. Bourgain, and F. Claeyssen, "Amplified Piezo Actuator APA® with viscoelastic material for machine tool semi-active damping system," *Journal of Machine Engineering*, vol. 13, no. 2, pp. 83–96, 2013.

[26] A. Harms, B. Denkena, N. Lhermet, and M. Tools, "Tool adaptor for active vibration control in turning operations," in *Proceedings of the 9th International Conference on New Actuators, ACTUATOR 2004*, 2004, pp. 694–697.

[27] P. Gardonio, "Sensors and actuators for active structural acoustic and active vibration feedback control," in *Proceedings of the IV ECCOMAS Thematic Conference on Smart Structures and Materials*, 2009, pp. 215–234.

[28] A. Preumont, *Mechatronics, dynamics of electromechanical and piezoelectric systems*. Dordrecht, Netherlands, 2006.

[29] S. J. Elliott, *Signal processing for active control*. Academic Press, 2001.

[30] S. J. Elliott and P. A. Nelson, *Active Control of Sound*. Academic Press, 1992.

[31] C. Paulitsch, P. Gardonio, and S. J. Elliott, "Active vibration damping using an inertial, electrodynamic actuator," *Journal of Vibration and Acoustics*, vol. 129, no. 39–47, pp. 282–293, 2007.

[32] M. J. Balas, "Direct Velocity Feedback Control of Large Space Structures," *Journal of Guidance, Control, and Dynamics*, vol. 2, no. 3. pp. 252–253, 1979.

[33] C. G. Díaz, C. Paulitsch, and P. Gardonio, "Smart panel with active damping units. Implementation of decentralized control," *The Journal of the Acoustical Society of America*, vol. 124, no. 2, pp. 898–910, 2008.

[34] P. Gardonio, S. Miani, F. Blanchini, D. Casagrande, and S. J. Elliott, "Plate with decentralised velocity feedback loops: Power absorption and kinetic energy considerations," *Journal of Sound and Vibration*, vol. 331, no. 8, pp. 1722–1741, 2012.

[35] M. Zilletti, S. J. Elliott, and P. Gardonio, "Self-tuning control systems of decentralised velocity feedback," *Journal of Sound and Vibration*, vol. 329, no. 14, pp. 2738–2750, 2010.

[36] M. Zilletti, S. J. Elliott, P. Gardonio, and E. Rustighi, "Experimental implementation of a self-tuning control system for decentralised velocity feedback," *Journal of Sound and Vibration*, vol. 331, no. 1, pp. 1–14, 2012.

[37] M. Zilletti, S. J. Elliott, and E. Rustighi, "Optimisation of dynamic vibration absorbers to minimise kinetic energy and maximise internal power dissipation," *Journal of Sound and Vibration*, vol. 331, no. 18, pp. 4093–4100, 2012.

[38] C. Paulitsch, P. Gardonio, and S. Elliott, "Active vibration damping using self-sensing, electrodynamic actuators," *Journal of Smart Materials and Structures*, vol. 15, no. 2, pp. 499–508, 2006.

[39] N. G. Stephen, "On energy harvesting from ambient vibration," *Journal of Sound and Vibration*, vol. 293, no. 1–2, pp. 409–425, 2006.

[40] C. Paulitsch, P. Gardonio, and S. J. Elliott, "Active vibration damping using an electrodynamic actuator with internal velocity sensor," *Proceedings of the SPIE, The International Society for Optical Engineering*, vol. 5760, pp. 305–316, 2005.

[41] C. Paulitsch, P. Gardonio, and S. J. Elliott, "Active vibration control using an inertial actuator with internal damping," *The Journal of the Acoustical Society of America*, vol. 119, no. 4, pp. 2131–2140, 2006.

[42] L. Benassi and S. J. Elliott, "Global control of a vibrating plate using a feedback-controlled inertial actuator," *Journal of Sound and Vibration*, vol. 283, no. 1–2, pp. 69–90, 2005.

[43] L. Cremer, M. Heckl, and B. A. T. Petersson, *Structure-borne sound; Structural vibrations and sound radiation at audio frequencies*. Springer, 2005.

[44] B. L. J. Gysen, J. J. H. Paulides, J. L. G. Janssen, and E. A. Lomonova, "Active elctromagnetic suspension system for improved vehicle dynamics," in *IEEE Vehicle Power and Propulsion Conference*, 2008, vol. 59, no. 3, pp. 1156–1163.

[45] L. Simeone, M. G. Tehrani, and S. J. Elliott, "Design of an electromagnetic-transducer energy harvester," *Journal of Physics: Conference Series*, vol. 744, no. 1, 2016.

[46] S. J. Elliott and M. Zilletti, "Scaling of electromagnetic transducers for shunt damping and energy harvesting," *Journal of Sound and Vibration*, vol. 333, no. 8, pp. 2185–2195, 2014.

[47] L. Dal Bo and P. Gardonio, "Vibration Energy Harvesting With Electromagnetic and Piezoelectric Seismic Transducers : Simulation and Experimental Results," in *Proceedings of the VIII ECCOMAS Thematic Conference on Smart Structures and Materials*, 2017, pp. 1–12.

[48] D. W. Miller and E. F. Crawley, "Theoretical and experimental investigation of space-realizable inertial actuation for passive and active structural control," *Journal of Guidance, Control, and Dynamics*, vol. 11, no. 5, pp. 449–458, 1988.

[49] D. K. Lindner, G. A. Zvonar, D. Borojevic, and V. Tech, "Nonlinear control of a proof-mass actuator," *Journal of Guidance, Control, and Dynamics Vol.*, vol. 20, no. 3, pp. 464–470, 1997.

[50] J. Scruggs and D. K. Lindner, "Optimal sizing of a proof-mass actuator," *American Institute for Aeronautics and Astronautics*, pp. 1–11, 1999.

[51] S. Griffin, J. Gussy, S. A. Lane, B. K. Henderson, and D. Sciulli, "Virtual skyhook vibration isolation system," *Journal of Vibration and Acoustics*, vol. 124, no. 1, pp. 63–67, 2001.

[52] S. J. Elliott, M. Serrand, and P. Gardonio, "Feedback stability limits for active isolation systems with reactive and inertial actuators," *Journal of Vibration and Acoustics*, vol. 123, no. 2, pp. 250–261, 2001.

[53] C. González Díaz and P. Gardonio, "Feedback control laws for proof-mass electrodynamic actuators," *Smart Materials and Structures*, vol. 16, no. 5, pp. 1766–1783, 2007.

[54] C. G. Díaz, C. Paulitsch, and P. Gardonio, "Active damping control unit using a small scale proof mass electrodynamic actuator," *The Journal of the Acoustical Society of America*, vol. 124, no. 2, pp. 886–897, 2008.

[55] P. Gardonio and C. G. Diaz, "Downscaling of proof mass electro-dynamic actuators for decentralised velocity feedback control on a panel," *Smart Materials and Structures*, vol. 19, no. 2, pp. 1–14, 2010.

[56] C. Paulitsch, P. Gardonio, S. J. Elliott, P. Sas, and R. Boonen, "Design of a lightweight, electrodynamic, inertial actuator with integrated velocity sensor for active vibration control of a thin lightly-damped panel," in *Proceedings of the International Conference on Noise and Vibration Engineering ISMA2004*, 2004, pp. 239–254.

[57] C. Paulitsch, *Vibration control with electrodynamic actuators*. Düsseldorf: VDI Verlag, 2005.

[58] H. Politansky and W. D. Pilkey, "Suboptimal feedback vibration control of a beam with a proof-mass actuator," *Journal of Guidance, Control, and Dynamics*, vol. 12, no. 5, pp. 691–697, 1989.

[59] W. L. Hallauer and S. E. Lamberson, "Experimental active vibration damping of a plane truss using hybrid actuation," in *Proceedings of the Structural Dynamics and Materials Conference, 30th Structures*, 1989, pp. 80–90.

[60] D. C. Zimmerman and D. J. Inman, "On the nature of the interaction between structures and proof-mass actuators," *Journal of Guidance, Control, and Dynamics*, vol. 13, no. 1, pp. 82–88, 1990.

[61] D. K. Lindner, T. P. Celano, and E. N. Ide, "Vibration suppression using a proofmass actuator operating in stroke/force saturation," *Journal of Vibration and Acoustics*, vol. 113, no. 4, pp. 423–433, 1991.

[62] D. K. Lindner, G. a. Zvonar, and D. Borojevic, "Performance and control of proof-mass actuators accounting for stroke saturation," *AIAA Journal of Guidance, Dynamics, and Control*, vol. 17, no. 5, pp. 1103–1108, 1994.

[63] E. Garcia, C. S. Webb, and M. J. Duke, "Passive and active control of a complex flexible structure using reaction mass actuators," *Journal of Vibration and Acoustics*, vol. 117, no. 1, pp. 116–122, 1995.

[64] Y. Okada, K. Matsuda, and H. Hashitani, "Self-sensing active vibration control using moving-coil-type actuator," *Journal of Vibration and Acoustics*, vol. 117, no. 4, pp. 411–415, 1995.

[65] S. Matunaga, Y. Yu, and Y. Ohkami, "Vibration suppression using acceleration feedback control with multiple proof-mass actuators," *AIAA Journal*, vol. 35, no. 5, pp. 856–862, 1997.

[66] J. Rohlfing, P. Gardonio, and S. J. Elliott, "Base impedance of velocity feedback control units with proof-mass electrodynamic actuators," *Journal of Sound and Vibration*, vol. 330, no. 20, pp. 4661–4675, 2011.

[67] S. H. Crandall, D. C. Karnopp, E. F. Kurtz, and D. C. Pridmore-Brown, *Dynamics of mechanical and electromechanical systems*. Krieger Pub Co. Malabar, 1982.

[68] F. Fahy and P. Gardonio, *Sound and structural vibration; Radiation, Transmission and Response*, no. 2. 2007.

[69] J. R. Brauer, *Magnetic actuators and sensors, 2nd Edition*. Wiley-IEEE Press, 2014.

[70] D. C. Zimmerman, G. C. Horner, and D. J. Inman, "Microprocessor controlled force actuator," *Journal of Guidance, Control, and Dynamics*, vol. 11, no. 3, pp. 230–236, 1988.

[71] S. Cinquemani, F. Braghin, and F. Resta, "Semi active tunable mass damper for helicopters," *Proceedings of the SPIE, The International Society for Optical Engineering*, vol. 10164. 2017.

[72] S. Cinquemani and F. Braghin, "Decentralized active vibration control in cruise ships funnels," *Journal of Ocean Engineering*, vol. 140, pp. 361–368, 2017.

[73] S. Cinquemani and H. Giberti, "Magnetic design of a new flat magnetostrictive actuators," *International Journal of Applied Engineering Research*, vol. 11, no. 24, pp. 11768–11774, 2016.

[74] J. Peirs, "Design of micromechatronic systems: scale laws, technologies, and medical applications, PhD Thesis," KU Leuven, Belgium, 2001.

[75] O. N. Baumann and S. J. Elliott, "Destabilization of velocity feedback controllers with stroke limited inertial actuators.," *The Journal of The Acoustical Society Of America*, vol. 121, no. 5, pp. 211–217, 2007.

[76] A. Kras, M. Brahim, T. Porchez, C. Bouchet, and F. Claeyssen, "Compact , lightweight , and efficient piezo-actuation chain for aeronautical applications," in *Proceedings of the 14th International Conference on New Actuators, ACTUATOR 2014*, 2014, pp. 23–25.

[77] A. Kras, O. Sosnicki, S. Rowe, F. Battistello, and F. Claeyssen, "Extreme performances of piezo system : high stroke , high frequency , high temperature," in *Proceedings of the 7th ECCOMAS Thematic Conference on Smart Structures and Materials, SMART2015*, 2015, pp. 1–8.

[78] D. Casagrande, P. Gardonio, and M. Zilletti, "Smart panel with time-varying shunted piezoelectric patch absorbers for broadband vibration control," *Journal of Sound and Vibration*, vol. 400, pp. 288–304, 2017.

[79] P. Gardonio and D. Casagrande, "Shunted piezoelectric patch vibration absorber on two-dimensional thin structures: Tuning considerations," *Journal of Sound and Vibration*, vol. 395, pp. 26–47, 2017.

[80] D. Casagrande, "Piezoelectric transducers for broadband vibration control, PHD Thesis," University of Udine, Italy, 2016.

[81] Y. Aoki, P. Gardonio, and S. J. Elliott, "Rectangular plate with velocity feedback loops using triangularly shaped piezoceramic actuators: Experimental control performance," *The Journal of the Acoustical Society of America*, vol. 123, no. 3, pp. 1421–1426, 2008.

[82] NEC / TOKIN, "Multilayer piezoelectric actuators," vol. 05. TOKIN, 2017.

[83] Cedrat Technologies, "Compact, dynamic, precise; Product Catalogue," vol. 4.1, p. 141, 2013.

[84] Noliac, "Amplified actuators," 2018. [Online]. Available: http://www.noliac.com/products/actuators/amplified-actuators/.

[85] S. Cinquemani, G. Cazzulani, A. Costa, and F. Resta, "Design of a stand-alone active damper for distributed control of vibration," in *Proceedings of the SPIE 9799 Active and Passive Smart Structures and Integrated Systems*, 2016, vol. 9799, pp. 1–8.

[86] S. J. Elliott, P. Gardonio, T. C. Sors, and M. J. Brennan, "Active vibroacoustic control with multiple local feedback loops," *The Journal of the Acoustical Society of America*, vol. 111, no. 2, pp. 908–915, 2002.

[87] W.S.N.Trimmer, "Microrobots and micromechanical systems," *Sensors and Actuators*, vol. 19, no. 3, pp. 267–289, 1989.

[88] A. Ghosh and B. Corves, *Introduction to micromechanisms and microactuators*. Springer, 2015.

[89] M. J. Madou, *Fundamentals of microfabrication: the science of miniaturization, first edition*. CRC Press, 1997.

[90] N. Bencheikh, A. Pagès, T. Forissier, T. Porchez, and A. Kras, "A bistable piezoelectric harvester for wideband mechanical frequency excitation," in *Proceedings of the 14th International Conference on New Actuators / ACTUATOR*, 2014.

[91] L. Dal Bo and P. Gardonio, "Comparison between electromagnetic and piezoelectric seismic vibration energy harvesters," in *Proceedings of the International Conference on Noise and Vibration Engineering ISMA2016*, 2016, pp. 681–694.

[92] S. Cinquemani, F. Resta, M. Monguzzi, D. Meccanica, and P. Milano, "Limits on the use of inertial actuators in active vibration control," in *Proceedings of the 9th International Conference on Computing, Communications and Control Technologies, CCCT*, 2011, pp. 1–6.

[93] J. M. Maciejowski, *Multivariable feedback design*. E L Dagless, 1989.

[94] S. Skogestad and I. Postlethwaite, *Multivariable feedback control: analysis and design*. John Wiley & Sons, 2005.

[95] L. Meirovitch, *Dynamics and control of structures*. New York: John Wiley & Sons, 1990.

[96] O. N. Baumann and S. J. Elliott, "The stability of decentralized multichannel velocity feedback controllers using inertial actuators," *The Journal of the Acoustical Society of America*, vol. 121, no. 1, pp. 188–196, 2007.

[97] L. I. Wilmshurst, M. Ghandchi-Tehrani, and S. J. Elliott, "Nonlinear vibrations of a stroke-saturated inertial actuator," in *Proceedings of the International Conference on Recent Advances in Structural Dynamics RASD 2013*, 2013, pp. 1–13.

[98] M. Dal Borgo, M. Ghandchi Tehrani, and S. J. Elliott, "Dynamic analysis of two nonlinear inertial actuators in active vibration control," in *Proceedings of the International Conference on Noise and Vibration Engineering ISMA2016*, 2016, pp. 1179–1190.

[99] M. Dal Borgo, M. G. Tehrani, and S. J. Elliott, "Dynamic analysis of nonlinear behaviour in inertial actuators," in *Proceedings of the International Conference on Recent Advances in Structural Dynamics RASD 2016*, 2016, pp. 1–12.

[100] M. Dal Borgo, M. G. Tehrani, and S. J. Elliott, "Nonlinear control and stability analysis of a stroke limited inertial actuator in velocity feedback," in *Proceedings of the 9th European Nonlinear Dynamics Conference, ENOC 2017*, 2017, vol. 2, no. 4, pp. 1–10.

[101] L. Benassi and S. J. Elliott, "Active vibration isolation using an inertial actuator with local displacement feedback control," *Journal of Sound and Vibration*, vol. 278, no. 4–5, pp. 705–724, 2004.

[102] L. Benassi, S. J. Elliott, and P. Gardonio, "Active vibration isolation using an inertial actuator with local force feedback control," *Journal of Sound and Vibration*, vol. 276, no. 1–2, pp. 157–179, 2004.

[103] C. P. Paulitsch, P. Gardonio, and S. J. Elliott, "Active vibration control using an inertial actuator with variable internal damping," *The Journal of the Acoustical Society of America*, vol. 119, no. 4, pp. 2131–2140, 2006.

[104] A. Preumont and N. Loix, "Active damping of a stiff beam-like structure with acceleration feedback," *Journal of Experimental mechanics*, vol. 34, no. 1, pp. 23–26, 1994.

[105] J. Rohlfing, S. J. Elliott, and P. Gardonio, "Feedback compensator for control units with proof-mass electrodynamic actuators," *Journal of Sound and Vibration*, vol. 331, no. 15, pp. 3437–3450, 2012.

[106] A. Lanzon and I. R. Petersen, "Stability robustness of a feedback interconnection of systems with negative imaginary frequency response," *IEEE Transactions on Automatic Control*, vol. 53, no. 4, pp. 1042–1046, 2008.

[107] C. J. Goh and T. K. Caughey, "On the stability problem caused by finite actuator dynamics in the collocated control of large space structures," *International Journal of Control*, vol. 41, no. 3, pp. 787–802, 1985.

[108] E. Omidi and S. N. Mahmoodi, "Implementation of H ∞ Modified Positive Position and Velocity Feedback Controllers for Active Vibration Control of Flexible Structures in Multimode," in *Proceedings of the American Control Conference (ACC)*, 2014, pp. 2735–2740.

[109] S. Poh and A. Baz, "Active Control of a Flexible Structure Using a Modal Positive Position Feedback Controller," *Journal of Intelligent Material Systems and Structures*, vol. 1, no. 3, pp. 273–288, 1990.

[110] A. Baz and S. Poh, "Optimal vibration control with modal positive position feedback," *Optimal Control Applications and Methods*, vol. 17, no. 2, pp. 141–149, 1963.

[111] I. Bar-Kana, R. Fischl, and P. Kalata, "Direct Position Plus Velocity Feedback Control of Large Flexible Space Structures," *IEEE Transactions on Automatic Control*, vol. 36, no. 10, pp. 1186–1188, 1991.

[112] N. Alujević, H. Wolf, P. Gardonio, and I. Tomac, "Stability and performance limits for active vibration isolation using blended velocity feedback," *Journal of Sound and Vibration*, vol. 330, no. 21, pp. 4981–4997, 2011.

[113] S. Gumuła and L. Łągiewka, "Conceptual design of vehicles protection against the impacts of collisions using the energy transfer method," *Journal of KONES Powertrain and Transport*, vol. 13, no. 1, pp. 269–277, 2006.

[114] M. C. Smith, "Synthesis of mechanical networks: The inerter," *IEEE Transactions on Automatic Control*, vol. 47, no. 10, pp. 1648–1662, 2002.

[115] M. C. Smith, "The inerter concept and its application," in *Society of Instrument and Control Engineers, SICE Annual Conference*, 2003, p. 40.

[116] C. Papageorgiou, N. E. Houghton, and M. C. Smith, "Experimental testing and analysis of inerter devices," *Journal of Dynamic Systems, Measurement, and Control*, vol. 131, pp. 1–11, 2009.

[117] C. Papageorgiou and M. C. Smith, "Laboratory experimental testing of inerters," in *Proceedings of the 44th IEEE Conference on Decision and Control*, 2005, pp. 3351–3356.

[118] M. Z. Q. Chen, C. Papageorgiou, F. Scheibe, F. Wang, and M. C. Smith, "The missing mechanical circuit element," *IEEE Circuits and Systems Magazine*, pp. 10–26, 2010.

[119] P. Brzeski, M. Lazarek, and P. Perlikowski, "Novel type of tuned mass damper with inerter which enables changes of inertance," *Journal of Sound and Vibration*, vol. 349, pp. 56–66, 2015.

[120] M. Zilletti, "Feedback control unit with an inerter proof-mass electrodynamic actuator," *Journal of Sound and Vibration*, vol. 369, pp. 16–28, 2015.

[121] N. Alujević, D. Čakmak, H. Wolf, and M. Jokić, "Passive and active vibration isolation systems using inerter," *Journal of Sound and Vibration*, vol. 418, pp. 163–183, 2018.

[122] P. Brzeski, E. Pavlovskaia, T. Kapitaniak, and P. Perlikowski, "The application of inerter in tuned mass absorber," *International Journal of Non-Linear Mechanics*, vol. 70, pp. 20–29, 2015.

[123] Y. Hu and M. Z. Q. Chen, "Performance evaluation for inerter-based dynamic vibration absorbers," *International Journal of Mechanical Sciences*, vol. 99, pp. 297–307, 2015.

[124] L. Marian and A. Giaralis, "Optimal design of a novel tuned mass-damper-inerter (TMDI) passive vibration control configuration for stochastically support-excited structural systems," *Probabilistic Engineering Mechanics*, vol. 38, pp. 156–164, 2015.

[125] I. F. Lazar, D. J. Wagg, and S. A. Neild, "A new vibration suppression system for semi-active control of a two-storey building," in *Proceedings of the 11th International Conference on Recent Advances in Structural Dynamics, RASD 2013*, 2013.

[126] I. F. Lazar, S. A. Neild, and D. J. Wagg, "Inerter-based Vibration Suppression Systems for Laterally and Base-Excited Structures," *Proceedings of the 9th International Conference on Structural Dynamics, EURODYN 2014*, pp. 1525–1530, 2014.

[127] I. F. Lazar, S. A. Neild, and D. J. Wagg, "Vibration suppression of cables using tuned inerter dampers," *Engineering Structures*, vol. 122, pp. 62–71, 2016.

[128] X. Jin, M. Z. Q. Chen, and Z. Huang, "Minimization of the beam response using inerter-based passive vibration control configurations," *International Journal of Mechanical Sciences*, vol. 119, no. October, pp. 80–87, 2016.

[129] A. Siami, H. R. Karimi, A. Cigada, E. Zappa, and E. Sabbioni, "Parameter optimization of an inerter-based isolator for passive vibration control of Michelangelo's Rondanini Pietà," *Mechanical Systems and Signal Processing*, vol. 98, pp. 667–683, 2018.

[130] Y. Shen, L. Chen, X. Yang, D. Shi, and J. Yang, "Improved design of dynamic vibration absorber by using the inerter and its application in vehicle suspension," *Journal of Sound and Vibration*, vol. 361, pp. 148–158, 2016.

[131] Y. Hu, M. Z. Q. Chen, and Y. Sun, "Comfort-oriented vehicle suspension design with skyhook inerter configuration," *Journal of Sound and Vibration*, vol. 405, pp. 34–47, 2017.

[132] P. Li, J. Lam, and K. C. Cheung, "Investigation on Semi-Active Control of Vehi-Cle Suspension Using Adaptive Inerter," in *Proceedings of the 21st International Congress on Sound and Vibration (ICSV21)*, 2014, pp. 1–8.

[133] M. C. Smith and F. Wang, "Performance benefits in passive vehicle suspensions employing inerters," *Vehicle System Dynamics*, vol. 42, no. 4, pp. 235–257, 2004.

[134] J. Salvi and A. Giaralis, "Concept study of a novel energy harvesting-enabled tuned mass-damper-inerter (EH-TMDI) device for vibration control of harmonically-excited structures," *Journal of Physics: Conference Series*, vol. 744, no. 1, pp. 1–13, 2016.

[135] P. Gardonio and M. J. Brennan, "Mobility and impedance methods in structural dynamics: an historical review," 2000.

[136] P. Gardonio and M. J. Brennan, "Mobility and impedance methods in structural dynamics," in *Advanced applications in acoustics, noise and vibration*, F. Fahy, Ed. London: Taylor and Francis, 2004, pp. 389–447.

[137] P. Gardonio and S. J. Elliott, "Passive and active isolation of structural vibration transmission between two plates connected by a set of mounts," *Journal of Sound and Vibration*, vol. 237, no. 3, pp. 483–511, 2000.

[138] P. Gardonio and S. J. Elliott, "Smart panels for active structural acoustic control," *Smart Materials and Structures*, vol. 13, no. 6, pp. 1314–1336, 2004.

[139] B. T. Wang, C. R. Fuller, and E. K. Dimitriadis, "Active control of noise transmission through rectangular plates using multiple piezoelectric or point force actuators," *The Journal of the Acoustical Society of America*, vol. 90, no. 5, pp. 2820–2830, 1991.

[140] R. D. Blevins, *Formulas for natural frequency and mode shape*. Van Nostrand Reinhold, 1979.

[141] G. Parmar, D. B. Hiemstra, Y. Chen, and S. Awtar, "A moving magnet actuator for large range nanopositioning," in *Proceedings of the ASME Conference*, 2011, pp. 41–48.

[142] D. B. Hiemstra, G. Parmar, and S. Awtar, "Performance tradeoffs posed by moving magnet actuators in flexure-based nanopositioning," *IEEE/ASME Transactions on Mechatronics*, vol. 19, no. 1, pp. 201–212, 2014.

[143] F. Bloch, N. Lhermet, P. Meneroud, and F. Claeyssen, "Space compliant moving coil actuator," in *Proceedings of the 9th International Conference on New Actuators, ACTUATOR 2004*, 2004, pp. 661–664.

[144] Actuators, "H2W Technologies, Inc." [Online]. Available: https://www.h2wtech.com/product/voice-coil-actuators/NCM02-17-035-2F.

[145] "Riverhawk Flexural Pivots." [Online]. Available: http://flexpivots.com/.

[146] "C-Flex Bearing Co." [Online]. Available: https://c-flex.com/.

[147] Y. Aoki, P. Gardonio, and S. J. Elliott, "Strain transducers for active control, lumped parameter model," 2006.

[148] Y. Aoki, P. Gardonio, D. Emo, and S. J. Elliott, "Stability and controllability of velocity feedback loops with triangularly shaped piezoelectric actuators," in *Proceedings of the International Symposium on Active Control of Sound and Vibration, Active 2006*, 2006, pp. 1–13.

[149] Y. Aoki, P. Gardonio, M. Gavagni, C. Galassi, and S. J. Elliott, "Parametric Study of a Piezoceramic Patch Actuator for Proportional Velocity Feedback Control Loop," *Journal of Vibration and Acoustics*, vol. 132, no. 6, pp. 1–10, 2010.